Universität Bonn

Physikalisches Institut

Search for the Standard Model Higgs boson pair production and new physics phenomena in the $b\bar{b}\tau^{+}_{had}\tau^{-}_{had}$ final state with the ATLAS detector

Alessandra Betti

A search for the Standard Model (SM) Higgs boson pair production and new physics phenomena in the $b\bar{b}\tau^{+}_{had}\tau^{-}_{had}$ final state is presented. The search uses 36.1 fb^{-1} of pp collisions data at a centre-of-mass energy of 13 TeV provided by the Large Hadron Collider (LHC) and recorded by the ATLAS experiment in 2015 and 2016. The observed (expected) 95% confidence level (CL) upper limit on the non-resonant di-Higgs production cross section is 16.4 (17.4) times the predicted SM cross section. The ratios of the Higgs boson self-coupling and of the top-quark Yukawa coupling to their SM expectations ($k_\lambda = \lambda_{HHH}/\lambda^{SM}_{HHH}$ and $k_t = y_t/y_t^{SM}$) are constrained at 95% confidence level respectively to $-9 < k_\lambda < 17$ and $-1.7 < k_t < 2$. The results of the $bb\tau_{had}\tau_{had}$ channel are statistically combined with the results of the $bb\tau_{lep}\tau_{had}$ channel and then further combined with the results of the $bbbb$ and $bb\gamma\gamma$ di-Higgs decay channels. The combined observed (expected) limit on the non-resonant di-Higgs production cross section corresponds to 6.7 (10.4) times the SM expectation and the triple Higgs self-coupling is constrained to $-5 < k_\lambda < 12.1$. Exclusion limits are also set on resonant Higgs boson pair production, probing a model with an extended Higgs sector based on two doublets, and a Randall-Sundrum bulk graviton model. In addition, a search for pair production of third generation scalar leptoquarks is performed in the $b\tau_{had}b\tau_{had}$ channel and combined with the $b\tau_{lep}\tau_{had}$ channel, setting limits on the leptoquark mass.

Physikalisches Institut der
Universität Bonn
Nussallee 12
D-53115 Bonn

BONN-IR-2019-08
July 2019
ISSN-0172-8741

Search for the Standard Model Higgs boson pair production and new physics phenomena in the $b\bar{b}\tau^{+}_{had}\tau^{-}_{had}$ final state with the ATLAS detector

Dissertation
zur
Erlangung des Doktorgrades (Dr. rer. nat.)
der
Mathematisch-Naturwissenschaftlichen Fakultät
der
Rheinischen Friedrich-Wilhelms-Universität Bonn

von
Alessandra Betti
aus
Rome, Italy

Bonn, 09.05.2019

Dieser Forschungsbericht wurde als Dissertation von der Mathematisch-Naturwissenschaftlichen Fakultät der Universität Bonn angenommen und ist auf dem Hochschulschriftenserver der ULB Bonn http://nbn-resolving.de/urn:nbn:de:hbz:5n-56528 elektronisch publiziert.

1. Gutachter:	Prof. Dr. Norbert Wermes
2. Gutachter:	Prof. Dr. Klaus Desch
Tag der Promotion:	31.07.2019
Erscheinungsjahr:	2019

Contents

CHAPTER 1

Introduction

The Standard Model (SM) theory encapsulates our best understanding of the fundamental particles and their interactions. Developed in the early 1970s, it is a self-consistent theory which has demonstrated huge successes in providing experimental predictions which have been confirmed by the experimental observations over time. In 2012, the discovery of a new particle, consistent with the SM Higgs boson, by the ATLAS and CMS experiments at the Large Hadron Collider (LHC) was a break-through for the experimental tests of the SM. Now, precise measurements of the Higgs boson couplings are very important to test the validity of the Brout-Englert-Higgs mechanism, the electroweak theory and the SM theory itself, as all the couplings are predicted by the SM theory, given the measured values of the masses of the particles and of the vacuum expectation value. The triple Higgs self-coupling, λ_{HHH}, is present in the SM theory and its value, corresponding in the theory to $m_H^2/2v$, controls the shape of the Higgs potential. The direct way to measure this coupling is studying the Higgs boson pair production process. In the SM, Higgs boson pairs can be produced at the LHC via gluon-gluon fusion (ggF) through top-quark loops and the triple Higgs self-interaction, thus the study of this process can allow one to measure the coupling λ_{HHH} and probe the structure of the Higgs potential. The SM cross section for Higgs pair production at the LHC via ggF with pp collisions at a centre-of-mass energy of $\sqrt{s} = 13$ TeV is $\sigma = 33.41$ fb [1–4], three orders of magnitude smaller than the single Higgs boson production cross section. The observation of this process and the measurement of the Higgs self-coupling λ_{HHH} is thus particularly challenging because of its small cross section and it is one of the main goals for the High Luminosity LHC (HL-LHC).

Although all the experimental measurements are so far in agreement with the Standard Model expectations, the SM theory is an incomplete theory as there are physics phenomena in nature that it cannot explain. Many theories beyond the Standard Model (BSM) have been developed trying to solve this. Modifications to the top-quark Yukawa coupling or to the Higgs self-coupling, or presence of new diagrams with new vertices, could enhance the di-Higgs production rate and modify the kinematic properties of the process showing hints of possible new physics BSM in the non-resonant di-Higgs production. Moreover, many BSM theories predict heavy resonances that could decay into a pair of Higgs bosons, such as a neutral scalar heavy Higgs in two-Higgs-doublet models or spin-2 Kaluza-Klein excitations of the graviton in the bulk Randall-Sundrum model. The presence of one of these resonances would also manifest in a modification of the di-Higgs production rate and kinematic as resonant production.

Searches for non-resonant and resonant di-Higgs production were performed by the ATLAS and CMS Collaborations in several decay channels using about 20 fb^{-1} of pp collisions data from the LHC Run 1 at a centre-of-mass energy of 8 TeV. The CMS statistical combination of the $b\bar{b}\gamma\gamma$ and $b\bar{b}\tau^+\tau^-$ channels set an observed (expected) upper limit on the non-resonant di-Higgs production cross section of 43 (47) times

the SM prediction [5], which was the best upper limit on this process before this thesis work was started. The ATLAS statistical combination of the $b\bar{b}b\bar{b}$, $b\bar{b}\gamma\gamma$, $b\bar{b}\tau^+\tau^-$ and $W^+W^-\gamma\gamma$ channels set an observed (expected) upper limit on the non-resonant di-Higgs production cross section of 70 (48) times the SM expectation [6]. These results show that the sensitivity to this process is very far from the observation, for which a much larger dataset is needed, making it a flagship analysis for the HL-LHC. It is nevertheless important to continue exploring di-Higgs production with the increase of the centre-of-mass energy and luminosity in the LHC Run 2 to develop improved analysis techniques and to test the presence of new physics BSM that might enhance the production rate.

This thesis presents a search for the SM Higgs boson pair production and new physics phenomena in the $b\bar{b}\tau^+_{had}\tau^-_{had}$ final state, exploring the di-Higgs decay channel where one Higgs boson decays to a b-quark pair and the other to a τ-lepton pair and both τ-leptons decay hadronically. This channel was never studied by the ATLAS Collaboration before as in the $b\bar{b}\tau^+\tau^-$ Run 1 analysis only the channel with one τ-lepton decaying hadronically and one decaying leptonically was included. The search is performed using 36.1 fb^{-1} of pp collisions data from the LHC Run 2 at a centre-of-mass energy of 13 TeV, recorded by the ATLAS experiment in 2015 and 2016. Particularly, the non-resonant di-Higgs production is studied both assuming SM couplings and variations of the triple Higgs self-coupling and of the top-quark Yukawa coupling. The BSM resonant di-Higgs production is also tested. The results from the $bb\tau_{had}\tau_{had}$ analysis developed and presented in this thesis are combined with the ones from the $bb\tau_{lep}\tau_{had}$ channel in this thesis work. The $bb\tau\tau$ results are then combined with the results from the other two di-Higgs most sensitive decay channels, $bbbb$ and $bb\gamma\gamma$. Moreover, a prospect study is performed in this thesis for the non-resonant di-Higgs search in the $bb\tau\tau$ channel, and then combined with the prospects of the $bbbb$ and $bb\gamma\gamma$ channels, assuming 3 000 fb^{-1} at $\sqrt{s}$ = 14 TeV expected to be collected at the HL-LHC. The work on di-Higgs searches presented in this thesis is embedded in three publications by the ATLAS Collaboration [7–9] and one by the Physics of the HL-LHC Working Group Collaboration [10], reporting results on Run 2 di-Higgs searches and prospects studies. The personal contributions of the author of this thesis to these four di-Higgs publications consisted in the development of the complete analysis in the $bb\tau_{had}\tau_{had}$ channel, with particular focus on background estimation, multivariate analysis and statistical interpretation, and in performing the statistical combination with the $bb\tau_{lep}\tau_{had}$ channel. Contribution was also given to the statistical combination of the $bb\tau\tau$ channel with the other di-Higgs decay channels, as support for the statistical interpretation of the $bb\tau\tau$ results, and to the prospect studies in the development of the extrapolation procedure for the $bb\tau\tau$ channel and in the statistical interpretation.

In addition to the di-Higgs search, new physics in the form of pair production of third generation scalar leptoquarks is also searched for in this thesis in the $b\tau_{had}b\tau_{had}$ final state. This analysis is based on the di-Higgs analysis and modified for the different signal hypotheses as the final state is the same. Previous searches for pair production of third generation scalar leptoquarks decaying to $b\tau b\tau$ were performed by the ATLAS and CMS Collaborations using respectively 4.7 fb^{-1} of pp collisions data from the LHC Run 1 at a centre-of-mass energy of 7 TeV and 19.7 fb^{-1} at a centre-of-mass energy of 8 TeV. The CMS results provided the most stringent constraint on the leptoquark mass before this thesis work was started excluding masses below 740 GeV assuming a branching ratio to $b\tau$ of 100% [11]. The ATLAS results excluded third generation leptoquarks with masses below 534 GeV [12]. The results of the leptoquark analysis presented in this thesis are combined with the ones from the $b\tau_{lep}b\tau_{had}$ channel and are published by the ATLAS Collaboration in Reference [13]. The contributions of the author to this publication consist in the re-optimisation of the event selection and reconstruction and in the development of the multivariate analysis for the $b\tau_{had}b\tau_{had}$ channel.

The thesis is structured as follows. First, an overview of the Standard Model including the Brout-Englert-Higgs mechanism as well as a summary of single Higgs and di-Higgs production and decay at

the LHC are presented in Chapter 2. An overview of BSM models for di-Higgs resonant production, and for other new physics phenomena that could manifest in the $bb\tau\tau$ final state, such as leptoquark pair production, is given in Chapter 3. Chapter 4 gives a description of the LHC and the ATLAS detector. The methods used for reconstructing the physics objects are detailed in Chapter 5. The complete description of the di-Higgs analysis performed in the $bb\tau_{had}\tau_{had}$ channel, including signal and background Monte Carlo simulations, objects and event selection, background estimation, multivariate analysis, systematic uncertainties, statistical interpretation and results, is given in Chapter 6. The statistical combination of the results from the $bb\tau_{had}\tau_{had}$ channel with the ones from the $bb\tau_{lep}\tau_{had}$ channel is presented in Chapter 7, where also the results from the combination of the $bb\tau\tau$, $bbbb$ and $bb\gamma\gamma$ channels are reported and the HL-LHC prospects study is described. The search for pair production of third generation scalar leptoquarks in the $b\tau_{had}b\tau_{had}$ channel is described in Chapter 8, where also the results from the combination of the $b\tau_{had}b\tau_{had}$ and $b\tau_{lep}b\tau_{had}$ are reported. Finally a summary of the analyses and conclusions are given in Chapter 9.

CHAPTER 2

The Standard Model and the Higgs boson

The Standard Model (SM) [14–20] describes the fundamental structure of matter. Everything in the universe is found to be made from a few basic building blocks called fundamental particles, governed by four fundamental forces. Our best understanding of how these particles and three of the forces are related to each other is encapsulated in the SM theory of particle physics. The SM theory was developed in the early 1970s and over time and through many experiments it has become established as a well-tested physics theory that explains almost all experimental results. One of the key elements of the SM is a particle called the Higgs boson. The existence of this particle was predicted by the SM and it was its only missing piece in the experimental observations until the discovery of a boson in 2012 [21, 22], made by the ATLAS and CMS experiments at the CERN's Large Hadron Collider (LHC), whose properties are consistent with the SM Higgs boson. This discovery was a break-through for the experimental tests of the SM and made it a consistent, even though still incomplete, theory of nature.

This chapter introduces the basic concepts of the SM theory, describes the SM gauge theory and the three fundamental forces included in it and explains the Brout-Englert-Higgs mechanism and the role of the Higgs boson. Finally, the properties of the Higgs boson and the crucial role played by the Higgs boson pair production process in the Higgs self-coupling measurement, and thus in probing the structure of the Higgs potential, are discussed.

2.1 Basic concepts

The fundamental particles that constitute the building blocks of matter occur in two basic types called quarks and leptons. Each group consists of six particles, which are organised in pairs, called "generations", having the same properties except the mass. The six quarks are paired in three generations: the "up quark" and the "down quark" form the first generation, followed by the "charm quark" and "strange quark" forming the second generation, then the "top quark" and "bottom quark" in the third generation. Quarks are all electrically charged, with up-type quarks having charge $+2/3$ and down-type quarks $-1/3$, and also carry a "colour" charge (R, G, B). The six leptons are similarly arranged in three generations: the "electron" and the "electron neutrino", the "muon" and the "muon neutrino", and the "tau" and the "tau neutrino". The electron, muon and tau are electrically charged, with charge -1, while the neutrinos are electrically neutral. The lightest particles make up the first generation, whereas the heavier particles belong to the second and third generations. All stable matter in the universe is made from particles that belong to the first generation, while the heavier particles of the second and third generation decay subsequentially into paricles of the lower generations. All these particles are fermions with spin $1/2$. In addition, each of these particles has a corresponding anti-particle, which has the same mass, spin and

lifetime properties but opposite sign of the quantum numbers related to the charges.

There are four fundamental forces at work in the universe: the electromagnetic force, the weak force, the strong force and the gravitational force. They involve different processes and have different strenghts. The electromagnetic force acts between electrically charged particles. The weak interaction is responsible for phenomena like nuclear β-decays and absorption and emission of neutrinos and it is approximately 1000 times weaker than the electromagnetic force. The strong interaction acts between coloured particles and it is responsible of holding together nuclei and it is roughly 100 times stronger than the electromagnetic force. The gravitational force appears between all types of massive particles and it is by far the weakest force being about 10^{38} times weaker than the electromagnetic force. The SM includes the electromagnetic, weak and strong forces. They result from the exchange of force-carrier particles, which are bosons with spin 1. Each fundamental force has its own corresponding boson: the electromagnetic force is carried by the "photon", the "W" and "Z" bosons are responsible for the weak force and the strong force is carried by the "gluon". However, the most familiar force in our everyday lives, gravity, is not part of the SM, as it is extremely difficult to combine in a single theory the quantum theory used to describe the microscopic world and the general theory of relativity used to describe the macroscopic world. Although not yet found, the "graviton" should be the corresponding force-carrying particle of gravity. Anyhow, the effect of gravity is so weak as to be negligible at the scale of the fundamental particles, so the SM still works well despite its exclusion of one of the fundamental forces.

There is one additional boson, with spin 0, completing the picture of the SM particles, the Higgs boson. The Higgs boson is responsible for giving the mass to the fermions and to the force-carrier bosons. Figure 2.1 shows a scheme of the fundamental particles of the SM with their quantum numbers (electric charge, spin, colour charge) and masses expressed in multiples of eV[1].

2.2 The Standard Model gauge theory

The Standard Model is a relativistic quantum field gauge theory, incorporating relativity and quantum mechanics, where particles are described as excitations of quantum fields and interactions are related to local gauge symmetries of the Lagrangian. From the theoretical perspective, the SM has a simple and elegant structure: it is a gauge theory based on the symmetry

$$SU(3)_C \otimes SU(2)_L \otimes U(1)_Y \,, \tag{2.1}$$

where

- $SU(3)_C$ is the symmetry group of the strong interaction and the letter C refers to the colour charge;
- $SU(2)_L \otimes U(1)_Y$ is the symmetry group of the electroweak interactions that unifies the weak and electromagnetic interactions, the letter L stands for left and indicates that the symmetry only involves left-handed particles and the letter Y stands for the weak hypercharge which is related to the electric charge (Q) and the weak isospin (T) by the formula $Q = T_3 + Y/2$, with T_3 being the third component of the weak isospin.

The matter particles are described by fermionic fields with spin $1/2$ and the force-carriers by bosonic fields with spin 1. The dynamics is determined by an action S written in terms of a Lagrangian density $\mathcal{L}(x)$ that contains the free Lagrangian of the fields ($\Phi(x)$), which accounts for their free propagation, and additional terms that respect the above symmetries and account for their interactions:

[1] Natural units are used, where $\hbar = c = k_B = 1$ and quantities like energy, momentum and mass can be measured in units of energy as the electronvolt: $[E] = [p] = [m] =$ eV $= 1.60218 \times 10^{-19} J$.

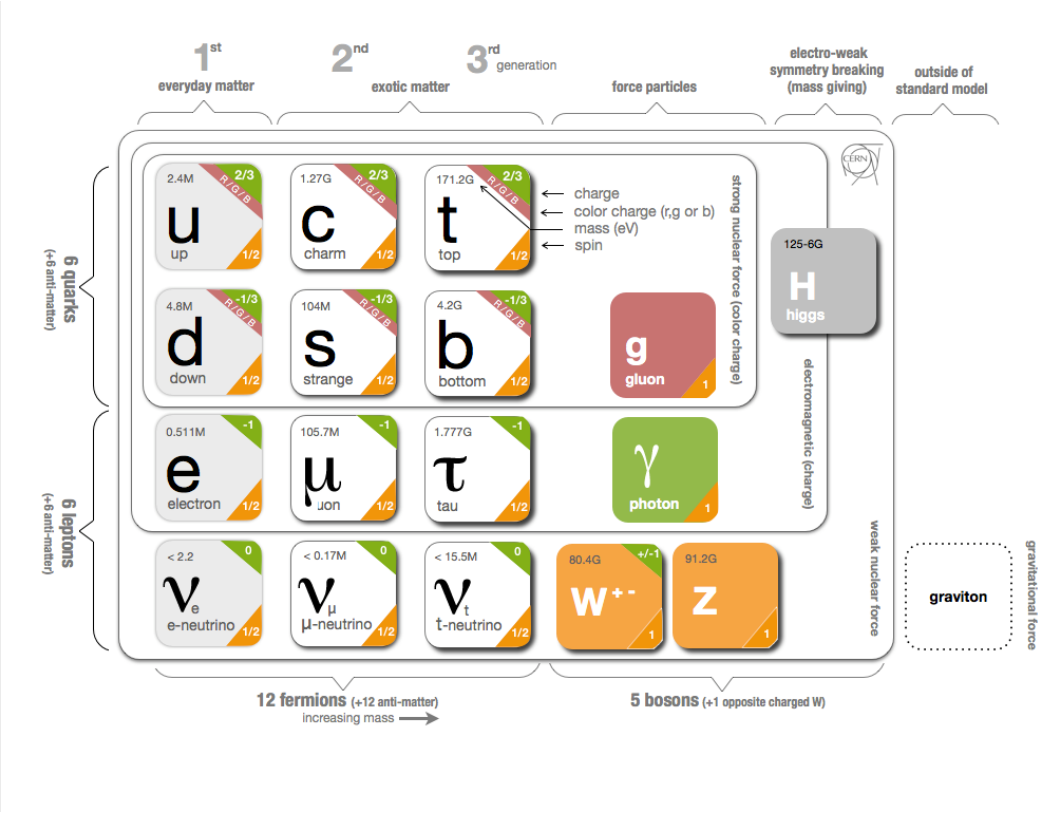

Figure 2.1: Fundamental particles of the Standard Model [23].

$$S = \int d^4x \; \mathcal{L}(x) \,. \tag{2.2}$$

The evolution of the system occurs along a path where the action is stationary

$$\delta S = \delta \int d^4x \; \mathcal{L}(\Phi(x), \partial_\mu \Phi(x)) = 0 \,, \tag{2.3}$$

which leads to the Euler-Lagrange equations that correspond to the equations of motion of the system:

$$\partial_\mu \left(\frac{\partial \mathcal{L}}{\partial(\partial_\mu \Phi)} \right) - \frac{\partial \mathcal{L}}{\partial \Phi} = 0 \,. \tag{2.4}$$

A gauge symmetry is any continuous transformation of the field

$$\Phi(x) \rightarrow \Phi'(x) = \Phi(x) + \delta\Phi \tag{2.5}$$

that does not change the Lagrangian and consequently does not change the equations of motion. According to the Noether's theorem, there is a conservation law that corresponds to any continuous symmetry of the Lagrangian:

$$\partial_\mu \frac{\partial \mathcal{L}}{\partial(\partial_\mu \Phi)} \delta\Phi = \partial_\mu J^\mu = 0 \,, \tag{2.6}$$

where J^μ is the conserved current and

$$Q = \int dx\ J^0 = \text{constant} \tag{2.7}$$

is the conserved charge associated to the symmetry.

In order to make cross section calculations for a certain process, a perturbative expansion of the action is used. Rules for calculating transition amplitudes between initial and final states can be derived from the Lagrangian, the Feynman rules, and they can be used to make perturbative calculations. They are graphically represented by diagrams in which fermions are represented by solid and straight lines, electroweak vector bosons by sinusoidal lines, gluons by cycloid lines and the Higgs boson by dashed straight lines. Vertices where lines meet represent interactions. The number of vertices gives the order of the term in the perturbation series expansion of the transition amplitude. The lowest possible order for a given process is called Leading Order (LO). Following the rules, the transition amplitude can be derived: each internal line corresponds to a factor of the virtual particle's propagator, each vertex gives a factor derived from the interaction term in the Lagrangian, and incoming and outgoing lines carry energy, momentum, and spin. In this thesis the Feynman diagrams are drawn with time running from left to right, so initial states are on the left and final ones on the right.

2.2.1 Quantum electrodynamics (QED)

Quantum electrodynamics (QED) is the first relativistic quantum field theory historically developed. It is an abelian gauge theory describing the dynamics of the interactions of fermions with the electromagnetic field.

The Lagrangian of a free massive fermion is given by:

$$\mathcal{L}_{Dirac}(x) = \bar{\psi}(x)(i\gamma^\mu\partial_\mu - m)\psi(x)\,, \tag{2.8}$$

where $\psi(x)$ is the fermionic field, γ^μ are the Dirac matrices and m is the mass of the fermion. The electrodynamic Lagrangian needs to be invariant under the local gauge transformation

$$\psi(x) \to \psi'(x) = e^{-ie\alpha(x)}\psi(x)\,, \tag{2.9}$$

where $\alpha(x)$ is a function that defines the local (depending on the space-time coordinates) phase transformation that belongs to the unitary abelian symmetry group $U(1)$. In order to have the Lagrangian invariant under this transformation it is necessary to introduce a gauge field $A_\mu(x)$, which is the photon field, and transforms as

$$A_\mu(x) \to A'_\mu(x) = A_\mu(x) + \frac{1}{e}\partial_\mu\alpha(x)\,. \tag{2.10}$$

The derivative ∂_μ has to be replaced by the covariant derivative

$$D_\mu = \partial_\mu + ieA_\mu\,, \tag{2.11}$$

where e is the electric charge of the fermion, and the Lagrangian can be written as:

$$\mathcal{L}_{QED}(x) = \bar{\psi}(x)(i\gamma^\mu D_\mu - m)\psi(x) - \frac{1}{4}F_{\mu\nu}(x)F^{\mu\nu}(x)\,, \tag{2.12}$$

where $F_{\mu\nu} = \partial_\mu A_\nu(x) - \partial_\nu A_\mu(x)$ is the electromagnetic field tensor. This Lagrangian contains the kinematic terms of the free Dirac Lagrangian and the free Lagrangian of the electromagnetic field and

the interaction term between fermions and the electromagnetic field.

2.2.2 Quantum chromodynamics (QCD)

Quantum chromodynamics (QCD) describes the strong interactions between quarks and gluons. It is a non-abelian gauge theory based on the symmetry group $SU(3)_C$. The letter C indicates that the symmetry is in the colour space, where the colour (R, G, B) is the charge related to the strong interaction. Quarks carry a colour charge and gluons carry a colour and an anti-colour charge. The free Lagrangian for the quarks is the Dirac Lagrangian:

$$\mathcal{L}(x) = \bar{q}(x)(i\gamma^\mu \partial_\mu - m)q(x)\,. \tag{2.13}$$

The chromodynamics Lagrangian needs to be invariant under local transformations

$$q(x) \rightarrow q'(x) = e^{i\alpha^a(x)T_a} q(x) \tag{2.14}$$

where $\alpha_a(x)$ is the arbitrary local parameter of the transformation and $T_a = \frac{\lambda_a}{2}$, with $a = 1, ..., 8$ and λ_a being the Gell-Mann matrices, are the generators of the non-abelian symmetry group $SU(3)$. The group is non-abelian and the algebra of the group is given by $[T_a, T_b] = if_{abc}T_c$ where f_{abc} are the structure constants of the group. Similarly to the QED case, in order to have the Lagrangian invariant under this transformation it is necessary to introduce eight gauge fields $G^a_\mu(x)$, that are the gluon fields, and transform as

$$G^a_\mu(x) \rightarrow G'^a_\mu(x) = G^a_\mu(x) - \frac{1}{g_s}\partial_\mu \alpha_a(x) - f^{abc}\alpha_b(x)G_{c\mu}(x)\,. \tag{2.15}$$

The derivative ∂_μ has to be replaced by the covariant derivative

$$D_\mu = \partial_\mu + g_s T^a G^a_\mu\,, \tag{2.16}$$

where g_s is the strong interaction coupling constant, and the Lagrangian can be written as:

$$\mathcal{L}_{QCD}(x) = \bar{q}(x)(i\gamma^\mu D_\mu - m)q(x) - \frac{1}{4}G^a_{\mu\nu}(x)G^{\mu\nu}_a(x)\,, \tag{2.17}$$

where $G^a_{\mu\nu} = \partial_\mu G^a_\nu(x) - \partial_\nu G^a_\mu(x) - g_s f^{abc} G_{b\mu} G_{c\nu}$ is the gluon field tensor. This Lagrangian contains the kinematic terms of the free Dirac Lagrangian of the quarks and the free Lagrangian of the gluon fields, the interaction term between the quarks and the gluon fields, but also the interaction between gluons themselves. The gluon self-interaction is the main difference between QCD and QED and it is particular of non-abelian theories. This interaction is responsible for the unique and salient features of QCD: the interaction strength $\alpha_s = g_s^2/4\pi$ between quarks becomes smaller as the distance between them gets shorter (or the energy scale gets larger) and larger as the distance between them becomes larger (or the energy scale gets smaller) as the gluon self-coupling has an anti-screening effect on the colour charge. This behaviour of α_s has two consequences:

- asymptotic freedom: at large energy scales quarks and gluons behave as free particles;
- colour confinement: quarks and gluons cannot be directly observed, only colour-neutral states can be observed, as they cannot be separated at low energy scales so they are confined into hadrons.

These two effects are very important for the understanding of the physics at hadron colliders, involing quarks and gluons and thus QCD processes in the initial and final states, as explained later on in Section 4.2.

2.2.3 Electroweak theory

The electroweak (EW) theory was developed by Glashow, Weinberg and Salam in order to combine the electromagnetic and weak interactions in a unified theory in which they are two manifestations of the same interaction. The unification is accomplished under the gauge symmetry group $SU(2)_L \otimes U(1)_Y$, where L and Y are respectively the left-handed weak isospin and the weak hypercharge, related to the electric charge (Q) and the weak isospin (T) by the formula $Q = T_3 + Y/2$, which are the generators of the symmetry group. Fermions are organised in doublets with weak isospin $T = 1/2$ for the left-handed states and singlets with $T = 0$ for the right-handed ones:

$$\chi_L = \begin{pmatrix} \nu_l \\ l \end{pmatrix}_L , \begin{pmatrix} q^u \\ q^d \end{pmatrix}_L \tag{2.18}$$

$$\psi_R = l_R , q^u_R , q^d_R , \tag{2.19}$$

with l indicating charged leptons, ν_l the corresponding neutrinos and $q^{u,d}$ the up-type and down-type quarks. The Lagrangian for these fermions is required to be invariant under local transformations of $SU(2)_L \otimes U(1)_Y$, which transform the fields as:

$$\chi_L(x) \rightarrow \chi'_L(x) = e^{i\beta(x)Y + i\alpha^a(x)\tau_a}\chi_L(x) \tag{2.20}$$

$$\psi_R(x) \rightarrow \psi'_R(x) = e^{i\beta(x)Y}\psi_R(x) , \tag{2.21}$$

where $\alpha(x)$ and $\beta(x)$ are the phase transformation factors of the local gauge $SU(2)_L$ and $U(1)_Y$ symmetry groups, $a = 1, 2, 3$ and $\tau_a = \frac{\sigma_a}{2}$, with σ_a being the Pauli matrices, are the generators of $SU(2)$. As for QED and QCD cases, one starts with the free Lagrangian and replaces the derivative with the covariant derivative:

$$D_\mu = \partial_\mu + igW^a_\mu\tau_a + ig'B_\mu Y , \tag{2.22}$$

where four gauge fields are introduced: W^a_μ, with $a = 1, 2, 3$, are the fields associated to the $SU(2)_L$ symmetry, B_μ is the field associated to the $U(1)_Y$ symmetry and g, g' are the respective coupling constants. The field strength tensors are:

$$W^a_{\mu\nu} = \partial_\mu W^a_\nu - \partial_\nu W^a_\mu + g\epsilon^{abc}W_{b\mu}W_{c\nu} \tag{2.23}$$

$$W_{\mu\nu} = \partial_\mu B_\nu - \partial_\nu B_\mu . \tag{2.24}$$

The resulting electroweak Lagrangian is:

$$\mathcal{L}_{EW}(x) = \bar{\chi}_L(x)\gamma^\mu\left(i\partial_\mu - g\frac{\tau_a}{2}W^a_\mu + \frac{g'}{2}B_\mu\right)\chi_L(x) + \bar{\psi}_R(x)\gamma^\mu(i\partial_\mu + g'B_\mu)\psi_R(x) - \frac{1}{4}W^a_{\mu\nu}(x)W^{\mu\nu}_a(x) - \frac{1}{4}B_{\mu\nu}B^{\mu\nu} . \tag{2.25}$$

The physical gauge bosons $\gamma, Z, W^\pm$ are given by:

$$A_\mu = W_\mu^3 \sin\theta_W + B_\mu \cos\theta_W \tag{2.26}$$

$$Z_\mu = W_\mu^3 \cos\theta_W - B_\mu \sin\theta_W \tag{2.27}$$

$$W_\mu^\pm = \frac{1}{2}(W_\mu^1 \mp W_\mu^2)\,, \tag{2.28}$$

where θ_W is the Weinberg angle defined in terms of the coupling constants g and g' through:

$$\sin\theta_W = \frac{g'}{\sqrt{g^2 + g'^2}} \qquad \cos\theta_W = \frac{g}{\sqrt{g^2 + g'^2}}\,, \tag{2.29}$$

and the electric charge can hence be written as

$$e = g\sin\theta_W = g'\cos\theta_W\,. \tag{2.30}$$

However, this Lagrangian describes the interaction between massless fermion fields and massless gauge fields. This is in contrast with the experimental observations of massive fermions and massive bosons, but adding mass terms would violate the gauge invariance. As described in Section 2.2.4, the solution to this problem is given by the introduction of an additional field, the Higgs field, with the mechanism of electroweak symmetry breaking which gives rise to massive gauge bosons. Mass terms for the fermions are introduced as well by introducing a gauge invariant interaction between the Higgs field and the fermions, i.e. the Yukawa interaction, as described in Section 2.2.5.

2.2.4 Brout-Englert-Higgs mechanism

In 1964, Higgs, Brout and Englert provided a model, today known as Brout-Englert-Higgs mechanism, to solve the mass problem for bosons and fermions preserving the gauge invariance. This model introduces a new scalar boson with a mechanism of spontaneous electroweak symmetry breaking: the Higgs boson.

In this model a complex scalar field in the form of a doublet of $SU(2)$ with $Y = 1$ is introduced:

$$\Phi = \begin{pmatrix} \phi^+ \\ \phi^0 \end{pmatrix} = \frac{1}{\sqrt{2}} \begin{pmatrix} \phi_1 + i\phi_2 \\ \phi_3 + i\phi_4 \end{pmatrix}. \tag{2.31}$$

Its Lagrangian can be written in terms of kinematic and potential terms as:

$$\mathcal{L}_{Higgs}(x) = (D_\mu \Phi)^\dagger D^\mu \Phi - V(\Phi) \tag{2.32}$$

where D_μ is the covariant derivative of $SU(2)_L \otimes U(1)_Y$

$$D_\mu = \partial_\mu + igW_\mu^a \tau_a + ig' B_\mu Y\,, \tag{2.33}$$

and $V(\Phi)$ is the potential term given by

$$V(\Phi) = \mu^2 \Phi\Phi^\dagger + \lambda(\Phi\Phi^\dagger)^2 \;= \mu^2\Phi^2 + \lambda\Phi^4\,, \tag{2.34}$$

with μ and λ being free parameters. This potential is symmetric under $SU(2) \otimes U(1)$ so the symmetry of the Lagrangian is preserved.

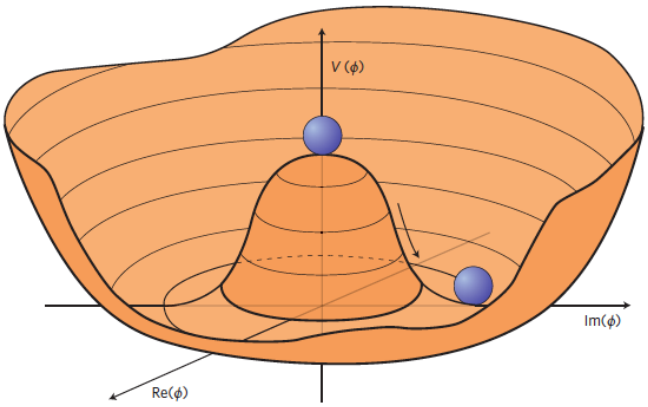

Figure 2.2: Illustration of the Higgs potential [24].

In order to have a stable theory the potential has to be inferiorly bounded so it has to have $\lambda > 0$, while the sign of μ^2 is not dermined. The minimum of the potential represents the vacuum state and the value of the field in the minimum of the potential gives the vacuum expectation value (vev) of the Higgs field $\langle\Phi\rangle \equiv v$. The vacuum expectation value of the Higgs field is the crucial quantity for the symmetry breaking and the Higgs mechanism. There are two possible scenarios depending on the sign of μ^2:

- $\mu^2 \geq 0$: the potential has a parabolic shape with a single minimum at $\Phi_0 = \langle\Phi\rangle \equiv v = 0$ and the ground state is symmetric under transformations of $SU(2) \otimes U(1)$;
- $\mu^2 < 0$: the potential has the shape shown in Figure 2.2 where $\Phi = 0$ corresponds to a local maximum rather than a minimum and there are degenerate minima corresponding to a circumference with radius

$$|\Phi_0| = \langle\Phi\rangle \equiv v = \sqrt{\frac{-\mu^2}{2\lambda}}\,. \tag{2.35}$$

In the second case, $\mu^2 < 0$, there are multiple states with the same vacuum energy. Although the potential is symmetric, the ground states are asymmetric: transformations of $SU(2) \otimes U(1)$ applied to one of the vacuum states will rotate it to a different orientation that describes a different physical state, so the symmetry is spontaneously broken. A particular ground state can be chosen with $\phi_1 = \phi_2 = \phi_4 = 0$ and $\phi_3 = v$:

$$\Phi_0 = \frac{1}{\sqrt{2}}\begin{pmatrix}0\\ v\end{pmatrix}. \tag{2.36}$$

The τ_1, τ_2 generators of $SU(2)$ mix the top and bottom components of the spinor, while τ_3 rotations of an angle θ only multiply them by an opposite phase that can be removed by a $U(1)$ rotation of $\theta/2$. Thus, under both a $SU(2)$ τ_3-rotation of θ and a $U(1)$ rotation of $\theta/2$ the vacuum is invariant. This combination of generators is $Q = \tau_3 + Y/2$, which is the electric charge, corresponds to the unbroken part of the gauge group, the $U(1)_{em}$ symmetry group. After the spontaneous symmetry breaking, three of the four degrees of freedom of the symmetry group are broken and give mass to the three gauge bosons $Z, W^{\pm}$, while one degree of freedom is unbroken and leaves one massless gauge boson, the photon. The electroweak symmetry group is thus broken with the pattern:

$$SU(2)_L \otimes U(1)_Y \rightarrow U(1)_{em}\,. \tag{2.37}$$

This can be seen in the Lagrangian by expanding the potential around the ground state. The field $\Phi(x)$ can be written in terms of $SU(2)$ transformations adding four scalar fields $\theta_1, \theta_2, \theta_3, h$, which parameterise fluctuations around the minimum:

$$\Phi(x) = e^{i\tau^a\theta_a/v}\begin{pmatrix} 0 \\ \frac{v+h}{\sqrt{2}} \end{pmatrix} \simeq \frac{1}{\sqrt{2}}\begin{pmatrix} \theta_2 + i\theta_1 \\ v + h - i\theta_3 \end{pmatrix}. \tag{2.38}$$

The fields $\theta_1, \theta_2, \theta_3$ are the massless Goldstone bosons generated by the electroweak symmetry breaking and they can be removed from the Lagrangian by doing a $SU(2)$ gauge transformation so that the resulting field, in the so called unitary gauge, can be written as:

$$\Phi(x) = \frac{1}{\sqrt{2}}\begin{pmatrix} 0 \\ v + h(x) \end{pmatrix}, \tag{2.39}$$

where $h(x)$ is the Higgs scalar field.

The Lagrangian becomes:

$$\mathcal{L}_{Higgs}(x) = \frac{1}{2}(\partial_\mu h)^2 + [m_W^2 W_\mu^+ W^{-\mu} + m_Z^2 Z_\mu Z^\mu]\left(1 + \frac{h}{v}\right)^2 - \lambda v^2 h^2 - \lambda v h^3 - \frac{1}{4}\lambda h^4\,. \tag{2.40}$$

The degrees of freedom carried by the massless Goldstone bosons are transfered to the massive $W^\pm$ and Z bosons. All boson mass terms can now be identified by looking at the terms which are quadratic in the fields:

$$m_h = \sqrt{2\lambda}v \tag{2.41}$$

$$m_W = \frac{gv}{2} \tag{2.42}$$

$$m_z = \frac{1}{2}v\sqrt{g + g'^2} = \frac{m_W}{\cos\theta_W}\,. \tag{2.43}$$

In addition, the Lagrangian contains triple and quartic coupling terms of the field h with the heavy gauge bosons $W^\pm$ and Z, which are proportional to the mass squared of the gauge boson, $\lambda_{VVH} = \frac{2m_V^2}{v}$ and $\lambda_{VVHH} = \frac{m_V^2}{v^2}$ respectively, and triple and quartic Higgs boson self-couplings which are proportional to the Higgs mass squared:

$$\lambda_{HHH} = \lambda v = \frac{m_h^2}{2v} \tag{2.44}$$

$$\lambda_{HHHH} = \frac{\lambda}{4} = \frac{m_h^2}{8v^2}\,. \tag{2.45}$$

The scale of the boson masses and of the couplings is given by the value of the vev v. It can be evaluated using the empirical value of the Fermi constant G_F from the muon decay, as $\frac{G_F}{\sqrt{2}} = \frac{g^2}{8M_W^2}$, so the vacuum expectation value can be written as:

$$v = \sqrt{\frac{1}{\sqrt{2}G_F}} \approx 246 \text{ GeV}\,. \tag{2.46}$$

Nevertheless, the Higgs boson mass m_h and the masses of the vector bosons cannot be predicted as λ and g, g' are free parameters of the theory. Precise measurements of the boson masses and of their couplings to the Higgs boson are important to test the validity of the Brout-Englert-Higgs mechanism, the electroweak theory and the SM theory itself. The aim of this thesis work is to search for di-Higgs production in order to test the triple Higgs self-coupling λ_{HHH} and therefore probe the structure of the Higgs potential.

2.2.5 Yukawa coupling and fermion masses

The Higgs mechanism, as described in the previous section, explains the masses of the vector bosons, but it cannot explain why fermions are massive. Adding directly mass terms for the fermions would break the gauge invariance of the Lagrangian, but a new gauge invariant interaction term between fermions and the Higgs field, called the Yukawa term, can be added assuming that the fermions acquire their masses from interactions with the Higgs field like the vector bosons do. For the leptons:

$$\mathcal{L}_{Leptons}(x) = -y_l(\bar{\chi}_L \phi \psi_R + \bar{\psi}_R \phi^* \chi_L)\,, \tag{2.47}$$

where y_l are free parameters for $l = e, \mu, \tau$. Using the parameterisation of the Higgs field of Equation 2.39, the term becomes:

$$\mathcal{L}_{Leptons}(x) = \frac{-y_l v}{\sqrt{2}}(\bar{l}_L l_R + \bar{l}_R l_L) - \frac{y_l}{\sqrt{2}}(\bar{l}_L l_R + \bar{l}_R l_L)h = -m_l \bar{l} l - \frac{m_l}{v}\bar{l} l h\,, \tag{2.48}$$

with the lepton masses given by $m_l = \frac{-y_l v}{\sqrt{2}}$. This term of the Lagrangian contains the kinematic term of the massive leptons and the interaction term of the leptons with the Higgs field, with a Yukawa-coupling that is proportional to the mass of the fermion, $y_l = \frac{m_l \sqrt{2}}{v}$. Since there are no right-handed neutrinos in the SM, the left-handed ones need to be massless.

The mass terms for the quarks follow in a similar way but, since there are also right-handed down-type quarks, both components of the doublet are massive. In order to build the upper component in the doublet its conjugate is needed:

$$\Phi_C = \begin{pmatrix} \phi^{0*} \\ -\phi^- \end{pmatrix}. \tag{2.49}$$

Using this, the term of the Lagrangian for the quarks is:

$$\mathcal{L}_{Quarks}(x) = -y_d^{ij}(\bar{u}_i, \bar{d}_i)_L \Phi d_{jR} - y_u^{ij}(\bar{u}_i, \bar{d}_i)_L \Phi_C u_{jR} + h.c.\,, \tag{2.50}$$

where y_q^{ij} are matrices for the quark families i, j and up and down-type quarks q. These Yukawa coupling matrices can be diagonalised if the left-handed quark fields are rotated by a unitary transformation, $u_L^i \to u_L'^i = U_u^{ij} u_L^j$ and $d_L^i \to d_L'^i = U_d^{ij} d_L^j$, where $V_{CKM} = U_u^\dagger U_d$ is the Cabibbo-Kobayashi-Maskava (CKM) matrix. Finally, the Lagrangian can be expressed, in the diagonal form and in the unitary gauge, as:

$$\mathcal{L}_{Quarks}(x) = -m_d^i \bar{d}_i d_i (1 + \frac{h}{v}) - m_u^i \bar{u}_i u_i (1 + \frac{h}{v})\,, \tag{2.51}$$

where again the fermion masses are given by $m_f = \frac{-y_f v}{\sqrt{2}}$ and it can be seen that the Yukawa-coupling between the fermion and the Higgs boson is proportional to the mass of the fermion $y_f = \frac{m_f \sqrt{2}}{v}$. The Yukawa-couplings are free parameters of the theory and so are the fermion masses. The Yukawa interaction between fermions and the Higgs boson gives mass to the fermions through a mechanism which is different from the one that gives mass to the vector bosons. Precise measurements of the Yukawa couplings are needed to test the validity of this mechanism. In this thesis work the top-quark Yukawa coupling to the Higgs boson is tested through the search for di-Higgs production.

2.3 The Higgs boson and Higgs pair production

The Higgs boson is predicted by the Brout-Englert-Higgs mechanism in the SM theory as described in Section 2.2.4. As it was the only particle whose experimental observation was missing after the formulation of this theory, a huge experimental effort has been undertaken for many years searching for it at the LEP, Tevatron and the LHC. On 4 July 2012, the ATLAS and CMS experiments at the CERN's Large Hadron Collider announced they had each observed a new particle compatible with the SM Higgs boson in the mass region around 125 GeV [21, 22]. The new particle was observed using pp collisions data recorded by the ATLAS and CMS experiments at the LHC at a centre-of-mass energy of $\sqrt{s} = 7$ TeV in 2011 and $\sqrt{s} = 8$ TeV in 2012. The ATLAS experiment observation was given by the combination of the decay channels $H \to ZZ^* \to 4l$, $H \to \gamma\gamma$ and $H \to WW^* \to lvlv$ with a significance of 5.9σ and the CMS experiment observation by the combination of the decay channels $H \to ZZ^* \to 4l$, $H \to \gamma\gamma$ and $H \to WW^* \to lvlv$, $H \to b\bar{b}$ and $H \to \tau^+\tau^-$ with a significance of 5.0σ (the Higgs boson production and decay modes are described in Section 2.3.1).

After the discovery, the properties of the new particle need to be studied in order to determine if all of them are in agreement with the predictions for the SM Higgs boson. To date, its mass has been measured [25] from the combination of the ATLAS and CMS results in the four leptons final state to be

$$m_H = 125.09 \pm 0.24\,(0.21_{stat} \pm 0.11_{syst})\ \text{GeV}\,, \tag{2.52}$$

and studies on the spin and parity quantum numbers show that the particle is compatible with the SM neutral spin-0 boson with $J^P = 0^+$ [26]. It was also proven that it couples to the gauge bosons and to the fermions of the third generation [27–32], with couplings being consistent with the SM predictions. However, the observed couplings need to be measured with higher precision in order to be compared with the expectations and check that there are indeed no deviations. Moreover, not all couplings predicted by the SM have been observed so far: couplings of the Higgs boson to fermions of the first and second generations and the Higgs self-coupling are still unobserved. Testing the Higgs self-coupling by studying the di-Higgs production process is the main goal of this thesis work.

2.3.1 Higgs production and decay

Given the measured mass values of the vector bosons and of the fermions, all their couplings to the Higgs boson described in Sections 2.2.4 and 2.2.5 are predicted by the SM theory. Therefore, all the Higgs boson production and decay modes, with their cross sections and branching ratios (BRs), can be predicted given also the mass of the Higgs boson.

The main Leading Order (LO) Feynman diagrams contributing to the Higgs production are shown in Figure 2.3 and the corresponding cross sections are shown in Figure 2.4 as a function of the centre-of-mass energy for $m_H = 125$ GeV. The gluon-gluon fusion (ggF) is the production mode with the largest

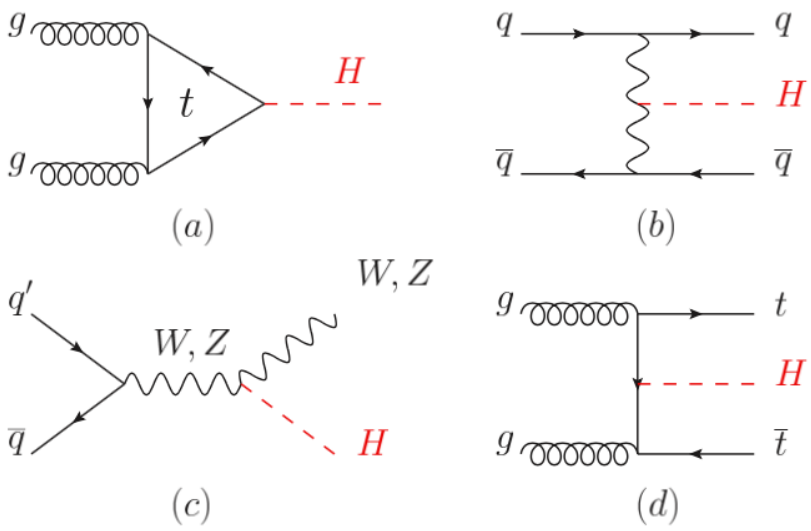

Figure 2.3: Main Leading Order (LO) Feynman diagrams contributing to the Higgs production in (a) gluon-gluon fusion (ggF), (b) vector-boson fusion (VBF), (c) Higgs-strahlung (or associated production with a gauge boson, VH), (d) associated production with a pair of top quarks (ttH) [20].

Decay	BR	Observed
bb	58%	✓
WW	22%	✓
gg	8.6%	
$\tau\tau$	6.3%	✓
cc	2.9%	
ZZ	2.6%	✓
$\gamma\gamma$	0.23%	✓
$Z\gamma$	0.15%	
$\mu\mu$	0.02%	

Table 2.1: Higgs boson decay branching ratios for $m_H = 125.09$ GeV [2].

cross section, 48.58 pb at $\sqrt{s} = 13$ TeV, followed by the vector-boson fusion (VBF), Higgs-strahlung (VH) and associated production with a pair of top quarks (ttH). All these production modes of the Higgs boson have been observed with cross sections compatible with the SM predictions.

Figure 2.5 shows the Higgs boson decay branching ratios as a function of its mass m_H and the corresponding values for a mass of $m_H = 125.09$ GeV are reported in Table 2.1. It has to be noted that since the Higgs boson does not couple to massless particles, like gluons and photons, it can decay into a pair of such particles only through quark triangle-loops, similarly to what happens in the ggF production, mostly populated by top-quark loops because of their high mass and the resulting large top-quark Yukawa coupling.

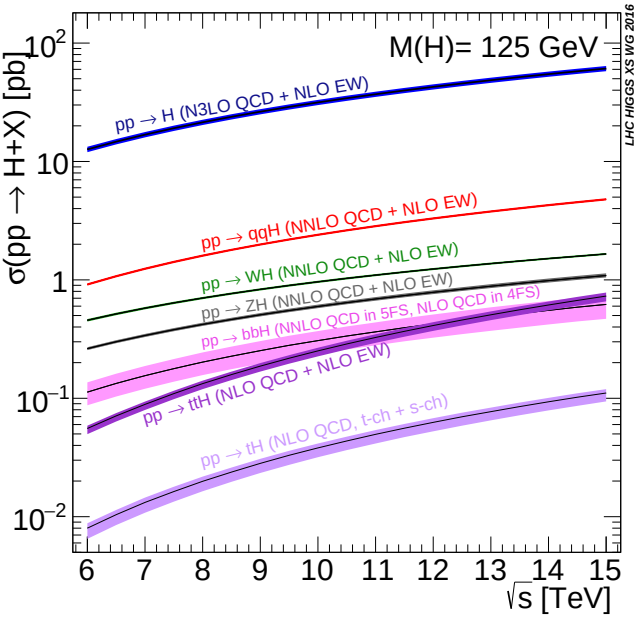

Figure 2.4: Standard Model Higgs boson production cross sections as a function of the centre-of-mass energy for $m_H = 125$ GeV [1].

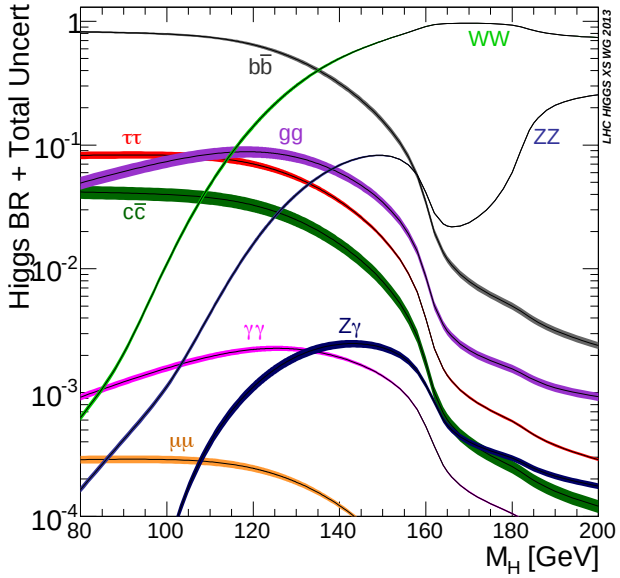

Figure 2.5: Standard Model Higgs boson decay branching ratios as a function of the Higgs mass m_H [1].

2.3.2 Higgs pair production and decay

The main goal of this thesis work is to search for Higgs boson pair production and test the Higgs couplings involved in this process. The dominant Higgs boson pair production mode is ggF through the destructive interference of two LO diagrams shown in Figure 2.6, involving top-quark loops and the triple Higgs self-coupling. In the box diagram of the top-quark loops the top-quark Yukawa coupling y_t is present in two vertices so the contribution of this diagram to the amplitude is proportional to y_t^2, while in the triangle diagram there is y_t in one vertex and the triple Higgs self-coupling λ_{HHH} in the other vertex and the contribution of this diagram is proportional to the product of y_t and λ_{HHH}. Therefore, studying this process allows to directly test both the triple Higgs self-coupling and the top-quark Yukawa coupling. The SM cross section for Higgs boson pair production via ggF at $\sqrt{s} = 13$ TeV [1–4], calculated at Next-to-Leading Order (NLO), is:

$$\sigma = 33.41\,\text{fb}\,, \tag{2.53}$$

three orders of magnitude smaller than the single Higgs production cross section. This accounts for more than 90% of the total Higgs boson pair production cross section, followed by the VBF production which is two orders of magnitude smaller, therefore only this production mode is considered in this thesis.

This process is not expected to be observed with the dataset analysed in this thesis work, corresponding to 36.1 fb^{-1} collected by the ATLAS experiment at the LHC, unless its cross section is enhanced by an anomalous Higgs boson coupling with the top-quark or triple Higgs self-coupling. The cross section depends on both couplings y_t and λ_{HHH}. Considering possible modifications of them, defining effective Higgs boson couplings $k_t = y_t/y_t^{SM}$ and $k_\lambda = \lambda_{HHH}/\lambda_{HHH}^{SM}$, the amplitude of the process can be written as:

$$A(k_t, k_\lambda) = k_t^2 B + k_t k_\lambda T\,, \tag{2.54}$$

where B represents the contribution of the box diagram and T the one of the triangle diagram (shown in Figure 2.6). The cross section can thus be expressed in terms of these two new parameters as:

$$\sigma \approx k_t^4|B|^2 + k_t^3 k_\lambda(BT + TB) + k_t^2 k_\lambda^2|T|^2 = k_t^4\left[|B|^2 + \frac{k_\lambda}{k_t}(BT + TB) + \left(\frac{k_\lambda}{k_t}\right)^2|T|^2\right]. \tag{2.55}$$

This parameterisation shows that the overall production cross section depends on both parameters k_t and k_λ, but the kinematics only depends on their ratio $\frac{k_\lambda}{k_t}$ that modifies the relative contribution of the two diagrams and thus the shape of the kinematic distributions. Figure 2.7 shows the dependence of the cross section on k_λ, given by a second order polynomial, and on k_t, given by a fourth order polynomial.

The cross section has a minimum at $\frac{k_\lambda}{k_t} = 2.4$, for which the maximum destructive interference between the two diagrams occurs. Figure 2.8 shows the shape of the distribution of the invariant mass of the di-Higgs system m_{HH} for various values of k_λ assuming $k_t = 1$ (so corresponding to various values of $\frac{k_\lambda}{k_t}$), showing how the kinematics of the process changes depending on the ratio of the two parameters. The box diagram has an invariant mass spectrum peaking around $2m_t$. When including the triangle diagram with the triple Higgs self-coupling, the invariant mass spectrum becomes generally softer with the increase of its contribution. However, the interference of the two diagrams also generates local minima in the differential cross section around $m_{HH} = 2m_t$, which are more pronounced for some k_λ values as it can be seen in Figure 2.8(b) for the case $k_\lambda = 2$. These effects cause a large change in signal acceptance in the region $0 < k_\lambda < 5$ with high interference, as shown later on in Section 6.3. In this thesis work, in addition to searching for the SM Higgs pair production process, constraints on the effective

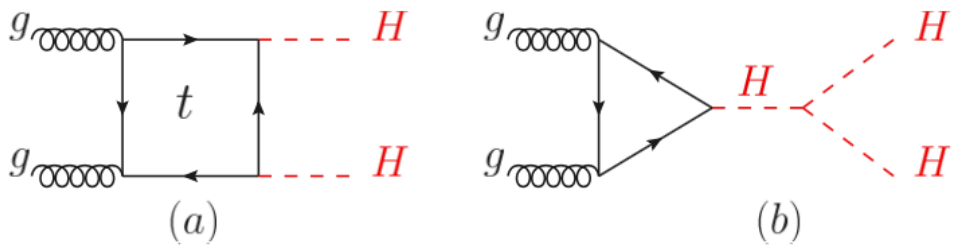

Figure 2.6: Leading Order (LO) Feynman diagrams contributing to *ggF* Higgs boson pair production through (a) a top-quark loop and (b) through the triple self-coupling of the Higgs boson [20].

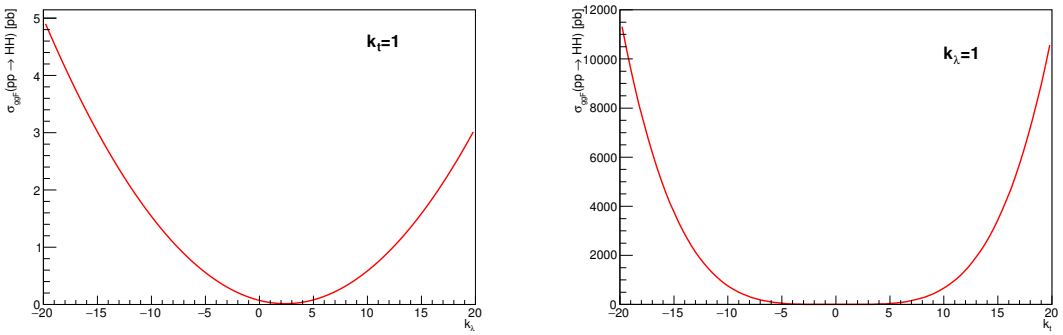

(a) (b)

Figure 2.7: Di-Higgs *ggF* production cross section (a) as a function of k_λ for $k_t = 1$ and (b) as a function of k_t for $k_\lambda = 1$.

couplings k_λ and k_t are set exploiting the kinematic changes connected to them.

The di-Higgs system decay has a variety of different final states resulting from all the possible combination of the decays of the two Higgs bosons. Figure 2.9 shows the branching ratios for all the possible combinations of Higgs decay channels that have been observed, assuming SM Higgs bosons with $m_H = 125.09$ GeV. The search presented in this thesis is performed in the $b\bar{b}\tau^+\tau^-$ final state, where one Higgs boson decays to a b-quark pair and the other to a τ-lepton pair, which has the third largest observable BR corresponding to 7.4%. Particularly, this work focuses on the final state with both τ-leptons decaying hadronically, $b\bar{b}\tau^+_{had}\tau^-_{had}$, representing the 42% of the $b\bar{b}\tau^+\tau^-$ decay. This is one of the most promising decay channels for the search for di-Higgs production as it has a good compromise between high BR and relatively clean signature that helps in separating the signal from the background processes. The results of this analysis are also combined in this thesis with the ones from the $b\bar{b}\tau^+_{lep}\tau^-_{had}$ channel and then with the ones from the other two most sensitive di-Higgs decay channels ($b\bar{b}b\bar{b}$ and $b\bar{b}\gamma\gamma$).

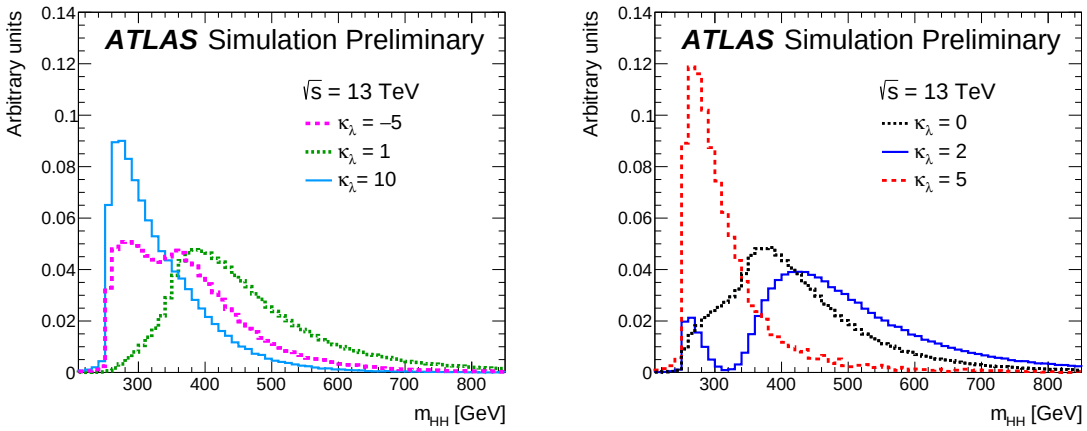

(a) (b)

Figure 2.8: Distribution of the invariant mass of the di-Higgs system m_{HH} for various values of k_λ assuming $k_t = 1$.

	bb	WW	ττ	ZZ	γγ
bb	33%				
WW	25%	4.6%			
ττ	7.4%	2.5%	0.39%		
ZZ	3.1%	1.2%	0.34%	0.076%	
γγ	0.26%	0.10%	0.029%	0.013%	0.0005%

Figure 2.9: Di-Higgs system decay branching ratios assuming SM Higgs bosons with $m_H = 125.09$ GeV.

CHAPTER 3

Beyond the Standard Model

Although all the experimental measurements are in agreement with the Standard Model expectations, the SM theory is an incomplete theory as there are physics phenomena in nature that it cannot explain. Moreover, the SM theory also has some issues in its theoretical and mathematical framework as some features are included in the theory in an ad hoc way. It is therefore believed that the SM could be extended to a more complete and natural theory. Many theories beyond the Standard Model (BSM) have been developed, which try to include the phenomena not explained in the SM theory and to solve some of the theoretical SM issues. In this chapter the limitations of the SM theory are summarised and a few BSM models, considered in this thesis work as they could be observed in the $b\bar{b}\tau^+\tau^-$ final state, are introduced.

3.1 Limitations of the SM

The limitations of the SM theory are given by phenomena that are observed in nature but are not explained by the theory and by theoretical and mathematical problems of the theory itself.

3.1.1 Phenomena not explained

There are several physics phenomena that are observed in nature but are not explained by the SM theory. Among them, there are:

- Gravity: the SM does not include a unified description of all the four fundamental forces. The gravitational interaction, which is described by the general relativity theory, is not included. This indicates that the SM breaks down at the gravitational scale $O(10^{19}$ GeV). A quantisation of the gravitational theory is needed and a new quantum field theory that can include it is required at the Planck scale.
- Dark matter and dark energy: cosmological and astrophysical observations show that the directly observable SM matter is only 5% of the energy of the universe and that there has to be another 95% made of dark matter and dark energy.
- Matter-antimatter asymmetry: the universe is made of mostly matter. Assuming that matter and antimatter were produced in equal amounts during the Big Bang, the observed amount of CP-violation is not sufficient to explain the asymmetry.
- Neutrino masses: in the SM neutrinos are massless, but the observation of neutrino oscillations implies that they have a non-zero mass. Mass terms for the neutrinos can be added to the SM by

hand, but these lead to new theoretical problems as the mechanism through which they acquire mass is not determined.

- Anomalies in the B-meson decay: several experiments (Belle, Babar and LHCb) have observed anomalies in the ratio of the decay of B-mesons to τ-leptons or muons predicted by the SM lepton universality [33, 34]. None of the observed deviations is statistically significant to claim a discovery, but they all point in the same direction, giving a potential sign of lepton universality violation and thus something amiss in the theory.

3.1.2 Theoretical problems

In the theoretical and mathematical formulation of the Standard Model some features are included in the theory in an ad hoc way or finely tuned. This is not a real problem of the theory, as the description of the observed phenomena works fine with these, but shows a lack of understanding and suggests that there could be a more fundamental theory.

- Number of free parameters: the SM theory has 18 free parameters (9 fermion masses, 3 CKM mixing angles and 1 CP-violating phase, 3 gauge couplings of the fundamental interactions, the Higgs mass and the Higgs vacuum expectation value) that need to be determined from experiments in order to have the prediction of the dynamics defined.

- Hierarchy problem (naturalness): the Higgs mass is much smaller than the Planck mass $O(10^{19}$ GeV). The mass of the Higgs boson receives quantum corrections proportional to the square of the scale at which the SM breaks down, which is to our knowledge at latest the gravitational scale, implying quantum corrections $O((10^{19}$ GeV$)^2)$. These very large corrections need to be precisely canceled out to leave the observed Higgs mass of $m_H = 125$ GeV. This cancellation requires a high level of fine-tuning (much higher than for the logarithmically divergent quantum corrections appearing in QED and QCD) and it is therefore considered unnatural.

- Unification: the unified description of the three fundamental forces included in the SM model describes them under the symmetry group $SU(3)_C \otimes SU(2)_L \otimes U(1)_Y$, which is given by the direct product of three symmetry groups with three different gauge coupling constants. The coupling constants run with the energy scale and unification under one symmetry group with one coupling constant, known as Grand Unification Theory (GUT), would be possible at high energy scale if the three constants converge at one point. However, extrapolations of the gauge couplings experimental measurements show that the three coupling constants get closer but do not precisely meet in one point at the energy scale $O(10^{16}$ GeV).

3.2 Supersymmetry

The supersymmetry (SUSY) theory [35] is one of the BSM theories that could give a solution to some of the SM limitations described above (hierarchy problem, unification and dark matter). The basic concept of the theory is to relate fermions and bosons by introducing new operators that turn fermionic states in bosonic states and vice versa. This extention predicts the existence of new particles which are supersymmetric partners of the SM ones and differ from them in spin by $1/2$.

In the minimal SUSY extension of the SM, called the MSSM (Minimal Supersymmetric Standard Model) [36, 37], the minum number of new particles (superparticles) and new interactions, consistent with the existence of supersimmetry, is realised. In this model all the particles are organised in doublets, vector

superfields, containing the vector bosons and their superpartners, and chiral superfields, containing the fermions and their superpartners. Squarks and sleptons are the scalar superpartners of the SM quarks and leptons. Gauginos are the fermionic superpartners of the SM gauge fields: the gluino is the superpartner of the gluon, three winos correspond to the superpartners of the three $SU(2)_L$ gauge fields and one bino to the $U(1)$ gauge field of the electroweak theory. Concerning the Higgs boson, the simplest theory is one with two Higgs superpartners, the higgsinos, and therefore two scalar Higgs doublets in order to generate the fermionic masses for both up-type and down-type quarks. For this reason the MSSM is also known as a two-Higgs-doublet model (2HDM). The higgsinos, winos and bino mix with each other resulting in six physical states: four neutralinos, which are electrically neutral fermions, and two charginos, which are electrically charged fermions.

Supersymmetry is one of the most popular BSM theories as it provides a solution to some of the SM problems:

- Hierarchy problem: in a supersymmetric theory the Planck-scale quantum corrections to the Higgs mass cancel between particles and superparticles, eliminating the naturalness problem.
- Unification: in a supersymmetric theory the running of the gauge coupling constants are modified and precise high energy unification of the couplings is achieved at the energy scale $O(10^{16}$ GeV).
- Dark matter: the lightest neutralino is a stable particle and it is a weakly interactive massive particle, thus it is a good dark matter candidate.

3.2.1 The two-Higgs-doublet model (2HDM)

Two-Higgs-doublet models (2HDM) [38] are models that predict the existence of two scalar Higgs doublets like the MSSM:

$$\Phi_1 = \begin{pmatrix} \phi_1^+ \\ \phi_1^0 \end{pmatrix} \qquad \Phi_2 = \begin{pmatrix} \phi_2^+ \\ \phi_2^0 \end{pmatrix} \tag{3.1}$$

with the minimum of the potential corresponding to

$$\Phi_{1,0} = \frac{1}{\sqrt{2}} \begin{pmatrix} 0 \\ v_1 \end{pmatrix} \qquad \Phi_{2,0} = \frac{1}{\sqrt{2}} \begin{pmatrix} 0 \\ v_2 \end{pmatrix}. \tag{3.2}$$

With two complex scalar $SU(2)$ doublets there are eight fields:

$$\Phi_a = \begin{pmatrix} \phi_a^+ \\ (v_a + \rho_a + i\eta_a)/\sqrt{2} \end{pmatrix} \tag{3.3}$$

with $a = 1, 2$. Three of those get absorbed to give mass to the $W^\pm$ and Z gauge bosons as in the SM and the remaining are five physical Higgs fields. There are two CP-even neutral scalars (H and h, with h being the lightest CP-even Higgs boson corresponding to the observed Higgs boson with $m = 125$ GeV), two charged scalars ($H^\pm$) and one CP-odd neutral pseudoscalar (A). Such a model can thus be described in terms of six parameters: four Higgs masses ($m_H, m_h, m_{H^\pm}, m_A$), the ratio of the two vacuum expectation values ($\tan\beta = v_1/v_2$) and the mixing angle (α) which diagonalises the mass matrix of the neutral CP-even Higgs bosons.

In this thesis work the search for Higgs boson pair production is also performed as a search for resonant production via ggF of a heavy neutral CP-even scalar Higgs boson of the 2HDM model, decaying into a pair of SM Higgs bosons, to set limits on its mass in the MSSM.

3.3 Extra dimensions

Extra dimension models [39] can also address some of the SM problems (hierarchy problem and gravity). In these models, additional space dimensions are included beyond the (3+1) observed space-time dimensions. The assumption is that the fields of the Standard Model are confined to a four-dimensional membrane, while gravity propagates in the additional spatial dimensions. The existence of additional n-dimensions implies that the effective Planck scale observed in 4-dimensions, $M_{PL} = 1.2209 \times 10^{19}$ GeV, is related to the fundamental $4 + n$-dimensional Planck scale, M, via the geometry. If the 4-dimensional and the n additional metrics are factorisable, the reduced Planck scale $\bar{M}_{PL} = M_{PL}/2\pi$ can be seen as the product of M and the volume of the compact space V_n:

$$\bar{M}_{PL}^2 = V_n M^{2+n} \,. \tag{3.4}$$

If the radius of the compact space is large enough (large extra dimensions, LED), the fundamental Planck scale can be around the electroweak scale and the hierarchy problem is solved (i.e. $M \sim O(\text{ TeV})$). However, in this type of models the hierchy problem between the Higgs boson mass scale and the Planck scale is solved, but a new hierarchy problem is introduced between the radius of the compact space, which needs to be very large, and the fundamental Planck scale ($R^{-1} \sim O(\text{ MeV})$ and $M \sim O(\text{ TeV})$). This problem is solved by introducing warped extra dimensions as in the Randall-Sundrum model.

3.3.1 Randall-Sundrum model

The Randall-Sundrum (RS) model [40] is an extra dimension model with only one additional warped extra dimension, more concretely a 5-dimensional anti-de Sitter space (AdS5) model. In this model the metric is not factorisable, but rather the four-dimensional metric is multiplied by a warp factor which is a rapidly changing function of the additional dimension:

$$ds^2 = e^{-2kR_c\phi}\eta_{\mu\nu}dx^\mu dx^\nu + R_c^2 d\phi^2 \,, \tag{3.5}$$

where $k \sim O(M_{PL})$ is the curvature scale of the space, R_c is the compactification radius, ϕ is the coordinate of the extra dimension with $0 \leq \phi \leq \pi$, $\eta_{\mu\nu}$ is the ordinary Minkowski metric and x^μ are the coordinates for the familiar four dimensions. The additional dimension is compact and has periodic boundary conditions in ϕ given by the identification of (x, ϕ) with $(x, -\phi)$. At fixed points $\phi = 0$ and $\phi = \pi$ there are the Planck brane and the TeV brane respectively, meaning that on each of these boundaries stands a four-dimensional world like the one we live in. It is assumed that gravity propagates in the whole bulk while the SM fields are localised in the TeV brane. The hierarchy between the Planck scale and the electroweak scale is given by the exponential warp factor via the relationship:

$$M_{PL}e^{-kR_c\pi} \sim O(\text{ TeV}) \,, \tag{3.6}$$

requiring not too large R_c to generate a large hierarchy since the source of the hierarchy is an exponential function of the compactification radius. The small exponential factor above ($O(10^{-16})$) is the source of the large hierarchy between the observed Planck and weak scales. A scheme of the 5-dimensional space of the RS theory is illustrated in Figure 3.1.

To explore the gravity effects on the TeV brane at $\phi = \pi$, the graviton field can be expanded, treated as small fluctuations around the background metric, into the RS Kaluza-Klein (KK) modes $h^n_{\mu\nu}(x)$ upon compactification. Then, the effective 4-dimensional interaction Lagrangian of the RS model is given by:

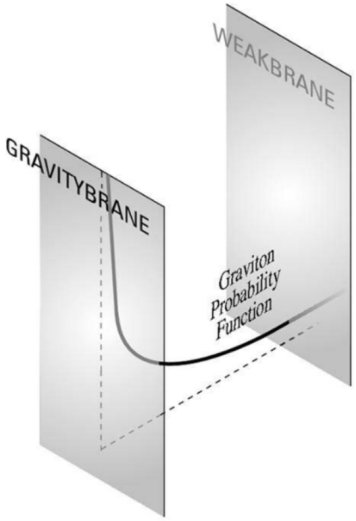

Figure 3.1: Scheme of the 5-dimensional space of the RS theory. The gravity (Planck) and weak (TeV) branes are the 4-dimensional boundaries of the extra dimension. The figure also illustrates the metric behaviour along the extra dimension [41].

$$\mathcal{L} = -\frac{1}{\bar{M}_{PL}} T^{\mu\nu} h^0_{\mu\nu}(x) - \frac{1}{\Lambda_\pi} T^{\mu\nu} \sum_{n=1}^{\infty} h^n_{\mu\nu} \,, \tag{3.7}$$

where $\Lambda_\pi = \bar{M}_{PL} e^{-kR_c\pi}$ and $T^{\mu\nu}$ represents the SM energy-momentum tensor. The couplings of the zero mode ($n = 0$), which is massless, and massive modes ($n = 1, 2, ...$) to the SM particles are proportional to $\frac{1}{\bar{M}_{PL}}$ and $\frac{1}{\Lambda_\pi}$ respectively. The mass of the n^{th} RS KK graviton excitation can be written as:

$$M_n = x_n k e^{-kR_c\pi} = \frac{x_n}{x_1} M_1 \,, \tag{3.8}$$

where x_n is the n^{th} root of the Bessel function. The mass splitting of the RS KK gravitons is of the TeV order, which implies that they can be produced as resonances at the LHC and should be observable as spin-2 particles that can be reconstructed from their decay products. The mass of the first KK mode M_1 and the effective coupling constant $c = \frac{k}{\bar{M}_{PL}}$ can be chosen as the two independent input parameters of the RS model. The total decay width of the n^{th} KK graviton can be written as:

$$\Gamma_n = \frac{1}{16\pi} x_n^2 M_n c^2 \Delta_n \,, \tag{3.9}$$

where $\Delta_n = \sum_V \Delta_n^{VV} + \sum_f \Delta_n^{ff} + \Delta_n^{HH}$ and Δ_n^{yy} is the coefficient for the decay $G^n_{KK} \to yy$, with y being a SM particle (V stands for vector-boson, f for fermion and H for the Higgs boson).

In this thesis work the search for Higgs boson pair production is also performed as a search for resonant production via ggF of a spin-2 KK graviton excitation G_{KK} in the bulk RS model, decaying into a pair of SM Higgs bosons, to set limits on its mass.

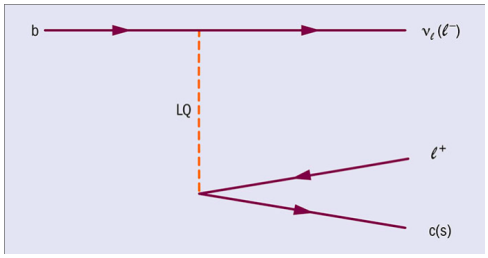

Figure 3.2: Example of a Feynman diagram of a possible leptoquark-mediated $b \to cl^+\nu_l$ or $b \to sl^+l^-$ transition [49].

3.4 Leptoquarks

Leptoquarks (LQ) [42] are predicted by many extensions of the SM, such as GUTs, technicolor and composite models, and provide a connection between the quark and lepton sectors which exhibit a similar structure in the SM. LQs can be scalar or vector bosons, with masses predicted at the TeV scale. They carry colour charge and fractional electric charge and possess both non-zero baryon and lepton numbers and therefore decay to a quark-lepton pair. They are often assumed to couple to a single generation of quarks and leptons following the minimal Buchmüller-Rückl-Wyler model [43], which is a model-independent approach to classify the production and the decay of LQs.

Recently, anomalies have been observed in B-meson decays giving a hint of possible violation of lepton universality. They could be attributed, if confirmed, to the exchange of LQs [44]. Particularly, anomalies in the ratio of the B-meson decay rate to τ-leptons and to muons have been observed by the BaBar, Belle and LHCb experiments with deviations from the SM of the order of four standard deviations [33, 45]. In order to explain these anomalies, flavour structure studies of LQ couplings have been performed, which show that predominant couplings to third-generation fermions are required [45–47]. Moreover, anomalies in the ratio of the B-meson decay rate to muons and to electrons observed by the LHCb collaboration [34, 48] could also be explained in a specific composite model, which predicts LQs decaying predominantly to third-generation fermions and LQs with masses around the TeV scale [48]. Figure 3.2 shows an example of a Feynman diagram of a possible leptoquark-mediated $b \to cl^+\nu_l$ or $b \to sl^+l^-$ transition, that could explain the anomalies observed in the B-meson decays. This motivates the interest in the search for third-generation LQs.

In pp collisions, LQs can be produced in pairs predominantly through gluon-gluon fusion or quark-antiquark annihilation processes. Feynman diagrams of such processes are shown in Figure 3.3. Third-generation LQs (LQ_3) can decay to $b\tau$ or $t\nu$ in case of up-type LQs (LQ_3^u) and $b\nu$ or $t\tau$ in case of down-type LQs (LQ_3^d), as shown in Figure 3.4. In this thesis work a dedicated search for pair production of third generation scalar leptoquarks has been performed in the $b\tau_{had}b\tau_{had}$ decay channel, based on the search for Higgs boson pair production performed in the same final state, to set limits on the LQ_3 mass.

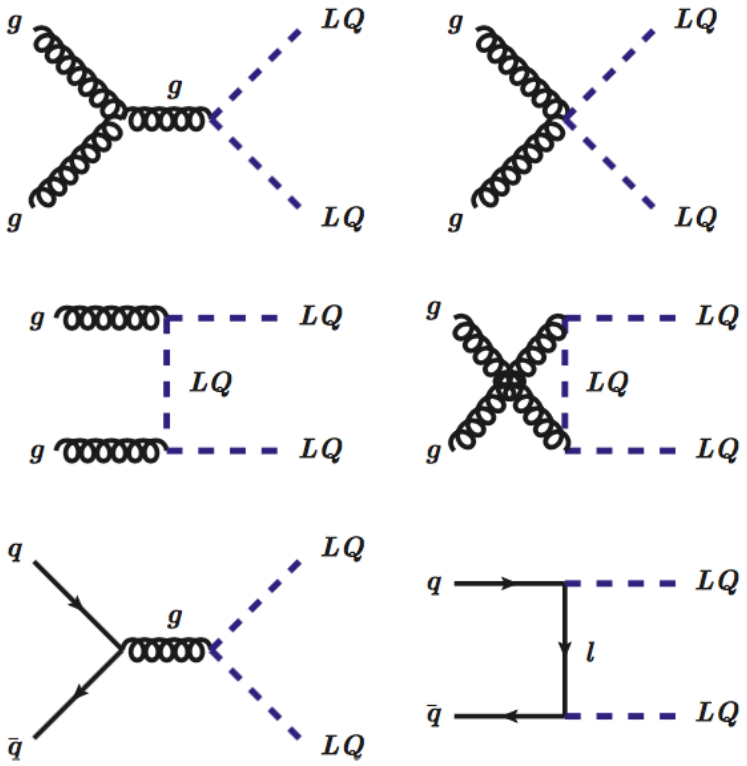

Figure 3.3: Leading Order Feynman diagrams of LQ pair production.

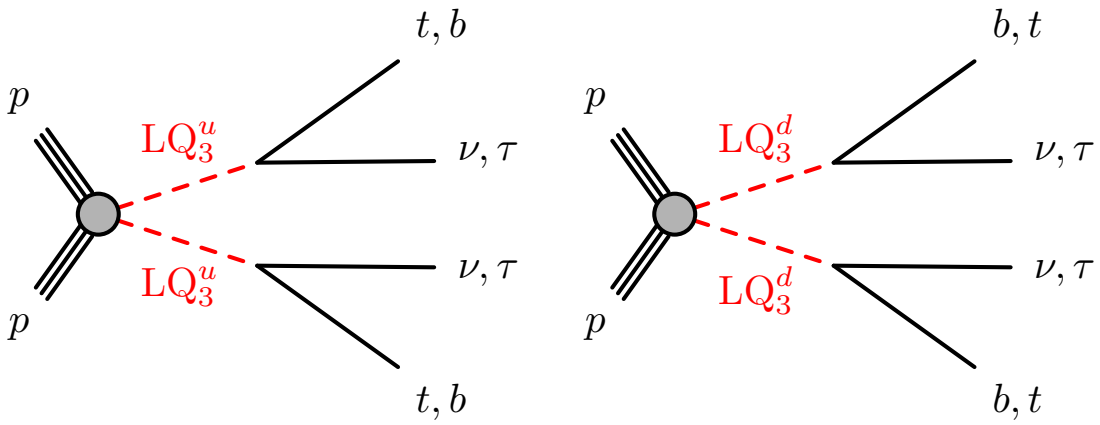

(a) (b)

Figure 3.4: Pair production and decay of a) LQ_3^u and b) LQ_3^d.

CHAPTER 4

The ATLAS experiment at the Large Hadron Collider

The European Organisation for Nuclear Research (CERN) is one of the largest centres for scientific research in the world, where the world's largest and most complex scientific instruments are employed to study the basic constituents of matter and probe the fundamental structure of the universe. The CERN laboratory sits at the French-Swiss border near Geneva. It was founded in 1954 to create an European scientific centre of excellence, it was one of Europe's first joint ventures and now it has 22 member states.

The instruments used at CERN are particle accelerators and detectors. A system of several accelerators boost beams of particles (protons and ions) to high energies before the beams are made to collide with each other in the Large Hadron Collider (LHC). Detectors observe and record the products of these collisions. One of these detectors is the ATLAS (A Toroidal LHC ApparatuS) experiment, whose data are used in this thesis.

This chapter introduces the Large Hadron Collider accelerator, provides a short description of pp collisions physics and gives an overview of the Monte Carlo simulations used in ATLAS. Then, it provides a short description of the ATLAS experiment, where the detector components that allow one to trigger on and collect the data events needed for physics analyses are described. More detailed descriptions of the structure and functions of each ATLAS subsystem can be found in References [50–52].

4.1 The Large Hadron Collider

The Large Hadron Collider [53] at CERN is the highest energy collider ever built, dedicated to accelerating and colliding protons and ions. It was designed to provide proton-proton (pp) collisions with a centre-of-mass energy of 14 TeV and an instantaneous luminosity of $10^{34}\,\mathrm{cm}^{-2}\mathrm{s}^{-1}$, and lead ion collisions at a centre-of-mass energy of 2.76 TeV per nucleon and an instantaneous luminosity of $10^{27}\,\mathrm{cm}^{-2}\mathrm{s}^{-1}$.

To reach such high energies a system of several accelerators is used as injector chain to the LHC, as illustrated in Figure 4.1. The proton source is a hydrogen bottle from which protons are extracted using electric fields and then injected into the first accelerator. Each machine boosts the protons up to a certain energy before injecting them into the next one, until they reach the LHC with an initial energy of 450 GeV. As illustrated in Figure 4.1, the rotating proton beams of the LHC, once accelerated to the designed energy, collide in four interaction points (the four yellow dots), where four particle detectors have been built in order to analyse the products of the high-energy collisions.

Data recorded by the ATLAS detector [52] are used in this thesis. The other three detectors are CMS (Compact Muon Solenoid) [54], ALICE (A Large Ion Collider Experiment) [55] and LHCb (b stands for

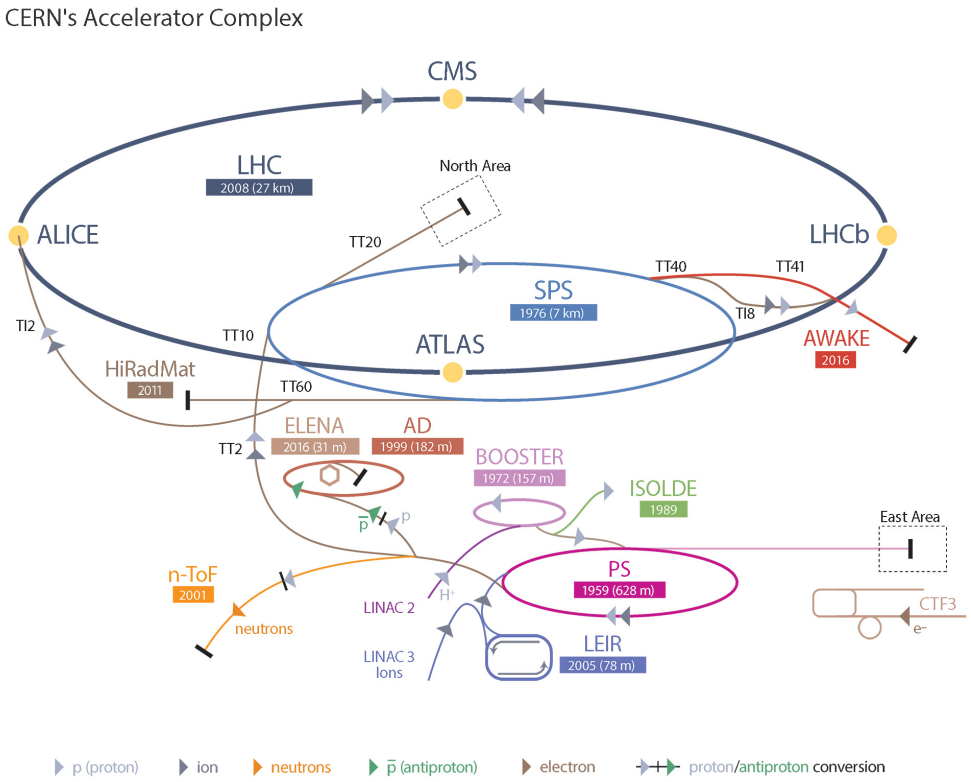

Figure 4.1: The layout of the LHC and the CERN accelerator complex acting as the injector chain for the LHC [53].

beauty) [56]. ATLAS and CMS are both general purpose detectors built with the goal to search for the SM Higgs boson and study its properties, to make SM precision measurements and to look for possible new physics beyond the SM. ALICE is a detector built to record and analyse the heavy ions collisions products in order to study the phenomenology of the strong interaction. LHCb is a detector dedicated to B-meson physics and flavour physics in general, investigating CP violation, lepton universality and lepton flavour violation. In addition, there are smaller experiments, such as TOTEM [57] and LHCf [58], installed at some distance from the interaction points to study the production of particles in the forward region (along the beam direction).

4.1.1 Machine design

The LHC is a 27 km long circular hadron collider housed in the tunnel built between 1984 and 1989 for the LEP (Large Electron-Positron) collider. The tunnel is located between 45 m and 170 m below the ground surface, between the Jura mountains and the Geneva airport.

Proton beams are injected from the CERN accelerator system into the LHC in a series of bunches of 1.15×10^{11} protons, and every beam is designed to have 2808 circulating proton bunches. The bunches are arranged in "trains" of 72 bunches, with 25 ns spacing within the train, and 12 empty bunches between two trains. In the LHC, the proton beams are accelerated by radio frequency (RF) cavities and they are bent around the LHC ring by large magnetic fields (8.33 T) given by dipoles. In addition to the dipoles, quadrupoles and higher order magnets are used to correct and focus the beam into the small area where collisions take place. In order to have two counter circulating proton beams along the same

circumference, oppositely oriented magnetic fields are needed. A single cryogenic structure is employed with a very complex twin-bore design, housing both proton rings in the same cryostat.

Collisions between circulating beams occur at every "bunch crossing", resulting in a peak collision rate of 40 MHz. The beams are squeezed to a transverse size of $\sim 17\,\mu$m at the interaction point (IP) to maximise the pp collision rate. Near the IP, the two beams are kept together in a single beam pipe, for approximately 140 m in each direction. To avoid unwanted collisions in the pipe, the beams stay on parallel orbits and when the beams are ready for colliding at the interaction point, the separation is removed.

The rate at which collisions occur depends on the instantaneous luminosity $\mathcal{L}$ and the collision cross section σ, related by:

$$\frac{dN}{dt} = \mathcal{L} \cdot \sigma \,. \tag{4.1}$$

The instantaneous luminosity is given by:

$$\mathcal{L} = \frac{N_b^2 n_b f_{\text{rev}} F \gamma}{4\pi\varepsilon\beta^*} \,, \tag{4.2}$$

where N_b is the number of particles per bunch, n_b the number of bunches per beam, f_{rev} the revolution frequency, F is a geometric function to account for the crossing angle between the beams, γ stands for the relativistic Lorentz factor, ε is the beam emittance (a measure of the uniformity of the momentum of particles in the beam) and β^* is a measure of how narrow the beam is at the interaction point. The integrated luminosity $L = \int \mathcal{L}\, dt$ is a measure of how many collisions have occurred. The number of events occurring for a given process with a given cross section σ_{process} corresponding to an integrated luminosity L is given by $N_{\text{process}} = L \cdot \sigma_{\text{process}}$. Since many of the interesting physics processes at the LHC have small cross sections, it is important to maximise the luminosity as much as possible.

4.1.2 The LHC operation schedule

The LHC started operating in November 2009 with pp collisions at a centre-of-mass energy of 900 GeV. The centre-of-mass energy had been rising during the first year and in 2010 it was successfully increased to 7 TeV. During the years 2010 and 2011 the LHC continued to run at $\sqrt{s} = 7$ TeV and in 2012 the centre-of-mass energy was increased to 8 TeV. At the end of its first phase of operation, named Run 1, the LHC delivered 5.5 fb^{-1} and 22.8 fb^{-1} at 7 TeV and 8 TeV, respectively.

The second phase of the LHC operation, named Run 2, started in 2015, after a long shutdown, with collisions at a centre-of-mass energy of 13 TeV. The peak instantaneous luminosity achieved was 1.38×10^{34} cm^{-2}s^{-1}, at a bunch crossing of 25 ns. The total luminosity delivered during the Run 2, which ended in December 2018, is 158 fb^{-1} and the ATLAS experiment recorded 149 fb^{-1}. The integrated luminosity delivered by the LHC and recorded by the ATLAS experiment in Run 2 as a function of time is shown in Figure 4.2. The data analysed in this thesis are a part of the data collected by the ATLAS experiment during the Run 2, in particular during the years 2015 and 2016, corresponding to an integrated luminosity of 36.1 fb^{-1} (after the application of the Good-Run-List requirement that ensures that all the relevant components of the ATLAS detector were fully operational during the data taking). The integrated luminosity delivered by the LHC and recorded by the ATLAS experiment in 2015 and 2016 as a function of time is shown in Figure 4.3.

Currently the LHC is in the second long shutdown phase and it will start operating again in 2021 with the Run 3. During Run 3 the LHC is expected to deliver an integrated luminosity of 300 fb^{-1} from collisions at a centre-of-mass energy of 14 TeV. After that there will be a third long shutdown followed

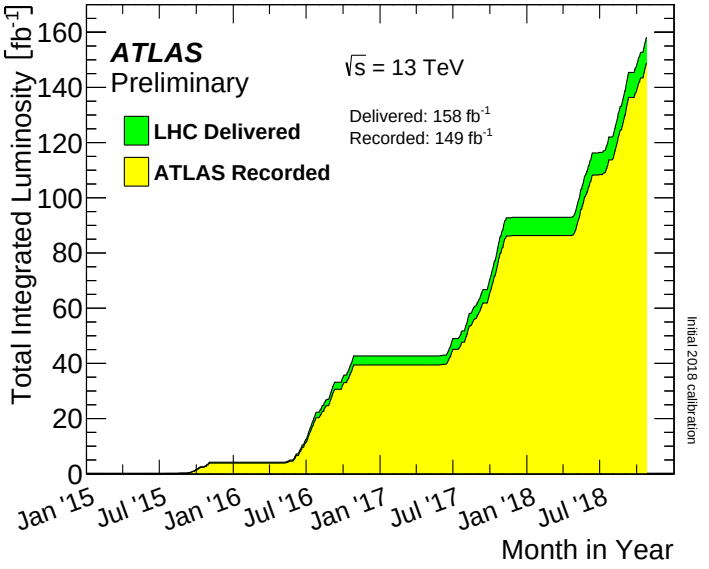

Figure 4.2: Integrated luminosity delivered by the LHC and recorded by the ATLAS experiment in Run 2 as a function of time [59].

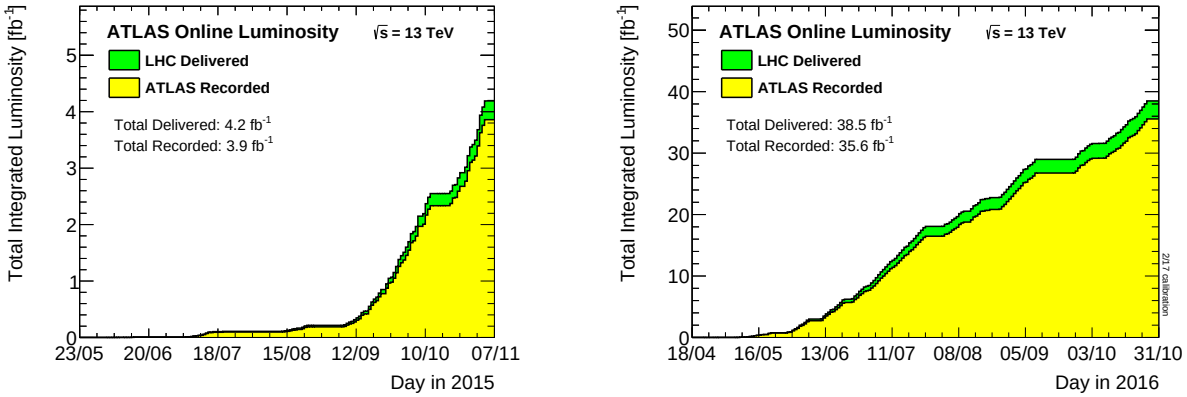

(a) (b)

Figure 4.3: Integrated luminosity delivered by the LHC and recorded by the ATLAS experiment in 2015 (a) and 2016 (b) as a function of time [59].

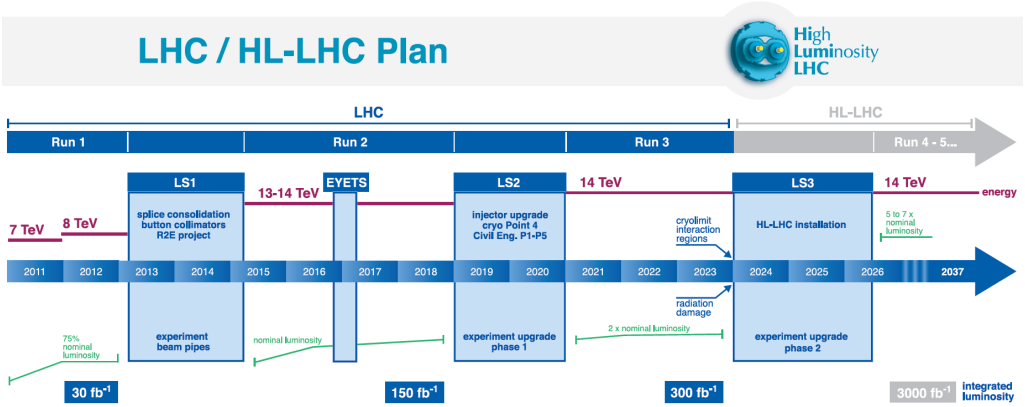

Figure 4.4: LHC operation schedule [60].

by a new operation period called High-Luminosity-LHC (HL-LHC), during which the instantaneous luminosity will reach $5 - 7 \times 10^{34}\,\mathrm{cm}^{-2}\mathrm{s}^{-1}$. The expected integrated luminosity delivered at the end of the HL-LHC is $3\,000\,\mathrm{fb}^{-1}$. The LHC operation schedule is shown in Figure 4.4. The results of the search for the SM Higgs boson pair production presented in this thesis are also extrapolated to the HL-LHC expected integrated luminosity.

4.2 Proton-proton collisions and simulation of physics processes

Proton-proton collisions are extremely complex due to the inner structure of the protons and the involvement of QCD processes. This section describes the phenomena involved in pp collisions and the simulation of the physics processes happening in the collisions and inside the ATLAS detector.

4.2.1 Physics of proton-proton collisions

In pp collisions the fundamental interaction occurs between partons, which are the quarks and gluons found inside the protons, that behave as free particles because of the QCD asymptotic freedom regime. The proton consists of "valence quarks", two up and one down quark, which define the quantum numbers of the proton. The quarks are bound by exchanging gluons, which also take part in parton interactions. The gluons can also temporarily split into quark-antiquark pairs, the "sea quarks", that can contribute in the parton interactions as well. The partons carry a fraction of proton momentum x_i, so the actual center-of-mass energy of the partonic interacion is:

$$\sqrt{\hat{s}} = \sqrt{x_1 x_2 s}\,, \tag{4.3}$$

where x_1 and x_2 correspond to momentum fractions of the interacting partons from each proton. The probability to find a parton with a certain momentum fraction x_i inside the proton is described by the parton distribution functions (PDF) [61, 62]. They depend on the parton type and on the momentum transfer scale Q^2 of the collision. The evolution in (x, Q^2) of the PDFs is described by the "DGLAP" equation [63]. Figure 4.5 shows the PDFs for protons at $Q^2 = 10\ \mathrm{GeV}^2$ and at $Q^2 = 10^4\ \mathrm{GeV}^2$. As it can be seen, gluons completely dominate among all partons which means that the LHC provides a very high "parton luminosity" for gluons. For this reason the LHC is sometimes called a "gluon collider", where processes initiated by a gluon-gluon interaction have a much larger cross section compared to the

ones initiated by quark-quark interactions.

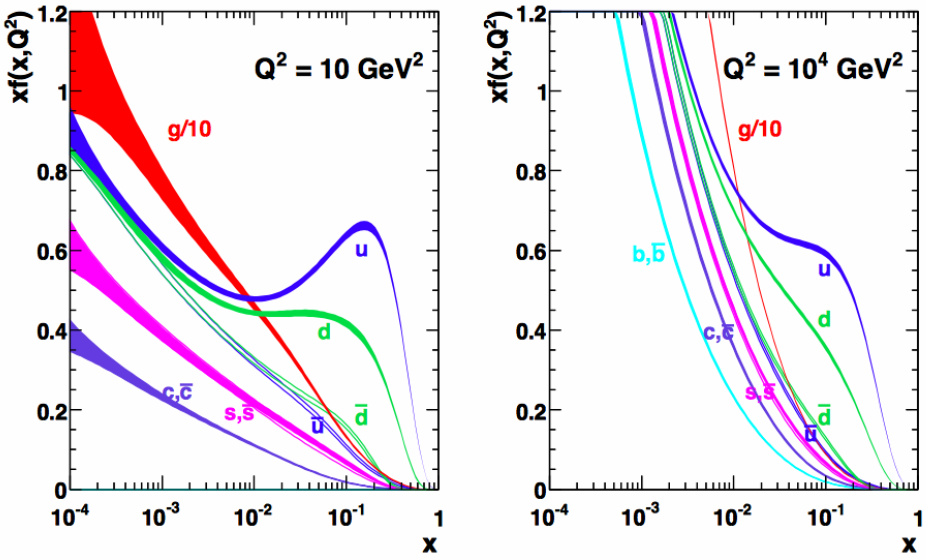

Figure 4.5: Parton distribution functions (PDFs) for protons at $Q^2 = 10$ GeV^2 (left) and at $Q^2 = 10^4$ GeV^2 (right) [62].

The interactions in pp collision can be described using the "factorisation theorem" that allows one to split the description of the phenomena occuring in the collision in several parts: the incoming protons and their parton contents described by the PDFs, the fundamental interaction (hard scattering) between the partons described by the matrix element (ME), the parton shower (PS) and hadronisation of the final state partons to the colour neutral hadrons. A schematic view of the different steps is shown in Figure 4.6. The $pp \to X$ cross section can thus be written as:

$$\sigma_{pp\to X} = \sum_{i,j} \int dx_i dx_j \int dz_k dz_m \; f_i(x_i,\mu_F^2) f_j(x_j,\mu_F^2) \; \hat{\sigma}_{i,j\to k,m}(\sqrt{\hat{s}}, \alpha_s(\mu_R^2)) \; D_k(z_k,\mu_F^2) D_m(z_m,\mu_F^2)\,, \tag{4.4}$$

where i, j are the interacting partons, $x_{i,j}$ their proton momentum fractions, $f_{i,j}$ their PDFs, $\hat{\sigma}_{i,j\to k,m}$ is the partonic cross section where k, m are the final state partons and $D_{k,m}$ are their fragmentation functions which describe the parton shower and hadronisation. In these calculations, the cross section is factorised into a perturbative part, the ME, and two non-perturbative parts, the PDFs and the PS. Two energy scales need to be set: the factorisation scale μ_F and the renormalisation scale μ_R. Substructures of loops and real emissions below these scales are only approximated instead of calculated precisely in perturbative QCD calulations. The factorisation scale μ_F represents the cut-off scale between the perturbative calculation of the partonic cross section and the non-perturbative measurements of the parton density functions and fragmentation functions. The renormalisation scale μ_R represents the cut-off in the partonic cross section calculation between the finite integral and the divergent integral, which is absorbed in the running coupling constant α_s that gains a dependence on μ_R. The factorisation and renormalisation scales are an artifact of perturbation theories with divergences. The cross section does not depend on the chosen scales if all orders in perturbation theory are included in the calculation. However, as the cross sections are calculated at a fixed order in perturbation theory, not all orders are included in the calculation and hence

the choice of the scales changes the prediction of the cross section. The two scales are usually set at the same value $\mu = \mu_F = \mu_R$, which is chosen to be in the order of the hard scattering scale.

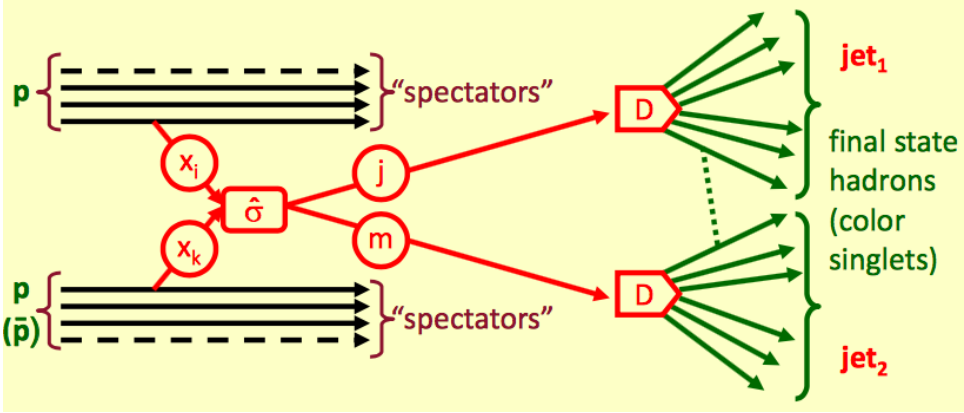

Figure 4.6: Schematic view of the different steps of a pp collision.

4.2.2 Simulation of physics processes

In order to be able to analyse and interpret the data recorded by the ATLAS experiment, a precise comparison with the theoretical predictions is needed to quantify the agreement between the data and the Standard Model or test possible new physics models. Monte Carlo (MC) event generators are employed to simulate events for signal and background processes. The full simulation consists in calculating the cross section of the process by evaluating the amplitudes of Feynman diagrams, generating events based on numerical MC techniques and simulating the resulting particles and their interactions with the detector material in order to predict how signal and background processes would appear in the detector.

An important aspect in the simulation of pp collisions is, indeed, the possibility to factorise the different steps in the collision process. As a first step, a pp collision is simulated by using the PDFs. Then, the two partons undergo the hard interaction which is computed at a fixed order in perturbation theory, using the so-called "parton-level generators" to simulate specific processes. After the hard scattering, the parton shower and hadronisation are simulated. Finally, the interaction of the final state particles with the detector material and the detector response are simulated.

Moreover, the underlying event, which describes additional interactions beyond the hard scattering event and its parton shower and hadronisation, needs to be simulated. These interactions are multiple parton interactions of the remaining partons in the proton that did not participate in the hard scattering. The energy scale of these additional interactions is only of the order of a few GeV, small compared to the hard scattering energy scale, and they produce a uniformly distributed underlying activity in the form of hadrons.

In addition, pile-up events, which are additional pp interactions in the crossing of two proton bunches, need to be simulated. They are separate collisions and are simulated separately from the hard scattering event. However, in the reconstruction of the event, they cannot be separated from the hard scattering event and therefore particles from pile-up events are part of the event signature.

A variety of MC generator programs exist. Some of these generators are so-called multi-purpose generators and can generate a full event, while some others are more specialised generators which can only simulate the hard scattering event and have to be interfaced to one of the other generators to describe the parton shower and hadronisation. After simulating the parton shower, hadronisation and

decay of hadrons, simulated events are passed to GEANT 4 [64, 65], a software package for simulating the interactions of particles with matter. A complete model of ATLAS, including all detector components is represented in GEANT 4. All interactions such as Bremsstrahlung, calorimeter showers, charge depositions etc. are simulated. All simulated events are then processed with the same trigger and reconstruction algorithms used for LHC collision data described in Chapter 5.

In this thesis the following MC generators are used to simulate signal and background processes:

- MADGRAPH 5 [66]: only generates the ME at LO precision. It is used in this thesis for the simulation of the BSM di-Higgs signal processes. For the PS description it is interfaced to PYTHIA.
- MADGRAPH5_aMC@NLO [67]: only generates the ME, providing NLO precision calculations. It is used in this thesis for the simulation of the SM di-Higgs and leptoquark signal processes. For the PS description it is interfaced to HERWIG ++ or PYTHIA.
- POWHEG-BOX [68]: only generates the ME, providing NLO precision calculations for a variety of processes. It is usually interfaced to PYTHIA for the description of the PS.
- SHERPA [69]: multi-purpose generator that provides NLO precision ME calculations for a variety of processes and includes the PS. It is usually the preferred generator for processes with additional jets, which SHERPA can include in the ME calculation up to two jets.
- PYTHIA [70, 71]: it is a multi-purpose generator that provides LO ME calculations and includes the PS. Since PYTHIA only provides LO ME precision it is not always used as a stand-alone generator, but as the PS model exhibits good agreement with data it is often used to provide the PS description for other generators.
- HERWIG ++ [72]: it is a multi-purpose generator. It is not usually used as a stand-alone generator, but it is used to provide the PS description.

In addition, the EVTGEN [73] program is also used to model the properties of the bottom and charm hadron decays in all simulations except SHERPA, which has its own implementation for the description of these decays.

4.3 The ATLAS detector

ATLAS is one of two general purpose particle physics detectors at the LHC. It is designed to detect particles from both pp and ion-ion interactions. The high centre-of-mass energy and the high luminosity of the LHC pp collisions allow for the study of physics at the TeV scale. The detector has been designed to allow several types of research:

- the search for the SM Higgs boson and the measurement of its properties;
- Supersymmetry searches;
- precision tests of electroweak interactions, flavour physics and QCD;
- measurements of the properties of the top quark;
- generic searches for new particles and interactions (the so-called exotic searches).

In order to deal with these challenges, ATLAS was designed to have:

Detector Component	Design Resolution	η Coverage	
		Measurement	Level 1 Trigger
Tracking	$\sigma_{p_T}/p_T = 0.05\% p_T \oplus 1\%$	±2.5	None
EM Calorimetry	$\sigma_E/E = 10\%/\sqrt{E} \oplus 0.7\%$	±3.2	±2.5
Hadronic Calorimetry			
Barrel and End-Cap	$\sigma_E/E = 50\%/\sqrt{E} \oplus 3\%$	±3.2	±3.2
Forward	$\sigma_E/E = 100\%/\sqrt{E} \oplus 10\%$	$3.1 < \|\eta\| < 4.9$	$3.1 < \|\eta\| < 4.9$
Muon Spectrometer	$\sigma_{p_T}/p_T = 10\%$ at $p_T = 1$ TeV	±2.7	±2.4

Table 4.1: Performance goals of the ATLAS detector. Units of p_T and E are GeV [50].

- full azimuthal coverage, for missing transverse energy measurement, and large acceptance in pseudo-rapidity;
- high granularity, to operate in an environment with high particle fluxes and overlapping events;
- precision tracking, to provide high momentum resolution and to allow the reconstruction of secondary vertices to identify b-hadrons and τ-leptons;
- precise electromagnetic calorimetry, for electron and photon identification and energy measurement;
- full-coverage hadronic calorimetry, for accurate jet and missing transverse energy measurements;
- high muon identification efficiency, momentum resolution and charge determination over a wide range of momentum;
- efficient triggering on low transverse-momentum objects.

In Table 4.1 the main performance goals of the ATLAS detector are given. Figure 4.7 shows a scheme of the ATLAS detector: it is the largest volume detector ever constructed for a particle collider, having the dimensions of a cylinder 44 m long and 25 m in diameter. It is longitudinally divided in three regions: the central part named "barrel" and the two external parts named "end-caps". It consists of an inner tracking detector (ID), which is surrounded by electromagnetic calorimeters, hadronic calorimeters and a muon spectrometer. The inner detector is immersed in an axial magnetic field of 2 T, produced by a solenoid, to allow for momentum measurement. The muon spectrometer is also immersed in a magnetic field, provided by an air-core toroid system. A two-level trigger system is used to select events to read out. The various sub-systems are described in detail in the following sections.

4.3.1 Coordinate system

The ATLAS coordinate system is a right-handed Cartesian system with the origin located at the nominal interaction point, as illustrated in Figure 4.8. The z-axis lies along the beam line, while the x-y plane is transverse to the beam line, with positive x pointing into the centre of the LHC ring and positive y pointing upward.

A cylindrical coordinate system is used when referring to the coordinates of a physics object in the detector. In this system, θ denotes the polar angle, r and ϕ denote the radius and the azimuthal angle in the x-y plane (transverse plane). The two angles, θ and ϕ, are measured, respectively, from the positive z-axis and from the positive x-axis.

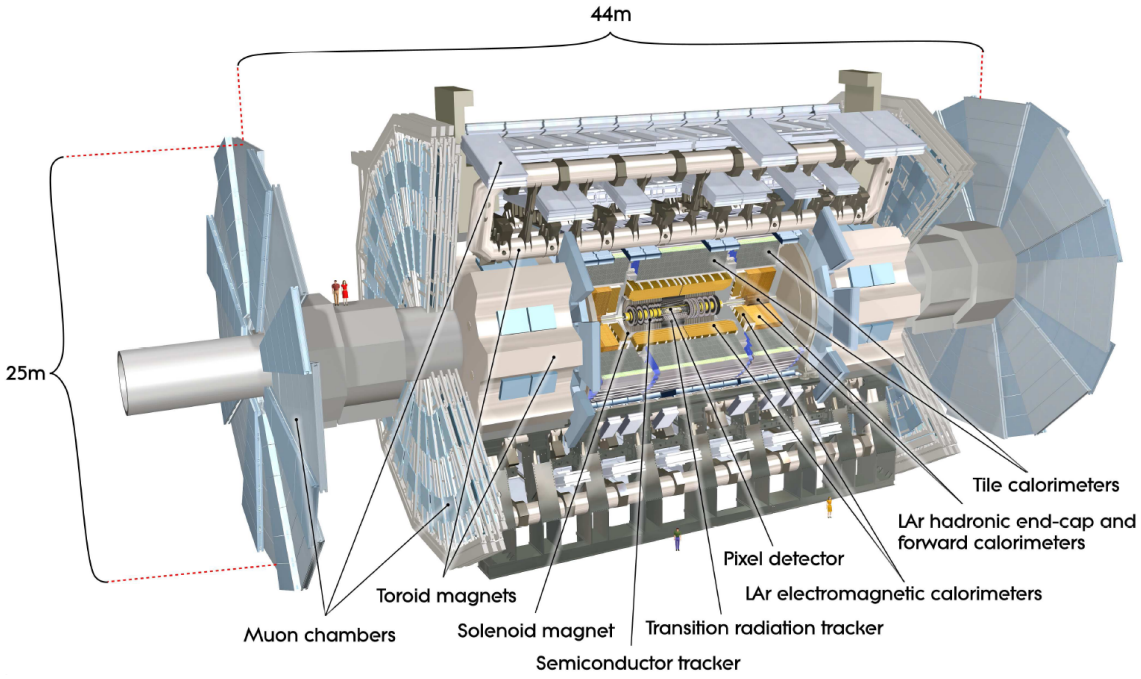

Figure 4.7: View of the ATLAS detector. The various detector sub-systems are labelled [74].

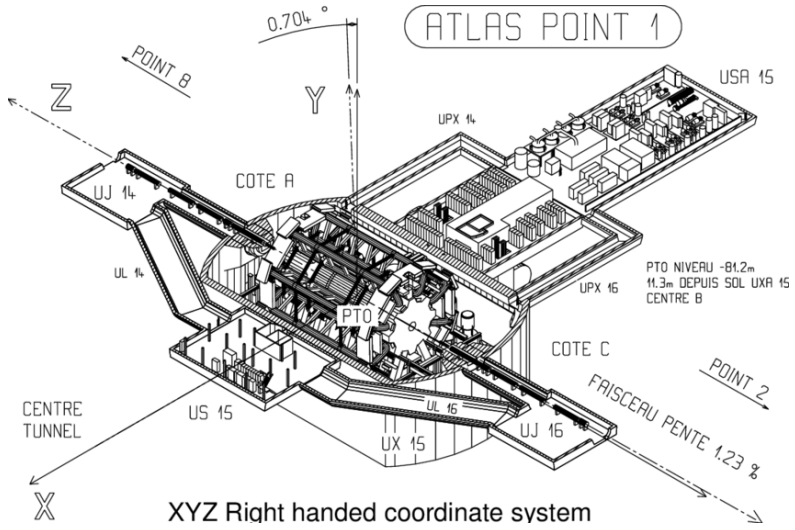

Figure 4.8: The coordinate system of the ATLAS detector [52].

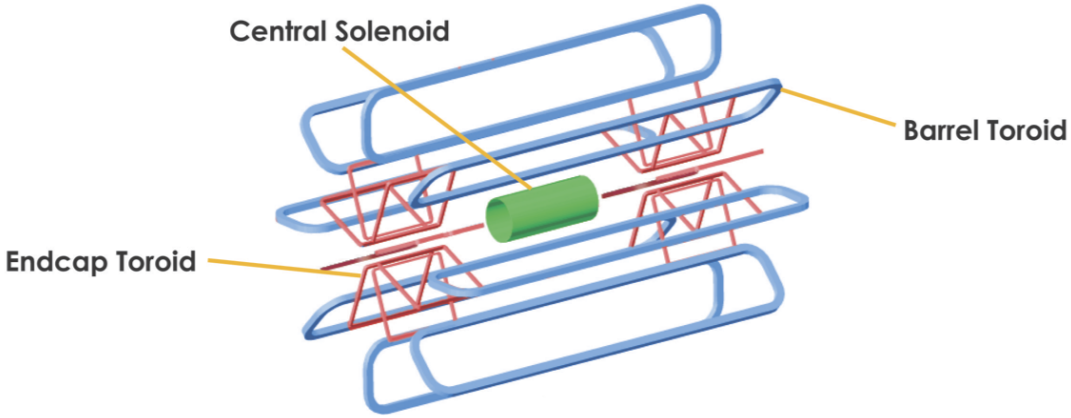

Figure 4.9: Layout of the ATLAS magnet system.

The energy and momentum of outgoing particles, E and p, are often projected onto the transverse plane where the laws of conservation of energy and momentum can be applied as energy and momentum of the initial state are known while the initial component along the z axis is not known. The transverse momentum is then defined as $p_{\mathrm{T}} = \sqrt{p_x^2 + p_y^2}$, and the transverse energy as $E_{\mathrm{T}} = E \sin\theta$.

The θ angle is usually converted into the pseudo-rapidity,

$$\eta = -\ln \tan\left(\frac{\theta}{2}\right), \tag{4.5}$$

which approaches the rapidity

$$y = \frac{1}{2} \ln \frac{E + p_z}{E - p_z}, \tag{4.6}$$

in the limit where $E \gg m$, with E being the energy of the particle, m its mass and p_z the longitudinal component of its momentum. The pseudo-rapidity is 0 in the transverse plane and infinite along the z axis, with $\eta = 1$ at 45° from the axis. The rapidity and the pseudo-rapidity are natural variables for describing angles in a system where the initial z-momentum is unknown, as in hadron colliders where the interactions occur between partons from the protons, since the difference in rapidity between two particles is invariant under boosts along the z axis. A commonly used quantity is the angular distance between objects in the $\eta - \phi$ plane, defined as $\Delta R = \sqrt{\Delta\eta^2 + \Delta\phi^2}$.

4.3.2 Magnets

The magnetic field is crucial for the measurement of the charged particles momentum as the momentum component of a charged track that is perpendicular to a uniform magnetic field can be estimated by measuring its bending radius R in a magnetic field B: $p[\,\mathrm{GeV}] = 0.3B[\mathrm{T}]R[\mathrm{m}]$. The ATLAS magnetic system [75] consists of three different types of superconducting magnets schematised in Figure 4.9.

The magnetic field in the inner detector is supplied by a central solenoid producing a 2 T field in the z-direction. The muon spectrometer magnetic field is provided by three air-core toroid magnets: the barrel toroid and the two end-cap toroids. The barrel toroid generates the magnetic field in the central zone of the muon spectrometer, along the tangential direction of the circumferences centered on the z-axis (ϕ direction). The end-cap toroids are two smaller toroids designed to provide the magnetic field in

the forward areas of the muon spectrometer. The magnetic field generated by the toroids has an intensity between 0.5 T and 4 T. As a result of the ATLAS magnetic system, the z and ϕ magnetic fields bend tracks in the ϕ direction in the inner detector, and in the η direction in the muon spectrometer.

4.3.3 Inner detector

The inner detector (ID) [76, 77] is the closest ATLAS apparatus element to the interaction point. It is designed for the reconstruction of the paths of charged particles produced in the pp collisions, as tracks, and of the primary verteces of the interactions and possible secondary vertices from the decay of long-lived particles.

The ID has a cylindrical shape around the interaction point with a radius of 1.1 m and a length of 6.2 m. The trajectories of the charged particles are reconstructed through high-resolution position measurements known as hits. The entire ID is immersed in the solenoidal magnetic field of 2 T provided by the barrel solenoid, which allows to measure the momentum and the charge of the particles from the curvature of the trajectory. Tracks and vertices are reconstructed using information from the ID as described in Section 5.1. Track and vertex reconstruction are crucial for the indentification of jets coming from b-quarks and hadronically decaying τ-leptons present in the final state studied in this thesis, as described in Section 5.4 and 5.6.

The inner detector provides accurate and efficient tracking for charged particles with $p_{\mathrm{T}} > 0.5$ GeV within $|\eta| < 2.5$, with a transverse momentum resolution of:

$$\frac{\sigma_{p_{\mathrm{T}}}}{p_{\mathrm{T}}} = 0.05\% p_{\mathrm{T}} \oplus 1\% \,, \tag{4.7}$$

as reported in Table 4.1.

Three technologies are exploited to measure track hits: an innermost pixel detector composed of silicon pixels, an intermediate silicon strip detector (SCT) and an outermost transition radiation tracker (TRT). They are briefly described in the following sections. Figure 4.10(a) shows a three-dimensional illustration of the ID layout, while Figure 4.10(b) includes a more detailed layout.

Silicon pixel tracker and the insertable B-Layer (IBL)

The silicon pixel detector is the closest ATLAS component to the beam. It is composed of layers of silicon pixels and it is designed to have a very high granularity for resolving primary and secondary interaction vertices. It consists of three cylindrical layers in the barrel region, positioned at the radial distances of 50.5, 88.5 and 122.5 mm and on disks perpendicular to the beams in the end-caps at the longitudinal distances of 49.5, 58.0 and 65.0 mm. The B-layer, positioned at a radius of 50.5 mm, plays an important role in detecting secondary vertices for the identification of jets coming from b-quark hadronisation. In 2014, during the first LHC long shutdown, a fourth pixel layer was installed inside the existing detector, the insertable B-Layer (IBL) at a radius of 33 mm from the beam axis [79]. The new pixel layer provides an additional space point very close to the interaction point, which significantly improves the b-jet identification. The detector layers are formed of silicon sensor modules and in total there are approximately 92 million pixels (consequently, readout channels) in the system.

Particles with $|\eta| < 2.5$ traverse the four layers of the detector in most cases producing four space-points. The pixel detector provides a resolution of $\sigma_{\phi} = 10\,\mu$m in the bending direction ($R - \phi$), and $\sigma_{z,\,R} = 115\,\mu$m in the z (R) direction of the barrel (end-caps). High precision in measuring the position of the hits allows to reconstruct the tracks and secondary verteces of the decay of short-lived particles

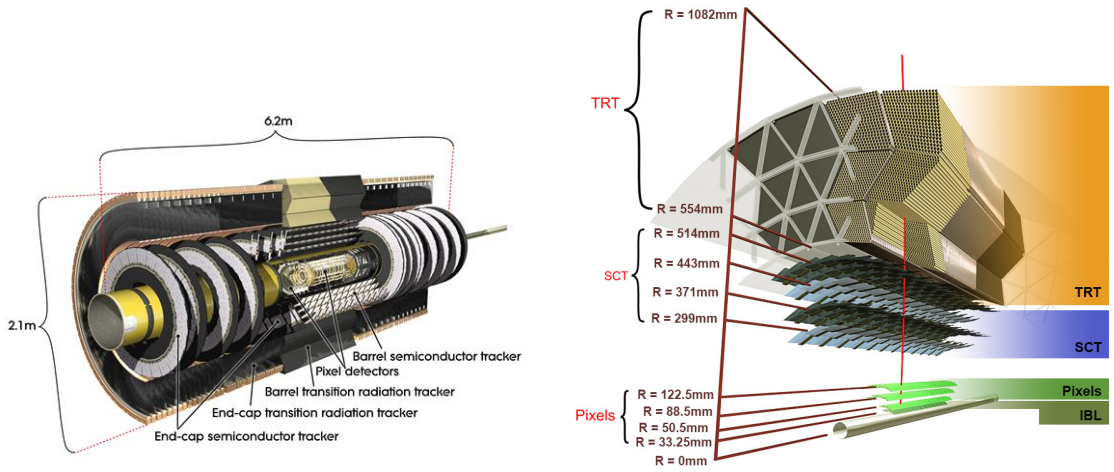

(a) (b)

Figure 4.10: (a) Layout of the ATLAS Inner detector. (b) A zoomed view of the ATLAS Inner detector, consisting of three subdetectors: the pixel detector and the Insertable B-layer, the demidonductor tracker and the transition radiation tracker [78].

and to measure the impact parameter of the tracks, which is crucial for the identification of jets from b-quarks and from hadronically decaying τ-leptons.

Semiconductor tracker (SCT)

The semiconductor tracker (SCT) is a silicon strip detector. It consists of four layers of strips axially placed with respect to the beam-pipe in the barrel and placed along the R direction on the end-caps. Other identical silicon-strip sensors are glued back-to-back with the first, creating between them a stereo angle of 40 mrad to form a two-sided module and make possible the measurement of the second coordinate. The entire SCT, including the barrel region and end-caps, is mapped to more than 6 million channels.

The spatial resolution of the detector is $\sigma_\phi = 17\,\mu\text{m}$ in the bending direction ($R-\phi$), and $\sigma_{z,R} = 580\,\mu\text{m}$ in the z (barrel) or R (end-cap) direction.

Transition radiation tracker (TRT)

The transition radiation tracker (TRT) is the most external part of the ATLAS inner detector. It is a straw drift tube tracker, with additional particle identification capabilities from transition radiation. It is composed of modules formed from bundles of 4 mm diameter straws, filled with a gas mixture consisting of 70% Xe, 27% CO_2 and 3% O_2 which are immersed in a propylene radiator. In the barrel the straws are parallel to the beam axis while in the end-caps the straws are radially disposed. Charged particles with $p_T > 0.5$ GeV and $|\eta| < 2.0$ will traverse at least 36 straws, except in the barrel to end-cap transition region ($0.8 < |\eta| < 1.0$) where only 22 straws will be traversed.

The TRT can only measure the position in the bending direction ($R - \phi$), with a spatial resolution of $\sigma_\phi = 130\,\mu\text{m}$. Despite the low resolution compared to the silicon trackers, and the lack of a measurement in the z direction, the TRT contributes significantly to the pattern recognition and momentum resolution thanks to the large number of measurements and longer measured track length. Moreover, when charged particles cross the boundary between the straw and the propylene fibres (foils) in the barrel (end-caps)

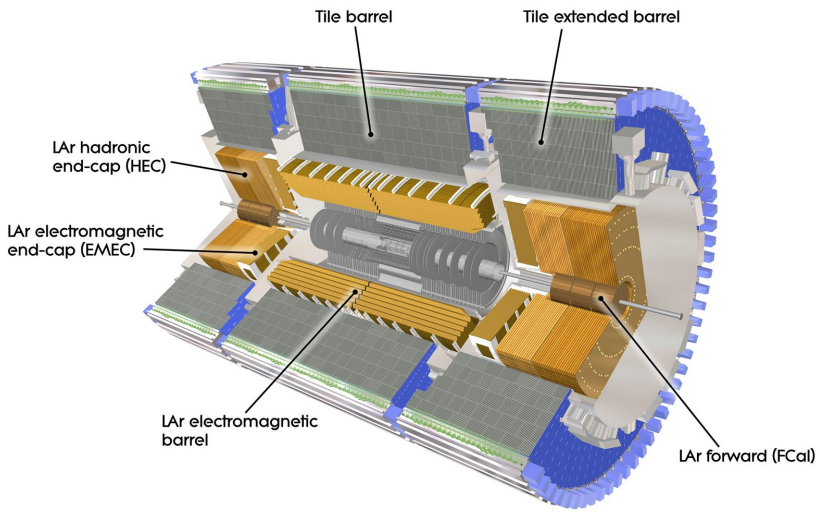

Figure 4.11: View of the ATLAS calorimeter system [81].

they emit transition radiation photons, which are absorbed by the Xenon gas mixture. The intensity of the emitted transition radiation depends on the γ-factor of the incoming particle, which depends on the mass of the particle at a given energy, and this information can be exploited for particle identification, especially for electron-pion discrimination.

4.3.4 Calorimeter system

The ATLAS calorimeter system [80] is placed outside the inner detector and its magnetic field. The purpose of the calorimeters is to measure the energy and position of particles. ATLAS uses sampling calorimeters, where different materials, sandwiched together in layers, are used to initiate the shower development (absorption) and to measure the energy of its constituents. The position measurement is obtained by segmenting the calorimeter in the z and ϕ directions. ATLAS calorimeters cover the range $|\eta| < 4.9$ and they are divided into two distinct subsystems, the electromagnetic calorimeter, for measuring the energy of electrons and photons, and the hadronic calorimeter, for measuring the energy of hadrons. Over the η region matched to the inner detector, the fine granularity of the electromagnetic calorimeter is ideally suited for precision measurements of electrons and photons energy. The less dense granularity of the rest of the calorimeter is sufficient to satisfy the physics requirements for jet energy measurements and missing transverse momentum measurements. Information from the calorimeter system are crucial for the reconstruction, identification and energy measurement of b-jets and hadronically decaying τ-leptons present in the final state studied in this thesis, as described in Section 5.4 and 5.6. A view of the ATLAS calorimeter system is shown in Figure 4.11.

Electromagnetic calorimeter (EM)

The electromagnetic (EM) calorimeter is the innermost calorimeter and it is used to measure the energy of electrons and photons. It is a sampling calorimeter where lead is used as absorber and liquid argon (LAr) is used as active material. It consists of accordion-shaped cells filled with liquid argon alternated with layers of lead.

The EM calorimeter consists of two half barrels (named EMB), extending to $|\eta| < 1.475$ (with a 4 mm gap at $z = 0$), and two wheels on each side in the end-caps (named EMEC), the first covering $1.375 < |\eta| < 2.5$ and the second covering $2.5 < |\eta| < 3.2$. Additional material needed to instrument and cool the detector creates a "crack" region at $1.375 < |\eta| < 1.52$, where the energy resolution is significantly degraded.

In the transverse direction, the calorimeter has three layers: a pre-sampler with very high granularity in η, which can reconstruct neutral pions decaying to two photons and particles whose shower already started in the inner detector. The pre-sampler is followed by longer towers with high granularity, which detect the bulk of the EM showers, and allow for measurements of the η and ϕ coordinates of the particles. The last layer detects showers generated from particles other than electrons or photons that start showering inside the EM calorimeter before leaving it.

The energy resolution of the ATLAS EM calorimeter is, as shown in Table 4.1:

$$\frac{\sigma_E}{E} = \frac{10\%}{\sqrt{E}} \oplus 0.7\% \, . \tag{4.8}$$

Hadronic calorimeter (HCal)

The hadronic calorimeter (HCal) surrounds the EM one and it is designed to measure the energy and direction of hadrons produced by the hadronisation of quarks and gluons. The ATLAS hadronic calorimeter is composed of three different parts:

Hadronic tile calorimeter It covers the region $|\eta| < 1.7$ and uses steel as absorber and plastic scintillator tiles as active material. It consists of a barrel covering $|\eta| < 0.8$ and two extended barrels covering $0.8 < |\eta| < 1.7$, and is located immediately behind the EM calorimeter. The scintillators are connected at each end to readout photomultiplier tubes by wavelength-shifting fibres. The fibres are grouped together to form readout cells, giving projective towers in η.

Hadronic LAr end-caps calorimeter (HEC) The HEC consists of two wheels per end-cap covering $1.5 < |\eta| < 3.2$ and located directly behind the EMEC. It uses copper as absorber and LAr as active material.

Forward calorimeter (FCal) The FCal covers $3.1 < |\eta| < 4.9$. Due to the high particle fluxes and energies in the forward region, the calorimeter must contain relatively long showers in the small volume allowed by design constraints, and thus must be very dense. It is divided into three compartments. The first is designed for electromagnetic measurements, and uses copper as a passive material with liquid argon as active material. The other two compartments are designed for hadronic measurements, and use tungsten as a passive material, chosen for its high density to provide containment and minimise the lateral spread of hadronic showers.

The energy resolution of the hadronic calorimeter is:

$$\frac{\sigma_E}{E} = \frac{50\%}{\sqrt{E}} \oplus 3\% \tag{4.9}$$

in the barrel and in the end-caps, while it is

$$\frac{\sigma_E}{E} = \frac{100\%}{\sqrt{E}} \oplus 10\% \tag{4.10}$$

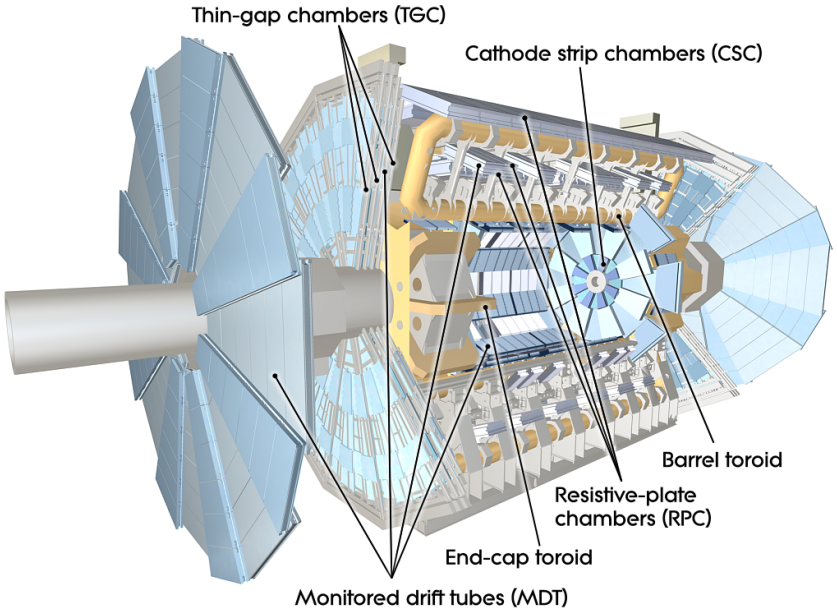

Figure 4.12: View of the ATLAS muon spectrometer [82].

in the forward region, as reported in Table 4.1.

4.3.5 Muon spectrometer

The muon spectrometer (MS) [82] is the outermost and largest detector of ATLAS. It fully covers the calorimeter system and occupies a large part of the ATLAS cavern. It is designed to identify muons and measure their momentum in the p_{T} range from about 10 GeV up to the order of 1 TeV. It adopts different detector technologies for accurate momentum and direction measurements of muons and efficient triggering.

Figure 4.12 illustrates the complete layout of the muon spectrometer. It covers the range $|\eta| < 2.7$ and, as shown in Table 4.1, its design benchmark is a 10% transverse momentum resolution for 1 TeV muon tracks. The four subsystems composing the muon spectrometer rely on four different gas detector technologies. Two of them, the resistive plate chambers (RPC) in the barrel region and the thin gap chambers (TGC) in the end-cap region, provide trigger signals, while the other two, the monitored drift tubes (MDT) and the cathode strip chambers (CSC) provide the momentum measurement. The MDT chambers provide high precision measurements in the bending direction over most of the detector acceptance while the CSC are used in the forward region where the particle flux is too high for the MDT chambers. The muon chambers are arranged in the barrel ($|\eta| < 1.05$) in three cylindrical layers around the beam axis, while in the end-cap regions ($1.05 < |\eta| < 2.7$) they are placed in three wheels.

4.3.6 Trigger system

As discussed in Section 4.1, the LHC is designed for bunch crossings every 25 ns, which translates into a bunch crossing rate of 40 MHz. Because of the high collision rate most events have to be discarded immediately in order to achieve sustainable data rates, as the ATLAS detector cannot read out and record the events at this frequency.

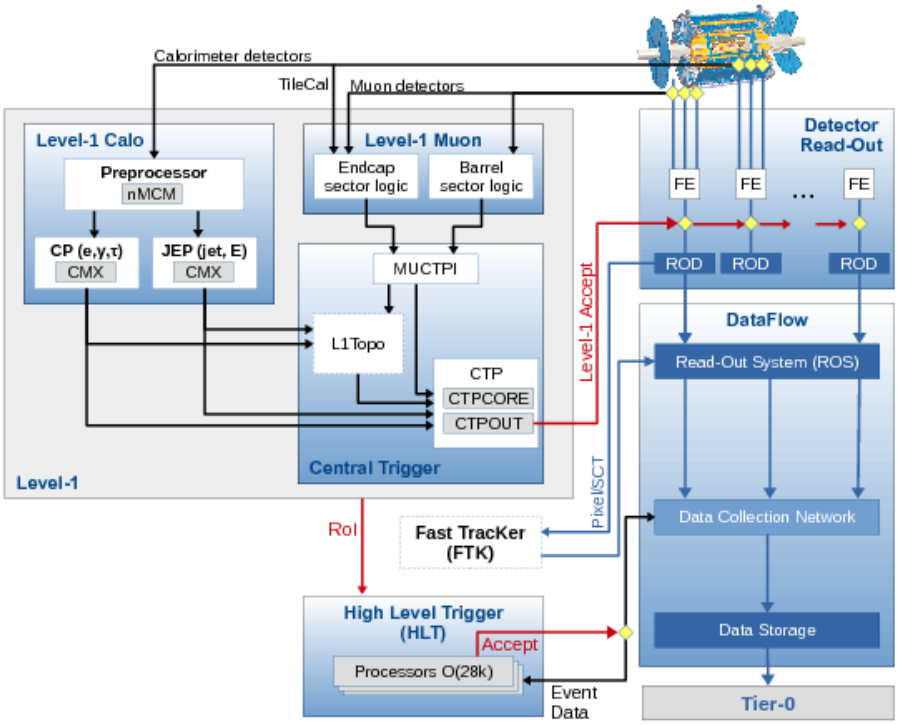

Figure 4.13: An overview of the ATLAS trigger and DAQ system [83].

The ATLAS trigger and data acquisition (TDAQ) system [83] identifies and records the interesting events. As shown in Figure 4.13, it analyses online events at two successive levels of increasing complexity that allow it to reduce the event rate through a hardware Level-1 (L1) and a software-based high-level trigger (HLT). The L1 trigger determines the regions of interest (RoIs) in the calorimeters and in the muon spectrometer using fast and dedicated hardware, and reducing the rate from 40 MHz to 100 kHz with about 2.5 µs of total latency. The HLT was born from the merging of the L2 and Event Filter levels that were used during the Run 1. It consists of fast algorithms accessing data from a RoI or using the full event information. It has access to the high-granularity and full-precision information from the calorimeters, the muon spectrometer and the inner detector, and it is software-based. The algorithms used in the HLT are similar to the physics objects reconstruction and identification alrgorithms described in Chapter 5, but they are less precise as they must be faster. They are used to select events containing physics objects which are electrons, muons, photons, jets or τ-lepton candidates that are events of interest for the ATLAS physics program. This trigger level reduces the rate of events by two orders of magnitude, reaching an average of 1 kHz with a latency of 0.2 µs.

The Data Acquisition (DAQ) system monitors the recording of the data on the storage disks. If the L1 system triggers an event, the DAQ moves the event data from the detector electronics to detector-specific Read-Out Drivers (ROD). If the event passes also the HLT, the event data are merged together and recorded to disk.

CHAPTER 5

Reconstruction of physics objects

Once the raw data have been recorded, the reconstruction and identification of all the physics objects in the final state is the first crucial step for physics interpretation in every analysis at ATLAS. Tracks are reconstructed in the inner detector and the muon spectrometer, while clusters of energy deposits are identified in the calorimeter systems. These information are then combined to reconstruct and identify particles like electrons, muons, photons, jets and τ-leptons, and to measure properties of the event such as the missing transverse energy. The signatures of different particles in the ATLAS detector are shown in Figure 5.1. The algorithms used in ATLAS to reconstruct and identify particles which are relevant for this thesis are described in this chapter.

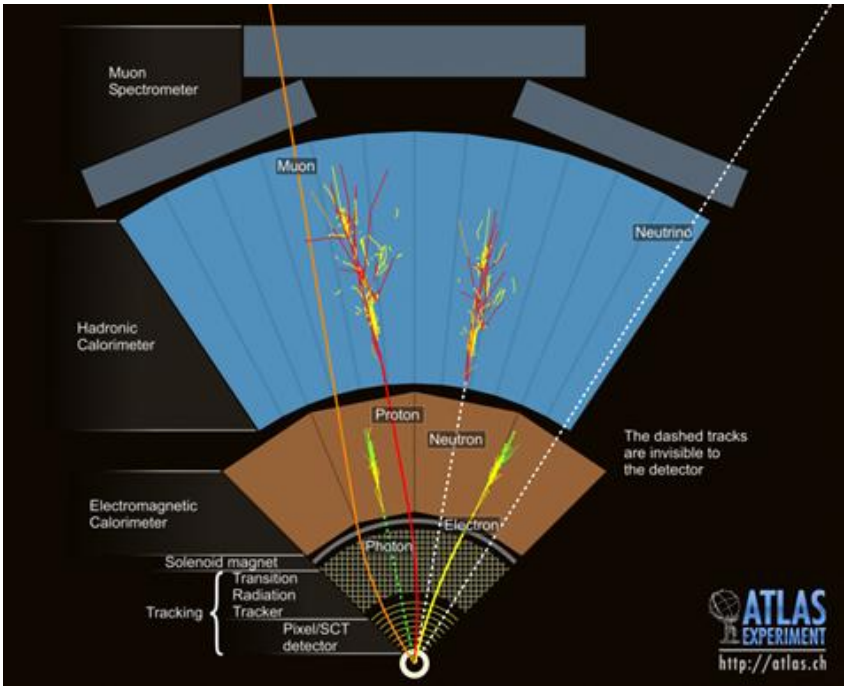

Figure 5.1: Overview of the signatures of different particles in the ATLAS detector [84].

5.1 Track and vertex reconstruction

The reconstruction of charged particle tracks starts from hits in the inner detector. When traversing the inner detector, particles describe an approximately helical path, due to the influence of the homogeneous magnetic field, and leave hits by interacting with the various detector components that they traverse, as described in Section 4.3.3. The particle tracks are reconstructed from these hits using dedicated algorithms known as tracking algorithms. The track reconstruction process consists of two steps: pattern recognition and track finding, followed by track fitting. A detailed description of the ATLAS tracking is given in Reference [85].

The main tracking algorithm is called "inside-out" tracking and begins in the first layers of the inner detector. The reconstruction starts from assembling clusters of hits in the pixel and SCT detectors. From these clusters, three-dimensional measurements referred to as space-points are created. They represent the point where the charged particle traversed the active material of the ID. Track seeds are formed from sets of three space-points and then a combinatorial Kalman filter [86] is used to build track candidates from the seeds, by including additional space-points from the remaining layers of the pixel and SCT detectors and updating the track parameters. As next step, ambiguity needs to be resolved, since several track candidates could share the same hits. In order to do this, the track is refitted with a χ^2 fit and a score is assigned to each track, based on the fit quality, the number of hits of the track, the presence of overlapping hits or "holes" (missing hits) and the track p_{T}. Then, ambiguities are solved by choosing the track with the largest score. The tracks are then extended into the TRT and, by using the full information of the three detectors, they are fitted once again with a high-resolution fit to extract the final track parameters.

A complementary tracking procedure, the "outside-in" tracking, is used to reconstruct the tracks that do not produce hits in the first layers of the inner detector, such as tracks coming from photon conversion or from the decays of long-lived particles. This tracking algorithm follows an analogous procedure to the "inside-out" tracking but starting from the TRT hits and working inwards.

The reconstructed tracks are described by six parameters estimated from the final track fit. The space coordinates of the track are described by the transverse distance from the interaction region, d_0, the impact parameter, and by z_0, the z coordinate of the point where the track is closest to the interaction region. The direction of the outgoing particle is described by η and ϕ, and the track momentum or curvature by q/p_{T}.

After tracks are reconstructed, interaction vertices can be reconstructed [87]. The reconstruction of primary vertices is organised in two steps: the primary vertex finding algorithm, dedicated to associate reconstructed tracks to the vertex candidates, and the vertex fitting algorithm, dedicated to reconstruct the vertex position. The reconstrucred tracks are used to find a vertex seed from their crossing point and the vertex position is determined using an adaptive vertex fitting algorithm [88], which takes as input the seed position and the tracks around it. Tracks incompatible with the vertex are used to seed a new vertex and the procedure is repeated until no unassociated tracks are left in the event or no additional vertex can be found. The primary vertex for each event is selected as the vertex with the highest $\sum_{\mathrm{tracks}}(p_{\mathrm{T}}^{\mathrm{track}})^2$.

5.2 Electron reconstruction and identification

Electrons are reconstructed by using tracking information from the ID and energy deposit information from the EM calorimeter [89]. Tracks are reconstructed according to the description of Section 5.1, while energy deposit clusters are formed from the energy deposits in the electromagnetic calorimeter using a cluster based algorithm. The algorithm divides the η-ϕ space into a grid of $N_\phi \times N_\eta$ elements ($\Delta\phi \times \Delta\eta = 0.025 \times 0.025$) and electron cluster seeds are searched as towers of $N_\phi \times N_\eta = 3 \times 5$ cells

with total cluster transverse energy above 2.5 GeV. The clusters are then formed around the seeds using a clustering algorithm [90] that allows for duplicates to be removed. A track-matched cluster is identified as an electron candidate, to distinguish between electrons that leave a track in the inner detector and photons that do not.

The reconstructed electron candidates contain a high contamination of electrons from photon conversions, non-isolated electrons from decays in jets and jets faking electrons. A multivariate likelihood-based identification algorithm is used to identify prompt electrons. Discriminating variables include the shape of the electromagnetic shower, the quality and length of the inner detector track and the track-calorimeter matching. Three levels of identification are provided for the electrons by cuts applied on the likelihood discriminator and, in order of increasing electron purity and decreasing electron efficiency, they are labelled as *loose*, *medium* and *tight* [89]. In the $HH \to b\bar{b}\tau^+\tau^-$ analysis, electrons are required to pass the *tight* working point requirements, that have an electron identification efficiency of about 85% and a jet mis-identification efficiency of about 0.2%. To further suppress the mis-identification, an isolation criterion, called "isolation", is defined for the electron candidate. It is defined as the sum of the p_{T} of tracks in the vicinity of the electron candidate with respect to the p_{T} of the electron candidate. In the $bb\tau\tau$ analysis presented in this thesis, a *loose* track isolation is chosen, which has a 99% electron efficiency. In this analysis, electrons reconstructed according to this definition are used in the $bb\tau_{lep}\tau_{had}$ channel, where one τ-lepton decays leptonically into an electron and the other decays hadronically. The same definition is also used in the $bb\tau_{had}\tau_{had}$ channel, where both τ-leptons decay hadronically, to veto events containing electrons in the signal region definition and to define control regions.

5.3 Muon reconstruction and identification

The muon reconstruction is based on the combination of measurements in the muon spectrometer, in the inner detector and in the calorimeters [91]. Four categories of reconstructed muons are defined, depending on the available information in the detector subsystems:

- combined muons: combination of a MS track with an ID track (they are the majority of the muon candidates and have the best purity and momentum resolution), they have an acceptance limited by the ID at $|\eta| < 2.5$;
- segment-tagged muons: combination of an ID track with an MS track segment;
- stand-alone muons: track reconstruction based only on MS measurements;
- calorimeter-tagged muons: ID tracks matched to calorimeter deposits consistent with a minimum ionising particle.

The muon identification is performed by applying quality requirements, that exploit specific features of each of the muon types, to suppress fake muons coming from pion and kaon decays and to select prompt muon candidates with robust momentum measurement. Four muon identification selections are provided: *loose*, *medium*, *tight* and *high-*p_T [91]. In the $HH \to b\bar{b}\tau^+\tau^-$ analysis presented in this thesis muons are required to pass the *medium* working point requirements, that have a muon identification efficiency of about 95%. and a mis-identification of hadrons of about 0.1%. An isolation selection criterion, based on tracks reconstructed in the inner tracker, to select muon candidates is defined in the same way as for electrons. In the analysis presented in this thesis a *loose* track isolation is chosen also for muons, which has a 99% muon efficiency. In this analysis, muons reconstructed according to this definition are used in the $bb\tau_{lep}\tau_{had}$ channel, where one τ-lepton decays leptonically into a muon and the other decays

hadronically. The same definition is also used in the $bb\tau_{had}\tau_{had}$ channel, where both τ-leptons decay hadronically, to veto events containing muons in the signal region definition and to define control regions.

5.4 Jet reconstruction and identification

Quarks and gluons produced in particle interactions undergo parton shower, by the mechanisms of gluon radiation and gluon splitting into quark-antiquark pairs, and hadronisation, producing a collimated group of particles known as jets. The goal of the jet reconstruction is to combine those particles in a physics object describing the characteristics of the initial parton.

The jet reconstruction starts by forming clusters of energy deposit in the calorimeters performing a three-dimensional topological clustering of individual calorimeter cell signals [92]. The algorithm clusters the energy deposits into so called "topo-clusters" and combines their four-momenta. Then, jets are reconstructed in ATLAS using the anti-k_t [93] clustering algorithm that sequentially combines topo-clusters into larger objects based on the momentum-weighted distance between clusters. For two objetcs i and j the algorithm defines:

$$d_{i,j} = \min(p_{\mathrm{T},i}^{-2},\, p_{\mathrm{T},j}^{-2}) \cdot \frac{\Delta R_{i,j}^2}{R^2} \tag{5.1}$$

and

$$d_{i,\mathrm{beam}} = p_{\mathrm{T},i}^{-2}\,, \tag{5.2}$$

where $p_{\mathrm{T},i}$ is the transverse momentum of the object i and ΔR the distance between the objects i, j. The parameter R controls the size of the jet and for standard jets in ATLAS this is chosen to be $R = 0.4$. The algorithm combines the two objects with the lowest $d_{i,j}$ into a single cluster, which means that objects are combined if they are very close or if a high-momentum object is surrounded by low-momentum objects. The jet is considered final if no more objects with $d_{i,j} < d_{i,\mathrm{beam}}$ are found.

After the jets are formed, the four-momentum of the jet, firstly computed simply from the sum of the four-momenta of the constituent objects, is corrected with the jet energy scale (JES) calibration [94], which consists of several consecutive stages derived from a combination of MC-based methods and in-situ techniques. The calibrations account for features of the detector, the jet reconstruction algorithm, jet fragmentation, and the busy data-taking environment resulting from multiple pp interactions, referred to as pile-up, as well as the difference in jet response between data and MC simulation. The JES calibrations are derived considering the mean of the jet response distribution E_{reco}/E_{truth}, in bins of p_{T} and η, to restore the jet response to unity. While the mean of the E_{reco}/E_{truth} distribution is corrected by the JES corrections, the width of the distribution, that quantifies the residual spread, and therefore the jet energy resolution (JER) [95], is limited by the intrinsic resolution of the calorimeters. Systematic uncertainties related to the JES and JER are important sources of uncertainties in analyses with jets in the final state.

5.4.1 *b*-tagging

The identification of jets coming from b-quark hadronisation, the so-called b-tagging, is crucial for analyses looking for processes with one or more b-quarks in the final state, as the $HH \to b\bar{b}\tau^+\tau^-$ analysis presented in this thesis. Several algorithms to identify jets coming from b-hadrons decays have been developed, exploiting the lifetime, high mass and decay multiplicity of b-hadrons and the hard b-quark fragmentation function.

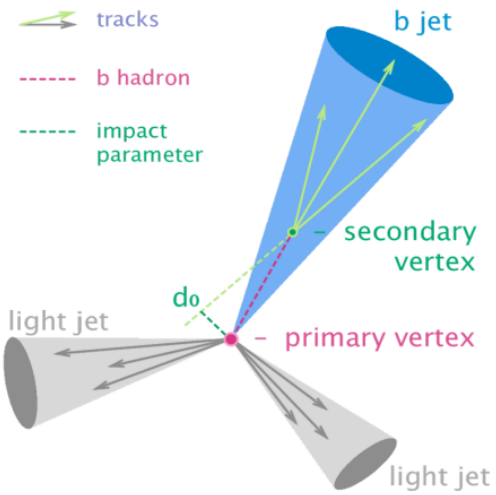

Figure 5.2: Diagram showing the principle of identification of jets initiated by b-hadron decays.

b-hadrons have lifetimes of the order of $\tau \sim 1.6\,\text{ps}$, which is long enough to make the hadron travel a few millimeters (2-3 mm) from the primary vertex before it decays, but too short to reach the calorimeters. For this reason an important feature that can be exploited to identify b-hadrons is the possibility to resolve a displaced secondary vertex of their decay in the inner detector. If a secondary vertex is identified, its distance to the primary vertex, the mass of all particles associated to the vertex and the impact parameter of the tracks are useful quantities used for the identification. b-jets can also be identified exploiting the high multiplicity of charged tracks and the high p_{T} of decay particles from b-hadrons. Figure 5.2 shows an illustration of the principle of identification of jets initiated by b-hadron decays.

The identification of b-quark jets in ATLAS is based on distinct strategies used in three basic b-tagging algorithms: impact parameter-based algorithms, an inclusive secondary vertex reconstruction algorithm and a decay chain multi-vertex reconstruction algorithm. The input variables of these b-tagging algorithms are combined in a multivariate discriminant (called MV2) that is the final default algorithm used by ATLAS [96, 97]. The ATLAS MV2 (multivariate tagger) is an algorithm based on a Boosted Decision Tree (BDT) which is trained on jets from simulated $t\bar{t}$ events, with b-jets being considered as signal and c- and light-flavour jets being considered as background.

Three MV2 variants were released, MV2c00, MV2c10 and MV2c20, trained on samples with different fractions of c-jets in order to modify the light versus c-jet rejection performance. The c-jet fraction of the training for MV2c10, which is the one used in the analysis presented in this thesis, is set at 7% such that the training is performed assigning b-jets as signal and a mixture of 93% light-flavour jets and 7% c-jets as background.

Several working points, corresponding to cuts at different values of the BDT output score of the b-tagging algorithm, are provided for different efficiencies in identifying real b-quark jets and rejecting c- and light quark jets. In particular, as mentioned above, in the analysis presented in this thesis the MV2c10 b-tagging algorithm is used. The MV2c10 tagger has also been chosen as the standard b-tagging discriminant for most of the ATLAS analyses. Figure 5.3 shows the BDT output for the recommended tagger, MV2c10, and Table 5.1 shows the operating points defined with benchmark performance values. In the $HH \to b\bar{b}\tau^+\tau^-$ analysis presented in this thesis, the 70% b-jet efficiency working point of the

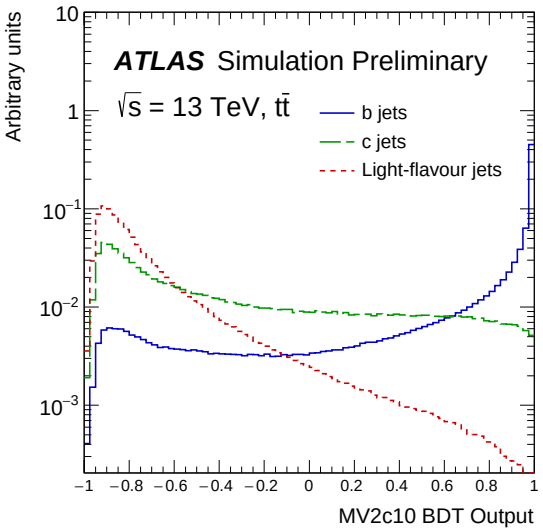

Figure 5.3: MV2c10 BDT output for b- (solid blue), c- (dashed green) and light-flavour (dotted red) jets [97].

BDT cut value	b-jet efficiency [%]	c-jet rejection	light-jet rejection	τ rejection
0.9349	60	34	1538	184
0.8244	70	12	381	55
0.6459	77	6	134	22
0.1758	85	3.1	33	8.2

Table 5.1: Operating points for the MV2c10 b-tagging algorithm, including benchmark numbers for the signal efficiency and background rejections rates defined as the inverse background efficiencies [97].

MV2c10 b-tagging algorithm is used to identify the b-jets.

The identification and mis-identification efficiencies depend on the p_T of the jet but they are found to be relatively stable for all jets between 20 GeV and 200 GeV. The efficiencies differ between simulated events and data therefore a calibration in the form of weights for simulated events is needed for each tagger and the selected b-jet identification efficiency. These so-called scale factors are derived separately for b-jets, c-jets and light jets as a function of the jet p_T and η from the ratio of the performance on data and simulated events. The uncertainties on these scale factors are important systematic uncertainties in analyses where the b-tagging algorithm is applied, like the $HH \to b\bar{b}\tau^+\tau^-$ presented in this thesis.

b-jet energy corrections

In analyses looking for processes with a resonance decaying to a pair of b-quarks it is useful to apply corrections to the measured b-jet energy to improve the invariant mass resolution of the b-jet pair. In the $HH \to b\bar{b}\tau^+\tau^-$ analysis, as in other analyses looking for processes with $H \to b\bar{b}$, the jet energy of the b-tagged jets measured in the calorimeter is corrected for the energy carried away by the muon from semi-leptonic decays of b-hadrons. The four-momentum from the closest muon in ΔR within a jet is added to the calorimeter-based jet energy after removing the energy deposited by the muon in the calorimeter (muon-in-jet correction) and the jet four-vector is then multiplied by a p_{T}-dependent correction, derived by comparing the truth-level and reconstructed b-jet p_{T}, to account for biases in the

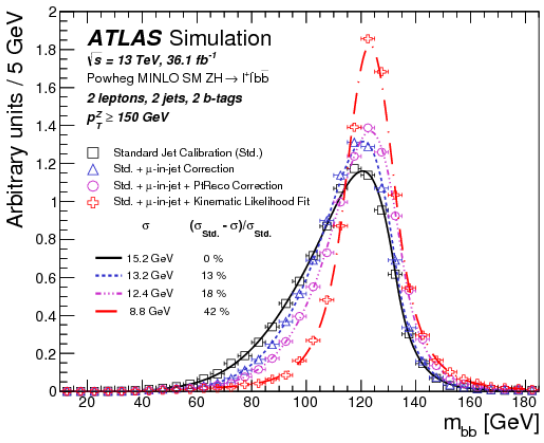

Figure 5.4: Di-b-jet invariant mass distribution after the standard jet calibration, after the muon-in-jet correction and after the resolution correction for $ZH \rightarrow l^+l^-bb$ simulated events [98].

response (resolution correction) [98]. The correction takes into account the effect of the momentum of the neutrinos produced in b-hadron semi-leptonic decays and improves the resolution of the di-b-jet mass distribution. Figure 5.4 shows the comparison of the di-b-jet invariant mass after the standard jet calibration, after the muon-in-jet correction and after the resolution correction for $ZH \rightarrow l^+l^-bb$ simulated events. It can be seen that the b-jet energy corrections give a better estimation of the di-b-jet mass in terms of peak position and relative width. In the $HH \rightarrow b\bar{b}\tau^+\tau^-$ analysis presented in this thesis the resolution of the di-b-jet mass is of about 20 GeV for the SM di-Higgs signal.

Truth-tagging

In analyses looking for processes with one or more b-quarks in the final state the b-tagging requirement leaves only very few Monte Carlo simulated events for non-dominant backgrounds with low b-jet multiplicity or that do not typically have b-quarks in the final state. This might result in badly modelled backgrounds due to the poor statistical power of the remaining samples therefore, in order to improve this, a "truth-tagging" technique is used to increase the sample statistics.

Truth-tagging replaces the application of the tagging requirements so that, instead of rejecting simulated events that do not pass the requirement, all simulated events are used and reweighted such that the effect of the tagging requirements is simulated and the statistical power of the full sample is preserved. For a given jet this involves sampling a random efficiency from a cumulative distribution built from tagging efficiencies above the chosen working point (70% in the $HH \rightarrow b\bar{b}\tau^+\tau^-$ analysis) and assigning to the jet the MV2c10 score corresponding to this efficiency. The efficiencies used to build the distribution are parameterised as a function of the jet flavour, p_{T} and η. After the generation of the MV2c10 values for the jets, the event is weighted by the efficiency of the selected jets to actually pass the b-tagging requirements used in the analysis. In the $HH \rightarrow b\bar{b}\tau^+\tau^-$ analysis truth-tagging is applied to all non-dominant MC background samples (so all except $t\bar{t}$ and $Z \rightarrow \tau^+\tau^- + bb$ processes).

5.5 Missing transverse energy

The "missing transverse energy" ($E_{\mathrm{T}}^{\mathrm{miss}}$) corresponds to the momentum which was not reconstructed in the transverse plane by the detector elements and it corresponds to the transverse momentum of particles that cannot be reconstructed directly because they do not interact with the detector material, like neutrinos.

The initial state of LHC collisions is well defined only in the transverse plane. Since the proton beams are aligned with the longitudinal axis and the transverse momenta that partons acquire inside the proton are negligible compared to the momentum of the proton, the transverse momentum in the initial state is zero. While the transverse momentum is known to be zero, the longitudinal momentum in a collision is unknown as it is $(x_1 - x_2) \times E_{beam}$, where the proton momentum fractions carried by the interacting partons, x_1 and x_2, cannot be predicted neither measured. For this reason, momentum conservation can only be imposed in the transverse plane where the initial state is known and the final state can be measured. If neutrinos, or other unknown weekly interacting particles, leave the detector with non-zero transverse momenta, the missing transverse momentum can be reconstructed using the conservation of the momentum in the transverse plane. The "missing transverse momentum" is defined as:

$$\vec{p_{\mathrm{T}}}^{\,\mathrm{miss}} = \vec{p_{\mathrm{T}}}^{\,\mathrm{initial}} - \vec{p_{\mathrm{T}}}^{\,\mathrm{final}} = -\vec{p_{\mathrm{T}}}^{\,\mathrm{final}}\,, \tag{5.3}$$

so it is equal to the negative reconstructed or visible momentum vector in the final state. A good knowledge of all objects considered for the vectorial sum is required for its reconstruction. The quantity used in ATLAS is called $E_{\mathrm{T}}^{\mathrm{miss}}$ (missing transverse energy), whose calculation algorithm [99] uses the calorimeter energy measurements to take advantage of their precise calibration for all particles except muons whose transverse momentum is directly measured in the muon spectrometer:

$$\vec{E_{\mathrm{T}}}^{\,\mathrm{miss}} = -\sum_{\text{electrons}} \vec{E_{\mathrm{T}}}^{\,e} - \sum_{\text{photons}} \vec{E_{\mathrm{T}}}^{\,\gamma} - \sum_{\text{jets}} \vec{E_{\mathrm{T}}}^{\,\mathrm{jet}} - \sum_{\text{muons}} \vec{p_{\mathrm{T}}}^{\,\mu}\,. \tag{5.4}$$

An additional term, called "soft term", is added to the so called "hard term" defined above. The soft term consists of the momentum sum of all tracks that are matched to the primary vertex but are not associated to any of the already included reconstructed objects. In the $b\bar{b}\tau^+\tau^-$ analysis presented in this thesis, the E_T^{miss} is expected to be present in the final state as there are neutrinos coming from the τ-lepton decay.

5.6 Hadronically decaying τ-lepton reconstruction and identification

The reconstruction and identification of hadronically decaying τ-leptons is very important for analyses looking for processes with τ-leptons in the final state. τ-leptons have a mass of 1.77 GeV, so they are much heavier than the other leptons, and have a lifetime of 0.29 ps. Because of their very short lifetime they typically decay, either leptonically (τ_{lep}) or hadronically (τ_{had}), before reaching the first layers of the ATLAS inner detector, so they can only be detected and reconstructed from their decay products.

The hadronic τ-lepton decay (τ_{had}) represents 65% of the possible decay modes. The hadronic decay products are one or three charged pions, in 72% and 22% of all cases respectively, and they are called "1-prong" and "3-prong" decays accordingly. Charged kaons are present in the majority of the remaining hadronic decays. In most hadronic decays, up to one associated neutral pion is also produced. The neutral and charged hadrons coming from the τ-lepton decay form the visible decay products of the τ-lepton, referred to as $\tau_{had-vis}$. The main background to the identification of hadronic τ-lepton decays is from jets of energetic hadrons produced via the fragmentation of quarks and gluons. Figure 5.5 shows an

Figure 5.5: Illustration of the typical signature of a QCD jet (left) and of a hadronic τ-lepton decay (right).

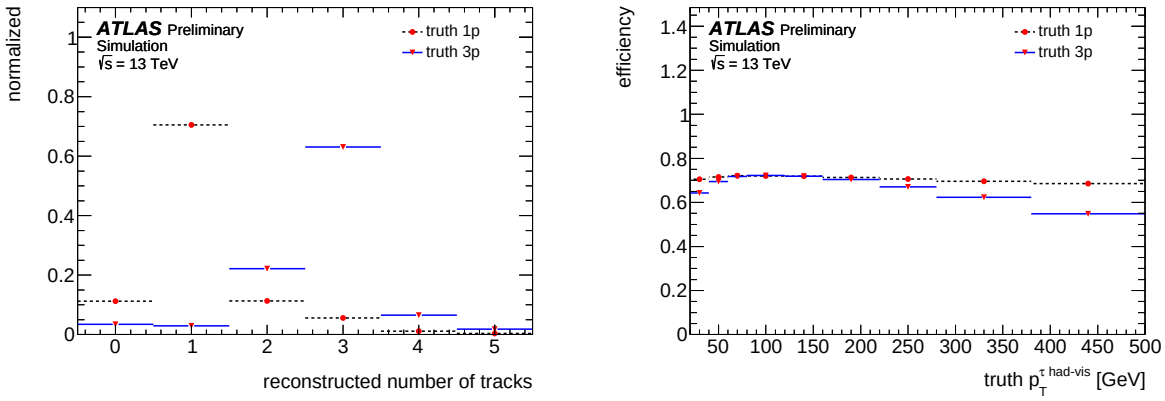

(a) (b)

Figure 5.6: Number of reconstructed tracks for τ_{had} candidates from MC true 1-prong and 3-prong τ-lepton decays (a) and efficiency for reconstructing the same number of tracks as the number of charged decay products of the τ-lepton as a function of the $\tau_{had-vis}$ p_{T} for 1-prong and 3-prong (b) [101].

ilustration of the typical signature of a QCD jet and of a hadronic τ-lepton decay. Differences between those two sigatures are exploited in the τ-identification algorithms.

In the ATLAS experiment, while leptonically decaying τ-leptons are just reconstructed as electrons or muons as it is not possible to distinguish them from prompt leptons, a dedicated identification algorithm is used to identify hadronically decaying τ-leptons [100, 101]. The τ-identification algorithm uses various discriminating variables combined in Boosted Decision Trees (BDT) to identify hadronically decaying τ-leptons and reject the jet background. Candidates for hadronically decaying τ-leptons are reconstructed using jets formed with the anti-k_t algorithm, with a radius parameter $R = 0.4$, and clusters of calorimeter cells are used as seeds of the $\tau_{had-vis}$ reconstruction algorithm. Tracks are associated to the $\tau_{had-vis}$ candidate requiring that they are in the core region of the jet, $\Delta R < 0.2$ around the $\tau_{had-vis}$ direction. Furthermore, requirements are imposed on the distance of closest approach of the track to the vertex in the transverse plane, $|d_0| < 1.0\,\mathrm{mm}$, and longitudinally, $|z_0 \sin\theta| < 1.5\,\mathrm{mm}$. This selection is optimised to maximise the fraction of 1-prong and 3-prong τ-lepton decays reconstructed with the correct charged particle multiplicity. Figure 5.6(a) shows the distribution of the number of reconstructed tracks for τ_{had} candidates from MC true 1-prong and 3-prong τ-lepton decays. The main cause of underestimation of the number of prongs is tracking inefficiency, while the leading cause for overestimation of the number of prongs comes from photon conversion tracks that pass the track selection criteria. The reconstruction efficiency is defined as the fraction of 1-prong (3-prong) hadronic τ-lepton decays which are reconstructed as 1-track (3-track) τ_{had} candidates and it is shown in Figure 5.6(b) as a function of the truth $p_{\mathrm{T}}^{\tau_{had-vis}}$.

This reconstruction of the $\tau_{had-vis}$ candidates provides very little rejection against the jet background. Rejection against jets is provided in a separate identification step using discriminating variables, which are based on the tracks and topo-clusters found in the core region ($\Delta R < 0.2$) or isolation region ($0.2 < \Delta R < 0.4$) around the $\tau_{had-vis}$ candidate direction, combined in a Boosted Decision Tree. The BDT is trained using hadronically decaying τ-leptons from a simulated $Z/\gamma^* \rightarrow \tau^+\tau^-$ sample as signal and jets from di-jets events as background. Two separate BDTs are trained for 1-prong and 3-prong τ-lepton decays using slightly different sets of variables. The BDT score distributions for signal and background events is displayed in Figure 5.7(a) for 1-prong decays and in Figure 5.7(b) for 3-prong ones. The performance of the τ-identification algorithm in terms of the inverse background efficiency, $1/\epsilon_{bkg}$, versus the signal identification efficiency are shown in Figure 5.8, where the identification efficiency is defined with respect to correctly reconstructed 1-prong or 3-prong candidates. Three fixed efficiency working points are defined by applying (p_{T}-dependent) cuts on the BDT score, named as *loose*, *medium* and *tight* [101]. The cuts are determined as a function of the $\tau_{had-vis}$ p_{T} in order to achieve a constant value for the combined reconstruction and identification signal efficiency. The three working points correspond to signal efficiencies of 60%, 55% and 45% for 1-prong and 50%, 40% and 30% for 3-prongs, with QCD jet mis-identification efficiencies of 4%, 2% and 1% for 1-prong and 4%, 1% and 0.2% for 3-prongs. The dependence of the efficiencies on the $\tau_{had-vis}$ p_{T} are shown in Figure 5.9(a) for 1-prong and in Figure 5.9(b) for 3-prong, showing that they are relatively flat. The efficiencies differ between simulated events and data therefore a calibration in the form of scale factors for simulated events is needed. These scale factors are derived as a function of the $\tau_{had-vis}$ p_T from the ratio of the performance on data and simulated events. The uncertainties on these scale factors are important systematic uncertainties in analyses where the τ-identification algorithm is applied, like the $HH \rightarrow b\bar{b}\tau^+\tau^-$ analysis presented in this thesis. In the $HH \rightarrow b\bar{b}\tau^+\tau^-$ analysis presented in this thesis the *medium* τ-identification working point is used for the selection of the signal hadronically decaying τ-leptons. This working point is also used to define "anti-τ_{had}", which are τ_{had} candidates that fail the *medium* working point requirements but still have a BDT score above a threshold of 0.35. This definition selects jets that are reasonably similar to those generated from the hadronic decay of a τ-lepton and they are used for the estimation of backgrounds with jets faking hadronically decaying τ-leptons as described later on in Section 6.4.

The Missing Mass Calculator (MMC)

In the τ-lepton decay one or two neutrinos are produced, in the hadronic and leptonic decays respectively, so the reconstructed τ_{had} visible four-momentum does not correspond to the total four-momentum as the full energy of the neutrinos cannot be determined. In analyses looking for processes with a resonance decaying to a pair of τ-leptons it is useful to adopt techniques to improve the di-τ invariant mass reconstruction compared to using the reconstructed visible mass, which is usually rather broad for signal and makes it difficult to separate it from the background.

In the $HH \rightarrow b\bar{b}\tau^+\tau^-$ analysis the Missing Mass Calculator (MMC) method [102] is used to reconstruct the invariant mass of the τ-lepton pairs. The MMC is a likelihood-based method that allows for a complete reconstruction of event kinematics in the $\tau^+\tau^-$ final states with significantly improved invariant mass resolution. The method requires solving an underconstrained system of equations for six to eight unknowns, depending on the number of neutrinos in the $\tau^+\tau^-$ final state. These unknowns include the x-, y-, and z-components of the momentum carried by the neutrinos for each of the two τ-leptons in the event, and the invariant mass of the two neutrinos from any leptonic τ decays. There are only four equations that connect these unknowns, so the number of unknowns (from six to eight, depending on the number of leptonic τ decays) exceeds the number of constraints and therefore the available information is not sufficient to find the exact solution. However, not all solutions of this underconstrained system

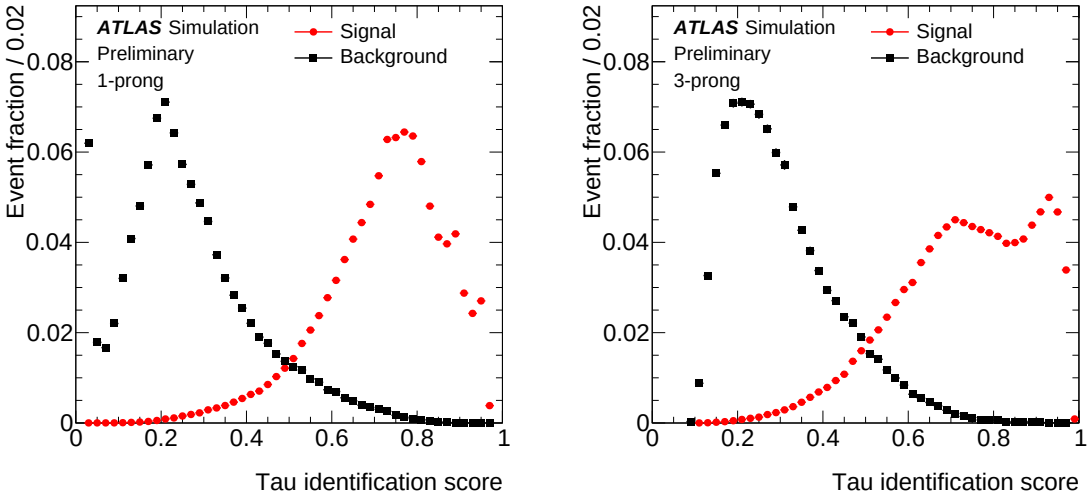

(a) (b)

Figure 5.7: BDT score for hadronic τ-lepton decays (red circles) and simulated multi-jet events (black squares) for 1-prong (a) and 3-prong (b) τ_{had} candidates [101].

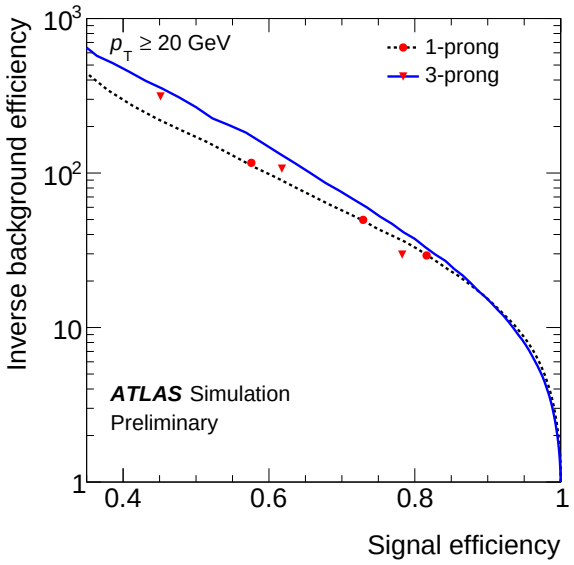

Figure 5.8: Inverse of the efficiency for mis-tagging QCD jets as a function of the identification efficiency for 1-prong and 3-prong τ_{had} candidates. The *loose*, *medium* and *tight* working points are shown on the lines. The working points do not stay exactly on the line because they correspond to variable cuts (p_T-dependent) to achieve an efficiency almost flat in p_T [101].

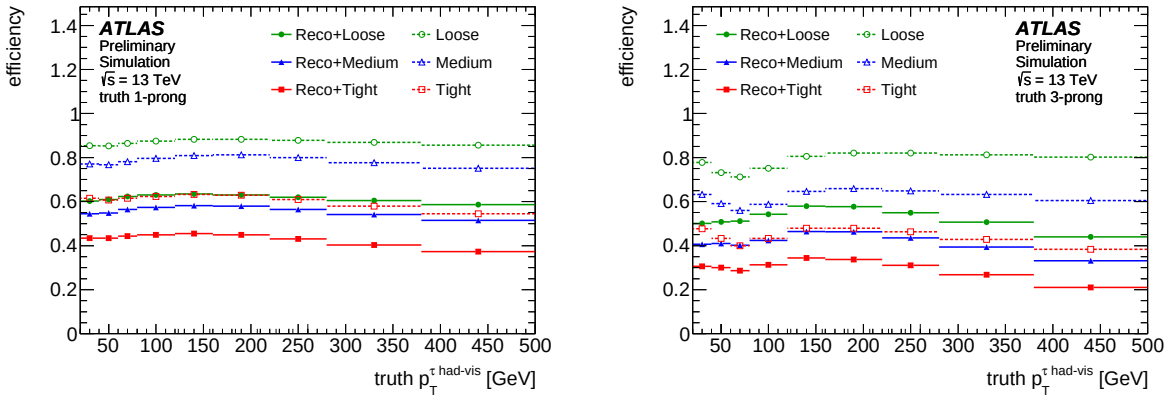

(a) (b)

Figure 5.9: Efficiency for τ_{had} identification (open symbols) and combined reconstruction and identification efficiency (full symbols) as a function of the $\tau_{had-vis}$ p_{T}, for 1-prong (a) and 3-prong (b) candidates [101].

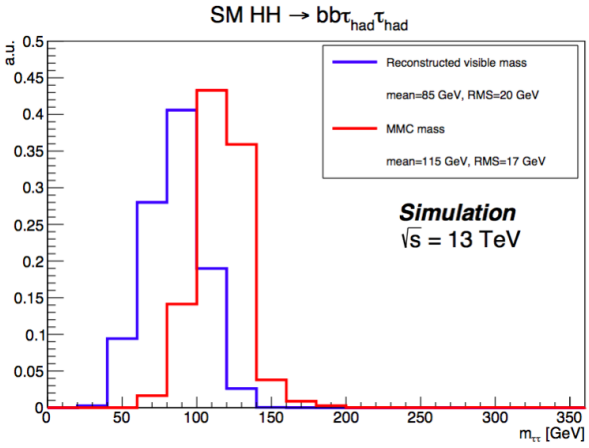

Figure 5.10: Di-τ reconstructed visible invariant mass and di-τ MMC invariant mass for $HH \rightarrow b\bar{b}\tau^{+}_{had}\tau^{-}_{had}$ simulated events.

are equally likely. The calculation uses the constraints from the measured x- and y-components of the missing transverse momentum, and the visible masses of both τ-lepton candidates. A scan is performed over the two components of the missing transverse momentum vector and the yet undetermined variables. Each scan point is weighted by its probability according to the $E_{\mathrm{T}}^{\mathrm{miss}}$ resolution and the τ-lepton decay topologies. The estimator for the $\tau^{+}\tau^{-}$ mass is defined as the most probable value of the scan points.

Figure 5.10 shows the comparison of the $\tau^{+}\tau^{-}$ reconstructed visible invariant mass and the MMC invariant mass for $HH \rightarrow b\bar{b}\tau^{+}_{had}\tau^{-}_{had}$ simulated events. It can be seen that the MMC gives a better estimation of the $\tau^{+}\tau^{-}$ mass in terms of peak position and relative width. In the $HH \rightarrow b\bar{b}\tau^{+}\tau^{-}$ analysis presented in this thesis the resolution of the di-τ mass is of about 15 GeV for the SM di-Higgs signal in the $bb\tau_{had}\tau_{had}$ channel, where both τ-leptons decay hadronically.

CHAPTER 6

Search for Higgs boson pair production in the $b\bar{b}\tau^{+}_{had}\tau^{-}_{had}$ channel

This chapter describes the search for Higgs boson pair production in the $b\bar{b}\tau^{+}_{had}\tau^{-}_{had}$ channel, where one Higgs boson decays to a b-quark pair and the other to a τ-lepton pair and both τ-leptons decay hadronically. This analysis is the main focus of this thesis work and it is part of the first ATLAS Run 2 di-Higgs to $b\bar{b}\tau^{+}\tau^{-}$ search, published in Reference [7]. The ATLAS $b\bar{b}\tau^{+}\tau^{-}$ analysis is performed in two sub-channels depending on the τ-leptons decay modes: one where both τ-leptons decay hadronically ($bb\tau_{had}\tau_{had}$), presented here as the complete analysis in this channel was developed in this thesis work, and the other where one τ-lepton decays leptonically and one hadronically ($bb\tau_{lep}\tau_{had}$). The combination of the two sub-channels is also performed in this thesis work and is presented in the next chapter.

The results of this search are interpreted in terms of an upper limit on the SM di-Higgs production cross section and limits on the triple Higgs self-coupling $k_\lambda = \lambda_{HHH}/\lambda^{SM}_{HHH}$ and on the top-quark Yukawa coupling $k_t = y_t/y_t^{SM}$ for the non-resonant search. Moreover, the data are also analysed to search for resonances decaying to a pair of Higgs bosons and interpreted in terms of upper limits on the resonance production cross section as a function of the resonance mass, constraining a model with an extended Higgs sector based on two doublets (2HDM) and a Randall-Sundrum (RS) bulk graviton model.

In the following sections all the aspects of the analysis are discussed. The signal and background samples are listed in Section 6.1. The object and event selections are discussed in Section 6.2 and 6.3 respectively. The background estimation is explained in Section 6.4. The multivariate analysis is described in Section 6.5. The list of systematic uncertainties is given in Section 6.6. The statistical interpretation is described in Section 6.7 and the results are presented and discussed in Section 6.8.

6.1 Data and Monte Carlo samples

The analysis uses pp collision data at a centre-of-mass energy of $\sqrt{s} = 13$ TeV recorded by ATLAS in 2015 and 2016, corresponding to an integrated luminosity of 36.1 fb^{-1} after the application of the Good-Run-List requirement (GRL) that ensures that all the relevant components of the ATLAS detector were fully operational during the data taking.

Monte Carlo (MC) samples used by this analysis are produced with the ATLAS simulation infrastructure [103] for both signal and background. Signal and background MC samples are described in the following sections.

Process	ME order	Generator	Parton shower	PDF	Tune
SM $HH \to b\bar{b}\tau^+\tau^-$	NLO	MadGraph5_aMC@NLO	Herwig ++	CT10	UEEE5
Non-resonant $HH \to b\bar{b}\tau^+\tau^-$ $k_\lambda = 0, 1, 2, 20$	LO	MadGraph 5	Pythia 8	NNPDF23LO	A14
$X \to HH \to b\bar{b}\tau^+\tau^-$ $m_X = 260, 275, 300, 325, 350, 400, 450,$ $500, 550, 600, 700, 1000$ GeV	LO	MadGraph 5	Pythia 8	NNPDF23LO	A14
$G_{KK} \to HH \to b\bar{b}\tau^+\tau^-$, $c = 1$ $m_G = 260, 300, 400, 500, 600, 700, 800,$ $900, 1000$ GeV	LO	MadGraph 5	Pythia 8	NNPDF23LO	A14
$G_{KK} \to HH \to b\bar{b}\tau^+\tau^-$, $c = 2$ $m_G = 260, 275, 300, 325, 350, 400, 450,$ $500, 550, 600, 700, 1000$ GeV	LO	MadGraph 5	Pythia 8	NNPDF23LO	A14

Table 6.1: List of MC generated signal samples used in the analysis.

6.1.1 Signal samples

The non-resonant SM di-Higgs signal sample is simulated assuming a Higgs boson mass of 125.09 GeV and SM ggF production diagrams with MadGraph5_aMC@NLO [67] at next-to-leading-order (NLO) using the CT10 PDF set [104] and interfaced to the Herwig ++ [72] parton shower and hadronisation model with the UEEE5 set of tuned parameters (tune) [105]. In the MC simulated sample, the finite top-quark mass effect is approximated in two-loop integrals using the so called "FT_{approx}" calculation[4]. Recently, the analytically unknown two-loop integrals are calculated numerically for the ggF di-Higgs production at NLO, including the full finite top-quark mass dependence. Thus, weights are calculated to correct the di-Higgs MC signal sample to the full NLO calculation. The weights are based on the calculations performed in References [3, 4] and are parameterised as a function of the di-Higgs invariant mass. The cross section is also scaled to the one evaluated at next-to-next-to-leading order (NNLO) and including next-to-next-to-leading logarithm (NNLL) corrections and NLO top-quark mass effects.

Non-resonant di-Higgs signal samples are simulated also with modified values of the triple Higgs self-coupling λ_{HHH}. Samples are simulated with $k_\lambda = 0, 1, 2, 20$, where $k_\lambda = \lambda_{HHH}/\lambda^{SM}_{HHH}$, using MadGraph 5 [66] at leading-order with the NNPDF23LO PDF set [106] and interfaced to the Pythia 8 [71] parton shower model with the A14 tune [107]. These four generated samples are then used to obtain non-resonant signal samples with any value of the couplings (k_λ, k_t) using the combination and reweighting procedure explained in the following section.

Signal samples of resonant di-Higgs production are simulated for the hypothesis of a resonance decaying to a pair of SM Higgs bosons in the extended Higgs sector of two-Higgs-doublet models (2HDM) and the bulk Randall-Sundrum (RS) graviton model with masses of the resonances from 260 GeV to 1 TeV. These models are simulated in MadGraph 5 at leading-order using the NNPDF23LO PDF set and interfaced to the Pythia 8 parton shower model with the A14 tune. The width of the heavy scalar, X, of the 2HDM model is fixed to 4 MeV (narrow width approximation). Graviton, G_{KK}, events are produced with values of the parameter $c = k/\bar{M}_{PL} = 1, 2$ (both the cross section and the width depend on c^2, with the width being 55 GeV and 220 GeV for $c = 1$ and $c = 2$ respectively, assuming a graviton mass of 1 TeV). The reconstructed m_{HH} distributions for different mass points of the heavy narrow width scalar, and RS gravitons with $c = 1, 2$ are shown in Figure 6.1.

The full list of MC generated signal samples used in the analysis is reported in Table 6.1.

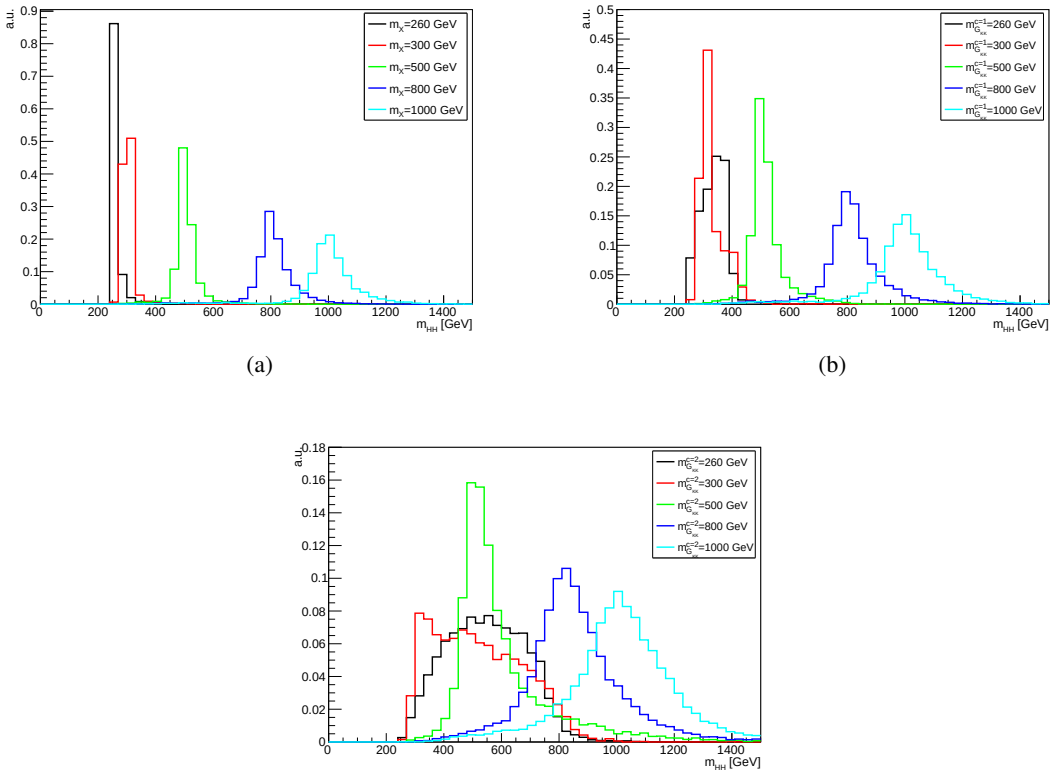

(a) (b)

(c)

Figure 6.1: Reconstructed m_{HH} distributions for different mass points of the a) heavy scalar, b) RS graviton with $c = 1$ and c) RS graviton with $c = 2$.

Non-resonant signals combination and reweighting

Signal samples of non-resonant di-Higgs production with variations of k_λ and k_t can be obtained making use of the Equation 2.55 described in Section 2.3.2. Particularly, this parameterisation is used to simulate signal distributions as a function of k_λ/k_t, as the kinematic depends only on this ratio, that can be used to test different values of (k_λ, k_t). In fact, it is possible to use three MC generated samples with different sets of parameters (k_λ, k_t) to simulate the signal distributions as a function of k_λ/k_t. This is done in this analysis by generating samples setting $(k_\lambda = 0, k_t = 1)$, $(k_\lambda = 1, k_t = 1)$ and $(k_\lambda = k_0, k_t = 1)$, with k_0 properly chosen for practical reasons. The choice of the k_λ and k_t values is arbitrary but the generated events should cover the whole m_{HH} range with sufficient statistics. Using the set of values above inserted in Equation 2.55, we can write the cross sections for the three samples, given by the squared amplitudes, in terms of the amplitudes of the box diagram B and the triangle diagram T as:

$$\sigma(k_\lambda = 0, k_t = 1) = |A(k_\lambda = 0, k_t = 1)|^2 \approx |B|^2 \tag{6.1}$$

$$\sigma(k_\lambda = 1, k_t = 1) = |A(k_\lambda = 1, k_t = 1)|^2 \approx |B|^2 + BT + TB + |T|^2 \tag{6.2}$$

$$\sigma(k_\lambda = k_0, k_t = 1) = |A(k_\lambda = k_0, k_t = 1)|^2 \approx |B|^2 + k_0(BT + TB) + k_0^2|T|^2 \,. \tag{6.3}$$

From these three equations, $|B|^2$, $|T|^2$ and $(BT + TB)$ can be written in terms of the cross sections of the three generated samples. Choosing $k_0 = 2$ we get:

$$|B|^2 = |A(k_\lambda = 0, k_t = 1)|^2 \tag{6.4}$$

$$|T|^2 = -\frac{5}{2}|A(k_\lambda = 0, k_t = 1)|^2 + 3|A(k_\lambda = 1, k_t = 1)|^2 - \frac{1}{2}|A(k_\lambda = 2, k_t = 1)|^2 \tag{6.5}$$

$$BT + TB = -\frac{3}{2}|A(k_\lambda = 0, k_t = 1)|^2 + 2|A(k_\lambda = 1, k_t = 1)|^2 - \frac{1}{2}|A(k_\lambda = 2, k_t = 1)|^2 . \tag{6.6}$$

The cross section for any (k_λ, k_t) can then be obtained by perfomring a combination of the three generated samples chosen as basis. The cross section can thus be rewritten as:

$$\sigma(k_\lambda, k_t) = |A(k_\lambda, k_t)|^2 = k_t^2 \left[\left(k_t^2 + \frac{k_\lambda^2}{2} - \frac{3}{2} k_\lambda k_t \right) |A(0,1)|^2 + (2k_\lambda k_t - k_\lambda^2)|A(1,1)|^2 + \left(\frac{k_\lambda^2 - k_\lambda k_t}{2} \right) |A(2,1)|^2 \right] . \tag{6.7}$$

This equation is used to obtain signal distributions for any (k_λ, k_t) from the three generated samples[1]. Particularly, the di-Higgs invariant mass distribution at truth-level, m_{HH}^{truth}, is derived for any (k_λ, k_t) combining the three generated samples.

The non-SM samples used as basis in the combination are simulated at LO. Thus, after having obtained the m_{HH}^{truth} distribution for several (k_λ, k_t) at LO, in order to propagate the kinematics from the LO to the NLO, a reweighting of the baseline NLO SM signal sample is performed. The weights are calculated for any LO (k_λ, k_t) sample obtained from the combination with respect to the LO $(k_\lambda = 1, k_t = 1)$ sample. For any $k_\lambda = x$, assuming k_t fixed to 1, they are derived as a function of m_{HH}^{truth} as:

$$w(k_\lambda = 1 \rightarrow k_\lambda = x, \text{bin } i) = \frac{m_{HH}^{\text{truth},k_\lambda = x, \text{bin } i}}{m_{HH}^{\text{truth},k_\lambda = 1, \text{bin } i}} . \tag{6.9}$$

These weights, derived at LO, are then applied to the NLO SM sample to obtain the NLO signal distributions for any (k_λ, k_t) used in the analysis.

To summarise the procedure, in order to obtain NLO non-resonant di-Higgs signal distributions with any (k_λ, k_t) values, three steps are performed:

- Combination of three LO generated samples using Equation 6.7 to obtain the m_{HH}^{truth} distribution for several (k_λ, k_t) at LO;
- Calculation of weights for any LO (k_λ, k_t) with respect to the LO $(k_\lambda = 1, k_t = 1)$ as a function of m_{HH}^{truth};
- Application of the weights to the NLO SM di-Higgs signal.

[1] In principle, other (k_λ, k_t) bases can be used, and for a different choice $k_0 = 20$ the equation can be rewritten as:

$$\sigma(k_\lambda, k_t) = |A(k_\lambda, k_t)|^2 = k_t^2 \left[\left(k_t^2 + \frac{k_\lambda^2}{20} - \frac{399}{380} k_\lambda k_t \right) |A(0,1)|^2 + \left(\frac{40}{38} k_\lambda k_t - \frac{2}{38} k_\lambda^2 \right) |A(1,1)|^2 + \left(\frac{k_\lambda^2 - k_\lambda k_t}{380} \right) |A(20,1)|^2 \right] . \tag{6.8}$$

Particularly, the basis $(k_\lambda, k_t) = \{(0,1), (1,1), (20,1)\}$ is used for all (k_λ, k_t) except $(k_\lambda = 2, 3, k_t = 1)$ where the basis $(k_\lambda, k_t) = \{(0,1), (1,1), (2,1)\}$ is used in order to obtain a smoother shape in a region with high interference.

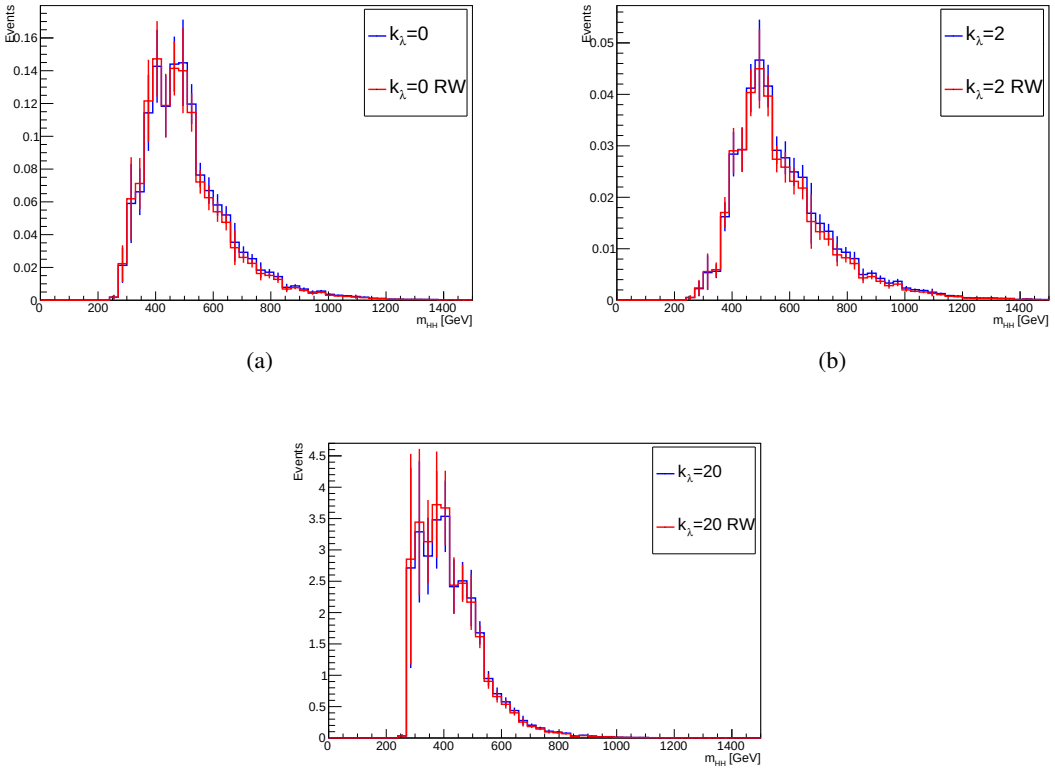

Figure 6.2: Comparison of the reconstructed m_{HH} distributions obtained using the combination and reweighting method (red) with the generated ones (blue) for di-Higgs non-resonant signal with a) $(k_\lambda = 0, k_t = 1)$, b) $(k_\lambda = 2, k_t = 1)$ and c) $(k_\lambda = 20, k_t = 1)$.

A validation test of the method is performed at LO comparing the signal distributions of the generated samples with the ones obtained by applying the obtained weights to the LO $(k_\lambda = 1, k_t = 1)$ sample. A comparison of the reconstructed m_{HH} distributions obtained using the combination and reweighting method with the generated ones is shown in Figure 6.2 for $(k_\lambda = 0, k_t = 1)$, $(k_\lambda = 2, k_t = 1)$ and $(k_\lambda = 20, k_t = 1)$, proving that the method works well given the good agreement. This validation test thus shows that the combination and reweighting procedure provides the same m_{HH} distributions as the simulated samples. The obtained NLO m_{HH} distributions for a subset of positive and negative k_λ values, with $k_t = 1$, are shown in Figure 6.3. The implementation of the reweighting method in this analysis and its validation were part of this thesis work in order to obtain non-resonant di-Higgs signal samples with variations of k_λ and k_t used for setting limits on these couplings.

6.1.2 Background samples

The dominant background processes for this search performed in the $bb\tau_{had}\tau_{had}$ channel are: $t\bar{t}$, multi-jet and Z bosons decaying to $\tau\tau$ produced in association with two heavy flavour jets (from bb, bc, cc), subsequently referred to as Z+heavy flavour (Z+HF).

The $t\bar{t}$ and single-top-quark background events were simulated using Powheg-box [68], with the CT10 PDF set, and MadSpin [108] (for all top processes, top-quark spin correlations are preserved and top

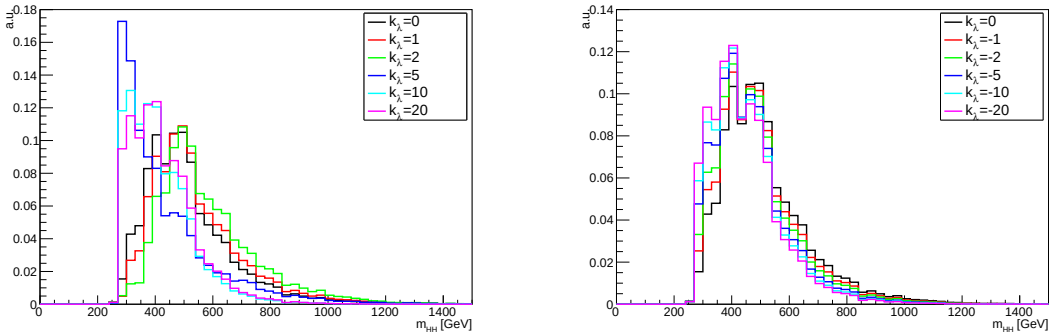

(a) (b)

Figure 6.3: Reconstructed m_{HH} distributions obtained using the combination and reweighting method for di-Higgs non-resonant signals with some positive k_λ values (left) and some negative k_λ values (right) for $k_t = 1$.

quarks are decayed using MadSpin). The parton showers were simulated using Pythia 6 [70] and the Perugia 2012 tune [109]. The $t\bar{t}$ background was scaled to match the NNLO+NNLL cross sections [110], while the single-top samples were corrected to NLO [111, 112] (approximate NNLO [113]) predictions for the t- and s-channel (Wt final state).

Events with W or Z bosons and associated jets were simulated with the Sherpa 2.2.1 generator [69], using the NNPDF30NNLO PDF set [114] and normalised to the NNLO cross sections [115].

Diboson and Drell–Yan backgrounds were produced with Sherpa 2.2.1 using the CT10NLO PDF set and the generator cross section predictions.

Quark-induced ZH processes were generated with Pythia 8, using the A14 tune and the NNPDF23LO PDF set. The samples were normalised to NNLO cross sections for QCD and NLO for electroweak processes [116–122]. The gluon-induced ZH process was generated with Powheg using the CT10 PDF set and using Pythia 8 with the AZNLO tune [123] to simulate parton showers. Cross sections [124–128] were scaled to NLO+NLL in QCD. SM single Higgs boson production in association with a top-quark pair (ttH) was simulated with MadGraph5_aMC@NLO with the NNPDF23LO PDF set and Pythia 8 was used to simulate the parton shower using the A14 tune, while the cross section was taken from Ref [2]. The contributions from other SM single Higgs boson processes are found to be negligible in this channel.

EvtGen v1.2.0 [73] was used to model the properties of bottom and charm hadron decays for all processes except those simulated in Sherpa. The detector response to the generated events was simulated with Geant 4 [64, 65].

To simulate the impact of multiple pp interactions that occur within the same bunch crossing (pile-up), minimum-bias events generated with Pythia 8 using the A2 [129] set of tuned parameters were overlaid on the hard scattering event. In addition to that, simulated events are reweighted to match the occurrence of pile-up events in data.

The full list of MC generated background samples used in the analysis is reported in Table 6.2.

6.2 Object selection

Objects arising from the pp collision products are reconstructed in ATLAS as described in Chapter 5. In the analysis presented here the following reconstruction and identification criteria are used:

Process	ME order	Generator	Parton shower	PDF	Tune
$t\bar{t}$ and single-top	NLO	Powheg-box	Pythia 6	CT10	Perugia 2012
Z/W+jets	NLO	Sherpa 2.2.1		NNPDF30NNLO	
Diboson and Drell-Yan	NLO	Sherpa 2.2.1		CT10NLO	
quark induced ZH	NLO	Pythia 8		NNPDF23LO	A14
qluon induced ZH	NLO	Powheg	Pythia 8	CT10	AZNLO
ttH	NLO	MadGraph5_aMC@NLO	Pythia 8	NNPDF23LO	A14

Table 6.2: List of MC generated background samples used in the analysis.

- electrons: required to have $p_T > 7$ GeV and $|\eta| < 2.47$ (with a veto on the barrel-endcap transition region of the calorimeter $1.37 < |\eta| < 1.52$) and pass the *tight* identification and *loose* isolation criteria;
- muons: required to have $p_T > 7$ GeV and $|\eta| < 2.7$ and pass the *medium* identification and *loose* isolation criteria;
- jets: reconstructed using the anti-kt algorithm with a radius parameter $R = 0.4$ and required to have $p_T > 20$ GeV and $|\eta| < 2.4$;
- b-jets: identified applying the 70% efficiency working point requirements of the MV2C10 b-tagging algorithm (for non-dominant backgrounds, e.g. all except $t\bar{t}$ and Z+HF, the truth-tagging technique is used);
- τ_{had}: required to have $p_T > 20$ GeV, $|\eta| < 2.5$ (with a veto on the barrel-endcap transition region of the calorimeter $1.37 < |\eta| < 1.52$), one or three tracks and pass the *medium* identification criteria;
- anti-τ_{had}: τ_{had} candidates with a τ-identification BDT score above the threshold of 0.35 but failing the *medium* identification requirement (jets reasonably similar to the ones generated from the hadronic decay of a τ-lepton, used for the estimation of backgrounds with jets faking τ_{had}).

6.2.1 Overlap removal

The physics objects reconstruction algorithms described in Chapter 5 are applied independently in the ATLAS event reconstruction. This means that the same detector object might be reconstructed multiple times as different physics objects. Since both electrons and jets are reconstructed from clusters in the calorimeters, electrons can also be reconstructed as jets, and jets can be reconstructed as electrons. Moreover, muons that radiate photons in the calorimeter might be reconstructed as electrons, since such muons are seen as a track pointing to a calorimeter cluster. Muons or electrons created inside jets might be mistaken for prompt leptons. Hadronically decaying τ-leptons are first reconstructed as jets and then identified as τ_{had} candidates applying the τ-identification algorithm so they can be considered τ_{had} or jets depending on the quality requirements that are applied. To remove the overlap between different objects, a hierarchy of objects has to be defined so that if two objects are found close to each other in the η-ϕ plane, the lower-priority object is discarded. The priorities and the criteria defined for the overlap removal are analysis-specific as they depend on which objects are most important for the analysis and the quality requirements applied on the different objetcs in the analysis.

In the analysis presented in this thesis the following overlap removal criteria are applied:

- remove jet if an electron and a jet have $\Delta R < 0.2$;

- remove electron if an electron and a jet have $0.2 < \Delta R < 0.4$;
- remove jet if a jet and a muon have $\Delta R < 0.4$ and the jet has less than three associated tracks with $p_{\mathrm{T}} > 500$ MeV;
- remove muon if a jet and a muon have $\Delta R < 0.4$ and the jet has three or more associated tracks with $p_{\mathrm{T}} > 500$ MeV;
- remove electron if an electron and a muon have $\Delta R < 0.2$ and they share an inner detector track;
- remove τ_{had} if an electron and a τ have $\Delta R < 0.2$;
- remove τ_{had} if a muon and a τ have $\Delta R < 0.2$;
- if a τ_{had} and a jet have $\Delta R < 0.2$ information about the b-tagging weight of the jet and the τ-identification working point of the τ_{had} candidate are taken into account, giving priority to the better reconstructed object in the following order: *medium* τ_{had}, b-tagged jet, anti-τ_{had}, light jet.

6.3 Event selection

An event selection is applied in order to select events compatible with containing a $bb\tau^{+}_{had}\tau^{-}_{had}$ final state. First, events are required to pass the selections applied online by the ATLAS trigger system during the data taking. Dedicated trigger algorithms to identify events containing one or two hadronically decaying τ-lepton candidates are used. Particularly, events are first tested to see if they pass a single-τ trigger (STT), and events which fail this are tested to see if they pass a di-τ trigger (DTT). In addition to the quality criteria applied to select events containing τ-like objects, triggers have also p_{T} thresholds: the STT has a p_{T} threshold of $80 - 160$ GeV (depending on the data taking period) on the τ_{had} candidate, while the DTT requires a p_{T} threshold of 35(25) GeV on the leading (sub-leading) τ_{had} candidate. During the 2016 data taking period the DTT also required the presence of an additional jet with a 25 GeV p_{T} threshold. Then, offline selection criteria are applied after the trigger selection depending on the fired trigger:

- all events must contain exactly two τ_{had};
- all events must contain at least two jets with $p_T > 20$ GeV;
- STT events:
  - the leading $\tau_{had-vis}$ must have $p_T > 100, 140, 180$ GeV for data periods where the trigger p_T threshold was $80, 125, 160$ GeV respectively (to be on the trigger efficiency plateau) and the sub-leading $\tau_{had-vis}$ is required to have $p_T > 20$ GeV;
  - the leading jet must have $p_T > 45$ GeV;
  - one of the two τ_{had} has to be matched to the object that fired the trigger;
- DTT events:
  - the leading (sub-leading) $\tau_{had-vis}$ must have $p_T > 40(30)$ GeV (to be on the trigger efficiency plateau);
  - the leading jet must have $p_T > 80$ GeV (due to the trigger requirement of the presence of a jet in the event and to be on the trigger efficiency plateau);

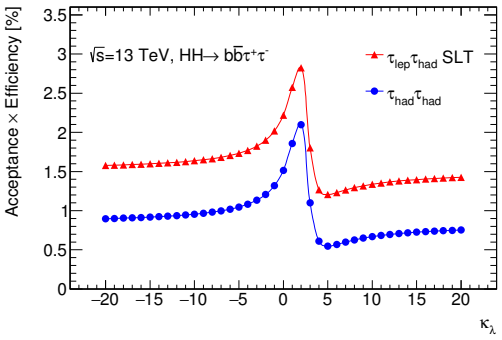

Figure 6.4: Acceptance times efficiency of the $bb\tau^{+}_{had}\tau^{-}_{had}$ event selection (blue line) for the non-resonant di-Higgs signals as a function of k_λ with $k_t = 1$. Values fot the $bb\tau_{lep}\tau_{had}$ event selection are also shown (red line).

  - both τ_{had} have to be matched to the objects that fired the trigger;
- the $m^{MMC}_{\tau\tau}$ must be above 60 GeV;
- the two τ_{had} must have opposite sign electric charge (OS);
- exactly two jets must be b-tagged;
- events containing electrons or muons are vetoed (to avoid overlap with the $bb\tau_{lep}\tau_{had}$ channel signal region and allow the combination).

Events fulfilling these requirements fall in the signal region (SR). Events failing some of these requirements are used to define control regions (CR) and validation regions (VR) used for the background estimation and validation as described in Section 6.4. Particularly, events containing at least one anti-τ_{had} instead of a τ_{had}, or containing two τ_{had} having same sign electric charge, or containing exactly two muons, or one light-lepton and one (anti-)τ_{had}, or having only 1 b-tagged jet are used in CRs and VRs.

The acceptance times efficiency of this $bb\tau^{+}_{had}\tau^{-}_{had}$ event selection is 1.9% for the SM di-Higgs signal. Values for the non-resonant di-Higgs signals as a function of k_λ, with $k_t = 1$, are shown in Figure 6.4. The acceptance shows a large change in the region $0 < k_\lambda < 5$ due to the strong interference of the two LO diagrams in this region. The acceptance has a maximum for $k_\lambda = 2$, as for this value the signal has the hardest m_{HH} spectrum, and a minimum for $k_\lambda = 5$, as for this value the signal m_{HH} spectrum is the softest, as it can be seen in Figure 6.3. Acceptance times efficiency values for the resonant di-Higgs signals are shown as a function of the resonance mass in Figure 6.5 for the heavy narrow width scalar and the RS graviton with $c = 1, 2$. The differences in the acceptance for the three resonant models are due to the effect of the different width of the resonances, which is most pronounced in the low mass region, as it can be seen in Figure 6.1.

6.4 Background estimation

The background composition of the signal region is shown in Figure 6.6. The major backgrounds are: the top-quark background, multi-jet events with jets faking hadronically decaying τ-leptons and $Z \to \tau^{+}\tau^{-}+$ heavy flavour jets.

MC simulated events are used to model the major background processes containing true-τ_{had} (reconstructed τ_{had} that are matched to generated τ_{had} within $\Delta R = 0.2$) and other minor background

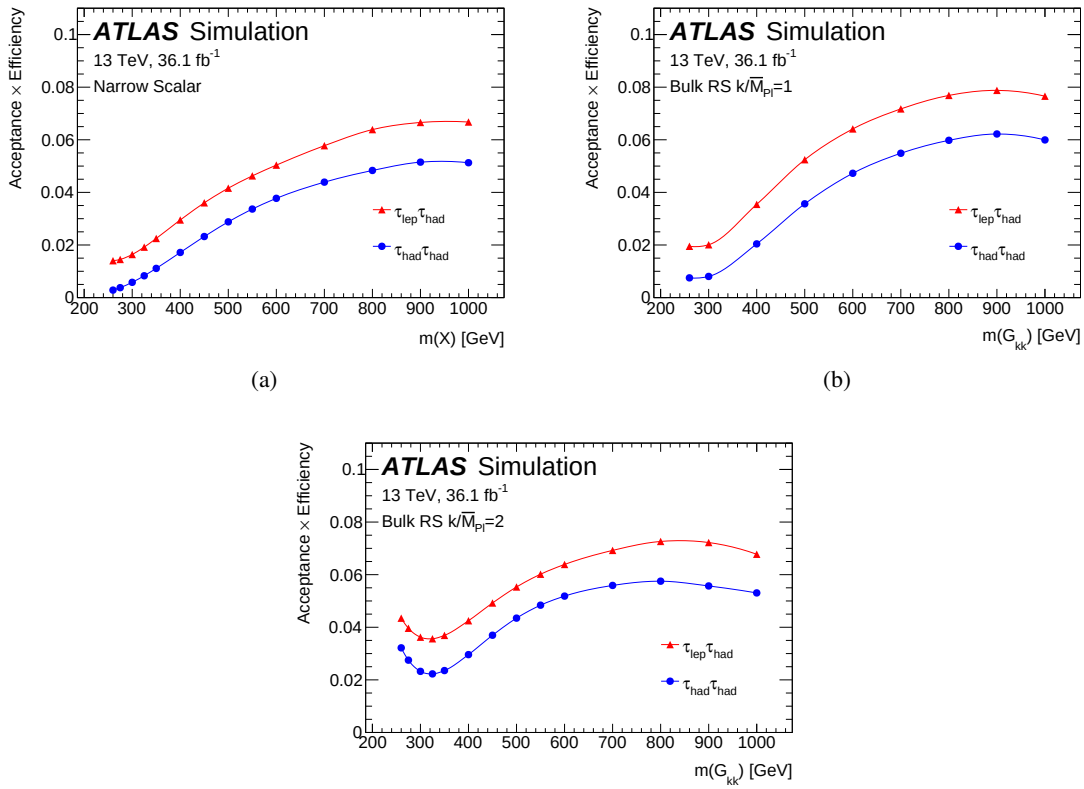

(a) (b)

(c)

Figure 6.5: Acceptance times efficiency of the $bb\tau^{+}_{had}\tau^{-}_{had}$ event selection (blue lines) for the resonant di-Higgs signals as a function of the resonance mass for a) the heavy narrow width scalar, b) the RS graviton with $c = 1$ and c) the RS graviton with $c = 2$. Values fot the $bb\tau_{lep}\tau_{had}$ event selection are also shown (red lines).

contributions. The contribution from backgrounds in which quark- or gluon-initiated jets are misidentified as hadronically decaying τ-leptons, subsequently referred to as fake-τ_{had}, are estimated using data-driven methods for the major backgrounds as they are not well described by the MC predictions. Particularly, two separate methods are used to estimate the multi-jet background contribution and the contribution of the fake-τ_{had} background from $t\bar{t}$ events. In both methods, a fake-τ_{had} enriched sample is obtained by requiring the presence of at least one anti-τ_{had} instead of a τ_{had}, with anti-τ_{had} and τ_{had} defined as in Section 6.2.

The contribution of the Z+ heavy flavour jets background is taken from the simulation but it is then normalised to the data in a dedicated control region.

The fake-τ_{had} and Z+heavy flavour jets background estimation techniques are described in details in the following sections. Figure 6.7 shows the background modelling validation: the data/prediction comparison in the distributions of the leading and sub-leading $\tau_{had-vis}$ p_{T} shows good agreement in the signal region. Moreover in the 1 b-tag and 2 b-tags SS validation regions, which are regions enriched with backgrounds containing jets faking τ_{had}, the data/prediction comparison shows a good understanding and modelling of the fake-τ_{had} backgrounds estimated with the data-driven methods.

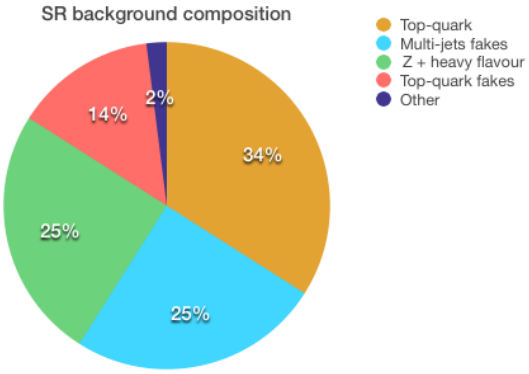

Figure 6.6: Background composition of the signal region.

6.4.1 Multi-jet background

The multi-jet background with jets faking hadronically decaying τ-leptons is estimated using a fully data-driven fake-factor (FF) method, as QCD processes with many jets and the object reconstruction effects causing misidentification of jets as hadronically decaying τ_{had} are not well described by MC simulations.

Four regions are defined depending on the τ-leptons identification requirement and sign of the electric charge and are used in the fake-factor method to estimate the multi-jet background:

- "ID OS": this is the SR, defined to contain events with two τ_{had} with opposite sign of the electric charge, as described in Section 6.3;
- "ID SS": the two τ_{had} are required to have same sign electric charge instead of opposite sign;
- "anti-ID OS": instead of two τ_{had}, at least one anti-τ_{had} must be present and the two objects must have opposite sign electric charge (there can be one τ_{had} and one anti-τ_{had} or two anti-τ_{had}, in case there are more anti-τ_{had} a random selection is applied to choose two of them);
- "anti-ID SS": same as the previous region but the two objects are required to have same sign electric charge.

In each of the three control regions defined above the contributions from other background processes, corresponding to about 5% of the number of data events in the region, are subtracted from the data using MC predictions. The fake-factors (FF) are then calculated from data in the "SS" regions as the ratio of the number of events in the "ID SS" region and the number of events in the "anti-ID SS" region:

$$FF = \frac{N_{SS}^{ID}}{N_{SS}^{anti-ID}} \,. \tag{6.10}$$

These FFs are then applied as event weights to the data events in the "anti-ID OS" region to obtain the estimation of QCD multi-jet events in the "ID OS" signal region:

$$N_{OS}^{ID} = N_{OS}^{anti-ID} \times FF \,, \tag{6.11}$$

assuming that the ratio of events in the "ID" and "anti-ID" regions is the same for the "SS" and "OS" regions.

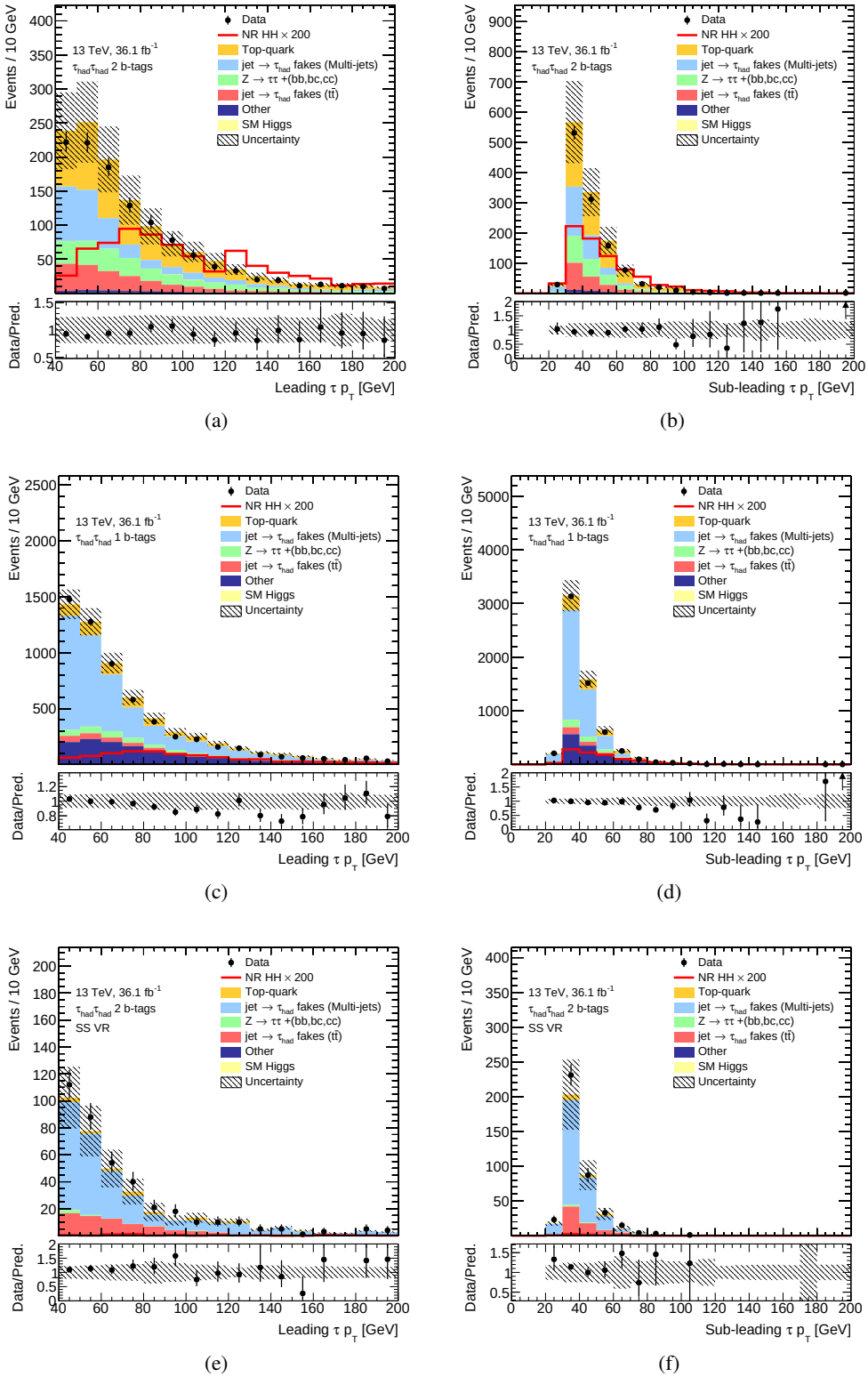

Figure 6.7: Data/prediction comparison in the distributions of the leading and sub-leading $\tau_{had-vis}$ p_{T} in the a),b) signal region, c),d) 1 b-tag and e), d) 2 b-tags SS validation regions. The uncertainty band includes both statistical and systematic uncertainties.

Region	FF
1p1p	0.0802 ± 0.0063
1p3p	0.0238 ± 0.0031
3p1p	0.0373 ± 0.0087
3p3p	0.0150 ± 0.0048

Table 6.3: Multi-jet fake-factors for STT events derived in the 1 b-tag region.

Region	TF
1p1p	0.936 ± 0.099
1p3p	1.09 ± 0.21
3p1p	1.12 ± 0.22
3p3p	1.17 ± 0.44

Table 6.4: Multi-jet FFs normalisation transfer factors from the 1 b-tag region to the 2 b-tags region.

The FFs are calculated separately for STT and DTT events, because the online trigger selection includes τ-identification requirements so the ratio of events falling in the "ID" and "anti-ID" regions depends on the trigger fired (as one trigger requires only one τ_{had} candidate and the other requires two of them). They are also derived separately for the four different possible combinations of the leading and sub-leading τ_{had} prongs, as the probability of the QCD jets to be misidentified as τ_{had} depends on the number of tracks: 1p1p, 1p3p, 3p1p and 3p3p. In addition, the FFs for DTT events, which are the majority of the events, are calculated in bins of leading and sub-leading $\tau_{had-vis}$ p_{T}, as the jet misidentification rate depends on it.

The FFs are derived in the 1 b-tag region, which has larger data statistics compared to the 2 b-tags region. It was checked that their dependence on the trigger selection, on the τ_{had} prongs combination and on the $\tau_{had-vis}$ p_{T} is the same in the 2 b-tags and 1 b-tag regions and only an overall offset in their values was observed between the two regions, due to the different jet flavour compositions of the two regions. This offset was found to be dependent on the τ_{had} prongs combination. To correct for this, transfer factors (TF), defined as the ratio of the FFs derived in the 2 b-tags region and in the 1 b-tag region, calculated inclusively in trigger decision and p_{T} (so only binned in τ_{had} prong combination), are applied to the FFs derived in the 1 b-tag region to correct their normalisation for the 2 b-tags region.

The FFs for the STT events are reported in Table 6.3 and the ones for DTT events are shown in Figure 6.8. The TFs are reported in Table 6.4.

6.4.2 $t\bar{t}$ with fake-τ_{had} background

For $t\bar{t}$ events where both reconstructed τ_{had} are real hadronically decaying τ-leptons, corresponding to 70% of the total $t\bar{t}$ background in the SR, the prediction is taken directly from the MC simulation. The background coming from $t\bar{t}$ events containing jets misidentified as τ_{had} estimated from MC simulations is corrected using τ_{had} fake-rates (FR), representing the probability for a jet from a hadronic W boson decay to mimic a τ_{had} candidate, derived from data. This is done because the effects causing misidentification of jets as hadronically decaying τ_{had} are not well described by MC simulations and the $t\bar{t}$ τ_{had} fake-rates are found to be different between data and MC simulations.

The FRs are derived from data in a dedicated $t\bar{t}$ control region, defined by applying the following selections:

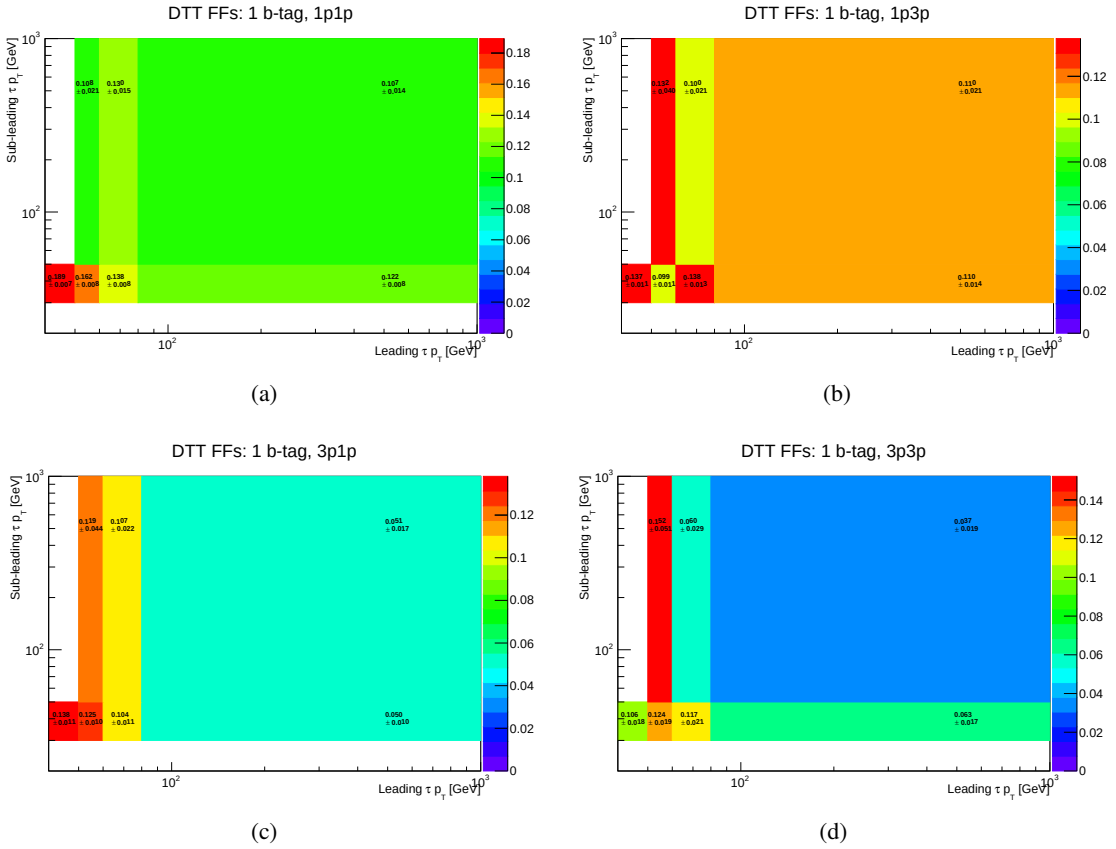

Figure 6.8: Multi-jet fake-factors for DTT events derived in the 1 b-tag region for the four possible combinations of leading and sub-leading τ_{had} prongs: a) 1p1p, b) 1p3p, c) 3p1p and d) 3p3p.

- events selected online using single lepton (electron or muon) triggers;
- exactly one electron or one muon with p_{T} 1 GeV above the trigger p_{T} threshold of 24 – 26 GeV (depending on the data taking period);
- exactly one τ_{had} candidate with τ-identification BDT score > 0.35 (includes anti-τ_{had} and τ_{had} candidates);
- at least two jets with $p_T > 20$ GeV;
- exactly 2 b-tagged jets;
- $m_T^W > 80$ GeV, with M_T^W being the transverse mass of the lepton and the E_T^{miss} calculated as $M_T^W = \sqrt{2p_T^{lep}E_T^{\mathrm{miss}}(1-\cos\Delta\Phi_{lep,E_T^{\mathrm{miss}}})}$.

This selection creates a data sample rich in $t\bar{t}$ events that is used to derive the fake-rates. The contribution from $t\bar{t}$ events with a true-τ_{had}, and from any other backgrounds (corresponding to 30% of the number of data events in this region), is subtracted from data using MC predictions leaving thus only the contribution from $t\bar{t}$ events with a fake-τ_{had} candidate. The fake-rates are then defined as the ratio of the number of events in which the τ_{had} candidate passes the τ-identification requirements, N^{ID}, and the total number of events in the control region, N^{total}:

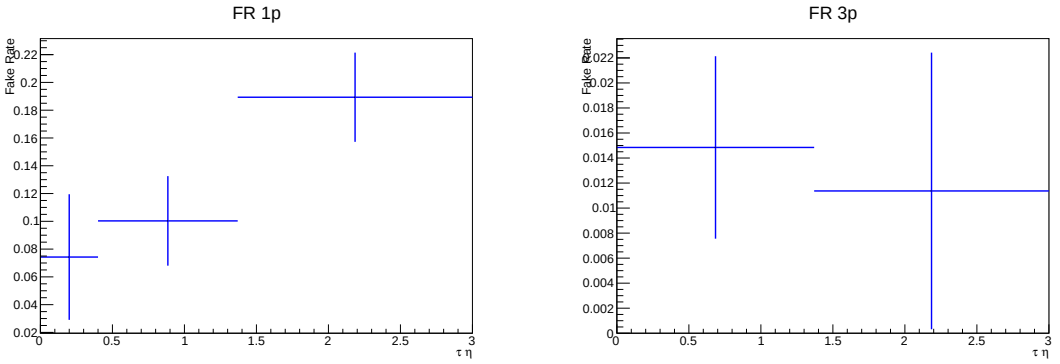

(a) (b)

Figure 6.9: τ_{had} $t\bar{t}$ fake-rates derived in the $t\bar{t}$ control region for a) 1-prong and b) 3-prong τ_{had}.

$$FR = \frac{N^{ID}}{N^{total}} . \tag{6.12}$$

The fake-rates are calculated separately for 1-prong and 3-prong τ_{had} and as a function of the $\tau_{had-vis}$ η, as shown in Figure 6.9. No dependence on the $\tau_{had-vis}$ p_{T} was observed in the p_{T} range covered by the jets in the selected $t\bar{t}$ events.

The FRs derived from data are then applied to fake-τ_{had} $t\bar{t}$ events from the MC simulations (containing one or two reconstructed τ_{had} which are not matched to generated τ_{had}) that pass the $bb\tau^{+}_{had}\tau^{-}_{had}$ channel offline event selection described in Section 6.3, but have not been required to pass the τ-trigger selections or any τ-identification requirement (beyond the minimal requirement of the τ-identification BDT score > 0.35). These requirements are not applied because they would bias the overall prediction as the FRs are calculated from events selected without applying the τ-trigger and τ-identification and have thus to be applied in the same way. However, the DTT $\tau_{had-vis}$ and jet p_{T} thresholds are applied to the fake-τ_{had} $t\bar{t}$ events to reproduce the correct p_{T} spectra expected in the SR. In the case where both the reconstructed τ_{had} are fake, the FRs are applied to both objects since they are a correction that needs to be applied per τ_{had}.

The method was tested by performing a closure test on MC using FRs calculated from the MC simulation itself, rather than from data, which provided a prediction compatible to the one obtained directly from the MC simulation without any correction applied.

6.4.3 Z+ heavy flavour jets background

The cross section of Z boson production in association with heavy flavour (b, c) jets is known to be not well predicted by the MC [130] so the contribution of these processes is normalised to data in a dedicated control region which is included in the final fit described in Section 6.7. Since the production of jets should be independent of the decay mode of the Z boson, $Z \to \mu^{+}\mu^{+}$ + heavy flavour jets events are selected, providing a region enriched in Z+ heavy flavour jets events (with purity of 25%) that is orthogonal to the signal region selection. These events are selected by requiring that:

- the event passes the online single muon trigger selection;
- there are exactly two muons with $p_T > 27$ GeV;

- there are at least two jets with the leading (sub-leading) jet having $p_T > 45(20)$ GeV;
- exactly two jets must be b-tagged;
- the di-muon invariant mass has to be $81 < m_{\mu\mu} < 101$ GeV (to select the Z peak);
- the di-b-jet mass has to be $m_{bb} < 80$ GeV or $m_{bb} < 140$ GeV (to remove the contribution from VH production with $H \to bb$).

The normalisation of the Z+ heavy flavour jets background is then determined from data by including this control region as a single bin histogram in the final fit, as described in Section 6.7.

6.5 Multivariate analysis

Boosted Decision Trees (BDTs) [131] are used in the analysis to improve the separation between signal and background and the overall sensitivity of the analysis. The use of this multivariate technique, developed and implemented in this thesis work, improved significantly the sensitivity of the analysis compared to the results obtained with cut-based approaches. Particularly, multivariate discriminants can provide better separation between signal and background compared to cut-based analyses, where simple cuts are applied on a set of discriminating variables, as they can make use of the information regarding linear and non-linear correlations between the discriminating input variables. Moreover, the machine-learning classification algorithms not only can be used to classify the events in two separate categories as it would be the case in a cut-based approach to define the signal region, but also provide a classification output distribution that can be itself used as final discriminating variable, with an increased separation power, that can be used in the final fit. The choice made in this thesis work of using the BDT output distribution as the final discriminant variable in the fit for this analysis resulted in a significantly improved sensitivity compared to the one obtained with other analysis strategies that were tested during the analysis development.

6.5.1 Short introduction to Boosted Decision Trees

BDTs are used in high-energy physics as classification method to classify events in different categories, generally "signal" (S) and "background" (B). A decision tree is a binary-tree structured classifier, as schematically illustrated in Figure 6.10. It takes several variables x_i of a training sample, in which the event category (signal or background) is known, as inputs and repeated left/right (yes/no) decisions are taken on one single variable at a time until a stop criterion is fulfilled (e.g. the maximal allowed depth of the tree, MaxDepth, or the minimum percentage of training events required in a node, MinNodeSize, is reached). Each split uses the variable that at the node gives the best separation between signal and background when being cut on. The leaf nodes at the bottom end of the tree are labeled "S" for signal and "B" for background depending on the majority of events that end up in the respective nodes. The phase space is thus split this way into many regions that are classified as signal or background.

Decisions during the training are taken according to various separation criteria: the standard criteria is the Gini-Index, defined as $p \cdot (1 - p)$, with p being the purity of the sample after the cut defined as:

$$p = \frac{S}{S + B}\,. \tag{6.13}$$

Since the splitting criterion is always a cut on a single variable, the training procedure selects the variable and cut value that optimises the increase in the separation index between the parent node and

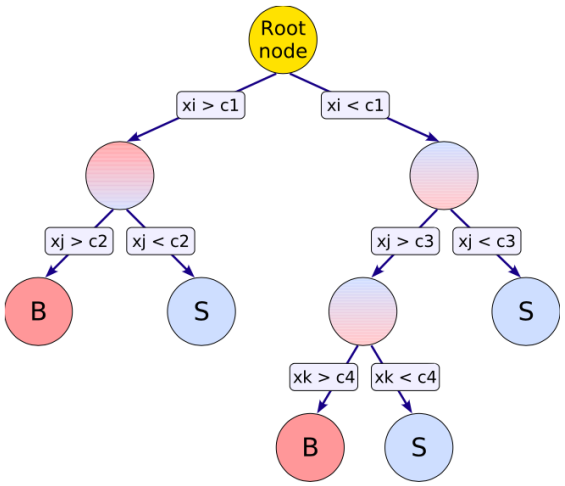

Figure 6.10: Schematic view of a decision tree [131].

the sum of the indices of the two daughter nodes, weighted by their relative fraction of events. The cut values are optimised by scanning over the variable range with a granularity that can be chosen (NCuts).

The "boosting" of a decision tree extends this procedure from one tree to several trees which form a forest. The trees are derived from the same training sample by reweighting events so that they have a different importance in each tree, and are then combined into a single classifier which is given by a weighted average of the individual decision trees. Boosting increases the stability of the response of the classifier with respect to statistical fluctuations and it is able to considerably improve the separation performance compared to a single decision tree. Several boosting algorithms can be used, the most common one is the "Adaptive" boosting, which is used in this analysis. In this boosting algorithm events that were misclassified during the training of a decision tree are given a higher event weight in the training of the following tree, by multiplying them by a common boost weight α. The boost weight is derived from the misclassification rate (err) of the previous tree:

$$\alpha = \frac{1 - err}{err} \,. \tag{6.14}$$

The weights of the entire event sample are then renormalised such that the sum of weights remains constant. Defining the result of an individual classifier as $h(x)$ (with x being the set of input variables), encoded for signal and background as $h(x) = +1$ and -1 respectively, the boosted event classification $y_{Boost}(x)$ is then given by:

$$y_{Boost}(x) = \frac{1}{N_{collection}} \sum_{i}^{N_{collection}} \ln(\alpha_i) \cdot h_i(x) \,, \tag{6.15}$$

where the sum is over all classifiers in the collection. Small (large) values for $y_{Boost}(x)$ indicate a background-like (signal-like) event. Once the training of the BDT is performed, the classification output of the BDT is thus a "score" which is assigned to events according to their values of the input variables indicating how "background-like" or "signal-like" the event is. This gives a separate distribution for background and signal events as shown in Figure 6.11. In this figure the distributions are shown for two separate signal and background samples, the training sample, which is the one used in the training phase of the BDT, and the testing sample which is an independent sample. By comparing the training and

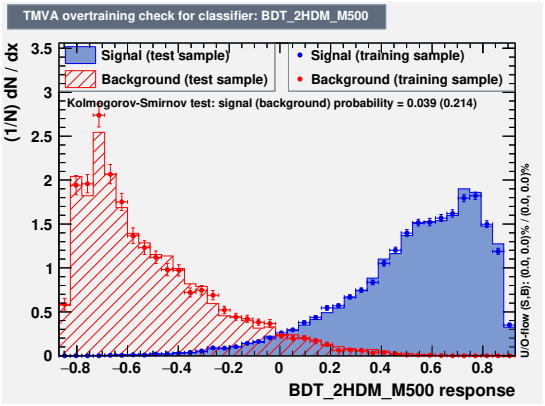

Figure 6.11: Example BDT score distribution for signal (blue) and background (red) events. This algorithm was trained to separate a 2HDM signal with $m_X = 500$ GeV from the background in the $b\bar{b}\tau^+_{had}\tau^-_{had}$ analysis.

testing BDT score distributions it is possible to check that the BDT is not "overtrained", meaning that features which are particular of the training sample but are not useful in general to separate signal and background are not exploited in the training. If the algorithm is overtrained the separation performance of the BDT results to be much less powerful on the testing sample compared to the training sample.

6.5.2 BDT training for the $HH \to b\bar{b}\tau^+_{had}\tau^-_{had}$ analysis

The BDT training for the $b\bar{b}\tau^+_{had}\tau^-_{had}$ analysis was fully developed in this thesis work. The training is performed to separate the signal from the total expected background. The training samples are the signal samples and the sum of the three major backgrounds, $t\bar{t}$, Z+jets and multi-jets, weighted by their predicted cross sections to reproduce the expected background composition. Particularly, for the $t\bar{t}$ and Z+jets backgrounds the MC prediction is used in the BDT training, while the multi-jet background included in the training is estimated with the data-driven fake-factor method as described in Section 6.4.1. The truth-tagging technique described in Section 5.4 is applied to both signal and MC background training samples in order to exploit the full statistics of these samples for the BDT training, which is performed after applying the signal region seletion described in Section 6.3. The training and application are k-folded (k=2) depending on the parity of the event number to ensure that they are statistically independent and avoid overtraining. Thus, for each BDT classifier two trainings are performed: one training is done on even event numbers and applied to odd event numbers while the second training is performed on odd event numbers and applied to even event numbers. The BDT is used in the same way on data in the analysis.

Separate dedicated BDTs are trained to target the several signal hypotheses considered in the analysis:

- one BDT targeting the SM di-Higgs signal, trained on it;
- one BDT targeting the non-resonant di-Higgs signal with enhanced triple Higgs self-coupling, trained on the non-resonant sample with $k_\lambda = 20$;
- one BDT targeting each mass point of the 2HDM signal, trained on the target mass sample combined with the two neighbouring mass samples;
- one BDT targeting each mass point of the RS graviton signal with $c = 1$, trained on the target mass sample combined with the two neighbouring mass samples;

- one BDT targeting each mass point of the RS graviton signal with $c = 2$, trained on the target mass sample combined with the two neighbouring mass samples.

The choice of the signal training samples used for the BSM non-resonant and resonant signals is the result of a study performed in this thesis and explained in details in Appendix A. In the non-resonant case, the training performed on the signal sample with $k_\lambda = 20$ is chosen as it shows good performance for all the BSM non-resonant signals considered in the analysis. In the resonant case, the best performance were obtained using trainings performed on the target mass signals, but the two neighbouring masses had to be included in each training in order to ensure the sensitivity of the BDT to signals with masses falling in between the ones of the available MC simulated signal samples.

The choice of the backgrounds included in the training and of their relative normalisations is the result of an optimisation procedure performed in this thesis to maximise the signal to total background separation. Several configurations were tested, including each background process in the training one by one, starting from the largest ones and including then the minors, and checking the performance of the BDT. The performance of the trainings can be compared by checking and comparing the ROC (Receiver Operating Characteristic) curves, showing the background rejection versus the signal efficiency. The training performed on the sum of the three major backgrounds ($t\bar{t}$, Z+jets and multi-jets) showed improved performance (with improvement of the order of 5% on the ROC curve integral) compared to the trainings performed on a single background, as all three have a comparable size in the signal region. The inclusion of other minor backgrounds did not show a visible increase in the performance (changes only of the order 0.1% on the ROC curve integral was observed).

All the BDTs are trained using the same set of input variables. The choice of the BDT input variables is the outcome of an optimisation procedure performed in this thesis. The optimisation started by performing the training with a set of about twenty variables which show a reasonable signal-to-background separation and a good modelling in MC. Then, several trainings were performed removing variables one by one or in groups. Especially variables which show a strong correlation with other variables and low separation between signal and background were removed. The reduction of the number of variables continued until a visible decrease in performance (>1% on the ROC curve integral) was observed for any of the signals, in order to obtain the minimum list of variables that can be used for all the signal hypotheses considered in the analysis. The final list of BDT inputs consists of six variables:

- m_{HH}: the invariant mass of the di-Higgs system reconstructed from the di-τ and di-b-jet four-vectors, with scaling factors of $m_H/m_{\tau\tau}^{MMC}$ and m_H/m_{bb} applied respectively (with $m_H = 125$ GeV), in order to improve the mass resolution;
- $m_{\tau\tau}^{MMC}$: the invariant mass of the di-τ system, calculated using the MMC;
- m_{bb}: the invariant mass of the di-b-jet system;
- $\Delta R(\tau, \tau)$: the ΔR between the two $\tau_{had-vis}$;
- $\Delta R(b, b)$: the ΔR between the two b-jets;
- E_T^{miss} Φ centrality: variable that quantifies the angular position in Φ of the E_T^{miss} with respect to the two $\tau_{had-vis}$. It is defined as:

$$E_T^{\text{miss}}\ \Phi\,\text{centrality} = \frac{A + B}{\sqrt{A^2 + B^2}}\,, \tag{6.16}$$

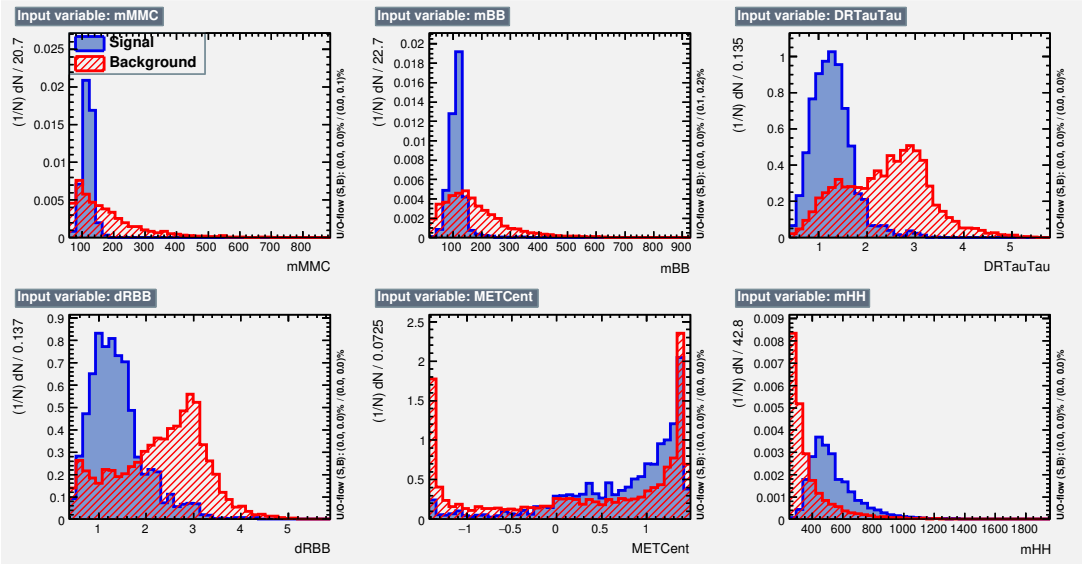

Figure 6.12: BDT input variables distributions for the SM di-Higgs signal (blue) and for the background (red).

where A and B are

$$A = \frac{\sin\Phi_{E_T^{\text{miss}}} - \Phi_{\tau_2}}{\sin\Phi_{\tau_1} - \Phi_{\tau_2}} \quad B = \frac{\sin\Phi_{E_T^{\text{miss}}} - \Phi_{\tau_2}}{\sin\Phi_{\tau_1} - \Phi_{\tau_2}}, \tag{6.17}$$

and it is:

- $= \sqrt{2}$ when the E_T^{miss} lies exactly between the two $\tau_{had-vis}$;
- $= 1$ if the E_T^{miss} is perfectly aligned with either of the $\tau_{had-vis}$;
- > 1 if the E_T^{miss} lies inside of the angular region defined by the two $\tau_{had-vis}$;
- < 1 if the E_T^{miss} lies outside of the angular region defined by the two $\tau_{had-vis}$.

The BDT input variables distributions for the SM di-Higgs signal and for the background are shown in Figure 6.12. Their linear correlation coefficients are shown in Figure 6.13 and their separation power is reported in Table 6.5, where the variables are ordered from the most discriminating one to the least discriminating one. The separation power of a discriminant variable y is defined as:

$$\langle S^2 \rangle = \int \frac{(\hat{y}_S(y) - \hat{y}_B(y))^2}{\hat{y}_S(y) + \hat{y}_B(y)} dy, \tag{6.18}$$

where $\hat{y}_S$ and $\hat{y}_B$ are the signal and background PDFs of y. The separation is zero for identical signal and background shapes, and it is one for shapes with no overlap.

The BDT training is performed using TMVA [131] version 4.2.1 of ROOT version 6.04/14. The Adaptive boosting algorithm is used and the list of training parameters which are different from the TMVA defaults are listed in Table 6.6. The parameters were optimised in order to obtain a training with best possible separation performance without overtraining issues. The Gradient boosting algorithm was also tested, but no improvement on the signal to background separation performance was found and the training was more sensible to overtraining. Moreover, a multilayer perceptron (MLP) neural network was

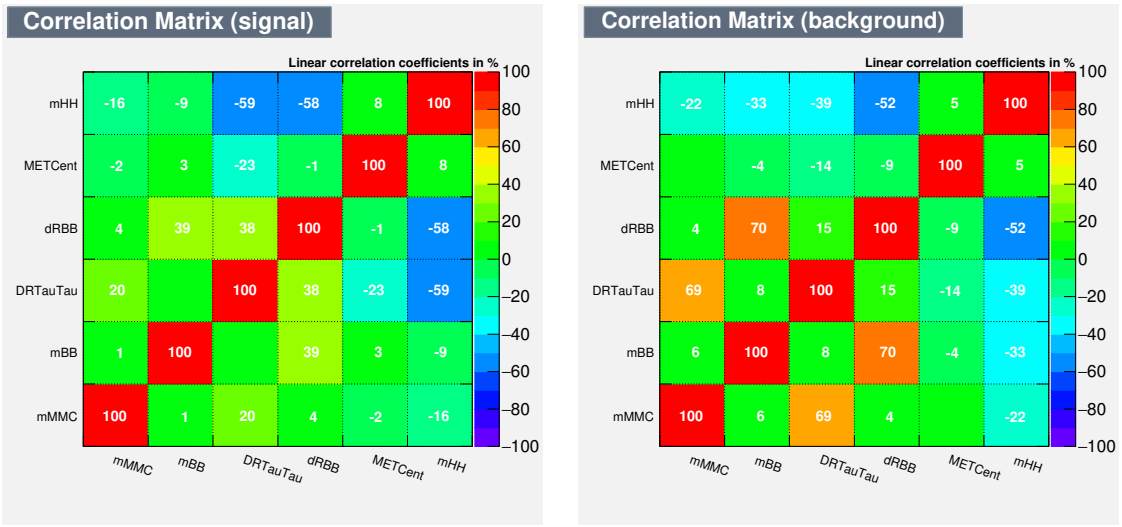

(a) (b)

Figure 6.13: BDT input variables linear correlation coefficients for a) SM di-Higgs signal b) the background.

Rank	Variable	Separation $\langle S^2 \rangle$
1	$\Delta R(\tau, \tau)$	0.46
2	$m_{\tau\tau}^{MMC}$	0.41
3	m_{HH}	0.41
4	m_{bb}	0.38
5	$\Delta R(b, b)$	0.34
6	E_T^{miss} Φ centrality	0.11

Table 6.5: BDT input variables separation power for the SM di-Higgs signal. Variables are ordered from the most discriminating one to the least discriminating one.

also tested and it was found to give performance compatible with the ones obtained with the more simple BDT algorithm.

The result of the BDT training for the SM di-Higgs signal is shown in Figure 6.14 and its performance, in terms of background rejection versus signal efficiency, are shown in Figure 6.15. The separation power of this BDT score discriminant is 0.76, which is much higher than the one of any of the single input variables. In Table 6.7 the signal efficiency at three given background efficiency points is given.

The BDT input variables importance, derived by counting how often the variables are used to split decision tree nodes, and by weighting each split occurrence by the squared separation gain that it has achieved and by the number of events in the node, is reported in Table 6.8. It has to be noted that the ranking of the variables according to their importance shown here does not coincide with the one according to their separation power as they are measurements of two different aspects. The ranking according to the separation power is done considering one single variable independently from the others, while the importance of the variable in the BDT training strongly depends on the full set of input variables and their correlations.

The BDT input variables distributions, their linear correlation matrices, BDT scores and ROC curves for other BDT trainings used in the analysis for the BSM di-Higgs signals are included in Appendix A.

BDT parameter	Value
BoostType	AdaBoost
NTrees	200
MaxDepth	4
MinNodeSize	5%
NCuts	100
AdaBoostBeta	0.15

Table 6.6: BDT training parameters.

Background efficiency	Signal efficiency
0.30	0.99
0.10	0.94
0.01	0.66

Table 6.7: Signal efficiency at three given background efficiency points for the SM di-Higgs BDT.

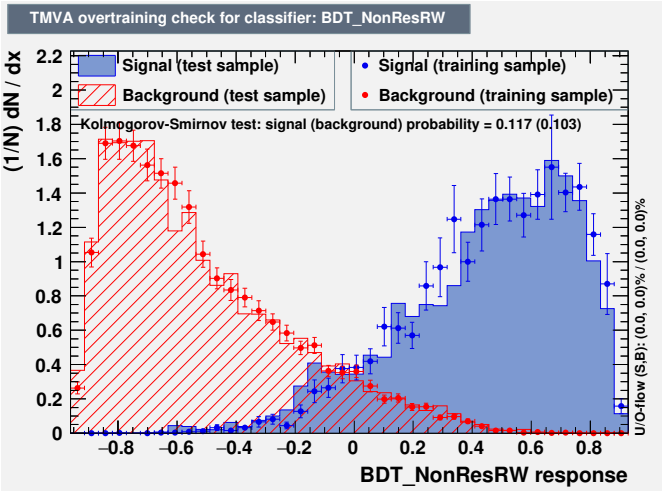

Figure 6.14: BDT score distribution for the SM di-Higgs signal (blue) and the background (red).

Rank	Variable	Importance
1	m_{HH}	0.22
2	$m_{\tau\tau}^{MMC}$	0.22
3	$\Delta R(\tau,\tau)$	0.19
4	$\Delta R(b,b)$	0.14
5	m_{bb}	0.13
6	E_T^{miss} Φ centrality	0.10

Table 6.8: BDT input variables importance for the SM di-Higgs signal. Variables are ordered from the most important one to the least important one.

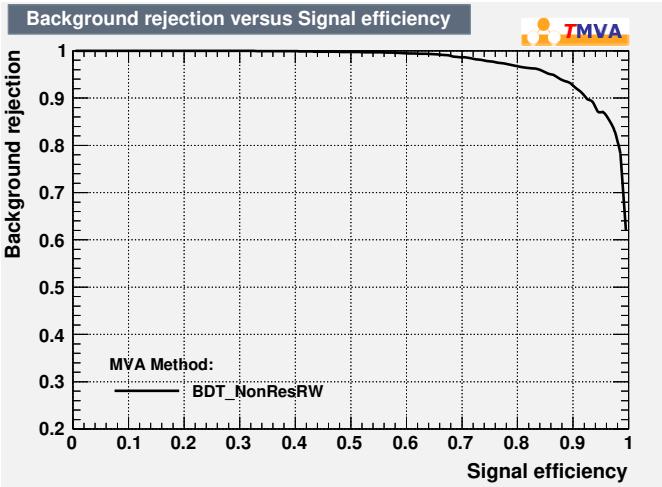

Figure 6.15: ROC curve for the SM di-Higgs BDT.

The BDT score distributions are used as final discriminant variables in the statistical analysis as described in Section 6.7.

6.6 Systematic uncertainties

Systematic uncertainties are all the uncertainties that are introduced by the analysis techniques. There are two main groups of sources of such uncertainties: the experimental uncertainties, which are related to the detector response and the object reconstruction and identification, and the modelling uncertainties, which are related to our knowledge of the MC simulated background and signal models and the data-driven backgrounds. All these uncertainties are propagated through the analysis and are included in the statistical analysis fit decribed in Section 6.7.

6.6.1 Experimental uncertainties

The experimental uncertainties depend on the data taking conditions, on the characteristics of the detector and on the object reconstruction and identification techniques. Those uncertainties are thus analysis-independent and are included in this analysis following the ATLAS Collaboration recommendations. They are described in the following and a list of all the experimental uncertainties included in the analysis is reported in Table 6.9.

Luminosity and pile-up

The uncertainty on the integrated luminosity recorded by the ATLAS experiment for the combined 2015+2016 dataset analysed in this thesis work is 2.1%. The luminosity value and its uncertainty are derived, following a methodology similar to that detailed in Reference [132], measuring the number of interactions in x-y beam-separation scans. This uncertainty is applied to the signal and to the background components whose normalisations are derived from MC simulation. An additional uncertainty related to the pile-up reweighting procedure (scaling applied to the simulated events in order to match the distribution of the average number of pile-up interactions in recorded data events), that is as large as the rescaling, is also applied [133].

Trigger

Trigger efficiency scale factors are calculated as a function of the triggering object p_{T} in order to correct the difference in trigger efficiency between simulation and data. Uncertainties on the trigger scale factors are propagated as systematic uncertainties related to the trigger selection.

τ_{had}

The τ_{had} reconstruction and identification efficiency is corrected in MC using scale factors derived as a function of the $\tau_{had-vis}$ p_T to account for differences between simulation and data. Uncertainties on the efficiency scale factors are included as systematic uncertainties [101]. The $\tau_{had-vis}$ energy scale is calibrated after reconstruction. The residual difference between simulation and data and the uncertainties on the energy scale corrections are included as systematic uncertainties [101]. Dedicated uncertainties on the τ-electron overlap removal are also included.

Jets

Jet energies need to be calibrated after reconstruction to account for features of the detector and of the jet reconstruction algorithm as well as the difference in jet response between data and MC simulation. Uncertainties on the jet energy scale corrections (JES) depend on p_{T} and η of the jet. There are several sources of uncertainties and they are grouped in three sets of uncorrelated uncertainties [94]. An uncertainty on the jet energy resolution (JER) is also included taking into account differences in energy resolution between simulations and data and experimental uncertainties connected to the measurement of the jet energy resolution [95].

b-tagging

Scale factors are applied in MC to account for flavour-tagging efficiency differences between simulation and data. They are measured separately for b, c, and light-flavour jets as a function of the jet p_{T} and η [96]. All these correction factors have different sources of uncertainties which are decomposed into uncorrelated components which result in three uncertainties for c-jets, four uncertainties for b-jets and five uncertainties for light-flavour jets.

E_T^{miss}

The systematic uncertainties related to the objects that are used to calculate the E_T^{miss} are propagated to its calculation. Additional systematic uncertainties connected to the E_T^{miss} scale and resolution, the efficiency of the track reconstruction that enters the soft term as well as the model that describes the underlying event are included to account for differences between simulations and data [99].

6.6.2 MC background and signal modelling uncertainties

The modelling uncertainties are uncertainties related to how well we know the MC simulated background and signal processes. They depend on the settings used in the theoretical cross section calculation and in the MC simulations: PDF sets, factorisation and renormalisation scales, α_s, matrix element generator and parton shower model and tuning parameters. The theoretical uncertainties on the cross section calculation only affect the normalisation and are analysis-independent, but the uncertainties on the acceptance, that affect both normalisation and shapes, depend on the selections applied in the analysis and thus need to

Systematic uncertainty	Type	Components
Luminosity	N	1
Pile-up	N	1
τ trigger efficiency	NS	6
τ reconstruction and identification efficiency	NS	4
τ-electron overlap removal	NS	2
τ energy scale	NS	2
Jet energy scale	NS	3
Jet energy resolution	NS	1
Jet flavour tagging	NS	14
E_T^{miss}	NS	3

Table 6.9: List of experimental systematic uncertainties. An "N" means that the uncertainty is taken as normalisation-only for all processes and channels affected, whereas "NS" means that the uncertainty is taken on both normalisation and shape. Some of the systematic uncertainties are split into several components for a more accurate treatment.

be estimated for each analysis. The estimation of the modelling uncertainties for the $HH \rightarrow bb\tau_{had}\tau_{had}$ analysis is thus part of this thesis work. These accpetance uncertainties are derived by comparing the predictions obtained with the nominal settings of the MC simulation used in the analysis with alternative samples generated with alternative settings. Their contribution is usually divided into a normalisation acceptance uncertainty, that affects the number of events predicted in the signal region, and a shape uncertainty affecting the shape of the final discriminant distribution.

The normalisation acceptance uncertainties are derived comparing the number of nominal expected events in the signal region with the one obtained for each alternative sample i:

$$\sigma^{i}_{Acc} = \frac{N_{nominal} - N^{i}_{variation}}{N_{nominal}} . \tag{6.19}$$

The contributions from the different variations are then added in quadrature to estimate the final normalisation acceptance uncertainty. When several regions are included in the final fit, a relative normalisation acceptance uncertainty can be estimated from the comparison of the relative amount of events predicted by the nominal model in one region “A” with respect to another region “B” and the same fraction in the alternative model:

$$\sigma^{A/B}_{Acc} = \frac{(N_A/N_B)_{nominal} - (N_A/N_B)_{variation}}{N_A/N_B} . \tag{6.20}$$

Acceptance effects on the shapes are treated separately as they do not change the amount of expected events (this is a technical choice done to disentangle the two effects and have the possibility to identify the effects that have a larger impact on the result). The shape uncertainties are derived comparing the distributions of several kinematical variables of the nominal sample with the ones of the alternative samples. The comparison is done by taking the normalised distributions (to exclude the normalisation effects that are considered separately) and calculating the ratio of the nominal and alternative number of events bin per bin. The shape uncertainty is approximated by fitting an analytical function to this binned ratio. This is done for each alternative sample and the symmetric up/down envelope of the variations is taken as the uncertainty. The variable that shows the largest variation is used to parameterise the final uncertainty which is then applied by reweighting the nominal events in dependence of this variable according to the obtained function describing the variation. The modelling uncertainties included in the

analysis are described in the following and a list of all these uncertainties is reported in Table 6.10.

Minor backgrounds: Z+ light flavour jets, di-boson, single-top, W+jets and single Higgs

The theoretical cross section uncertainties for Z+ light jets, diboson and single-top production are 5%, 6% and 5% respectively. They are obtained combining PDF, α_s and scale variation uncertainties in quadrature, following the procedure described in Reference [134].

On the very small W+jets background (<1% of the total background in the signal region) a conservative 50% uncertainty is assigned to cover cross section and acceptance uncertainties. This is estimated by inflating the 30% uncertainty obtained in the VH resonances analysis [135] from PDF, factorisation and renormalisation scale and α_s variations and generator comparison, to cover in addition the fake-τ_{had} contribution. The uncertainty on this background in the $bb\tau_{had}\tau_{had}$ analysis is expected to be the one obtained in the $ZH \to llbb$ category of the VH resonances analysis, as the phase space selected by the two analyses is very similar, with the addition of the uncertainty on the fake-τ_{had} component. The uncertainty on the fake-τ_{had} component was estimated by comparing the MC and the data-driven prediction for W+jets with τ_{had} fakes in the 0 b-tags region of the $bb\tau_{lep}\tau_{had}$ channel and it was found to be 31%. Adding in quadrature this 31% and the 30% from the VH resonances analysis the total uncertainty is estimated to be 43%. A total uncertainty of 50% is thus applied on the W+jets background to be on the conservative side, considering that this background accounts for less than 1% of the total background in the signal region and has no impact on the result.

Uncertainties on the single Higgs background are taken from the latest ATLAS experimental uncertainties: a normalisation uncertainty of 28% is applied to the ZH background component [130] and a 30% normalisation ucertainty is applied to the top-quark pair associated Higgs production background (ttH) [136].

Major background: $t\bar{t}$

The $t\bar{t}$ background is divided in this analysis in a "true" component, where both the reconstructed τ_{had} are real τ-leptons and a "fake" component containing events where at least one of the two τ_{had} is fake. The true component is taken from the MC prediction, while the fake component is corrected with data-driven fake-rates as described in Section 6.4.2. The theoretical and generator-level modelling uncertainties are thus applied only to the true component.

The theoretical cross section uncertainty is 6% [110]. Uncertainties arising due to the hard scattering generation are estimated by comparing a sample generated with MadGraph5_aMC@NLO and showered using Herwig ++ to a sample generated with the nominal Powheg and also showered with Herwig ++ . The nominal Powheg+Pythia 6 factorisation and renormalisation scales are varied by a factor of two up and down, and the fragmentation model is also compared to the Powheg+Herwig simulation. The total normalisation uncertainty is derived by summing in quadrature the different contributions, resulting in 34% for the up variation and 37% for the down variation in the signal region and 11% for the up and down variations in the Z+ heavy flavour control region. The shape uncertainties in the signal region are parameterised as a function of the two variables that show the largest variation: the invariant mass m_{bb} and the transverse momentum p_T^{bb} of the di-b-jet system. These uncertainties are then propagated through the analysis as a shape uncertainty on the BDT score.

Major background: Z+ heavy flavour jets

The Z + heavy flavour background normalisation is derived from data by including a dedicated control region defined as in Section 6.4.3 in the statistical fit. Thus, the theoretical cross section uncertainty does

not need to be applied on this background. However, acceptance uncertainties need to be applied in the signal region to account differences in the normalisation between the control region and the signal region and shape uncertainties.

For this background the uncertainties due to the choice of the PDF set are estimated using different sets of event weights included in the Sherpa samples. The PDF variations include 100 replicas of the nominal NNPDF30 PDF set as well as central values for two different PDF sets, MMHT2014nnlo68cl and CT14nnlo. The NNPDF intra-PDF uncertainty is estimated as the standard deviation of the set of the 101 NNPDF30 sets. The envelope of the differences between the central values of the nominal NNPDF set and the other two PDF sets is taken as an additional uncertainty. Uncertainties related to the choice of renormalisation and factorisation scales are also evaluated using event weights included in the Sherpa samples, varying the scales either together or independently up and down by a factor of two. The envelope of these variations is taken as the overall uncertainty related to the choice of the scale. The nominal samples are also compared to the samples simulated using MadGraph5_aMC@NLO at LO interfaced to the Pythia 8 parton shower model, where the NNPDF23LO PDF set is used together with the A14 tune and the EvtGen program is used for properties of the bottom and charm hadron decays.

As the Z+ HF normalisation is derived from data in the corresponding Z+ HF control region, the variations described above are used to derive a relative normalisation uncertainty between the control region and the signal region by comparing the ratios of expected events in the two regions obtained with the nominal and alternative samples. The relative normalisation uncertainty to be applied in the signal region is found to be 34% for the up/down variations. The shape discrepancy from the nominal sample in the signal region is parameterised as a function of m_{bb} and p_T^{bb}, as these variables show the largest variations, and is propagated through the analysis as a shape uncertainty on the BDT score.

Signal

The theoretical cross section with uncertainties for SM Higgs pair-production is $33.41^{+4.3}_{-6.0}$ (scale) ±5 (theory) ±2.3 (α_s) ±2.1 (PDF) fb [1–4]. The theoretical uncertainties are added in quadrature, summing up to 8% which is applied as a normalisation uncertainty on the signal prediction. Uncertainties on the acceptance are also considered. Samples are generated with modified parameters to probe uncertainties on the PDFs, uncertainties on renormalisation and factorisation scales and uncertainties due to the modelling of the parton shower and the underlying event. The PDF uncertainties and the renormalisation and factorisation scale uncertainties are found to be neglegible (< 1%). The uncertainty on the parton shower modelling is calculated to be 9% on the normalisation, comparing the predictions obtained using Pythia 8 to the the nominal Herwig ++ . No significant shape effect is observed on any of the kinematical variables or on the BDT score distribution.

For the resonant signals the PDF uncertainties are also found to be negligible. The renormalisation and factorisation scale uncertainties, estimated considering only two variations, both renormalisation and factorisation scales varied by a factor of 2 (up) or 0.5 (down), have a 2% effect on the normalisation. The parton shower uncertainties, estimated comparing the predictions obtained using Herwig ++ to the the nominal Pythia 8 have a 10% effect on the normalisation. Adding quadratically the two contributions an overall 12% normalisation uncertainty is applied to all resonant signals. No significant shape effect is observed on any of the kinematical variables or on the BDT score distribution.

6.6.3 Data-driven fake-τ_{had} background uncertainties

As descibed in Section 6.4, the multi-jet background and the background containing fake-τ_{had} from $t\bar{t}$ are estimated using data-driven methods. These methods introduce systematic uncertainties due to the

Systematic uncertainty	Type	Size of normalisation	Components
Z+ light flavour jets			
Cross section	N	5%	1
Diboson			
Cross section	N	6%	1
single-top			
Cross section	N	5%	3
W+jets			
Cross section plus acceptance	N	50%	1
ZH			
Experimental uncertainty	N	28%	1
ttH			
Experimental uncertainty	N	30%	1
$t\bar{t}$			
Cross section	N	6%	1
Acceptance in SR	NS	34% up, 37% down	3
Acceptance in Z+ HF CR	N	11%	1
Z+ heavy flavour jets			
Acceptance	N	freely floating	1
Acceptance in SR relative to Z+ HF CR	NS	34%	3
SM HH signal			
Cross section	N	8%	1
Acceptance	N	9%	1
Resonant signals			
Acceptance	N	12%	1

Table 6.10: List of modelling systematic uncertainties. An "N" means that the uncertainty is taken as normalisation-only for all processes and channels affected, whereas "NS" means that the uncertainty is taken on both normalisation and shape. Some of the systematic uncertainties are split into several components for a more accurate treatment.

statistics of the data samples used to derive the fake-factors or the fake-rates, the subtraction of the other backgrounds entering the control regions, and the extrapolation of the estimation from the control regions to the signal region. The uncertainties on the data-driven fake-τ_{had} backgrounds included in the analysis are described in the following and a list of all these uncertainties is reported in Table 6.11.

Multi-jet

As described in Section 6.4.1, the multi-jet background is estimated using a data-driven fake-factor method. Several sources of uncertainties related to this method are considered.

The fake-factors derived from data for the multi-jet background estimation are varied up and down by their statistical uncertainty. A systematic uncertainty due to variations in the subtracted contributions of Z/W+jets, top, diboson and Higgs boson background processes in the control regions (corresponding in total to 5% of the data events in each of the regions) is estimated by varying these up and down by a conservative 50% before re-calculating the fake-factors. Both these uncertainties are propagated by re-deriving the multi-jet background estimation with the varied fake-factors and then propagating this through the full analysis to the BDT score distribution. They are included as both normalisation and

shape effects.

The transfer factors (defined as the ratio of the inclusive fake-factors in the 2 b-tags region and in the 1 b-tag region) are also varied within their statistical uncertainties to evaluate a normalisation uncertainty for the extrapolation from the 1 b-tag to the 2 b-tags region.

In order to account for differences in the fake-τ_{had} composition between the opposite-sign (OS) region, where the fake-factors are applied, and the same-sign (SS) region, where they are derived, the fake-factors are re-calculated in two QCD-enriched regions (requiring $\Delta\Phi(\tau,\tau) > 2$) one with SS and one with OS and are compared as a function of the leading $\tau_{had-vis}$ p_{T}. The difference between the FFs derived in the QCD-enriched OS and SS regions is applied as a p_{T}-dependent variation to the nominal fake-factors derived in the SS region for the QCD background estimation.

Additional possible effects are taken into account in a "non-closure" systematic uncertainty derived in the 1 b-tag OS validation region from the comparison of the QCD background prediction and the data subtracting the other background contributions predicted by the MC. This difference is parameterised as a function of the sub-leading-$\tau_{had-vis}$ p_{T}, as this variables is the one showing the strongest non-closure shape, and applied as a variation on the QCD background prediction.

$t\bar{t}$ with fake-τ_{had}

As described in Section 6.4.2, the $t\bar{t}$ background with jets faking τ_{had} from the MC is corrected using fake-rates derived from data. Several sources of uncertainties related to this method are considered.

The fake-rates are varied up and down by their statistical uncertainty. This variation is applied by propagating the new fake-rates and obtaining a variation of the fake-τ_{had} $t\bar{t}$ prediction.

In order to evaluate the uncertainty due to the subtraction of the contribution of the MC true-τ_{had} $t\bar{t}$ in the control region used to derive the fake-rates, the experimental and modelling uncertainties are applied to this component and the fake-rates are re-derived for the variations up and down of this subtracted background for both sources of uncertainties. Particularly, the effect of the experimental uncertainties on the true-τ_{had} $t\bar{t}$ component on the fake-rates is applied by propagating the new fake-rates and obtaining normalisation and shape variations of the fake-τ_{had} $t\bar{t}$ prediction. The effect of the large modelling uncertainties on the subtracted true-τ_{had} $t\bar{t}$ results on a 100% variation of the fake-τ_{had} $t\bar{t}$ prediction and it is included as a normalisation uncertainty.

The m_T^W cut applied in the definition of the control region where the fake-rates are derived is varied from its nominal value of 80 GeV to 65 GeV, making the control region closer to the signal region. The fake-rates are re-derived and propagated through the analysis to obtain an uncertainty related to the extrapolation from the control region to the signal region, included as normalisation and shape uncertainty.

Additionally, a $\tau_{had-vis}$ p_{T} dependent systematic uncertainty is applied to account for the non fully correct $\tau_{had-vis}$ p_{T} distribution obtained with the fake-rate method due to applying only DTT p_{T} threshold cuts to the fake-τ_{had} $t\bar{t}$ events and not also the STT p_{T} cuts.

6.7 Statistical analysis

This analysis, as often happens in particle physics, is a search for a process that is predicted by the theory but has not yet been seen. The analysis of the data in a search for a new phenomenon is a statistical hypothesis test. To discover a new signal process one defines the null hypothesis, H_0, describing the known processes which constitute the background, and tests the level of agreement of the observed data with this null hypothesis. If the observed data are not compatible with the null hypothesis a discovery

Systematic uncertainty	Type	Size of normalisation	Components
Multi-jet			
Statistics	NS	9%	1
MC subtraction	NS	3%	1
Transfer factors	N	15%	1
SS-OS	NS	10%	1
Non-closure	NS	3%	1
$t\bar{t}$ with fake-τ_{had}			
Statistics	NS	34%	1
MC subtraction	NS	100%	2
M_T^W cut	NS	16%	1
Trigger p_{T} thresholds	NS	4%	1

Table 6.11: List of systematic uncertainties on the data-driven background estimations for fake-τ_{had}. An "N" means that the uncertainty is taken as normalisation-only for all processes and channels affected, whereas "NS" means that the uncertainty is taken on both normalisation and shape. Some of the systematic uncertainties are split into several components for a more accurate treatment.

can be claimed. To set exclusion limits on a new signal, the incompatibility of the alternative background plus signal hypothesis, H_1, with the data is instead tested. If the observed data are not compatible with the background plus signal hypothesis the presence of the new signal can be excluded. The outcome of the search can be quantified by computing a p-value, which gives the probability, under the assumption of H, of finding data of equal or greater incompatibility with the predictions of H. The given hypothesis is considered incompatible with the observed data if the p-value is below a certain threshold. The p-value is usually converted into an equivalent significance, Z, defined such that a Gaussian distributed variable with Z standard deviations above its mean has an upper-tail probability equal to p:

$$Z = \Phi^{-1}(1 - p)\,, \tag{6.21}$$

where Φ^{-1} is the quantile (inverse of the cumulative distribution) of the standard Gaussian. The thresholds used to claim a discovery or an exclusion limit are arbitrary: the particle physics community has chosen a threshold of $Z = 5$, corresponding to $p = 2.87\times10^{-7}$ to reject the backround-only hypothesis and claim a discovery, while for purposes of excluding an alternative signal hypothesis, a threshold $p = 0.05$ (i.e. 95% confidence level) is used, which corresponds to $Z = 1.64$. Exclusion limits are set in absence of a discovery of a new signal, so when the observed data are found to be compatible with the null hypothesis given the chosen thresholds. They are usually upper limits on the cross section of the new signal, giving a statement meaning that such a process, if it exists, is produced with a cross section below this quantity, with a certain given probability (95% confidence level).

It is useful during the development of the analysis to quantify the sensitivity of the analysis by reporting the expected significance or the expected exclusion limit before looking at the observed data. This can be done computing the median significance or the median exclusion limit using "Asimov"[2] datasets built under a given assumption, H_1 to emulate the presence of the signal or H_0 to emulate the background-only, instead of the real observed data.

[2] An "Asimov" dataset is a dataset in which all observed quantities are set equal to their expected values.

6.7.1 Profile likelihood ratio

In particle physics a frequentist approach is adopted with a profile likelihood ratio used as a test statistic [137] to calculate p-values. In addition to the parameter of interest such as the cross section of the signal process, the signal and background models also contain nuisance parameters, given by the systematic uncertainties, whose values are not taken as known a priori but rather must be fitted (profiled) from the data. The hypothesis test is done using a binned distribution of a discriminating variable x for which the likelihood function can be written as the product of the Poisson probabilities for all bins:

$$L(n|\mu,\theta) = \prod_{i=1}^{N} \frac{(\mu s_i + b_i)^{n_i}}{n_i!} e^{-(\mu s_i + b_i)}, \tag{6.22}$$

where n is the number of data events, μ is the signal strength defined as $\mu = \sigma/\sigma_{theory}$ ($\mu = 1$ corresponds to the theory expectation and $\mu = 0$ corresponds to no signal), s is the number of expected signal events, b the number of expected background events and θ represents a set of nuisance parameters on which the prediction of signal and background depend. The nuisance parameters can be either known or estimated by the MC or can be evaluated from the data.

The profile likelihood ratio is then defined as:

$$\lambda(\mu) = \frac{L(\mu, \hat{\hat{\theta}})}{L(\hat{\mu}, \hat{\theta})}. \tag{6.23}$$

The numerator of this ratio is the profile likelihood function: the quantity $\hat{\hat{\theta}}$ is the value of θ that maximises the likelihood L for the specified value of μ (it is the conditional maximum-likelihood estimator of θ) and thus is a function of μ. The denominator is the maximised (unconditional) likelihood function: $\hat{\mu}$ and $\hat{\theta}$ are the values obtained by maximising the likelihood, so they are the maximum-likelihood (ML) estimators of μ and θ. From the definition of $\lambda(\mu)$, it follows that $0 \leq \lambda \leq 1$, with λ close to 1 implying good agreement between the data and the tested value of μ. The test statistics which is used is defined starting from the profile likelihood ratio as:

$$q_\mu = -2 \ln \frac{L(\mu, \hat{\hat{\theta}})}{L(\hat{\mu}, \hat{\theta})}, \tag{6.24}$$

where higher values of q_μ correspond to increasing incompatibility between the data and the tested μ. The hypothesis test is therefore performed by measuring the level of incompatibility between the observed data and the hypothesised μ value directly using the test statistics q_μ as a measurement of the discrepancy and computing the p-value:

$$p_\mu = \int_{q_{\mu,obs}}^{\infty} f(q_\mu|\mu) dq_\mu, \tag{6.25}$$

where $q_{\mu,obs}$ is the value of the test statistics obtained with the observed data and $f(q_\mu|\mu)$ is the probability density function of q_μ under the assumption of the signal strength μ.

Discovery

In order to make a discovery of a new signal it is needed to falsify the null hypothesis H_0, which is the background-only hypothesis, by showing that the observed data are incompatible with it. This can be done by using the test statistics q_0:

$$q_0 = -2 \ln \frac{L(0, \hat{\hat{\theta}})}{L(\hat{\mu}, \hat{\theta})}, \tag{6.26}$$

which is Equation 6.24 for $\mu = 0$, and calculating its observed p-value

$$p_0 = \int_{q_{0,obs}}^{\infty} f(q_0|0) dq_0 . \tag{6.27}$$

If p_0 is below the 2.87×10^{-7} threshold, corresponding to a 5σ significance, it means that the observed data are incompatible with the background-only hypothesis and thus it is possible to claim a discovery. The sensitivity of the experiment to the discovery of a given signal can be evaluated by calculating the expected median significance using an Asimov dataset built with background plus signal with $\mu = 1$ instead of the real observed data.

Exclusion limit

The test statistics shown in Equation 6.24 can also be used for the exclusion of a given theory by calculating it for $\mu = 1$:

$$q_1 = -2 \ln \frac{L(1, \hat{\hat{\theta}})}{L(\hat{\mu}, \hat{\theta})} . \tag{6.28}$$

The lower is the value of q_1 the more the data are compatible with the theory and the less compatible with the pure background expectations. The probability density function of q_1 given $\mu = 1$ or $\mu = 0$ can be evaluated starting from MC samples. Calling respectively $f(q_1|1)$ and $f(q_1|0)$ the two pdf's, the separation between the two determines the capability of the analysis to discriminate the searched model with respect to the background. First it is useful to evaluate the expected exclusion limit on the new signal, which is an important parameter in the design of the analysis itself. Defining $\tilde{q}_1$ as the median of the $f(q_1|0)$ function, which is a sort of average outcome for a background-only experiment, one can calculate the so called CL^{exp}_{s+b} as:

$$CL^{exp}_{s+b} = \int_{\tilde{q}_1}^{\infty} f(q_1|1) dq_1 , \tag{6.29}$$

which is the median confidence level (CL) with which the experiment can exclude the signal with $\mu = 1$ in case of background-only. The smaller is the expected CL obtained in this way, the higher is the capability of the experiment to exclude the signal. Calculating the q_1^{obs} with the observed data the observed exclusion confidence level is:

$$CL^{obs}_{s+b} = \int_{q_1^{obs}}^{\infty} f(q_1|1) dq_1 . \tag{6.30}$$

An illustration of how CL^{exp}_{s+b} and CL^{obs}_{s+b} are obtained is shown in Figure 6.16.

The method that is widely used for setting exclusion limits for new physics signals is the so called "modified frequentist approach", CL_s [138], which is a more conservative approach compared to the CL_{s+b}, adopted to avoid excluding signals because of underfluctuations of the background. The CL_b can be defined as:

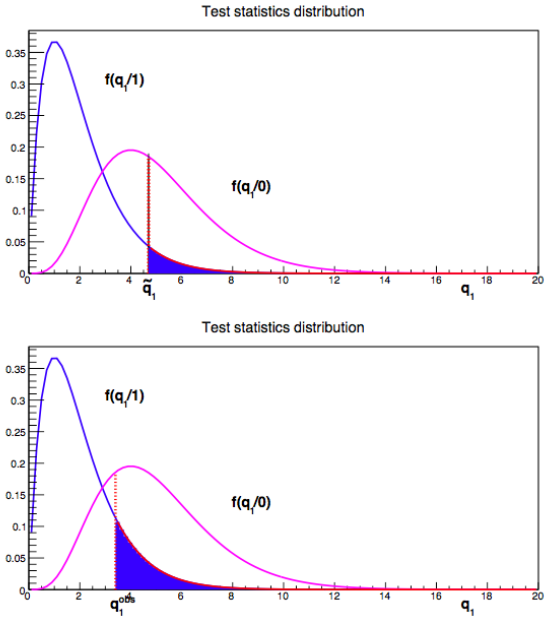

Figure 6.16: Construction of the CL_{s+b}^{exp} (upper plot) and CL_{s+b}^{obs} (lower plot). In both cases the CL_{s+b} is given by the blue area.

$$CL_b^{obs} = \int_{q_1^{obs}}^{\infty} f(q_1|0)dq_1 \,. \tag{6.31}$$

If the background underfluctuates, the CL_{s+b} can be small but also the CL_b would be small, meaning that q_1^{obs} is not compatible with the signal plus background hypothesis but it is not compatible with the background-only hypothesis either. In this case using the CL_{s+b} one would exclude the signal just because of a background underfluctuation. In order to avoid this unmotivated exclusion, the *CLs* method is used, which uses as confidence level the CL_s quantity:

$$CL_s = \frac{CL_{s+b}}{CL_b} \,. \tag{6.32}$$

The CL_s is always larger than CL_{s+b} so this is a conservative choice because with this prescription it is more difficult to exclude possible signals. If the CL_s is lower than 5% the observed data can exclude the signal with $\mu = 1$ at 95% CL. In searches for new physics exclusion limits are usually set on the signal strength μ (or on the cross section) rather than just checking whether a signal with a given cross section and $\mu = 1$ is excluded or not. The test statistics q_μ is a function of μ, and for each value of μ the analysis illustrated above for the case $\mu = 1$ can be repeated to determine the value of $\mu = \mu^*$ for which the *CLs* is equal to 5%. By increasing μ, the $CL_s(\mu)$ decreases, so the value μ^* is the upper limit on μ, meaning that a signal with $\mu \geq \mu^*$ can be excluded at the 95% CL.

6.7.2 Fit model for the $HH \to b\bar{b}\tau_{had}^+\tau_{had}^+$ analysis

As described in Section 6.5, dedicated BDTs are trained for each signal hypothesis tested in the analysis. For each signal model considered, a binned profile likelihood ratio fit is performed on the BDT score distribution.

The BDT score distributions are first built with a very fine binning and are then rebinned from the right-hand side (high-BDT-score region) until the relative uncertainty on the background is less than 50% multiplied by the fraction of the signal present in the bin, plus an offset of 1%. In the case where there is no signal the background uncertainty is 1%, while a bin containing 100% of the signal would have a 50% uncertainty on the background. The chosen value of the relative background uncertainty of 50% is the result of an optimisation performed in this thesis work to obtain a balance between having the most shape information on the signal-to-background separation given by the BDT score distribution and keeping the uncertainty on the background low enough in order not to degrade the result because of a too large uncertainty (and also have at least 5 expected background events in the last bin to guarantee the stability of the fit). This was done by performing a scan on the value of the relative background uncertainty and performing the statistical analysis for each tested value and checking the sensitivity of the analysis and the stability of the fit.

In addition to the BDT score distribution in the signal region, the one-bin Z+ heavy flavour control region defined as in Section 6.4.3 is also included in the fit to determine the normalisation of this background from the data by performing a simultaneous fit of the two regions.

All sources of systematic uncertainties described in Section 6.6 are considered as nuisance parameters (NP) in the profile likelihood. The effect of each NP is split in normalisation and shape components. A "smoothing" procedure is applied on the shape variations to prevent artefacts due to statistical fluctuations in these variations influencing the result. In order to do this, the normalised shape variations of each background are calculated bin by bin and are then parameterised using a monotonic step function. After smoothing the new distribution representing the smoothed shape variation is built from the nominal distribution using the smoothed relative shape variation. Moreover, to reduce the complexity of the fit, nuisance parameters that have a negligible effect are removed. This is done separately for the effects on the normalisations and on the shapes of each of the backgrounds that are affected by the NP. The effect of a NP on the normalisation is considered negligible if its variation is below 0.5% and the effect on the shape is considered negligible if the normalised variation in any given bin does not exceed 0.5%.

6.7.3 Profile likelihood fit: test of the background-only hypothesis

In order to assess the compatibility of the observed data with the SM background-only hypothesis a background-only profile likelihood fit is performed. The fit results have to be investigated in order to validate the goodness of the fit. It is necessary to check the post-fit data/prediction agreement by looking at the overall predicted yields in the signal region and checking that the post-fit BDT input variables and the BDT scores distributions are well modelled in the signal region and also in the validation regions.

The post-fit number of expected background events and observed data events in the signal region are reported in Table 6.12, together with the expected number of signal events. Also, the post-fit number of events in the last two bins of the SM BDT distribution, which are the most sensitive bins as they contain most of the expected signal and have highest expected significance, are reported in Table 6.13. The total observed number of events are found to be compatible with the post-fit number of background events, from a background-only fit, in the signal region and in the high-BDT score region.

The post-fit distributions of the BDT input variables in the signal region are shown in Figure 6.17. They show good agreement between the observed data and the background prediction for all the variables. For checking the modelling of the major backgrounds in the BDT score distribution, three validation regions are checked: the 2 b-tags SS region which is a QCD enriched region, and a top-quark and a Z+ HF background enriched regions. The post-fit BDT distributions of the SM BDT in these three validation regions are shown in Figure 6.18. They show good modelling of the multi-jet τ_{had} fakes, top-quark and Z+ HF backgrounds. The post-fit BDT distribution of the SM BDT in the signal region is

Component	Events
$t\bar{t}$	360 ± 100
Single top	39.7 ± 5.9
Multi-jet τ fakes	294 ± 57
$t\bar{t}$ τ-fakes	160 ± 120
Z + HF	291 ± 91
SM single Higgs	9.2 ± 2.1
Other	22.9 ± 5.9
Total background	1178 ± 40
Data	1180
SM HH	0.75 ± 0.14
X(300 GeV)	17.9 ± 3.6
X(500 GeV)	2.84 ± 0.54
X(1000 GeV)	0.0222 ± 0.0044
G_{kk}(300 GeV, c = 1)	13.1 ± 2.6
G_{kk}(500 GeV, c = 1)	36.3 ± 7.0
G_{kk}(1000 GeV, c = 1)	2.11 ± 0.43
G_{kk}(300 GeV, c = 2)	240 ± 46
G_{kk}(500 GeV, c = 2)	187 ± 36
G_{kk}(1000 GeV, c = 2)	7.9 ± 1.6

Table 6.12: Post-fit expected number of background events, determined from a background-only fit, compared to the observed number of data events in the signal region. The expected number of signal events is also reported. The total background is not identical to the sum of the individual components since the latter are rounded for presentation, while the sum is calculated with the full precision before being subsequently rounded. Systematic uncertainties are included. Due to the large correlations, individual uncertainties can be significantly larger than the total uncertainty.

shown in Figure 6.19. This BDT score distribution used as final discriminant is well described by the background-only prediction also in the signal region. The post-fit background normalisations in the Z+ heavy flavour control region included in the fit are also shown in Figure 6.20.

Moreover, other checks are performed to validate the quality of the statisitical model and of the background modelling. The NP "pulls", defined as the difference between the $\hat{\theta}$ estimation from the likelihood maximisation and the initial value of the NP, normalised to the value of the uncertainty, are checked both performing the fit to an Asimov dataset built with $\mu = 0$ and the fit to the observed data with floating μ. The NP pulls from the fit of the SM BDT distribution are shown in Figure 6.21 (the descritpion of the NPs is given in Tables B.1, B.2, B.3 in Appendix B). It can be seen that the model describes the data well as none of the nuisance parameters shows unexpected deviations or under/overconstraints. The post-fit Z+ HF normalisation factor, which is a freely floating NP in the fit (named norm_Zbb), determined from data in the dedicated control region included in the fit, is 1.39 ± 0.18. This result is compatible with what was expected given that the cross section of this process is known to be not well predicted by the MC simulation and it is compatible with what was found by other analyses [130]. The NPs which are constrained from the fit correspond to: the modelling normalisation uncertainty on the $t\bar{t}$ background (named TtbarAcc2Tag), the uncertainty on the data-driven fake-τ_{had} $t\bar{t}$ background coming from the subtraction of the true-τ_{had} $t\bar{t}$ in the control region where the fake-rates are derived (named FR_ttbarNorm) and the modelling uncertainty on the Z+ HF background relative normalisation

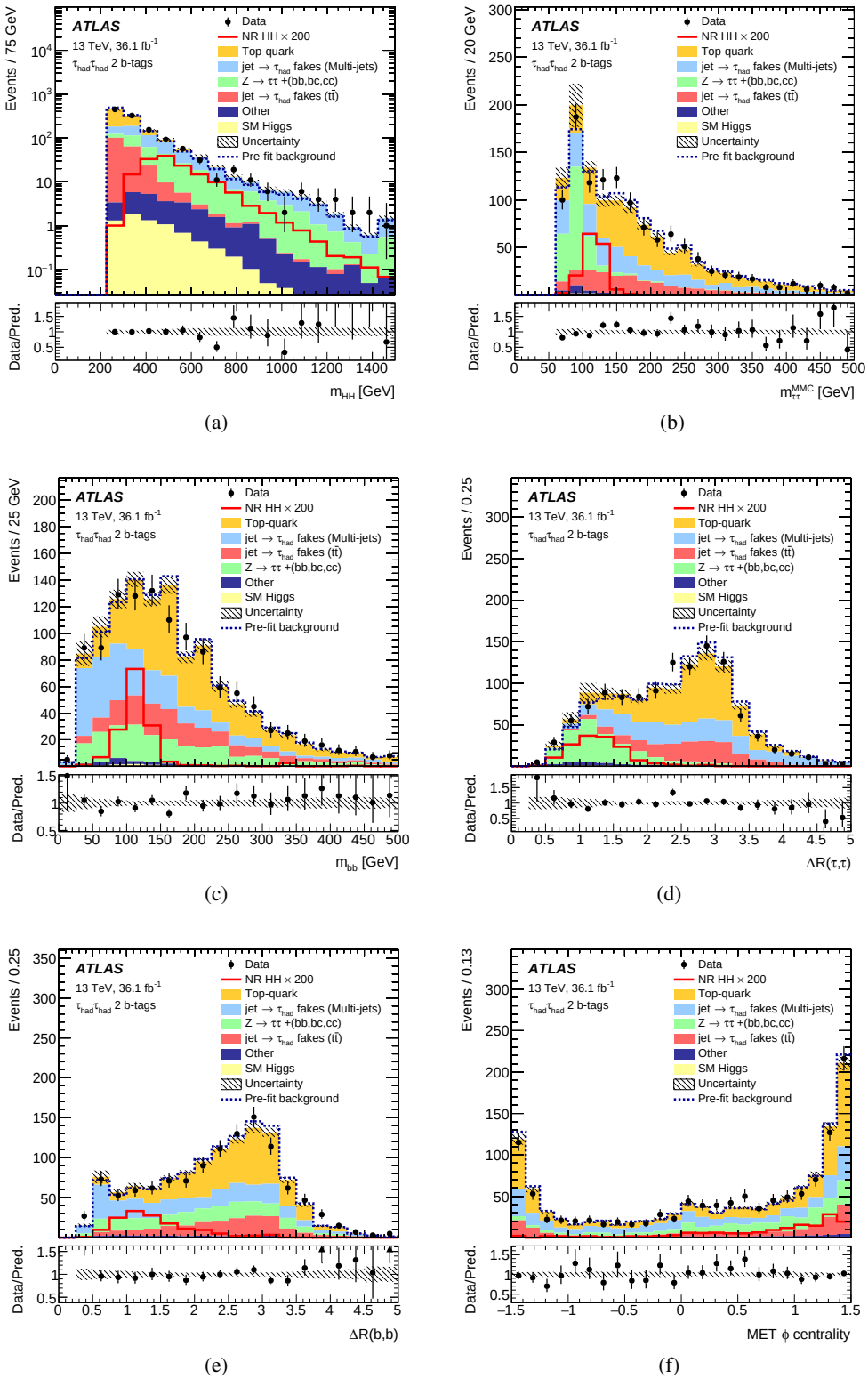

Figure 6.17: Post-fit distributions of the BDT input variables in the signal region. All background components are scaled to their normalisations as determined in the fit. The pre-fit normalisation of the sum of all background components predicted by the simulated events is given by the dashed blue line. The SM di-Higgs signal distribution is also shown with a normalisation of 200 times the SM prediction. The shaded bands represent the total post-fit uncertainty with NPs profiled to the data.

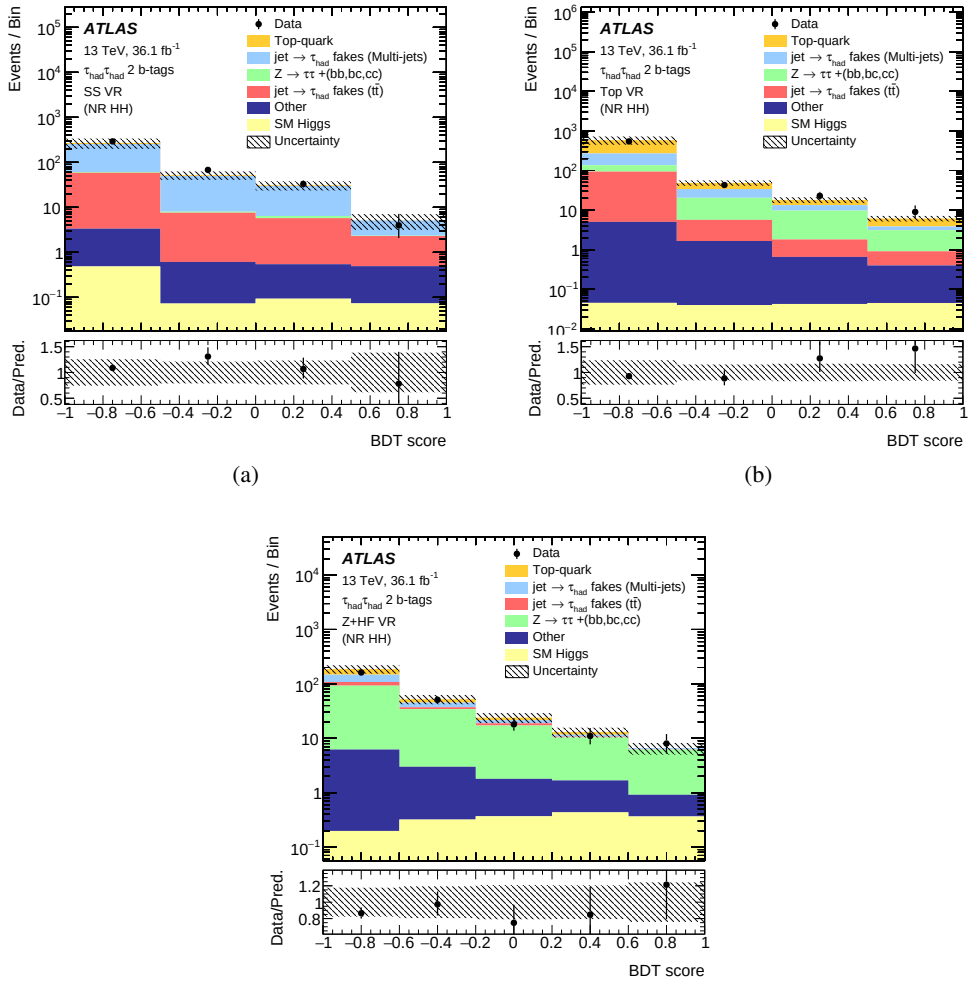

Figure 6.18: Post-fit distribution of the SM BDT in the a) SS , b) top-quark and c) Z+HF validation regions. All background components are scaled to their normalisations as determined in the fit. The shaded bands represent the total post-fit uncertainty with NPs profiled to the data.

Component	Events
$t\bar{t}$	4.5 ± 1.4
Single top	1.06 ± 0.57
Multi-jet τ fakes	3.89 ± 0.87
$t\bar{t}$ τ-fakes	1.9 ± 1.4
Z + HF	12.6 ± 3.6
SM single Higgs	1.54 ± 0.41
Other	1.09 ± 0.32
Total background	26.7 ± 3.5
Data	20
SM HH	0.55 ± 0.10

Table 6.13: Post-fit expected number of background events, determined from a background-only fit, compared to the observed number of data events in the last two bins of the SM BDT distribution in the signal region. The expected number of signal events is also reported. The total background is not identical to the sum of the individual components since the latter are rounded for presentation, while the sum is calculated with the full precision before being subsequently rounded. Uncertainties include systematics. Due to the large correlations, individual uncertainties can be significantly larger than the total uncertainty.

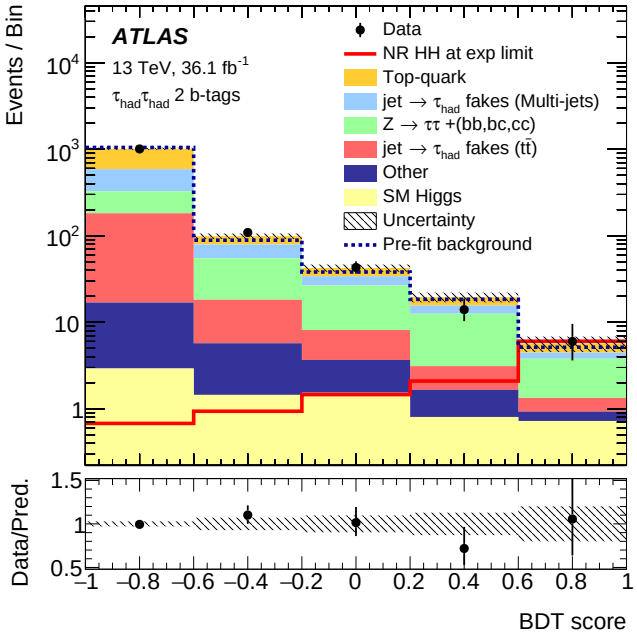

Figure 6.19: Post-fit distribution of the SM BDT in the signal region. All background components are scaled to their normalisations as determined in the fit. The pre-fit normalisation of the sum of all background components predicted by the simulated events is given by the dashed blue line. The SM di-Higgs signal distribution is also shown with a normalisation scaled to the expected exclusion limit. The shaded bands represent the total post-fit uncertainty with NPs profiled to the data.

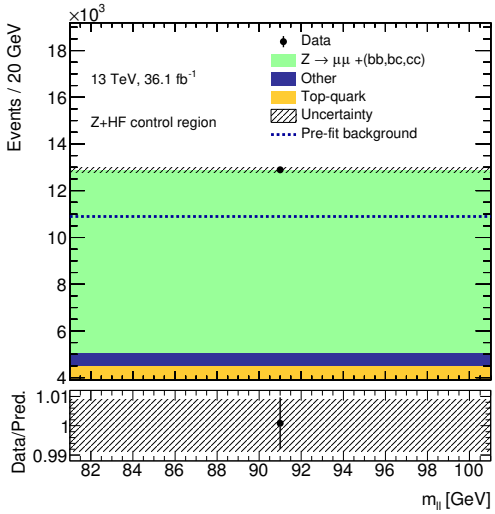

Figure 6.20: Post-fit background normalisations in the Z+ heavy flavour control region. All background components are scaled to their normalisations as determined in the fit. The pre-fit normalisation of the sum of all background components predicted by the simulated events is given by the dashed blue line. The shaded bands represent the total post-fit uncertainty with NPs profiled to the data.

between the control region and the signal region (named RatioHHSRZhfAcc2Tag). These uncertainties are expected to be constrained from the fit as they are analysis-dependent and were estimated in this analysis in a very conservative way.

The fractional impact of the NPs on the best fit value of the signal strength μ from a background plus signal fit is also checked and it is shown for the SM BDT fit in Figure 6.21, where the systematic uncertainties are listed in decreasing order of their impact on μ and only the first 15 NPs are shown. It can be seen that the most important systematic uncertainties are the modelling uncertainties on the major backgrounds present in the high-BDT score region, the uncertainties related to the τ_{had} trigger, reconstruction and identification efficiencies and the uncertainties related to the data-driven fake-τ_{had} backgrounds. The total impact of systematic uncertainties corresponds to 30% of the total uncertainty on the best fit μ, meaning that the result of this analysis is limited by the current available data statistics and not by systematic uncertainties.

Similar results are obtained also from the fit of the other BDT distributions used for testing non-resonant and resonant BSM signal hypotheses. The BDT distributions used as final discriminants, the NP pulls and rankings are reported in Appendix B.

As no significant excess over the expected background from SM processes is observed in any of the tested distributions, no evidence for the presence of a signal is found. The data are thus used to set upper limits on the non-resonant and resonant di-Higgs production cross section, presented in the next section.

6.8 Results

As the observed data are found to be compatible with the background-only hypothesis, they are used to set exclusion upper limits on the non-resonant and resonant di-Higgs production cross section. The upper limits are computed at 95% CL performing a profile likelihood ratio test with the test statistics q_1 following the *CLs* prescription [138].

As for the test of the background-only hypothesis, the BDT score distributions for each signal model

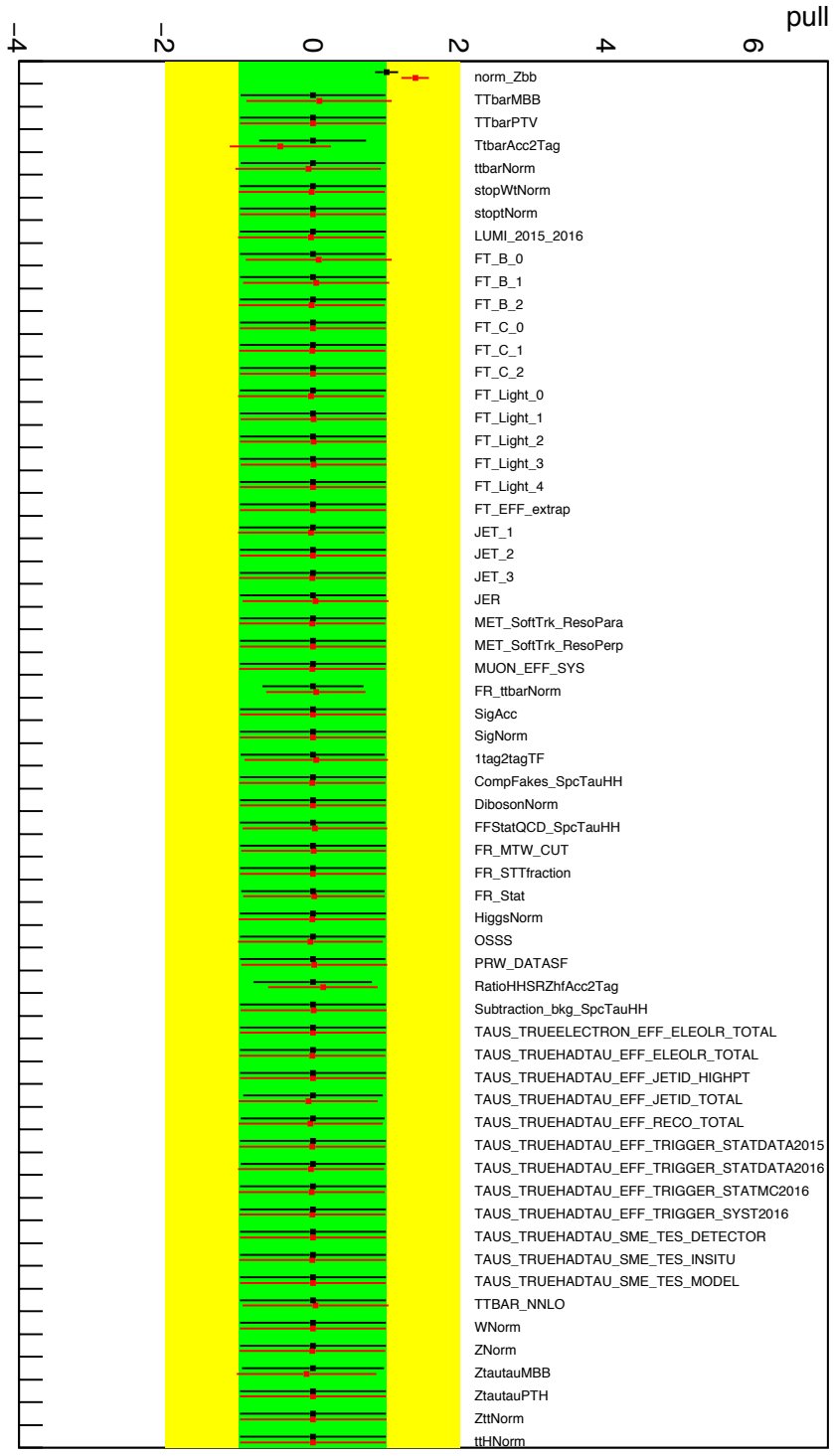

Figure 6.21: NP pulls from the fit of the SM BDT to an Asimov dataset with $\mu = 0$ (black) and to the observed data (red). The associated error bars show the fitted uncertainties of the NPs, relative to their nominal uncertainties.

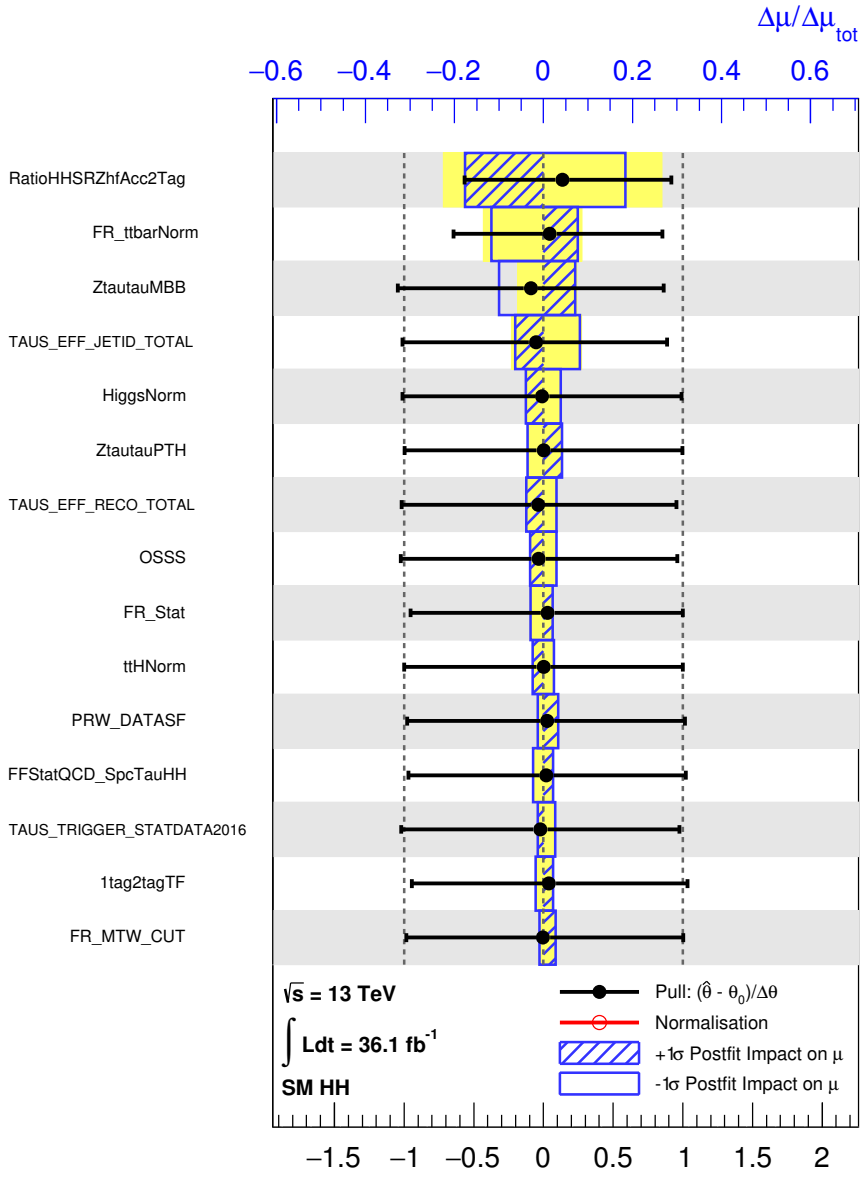

Figure 6.22: Fractional impact of the NPs on the SM best fit value of the signal strength μ. The NPs are listed in decreasing order of their impact on μ, only the first 15 NPs are shown. The boxes show the variations of μ, referring to the top x-axis, when fixing the corresponding individual nuisance parameter θ to its fitted value $\hat{\theta}$ modified upwards or downwards by its fitted uncertainty, and performing the fit again, with all the other parameters allowed to vary. The hatched and open areas correspond to the upwards and downwards variations, respectively. The black circles, with associated error bars, referring to the bottom x-axis, show the pulls.

	Observed	-2σ	-1σ	Median expected	$+1\sigma$	$+2\sigma$
$\sigma(HH \to bb\tau\tau)$ [fb]	40.0	22.8	30.6	42.4	59.1	79.2
$\mu = \sigma/\sigma_{SM}$	16.4	9.3	12.5	17.4	24.2	32.4

Table 6.14: Observed and expected upper limits on the SM di-Higgs production cross section times the $bb\tau\tau$ BR at 95% CL, and their ratios to the SM prediction. The $\pm 2\sigma$ and $\pm 1\sigma$ variations about the expected limit are also shown.

are used as final discriminants for the limit setting.

An upper limit is set on the SM di-Higgs production cross section using the dedicated SM BDT. The results are reported in Table 6.14, where the upper limit is expressed in terms of the production cross section times $bb\tau\tau$ BR and in terms of the signal strength μ. The median expected upper limit on μ of 17.4 obtained in this analysis is the best upper limit on this process obtained from a single decay channel analysis up to date. The best sensitivity obtained in this channel with the analysis developed in this thesis is the result of the use of a BDT to separate signal and background and of the use of the BDT score distribution as final discriminant for the statistical analysis. The choice of this analysis strategy improved significantly (by about a factor 2.5) the result compared to the one obtained with other analysis strategies that were tested during the analysis development, as shown in Appendix C. The observed upper limit on μ of 16.4 is in agreement with the median expected, showing that the background model is well understood.

The median expected upper limit on μ obtained removing all the systematc uncertainties is 13.6, meaning that the impact of these uncertainties on the result is of the order of 30% and thus that this result is limited by the current available data statistics.

Upper limits on the non-resonant di-Higgs production cross section are also set as a function of k_λ and k_t using the BDT trained on the non-resonant signal with $k_\lambda = 20$ (enhanced triple Higgs self-coupling). The upper limits on the cross section as a function of these two parameters can be used to set limits on the parameters themselves by comparing the results to the theoretical cross section. Figure 6.23 shows the expected and observed upper limits on the non-resonant di-Higgs production cross section times $bb\tau\tau$ BR as a function of k_λ. The shape of the limit curve as a function of k_λ comes from the convolution of the effects of the signal acceptance dependence on k_λ and of the different signal-to-background separation given by the different m_{HH} spectra described in Section 6.3. By comparing the expected and observed upper limits on the cross section with the theoretical prediction of the cross section as a function of k_λ with $k_t = 1$, exclusion limits can be set on the parameter k_λ itself with the assumption of $k_t = 1$. From the obtained results it is found that the values $k_\lambda < -9$ and $k_\lambda > 17$ are excluded at 95% CL.

The results can also be interpreted to set limits as a function of k_t with fixed $k_\lambda = 1$ as the shape of the distributions used as final discriminants only depend on the ratio k_λ/k_t. Figure 6.24 shows the expected and observed upper limits on the non-resonant di-Higgs production cross section times $bb\tau\tau$ BR as a function of k_t. By comparing the results with the theoretical cross section as a function of k_t with $k_\lambda = 1$, exclusion limits can be set on the parameter k_t itself with the assumption of $k_\lambda = 1$. From the obtained results it is found that the values $k_t < -1.7$ and $k_t > 2$ are excluded at 95% CL.

The results of the search for resonant di-Higgs production are presented as exclusion limits, calculated using the dedicated BDT score distributions, on the cross section times $bb\tau\tau$ BR as a function of the resonance mass for the narrow width scalar X of the 2HDM and for the RS graviton G_{KK} with $c = 1$ and $c = 2$. Figure 6.25 shows the expected and observed limits for the three considered models. The shape of the limit curve as a function of the resonance mass is given by the effects of the signal acceptance dependence on the mass and of the different signal-to-background separation given by the different m_{HH} spectra. Differences between the results for the three models are also due to the differences in the

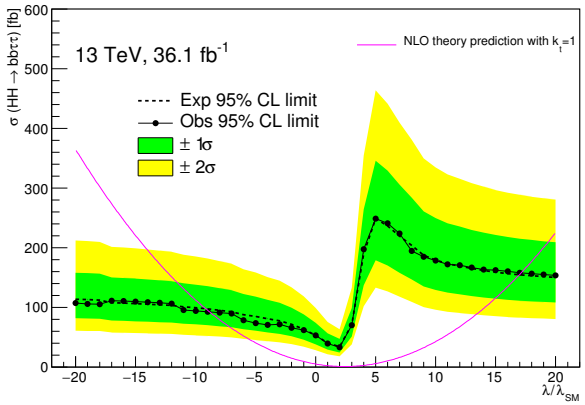

Figure 6.23: Expected and observed upper limits on the non-resonant di-Higgs production cross section times $bb\tau\tau$ BR as a function of k_λ. The yellow and green bands represent the $\pm 2\sigma$ and $\pm 1\sigma$ variations about the expected limit. The theoretical prediction of the cross section as a function of k_λ with $k_t = 1$ is also shown.

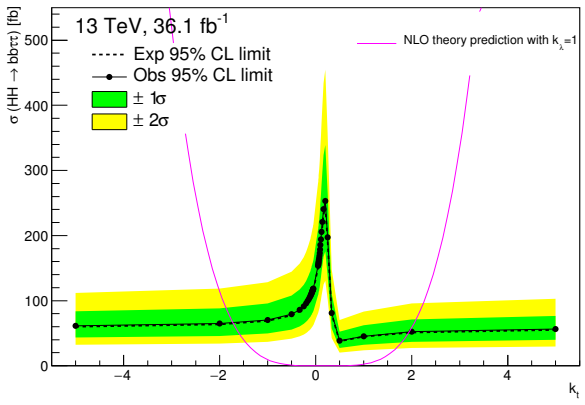

Figure 6.24: Expected and observed upper limits on the non-resonant di-Higgs production cross section times $bb\tau\tau$ BR as a function of k_t. The yellow and green bands represent the $\pm 2\sigma$ and $\pm 1\sigma$ variations about the expected limit. The theoretical prediction of the cross section as a function of k_t with $k_\lambda = 1$ is also shown.

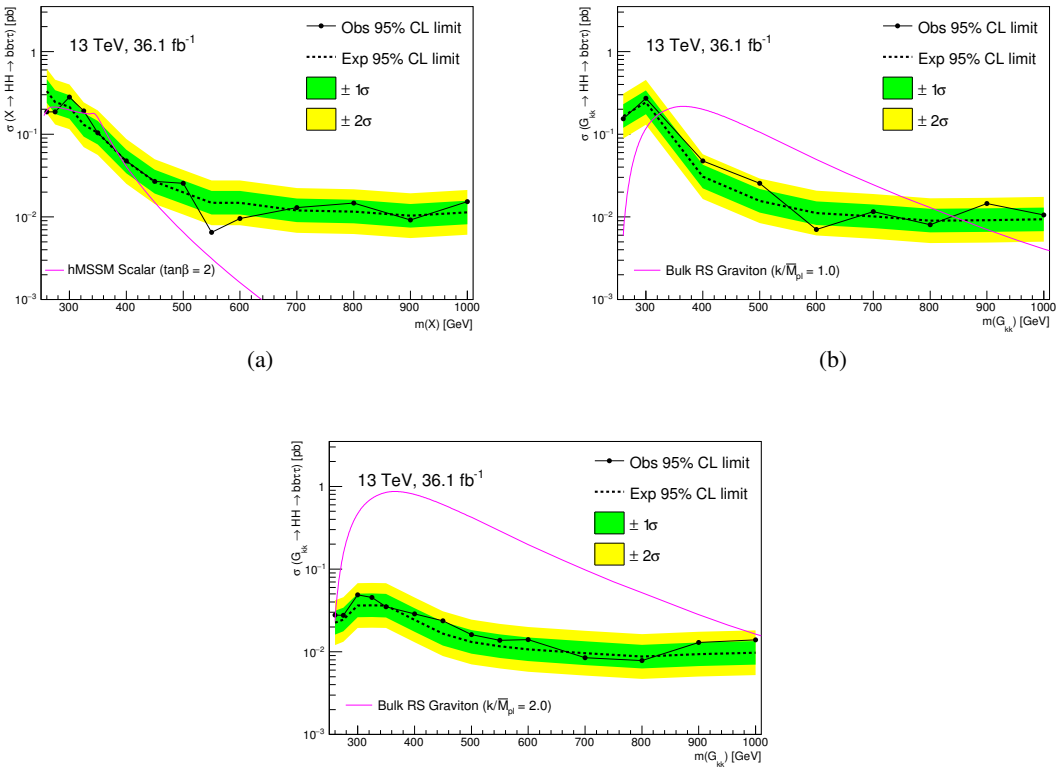

Figure 6.25: Expected and observed upper limits on the resonant di-Higgs production cross section times $bb\tau\tau$ BR as a function of the resonance mass for a) the narrow width scalar of the 2HDM, b) the RS graviton with $c = 1$ and c) the RS graviton with $c = 2$. The yellow and green bands represent the $\pm 2\sigma$ and $\pm 1\sigma$ variations about the expected limit. The theoretical predictions of the cross section for the three considered models are also shown.

signal acceptances arising from the different resonance widths. For masses above 500 GeV these effects are not important and the results are comparable for the three models. By comparing the results with the theoretical predictions of the cross section for a given model it is possible to constrain the allowed mass range for some BSM models. For scalar resonances, the results are interpreted in a simplified minimal supersymmetric model, the MSSM: the mass range 329 GeV $< m_X <$ 376 GeV is excluded at 95% CL for $\tan\beta = 2$, where $\tan\beta$ is the ratio of the vacuum expectation values of the scalar doublets. Randall-Sundrum gravitons are excluded at 95% CL in the mass range 334 GeV $< m_{G_{KK}} <$ 839 GeV assuming $k/\bar{M}_{Pl} = 1$. In the case of $k/\bar{M}_{Pl} = 2$, the full tested mass range, 260 GeV $< m_{G_{KK}} <$ 1000 GeV, is excluded.

CHAPTER 7

Combination with other channels and measurement prospects at the HL-LHC

The results of the $HH \to b\bar{b}\tau^+\tau^-$ analysis performed in this thesis in the $\tau_{had}\tau_{had}$ channel, where both τ-leptons decay hadronically, as described in Chapter 6 are combined with the ones obtained in the $\tau_{lep}\tau_{had}$ channel, where one τ-lepton decays leptonically and one hadronically. The statistical combination of the two $bb\tau\tau$ sub-channels is part of this thesis work. The procedure and the combined results are described in this chapter and published in Reference [7].

In addition, these results are also combined with the ones from the other two most sensitive di-Higgs decay channels, $b\bar{b}b\bar{b}$ and $b\bar{b}\gamma\gamma$. The results of this combination are briefly summarised here and published in Reference [8].

Moreover, a prospect study for the non-resonant di-Higgs search is performed in this thesis in the $b\bar{b}\tau^+\tau^-$ channel and then combined with the prospects of the other two di-Higgs most sensitive decay channels ($b\bar{b}b\bar{b}$ and $b\bar{b}\gamma\gamma$) assuming 3 000 fb^{-1} at $\sqrt{s}$ = 14 TeV expected to be collected at the HL-LHC. The extrapolation procedure and the results obtained for the $b\bar{b}\tau^+\tau^-$ analysis are described here and published in References [9, 10]. The combined results are also reported here for completeness.

7.1 Combination with the $bb\tau_{lep}\tau_{had}$ channel

First, a short overview of the analysis performed in the $bb\tau_{lep}\tau_{had}$ channel is given here to introduce the main aspects needed to describe the combination of the two $bb\tau\tau$ sub-channels. Then, the fit model for the combination is described and the $bb\tau\tau$ combined results are presented.

7.1.1 Overview of the $bb\tau_{lep}\tau_{had}$ channel analysis

The physics objects reconstruction and selection for the $bb\tau_{lep}\tau_{had}$ channel is the same as the one used for the $bb\tau_{had}\tau_{had}$ channel described in Section 6.2. Then, an event selection is applied in order to select events compatible with containing a $bb\tau_{lep}\tau_{had}$ final state. The difference between the two sub-channels is in the reconstruction of the $H \to \tau^+\tau^-$ candidate. In the $bb\tau_{had}\tau_{had}$ channel presented in Chapter 6 both τ-leptons decay hadronically, while in the $bb\tau_{lep}\tau_{had}$ channel described here one τ-lepton decays leptonically into an electron or a muon and one decays hadronically. As the leptonically decaying τ-leptons cannot be distinguished from prompt leptons and are just reconstructed as electrons or muons, the selections applied in this channel are defined to select $bbl\tau_{had}$ events.

Events are first selected checking if they pass the online ATLAS trigger requirements of single-lepton triggers (SLT), requiring the presence of an electron or a muon in the event, and lepton-plus-τ triggers (LTT), requiring the presence of an electron or a muon and a hadronically decaying τ-lepton. The SLT requires electrons or muons with $p_{\mathrm{T}} > 24-26$ GeV (depending on the data taking period). Any event that fails the SLT is tested to see if it passes the LTT. The LTT requires either an electron with $p_{\mathrm{T}} > 17$ GeV or a muon with $p_{\mathrm{T}} > 14$ GeV, and in both cases, a $\tau_{had-vis}$ with $p_{\mathrm{T}} > 25$ GeV. During the 2016 data taking period the LTT also required the presence of an additional jet passing a 25 GeV p_{T} threshold.

The two types of triggers are used to select events in such a way to build two orthogonal regions. The following selections are applied, depending on the trigger fired:

- all events must contain exactly one electron or one muon with p_{T} 1 GeV above the trigger threshold used in the corresponding data taking period;
- all events must contain exactly one $\tau_{had-vis}$ with $p_T > 20$ GeV;
- all avents must contain at least two jets with p_{T} >20 GeV;
- SLT events:
  - the leading jet must have $p_T > 45$ GeV;
- LTT events:
  - an upper threshold on the electron or muon p_{T} equivalent to the SLT thresholds for the corresponding data taking period is applied in order to build two orthogonal regions;
  - the $\tau_{had-vis}$ must have $p_T > 30$ GeV;
  - the leading jet must have $p_T > 80$ GeV (due to the trigger requirement of the presence of a jet in the event and to be on the trigger efficiency plateau);
- the $m_{\tau\tau}^{MMC}$ must be above 60 GeV;
- the light lepton and the τ_{had} must have opposite sign electric charge;
- exactly two jets must be b-tagged;
- no other electrons or muons must be present.

The events passing these requirements constitute two orthogonal signal regions, named SLT and LTT regions. The acceptance times efficiency of this ($bb\tau_{lep}\tau_{had}$) event selection is 2.6% for the SM di-Higgs signal. Values for the non-resonant di-Higgs signals as a function of k_λ with $k_t = 1$ are shown in Figure 6.4. Values for the resonant di-Higgs signals are shown as a function of the resonance mass in Figure 6.5 for the heavy narrow width scalar, the RS graviton with $c = 1, 2$. In these plots, it can be seen that the shapes of the acceptance times effciciency curves are the same for the two $bb\tau\tau$ sub-channels, as expected from the same behaviour of the signal kinematical distributions, but the $bb\tau_{lep}\tau_{had}$ channel shows larger values. This is expected because the reconstruction and identification efficiency is larger for light leptons compared to τ_{had} and also because in this sub-channel the p_{T} thresholds applied in the trigger selection are lower.

The background composition of the two $bb\tau_{lep}\tau_{had}$ signal regions is shown in Figure 7.1. The major background is the top-quark background. MC simulated events are used to model the major background processes containing true-τ_{had} and other minor background contributions. The contribution

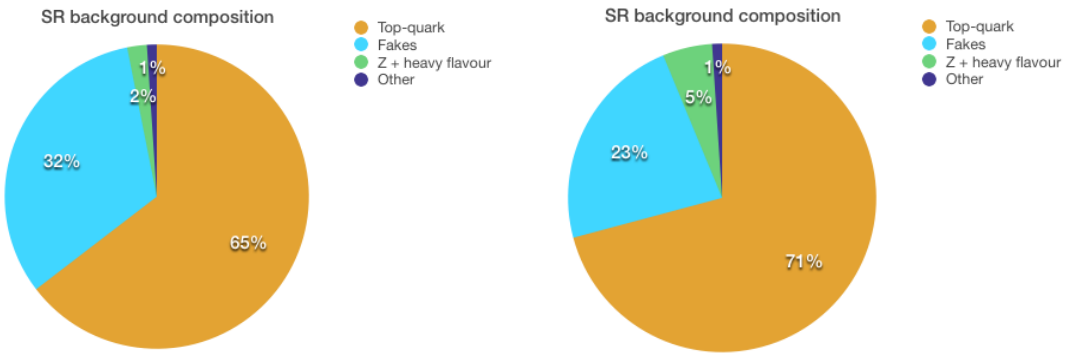

(a) (b)

Figure 7.1: Background composition of the a) SLT and b) LTT $\tau_{lep}\tau_{had}$ signal regions.

SLT resonant	SLT non-resonant and LTT
m_{HH}	m_{HH}
$m_{MMC}^{\tau\tau}$	$m_{MMC}^{\tau\tau}$
m_{bb}	m_{bb}
$\Delta R(\tau, lep)$	$\Delta R(\tau, lep)$
$\Delta R(b, b)$	$\Delta R(b, b)$
m_T^W	m_T^W
$\Delta\Phi(H, H)$	
E_T^{miss}	
E_T^{miss} Φ centrality	
$\Delta p_{\mathrm{T}}(\tau, lep)$	
sub-leading jet p_{T}	

Table 7.1: BDT input variables for the $\tau_{lep}\tau_{had}$ channel.

of backgrounds in which quark- or gluon-initiated jets are misidentified as hadronically decaying τ-leptons (fake-τ_{had}) is estimated using a data-driven combined fake-factor method for $t\bar{t}$, QCD and W+jets backgrounds. The fake-factors are calculated separately for each process in a dedicated control region, in order to account for the different sources of fake-τ_{had}, and are used to calculate a combined fake-factor which is used to estimate the total fake-τ_{had} background in the signal region. The combined fake-factor is calculated as $FF(\mathrm{comb}) = FF(\mathrm{QCD}) \times \mathrm{r_{QCD}} + FF(t\bar{t}/W + \mathrm{jets}) \times (1 - \mathrm{r_{QCD}})$, where $\mathrm{r_{QCD}}$ is defined as the fraction of fake-τ_{had} from (predominantly multi-jet) processes contributing to the data in the fake-τ_{had} enriched template region that are not accounted for by simulated background processes (less than 5%).

Also in this channel BDTs are used to separate signal and background. Separate BDT trainings are performed in the two $\tau_{lep}\tau_{had}$ signal regions. The list of BDT input variables is reported in Table 7.1. The BDT score distributions in the signal regions are used as final discriminants.

7.1.2 Fit model for the $HH \to b\bar{b}\tau^+\tau^-$ combined fit

In the $bb\tau\tau$ combined fit performed in this thesis three signal regions are fitted simultaneously, the $\tau_{had}\tau_{had}$ channel signal region and the two $\tau_{lep}\tau_{had}$ channel signal regions, together with the one-bin Z+

heavy flavour control region. For each tested signal model the corresponding BDT score distributions are fitted to the data in the three signal regions.

In the combined fit all the experimental uncertainties are correlated among the four regions included in the fit. The modelling uncertainties on the MC estimated backgrounds and on signal are also correlated, while the uncertainties on the data-driven backgrounds are fully decorrelated as they arise from completely independent methods.

However, some of the systematic uncertainties on the major backgrounds are treated differently in the $bb\tau\tau$ combined fit compared to the $\tau_{had}\tau_{had}$ channel fit described in Section 6.7. Particularly, the uncertainties on the normalisation of the $t\bar{t}$ background need a special treatment. The $\tau_{lep}\tau_{had}$ channel signal region contains a large fraction of $t\bar{t}$ background, which populates most of the low-BDT score bins. Thus, in this channel it is possible to determine the normalisation of this background from data. For this reason, the $t\bar{t}$ normalisation is set as a freely flotaing NP in the combined fit, in the same way as the Z+ heavy flavour normalisation. The the $t\bar{t}$ normalisation is constrained from the low-BDT score region of the $\tau_{lep}\tau_{had}$ channel. An uncertainty on the relative normalisation of the $t\bar{t}$ background between the different regions needs to be applied in the $\tau_{had}\tau_{had}$ channel signal region and in the Z+ heavy flavour control region in order to take into account the extrapolation of this normalisation from the $\tau_{lep}\tau_{had}$ channel signal region, where it is determined, to the other two regions and cover potential differences. The relative uncertainty is estimated by comparing the ratios of expected events in the two regions obtained with the nominal sample and the systematic variations. In the $\tau_{had}\tau_{had}$ channel signal region this uncertainty is found to be to be 30% for the up variation and 32% for the down variation. In the Z+ heavy flavour control region it is found to be 8% for the up variation and 9% for the down variation.

7.1.3 Profile likelihood fit: test of the background-only hypothesis

The results of the test of the background-only hypothesis from the $b\bar{b}\tau^{+}\tau^{-}$ combined fit are investigated in order to validate the goodness of the fit.

The post-fit number of expected background events and observed data events in the $\tau_{lep}\tau_{had}$ channel signal regions are reported in Table 7.2, together with the expected signal events. Also, the post-fit number of events in the last two bins of the SM BDT distribution are reported in Table 7.3. The total observed number of events are found to be compatible with the post-fit number of background events, from a background-only fit, in the signal region and in the high-BDT score region.

The post-fit BDT distributions of the SM BDT scores in the two $\tau_{lep}\tau_{had}$ signal regions are shown in Figure 7.2. These BDT score distributions used as final discriminants, together with the one in the $\tau_{had}\tau_{had}$ signal region, are well described by the background-only prediction.

The NP pulls from the $bb\tau\tau$ combined fit of the SM BDT score distributions are shown in Figure 7.3 (the NPs included here are the ones from the $\tau_{had}\tau_{had}$ channel described in Appendix B and the ones from the $\tau_{lep}\tau_{had}$ channel). It can be seen that the model describes the data well as none of the nuisance parameters shows unexpected deviations or under/overconstraints. The post-fit Z+ HF normalisation factor, which is a freely floating NP in the fit (named norm_Zbb), determined from data in the dedicated control region included in the fit, is 1.34 ± 0.16. This result is compatible with what was found in the $\tau_{had}\tau_{had}$ channel fit and with what was found by other analyses [130]. The post-fit $t\bar{t}$ normalisation factor, which is also a freely floating NP in the $bb\tau\tau$ combined fit (named norm_ttbar), determined from data in the low-BDT region of the $\tau_{lep}\tau_{had}$ SLT channel signal region, is 1.06 ± 0.13 thus compatible with expectation. The NPs which are constrained from the fit correspond to the modelling uncertainties on the $t\bar{t}$ and Z+ HF backgrounds, their relative normalisation uncertainties between regions and the uncertainties on the data-driven backgrounds with fake-τ_{had}. These uncertainties are expected to be constrained from the fit as they are analysis-dependent and were estimated in this analysis in a very

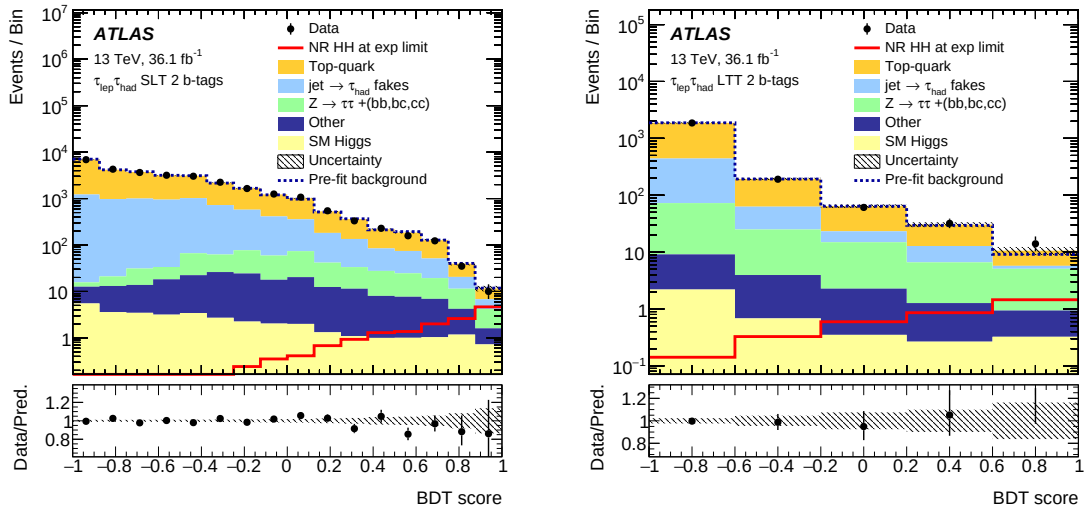

(a) (b)

Figure 7.2: Post-fit distributions of the $\tau_{lep}\tau_{had}$ channel SM BDTs in the a) SLT and b) LTT signal regions. All background components are scaled to their normalisations as determined in the fit. The pre-fit normalisation of the sum of all background components predicted by the simulated events is given by the dashed blue line. The SM di-Higgs signal distribution is also shown with a normalisation scaled to the expected exclusion limit. The shaded bands represent the total post-fit uncertainty with NPs profiled to the data.

conservative way.

Moreover, Figure 7.4 shows the comparison between the NP pulls from the $bb\tau\tau$ combined fit, from the $\tau_{had}\tau_{had}$ channel fit and from the $\tau_{lep}\tau_{had}$ channel fit of the SM BDT scores to the observed data. It can be seen that all the NP pulls from the $bb\tau\tau$ combined fit are compatible with the pulls from the single channel fits, meaning that the correlations between the NPs in the three signal regions included in the combined fit are not introducing any unexpected behaviour. It should be noticed that one NP (named RatioHHSRTtbarAcc2Tag) is only present in the combined fit as it is the NP corresponding to the $t\bar{t}$ relative normalisation uncertainty between the $\tau_{had}\tau_{had}$ channel and the $\tau_{lep}\tau_{had}$ SLT channel signal regions.

The fractional impact of the NPs on the best fit value of the signal strength μ from a background plus signal fit is also checked for the $bb\tau\tau$ combined fit and it is shown for the SM BDT fit in Figure 7.5, where the systematic uncertainties are listed in decreasing order of their impact on μ and only the first 15 NPs are shown. It can be seen that the most important systematic uncertainties are the modelling uncertainties on the major backgrounds present in the high-BDT score region, together with the relative uncertainties between regions for the freely floating background normalisations, the uncertainties related to the τ_{had} trigger, reconstruction and identification efficiencies and the uncertainties related to the data-driven fake-τ_{had} backgrounds. The ranking of the NPs in the $bb\tau\tau$ combined fit is following the importance of the uncertainties in the single channel fits and the importance of the channel. Similar results are obtained also from the fit of the other BDT distributions used for testing non-resonant and resonant BSM signal hypotheses.

Component	Events in SLT SR	Events in LTT SR
$t\bar{t}$	17800 ± 1100	1475 ± 94
Single top	1130 ± 110	72.9 ± 7.6
τ fakes	9000 ± 1100	475 ± 76
Z + HF	416 ± 97	117 ± 28
SM single Higgs	38 ± 10	4.1 ± 1.0
Other	197 ± 32	14.5 ± 2.3
Total background	28610 ± 180	2159 ± 46
Data	28612	2161
SM HH	0.99 ± 0.13	0.225 ± 0.033
X(300 GeV)	39.1 ± 6.3	11.8 ± 1.9
X(500 GeV)	3.41 ± 0.52	0.88 ± 0.13
X(1000/800 (LTT) GeV)	0.0267 ± 0.0041	0.0228 ± 0.0035
G_{kk}(300 GeV, c = 1)	23.6 ± 3.7	7.5 ± 1.2
G_{kk}(500 GeV, c = 1)	42.4 ± 6.4	9.9 ± 1.5
G_{kk}(1000/800 (LTT) GeV)	2.60 ± 0.40	1.06 ± 0.16
G_{kk}(300 GeV, c = 2)	327 ± 50	82 ± 13
G_{kk}(500 GeV, c = 2)	193 ± 29	39.7 ± 6.1
G_{kk}(1000/800 (LTT) GeV)	8.6 ± 1.3	3.63 ± 0.56

Table 7.2: Post-fit expected number of background events, determined from a background-only fit, compared to the observed number of data events in the $\tau_{lep}\tau_{had}$ channel signal regions. The expected number of signal events is also reported. The total background is not identical to the sum of the individual components since the latter are rounded for presentation, while the sum is calculated with the full precision before being subsequently rounded. Systematic uncertainties are included. Due to the large correlations, individual uncertainties can be significantly larger than the total uncertainty.

Component	Events in SLT SR	Events in LTT SR
$t\bar{t}$	18.2 ± 4.2	23.2 ± 1.7
Single top	6.4 ± 1.3	3.7 ± 1.2
τ fakes	12.0 ± 2.3	6.6 ± 1.5
Z + HF	10.2 ± 2.6	7.7 ± 3.1
SM single Higgs	1.94 ± 0.43	0.58 ± 0.14
Other	3.89 ± 0.69	1.51 ± 0.36
Total background	45.7 ± 4.5	39.5 ± 3.0
Data	45	47
SM HH	0.49 ± 0.07	0.16 ± 0.02

Table 7.3: Post-fit expected number of background events, determined from a background-only fit, compared to the observed number of data events in the last two bins of the SM BDT distribution in the $\tau_{lep}\tau_{had}$ channel signal regions. The expected number of signal events is also reported. The total background is not identical to the sum of the individual components since the latter are rounded for presentation, while the sum is calculated with the full precision before being subsequently rounded. Systematic uncertainties are included. Due to the large correlations, individual uncertainties can be significantly larger than the total uncertainty.

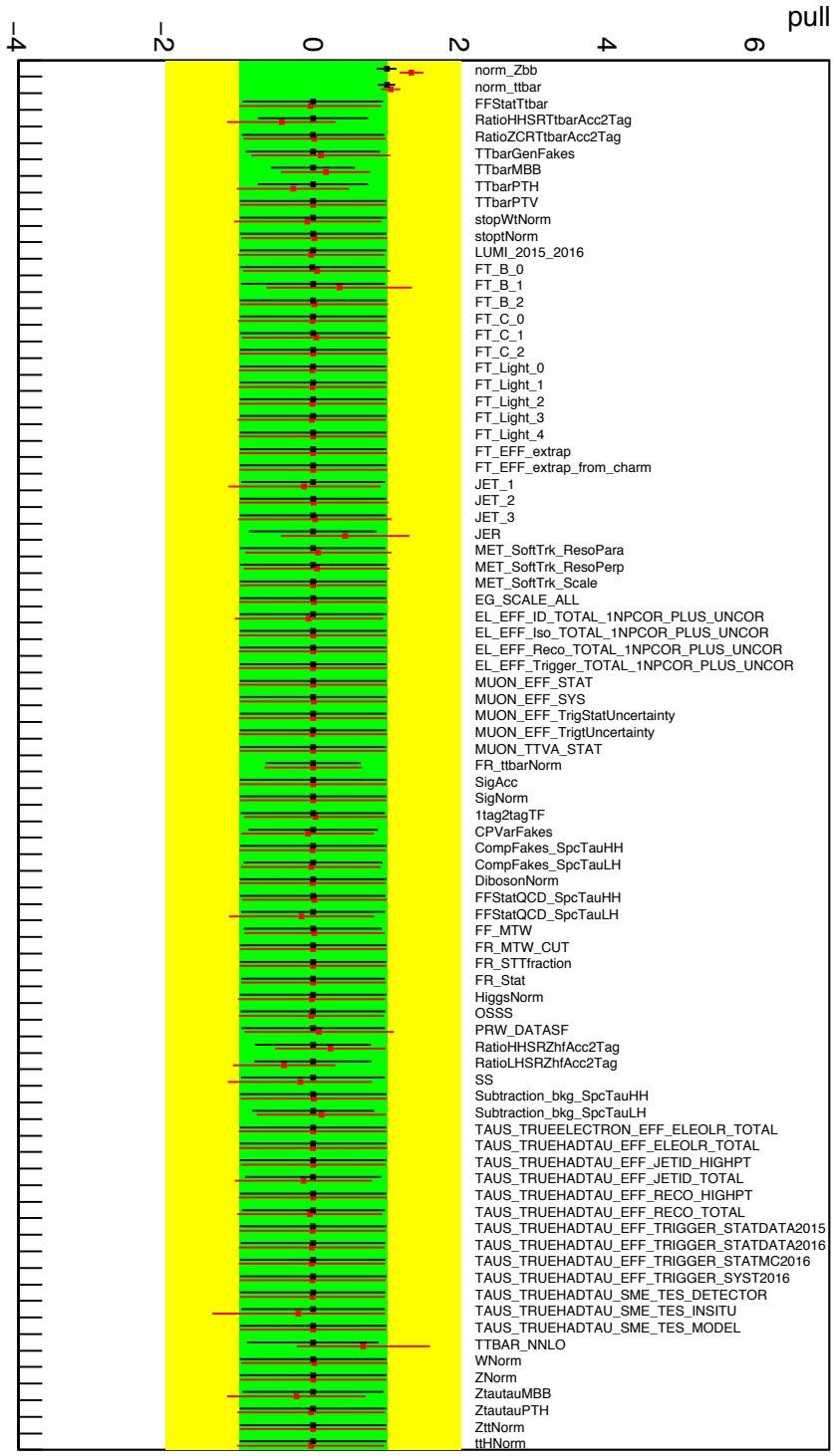

Figure 7.3: NP pulls from the $bb\tau\tau$ combined fit of the SM BDTs to an Asimov dataset with $\mu = 0$ (black) and to the observed data (red). The associated error bars show the fitted uncertainties of the NPs, relative to their nominal uncertainties.

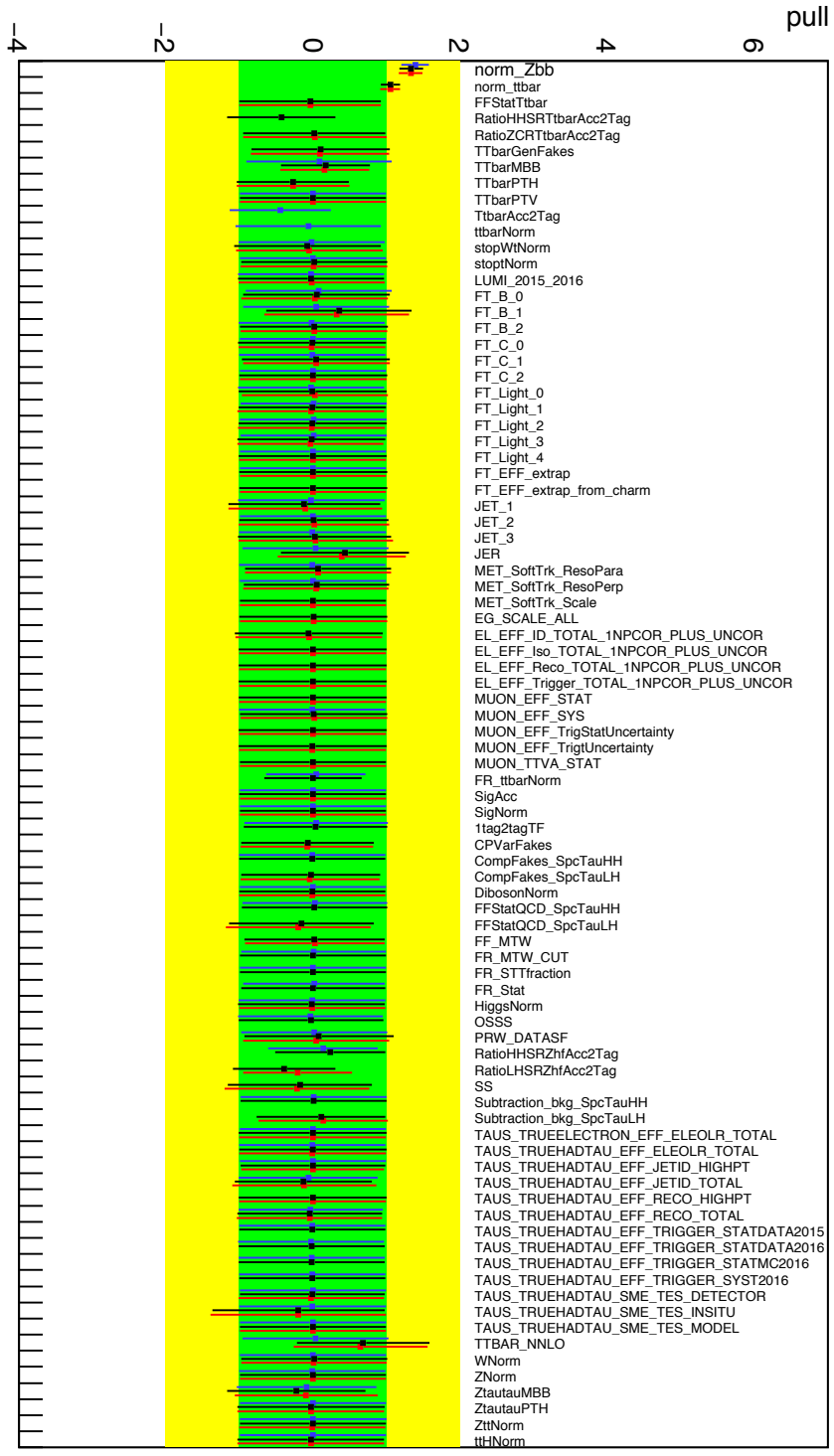

Figure 7.4: Comparison of the NP pulls from the $bb\tau\tau$ combined fit (black), from the $\tau_{had}\tau_{had}$ channel fit (blue) and from the $\tau_{lep}\tau_{had}$ channel fit (red) of the SM BDTs to the observed data.

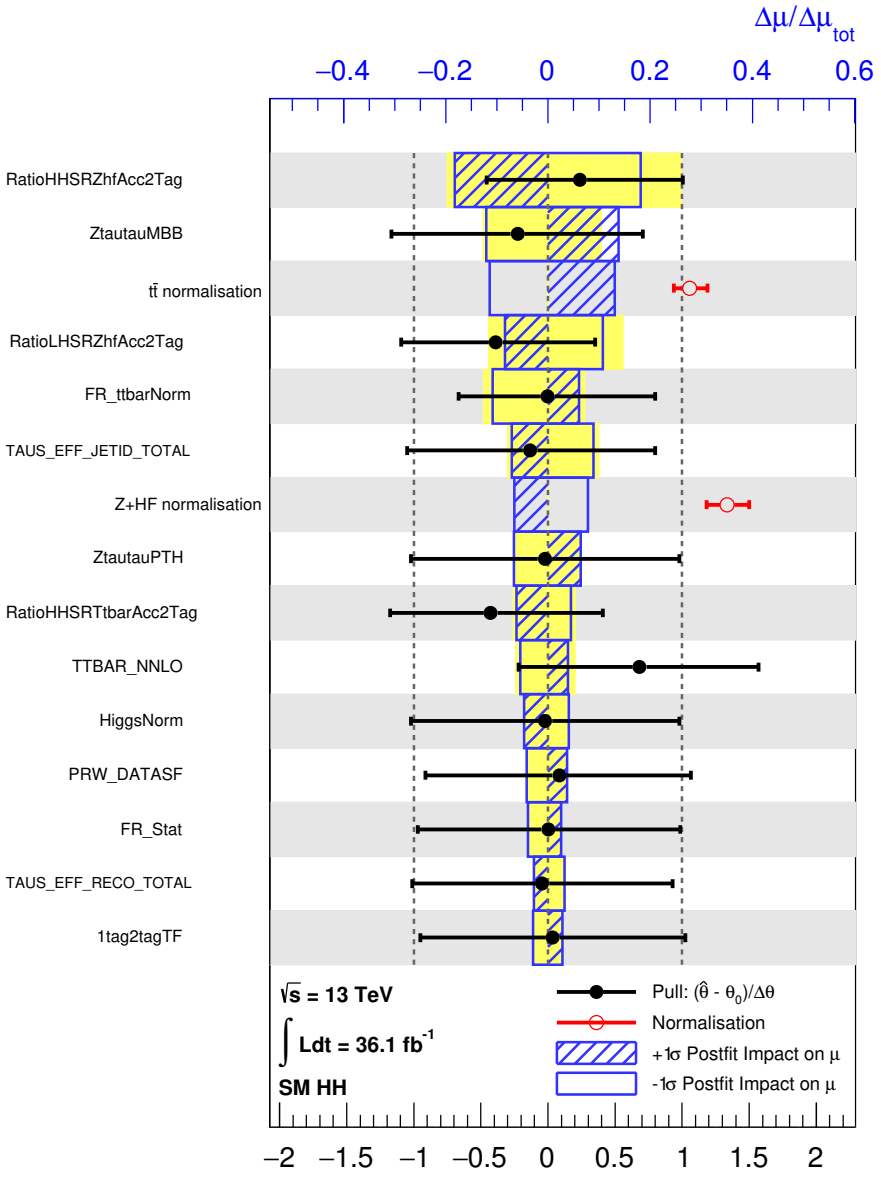

Figure 7.5: Fractional impact of the NPs on the $bb\tau\tau$ combined SM best fit value of the signal strength μ. The NPs are listed in decreasing order of their impact on μ, only the first 15 NPs are shown. The boxes show the variations of μ, referring to the top x-axis, when fixing the corresponding individual nuisance parameter θ to its fitted value $\hat{\theta}$ modified upwards or downwards by its fitted uncertainty, and performing the fit again, with all the other parameters allowed to vary. The hatched and open areas correspond to the upwards and downwards variations, respectively. The black and red circles, with associated error bars, referring to the bottom x-axis, show the pulls. The red circles correspond to the freely floating NPs.

		Observed	-2σ	-1σ	Median expected	$+1\sigma$	$+2\sigma$
$\tau_{had}\tau_{had}$	$\sigma(HH \to bb\tau\tau)$ [fb]	40.0	22.8	30.6	42.4	59.1	79.2
	$\mu = \sigma/\sigma_{SM}$	16.4	9.3	12.5	17.4	24.2	32.4
$\tau_{lep}\tau_{had}$ SLT	$\sigma(HH \to bb\tau\tau)$ [fb]	52.0	38.4	52.0	72.0	100	134
	$\mu = \sigma/\sigma_{SM}$	21.3	15.7	21.1	29.3	40.8	55.0
$\tau_{lep}\tau_{had}$ LTT	$\sigma(HH \to bb\tau\tau)$ [fb]	326	123	165	229	319	428
	$\mu = \sigma/\sigma_{SM}$	134	50.4	67.7	93.9	131	175
$\tau_{lep}\tau_{had}$ combined	$\sigma(HH \to bb\tau\tau)$ [fb]	57.0	37.2	49.9	69.3	96.5	129.3
	$\mu = \sigma/\sigma_{SM}$	23.5	15.2	20.5	28.4	39.5	53.0
$bb\tau\tau$ combined	$\sigma(HH \to bb\tau\tau)$ [fb]	30.9	19.4	26.0	36.1	50.2	67.3
	$\mu = \sigma/\sigma_{SM}$	12.7	7.9	10.7	14.8	20.6	27.6

Table 7.4: Observed and expected $bb\tau\tau$ combined upper limits on the SM di-Higgs production cross section times the $bb\tau\tau$ BR at 95% CL, and their ratios to the SM prediction. The $\pm2\sigma$ and $\pm1\sigma$ variations about the expected limit are also shown. Results from the single sub-channels are also included.

	$\tau_{had}\tau_{had}$	$\tau_{lep}\tau_{had}$ SLT	$\tau_{lep}\tau_{had}$ LTT
$S/\sqrt{S+B}$ full SR	0.022	0.0059	0.0048
$S/\sqrt{S+B}$ last two BDT bins	0.10	0.07	0.025

Table 7.5: Sensitivity for the SM di-Higgs signal expressed in terms of $S/\sqrt{S+B}$ in the three signal regions and in the last two bins of the BDT score distributions.

7.1.4 Results

As the observed data are found to be compatible with the background-only hypothesis in all the three signal regions for all the BDT distributions, they are used to set $bb\tau\tau$ combined exclusion upper limits on the non-resonant and resonant di-Higgs production cross section. As for the test of the background-only hypothesis, the BDT score distributions for each signal model are used as final discriminants in the three signal regions for the limit setting. The LTT signal region is not included in the fit for the calculation of the non-resonant limits as a function of the varied couplings and for the resonant limits for masses above 800 GeV as this region is found to be much less sensitive compared to the other two regions (the effect on the final results of including this region is of the order of 1%).

The $bb\tau\tau$ combined results for the SM di-Higgs process are reported in Table 7.4, where the upper limit is expressed in terms of the production cross section times $bb\tau\tau$ BR and in terms of the signal strength μ. The combined observed (expected) upper limit on μ is 12.7 (14.8). The upper limits obtained from the single sub-channels are also included, showing that the $\tau_{had}\tau_{had}$ channel is the most sensitive and it is the channel driving the $bb\tau\tau$ combined sensitivity. The reason for this can be understood looking at the number of expected signal and background events in the three signal regions. From Tables 6.12, 7.2, 6.13 and 7.3 it is possible to compare the sensitivities for the SM di-Higgs signal in the three signal regions and in the last two bins of the BDT score distributions by calculating the quantity $S/\sqrt{S+B}$, reported in Table 7.5, which shows that the $\tau_{had}\tau_{had}$ channel has the best sensitivity in the full signal region and in the last two bins of the BDT score distribution.

Figure 7.6 shows the $bb\tau\tau$ combined expected and observed upper limits on the non-resonant di-Higgs production cross section times $bb\tau\tau$ BR as a function of k_λ for $k_t = 1$. From the obtained results it is found that the values $k_\lambda < -7$ and $k_\lambda > 16$ are excluded at 95% CL. Figure 7.7 shows the $bb\tau\tau$ combined

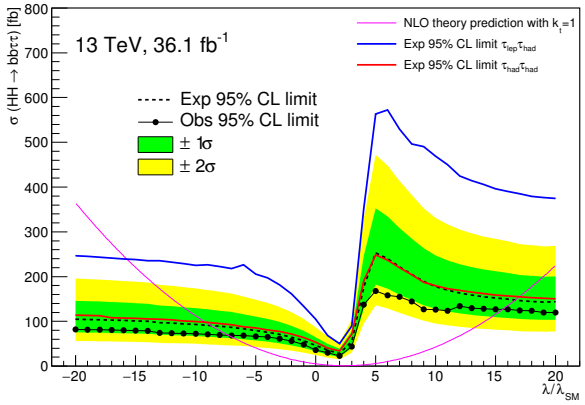

Figure 7.6: Expected and observed $bb\tau\tau$ combined upper limits on the non-resonant di-Higgs production cross section times $bb\tau\tau$ BR as a function of k_λ. The yellow and green bands represent the $\pm 2\sigma$ and $\pm 1\sigma$ variations about the expected limit. Expected limits from the single channels are also overlaid, in blue for the $\tau_{lep}\tau_{had}$ channel and red for the $\tau_{had}\tau_{had}$ one. The theoretical prediction of the cross section as a function of k_λ with $k_t = 1$ is also shown.

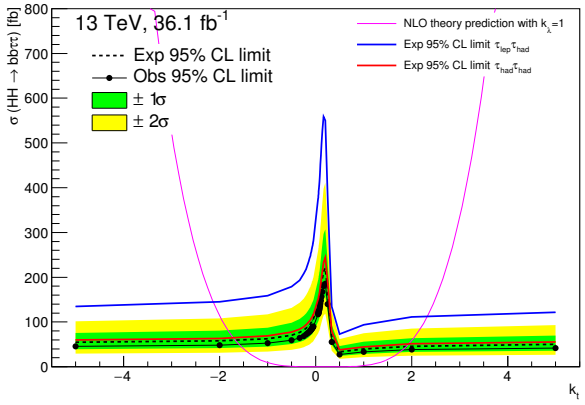

Figure 7.7: Expected and observed $bb\tau\tau$ combined upper limits on the non-resonant di-Higgs production cross section times $bb\tau\tau$ BR as a function of k_t. The yellow and green bands represent the $\pm 2\sigma$ and $\pm 1\sigma$ variations about the expected limit. Expected limits from the single channels are also overlaid, in blue for the $\tau_{lep}\tau_{had}$ channel and red for the $\tau_{had}\tau_{had}$ one. The theoretical prediction of the cross section as a function of k_t with $k_\lambda = 1$ is also shown.

expected and observed upper limits on the non-resonant di-Higgs production cross section times $bb\tau\tau$ BR as a function of k_t for $k_\lambda = 1$. From the obtained results it is found that the values $k_t < -1.6$ and $k_t > 1.8$ are excluded at 95% CL. In both plots the expected limits from the single channels are also overlaid, showing that most of the combined sensitivity on these couplings comes from the $\tau_{had}\tau_{had}$ channel.

Figure 7.8 shows the $bb\tau\tau$ combined expected and observed upper limits on the resonant di-Higgs production cross section times $bb\tau\tau$ BR as a function of the resonance mass for the three considered models. For scalar resonances the mass range 305 GeV $< m_X <$ 402 GeV is excluded at 95% CL for the MSSM with $\tan\beta = 2$. Randall-Sundrum gravitons are excluded at 95% CL in the mass range 325 GeV $< m_{G_{KK}} <$ 885 GeV assuming $k/\bar{M}_{Pl} = 1$. In the case of $k/\bar{M}_{Pl} = 2$, the full tested mass range, 260 GeV $< m_{G_{KK}} <$ 1000 GeV, is excluded. In all plots the expected limits from the single channels are also overlaid, showing that most of the combined sensitivity comes from the $\tau_{had}\tau_{had}$ channel for all

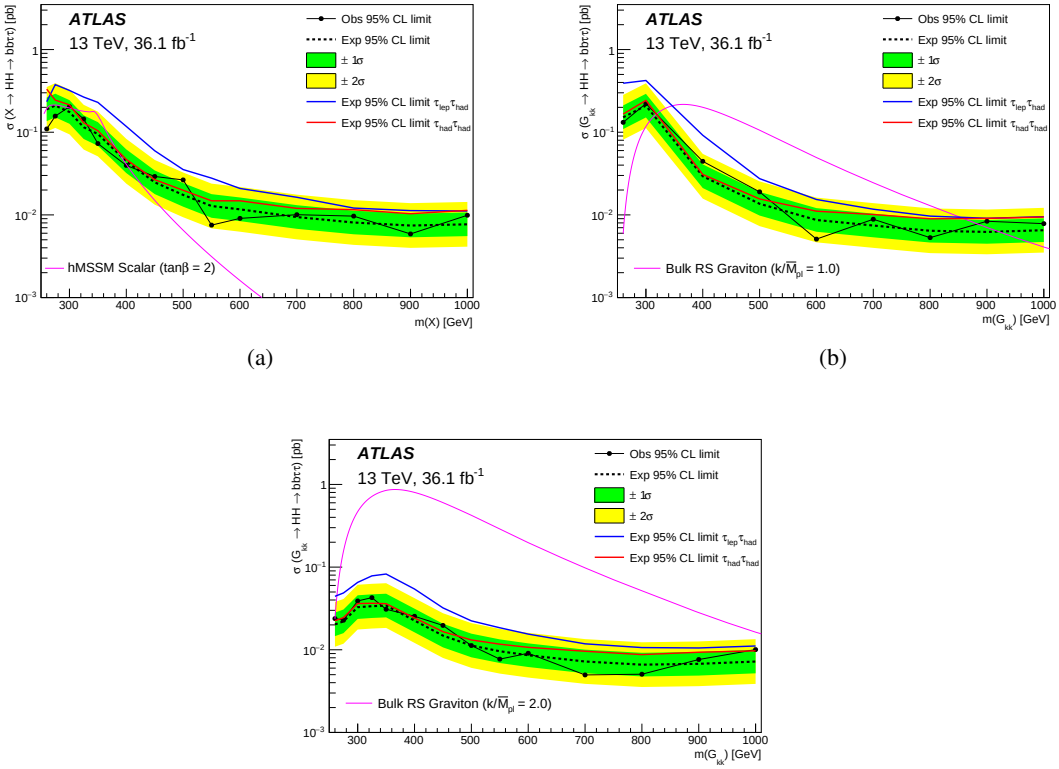

Figure 7.8: Expected and observed $bb\tau\tau$ combined upper limits on the resonant di-Higgs production cross section times $bb\tau\tau$ BR as a function of the resonance mass for a) the narrow width scalar of the 2HDM, b) the RS graviton with $c = 1$ and c) the RS graviton with $c = 2$. The yellow and green bands represent the $\pm 2\sigma$ and $\pm 1\sigma$ variations about the expected limit. Expected limits from the single channels are also overlaid, in blue for the semi-leptonic channel and red for the fully hadronic one. The theoretical predictions of the cross section for the three considered models are also shown.

considered models for masses below 700 GeV, while in the high mass region the two sub-channels have comparable sensitivities.

7.2 Combination with other di-Higgs channels

The results of the $HH \to b\bar{b}\tau^+\tau^-$ analysis presented in this thesis are combined with the results from the other two most sensitive di-Higgs decay channels: $b\bar{b}b\bar{b}$ and $b\bar{b}\gamma\gamma$. Figure 7.9 shows the di-Higgs combined upper limits on the SM di-Higgs production cross section. The combined observed (expected) upper limit on μ is 6.4 (10.4), which is the current world best upper limit set on the production cross section for this process. The upper limits from the $bbbb$, $bb\tau\tau$ and $bb\gamma\gamma$ channels are also shown. The $bb\tau\tau$ channel is the most sensitive channel thanks to the relatively high BR and clean signature, which provide a good signal over background ratio in the signal regions, and to the chosen analysis strategy of using the BDT score distribution as final discriminant variable in the fit that significantly improved the sensitivity of this channel. The small difference between the $bb\tau\tau$ result shown here and the one shown in Section 7.1 is due to the fact that in the combination result the theoretical cross section uncertainties

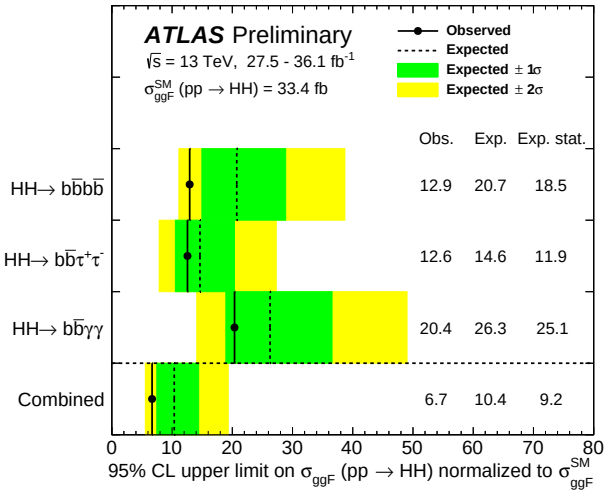

Figure 7.9: Expected and observed di-Higgs combined upper limits on the SM non-resonant di-Higgs production cross section. The yellow and green bands represent the $\pm 2\sigma$ and $\pm 1\sigma$ variations about the expected limit. The upper limits from the *bbbb*, *bbττ* and *bbγγ* channels are also shown.

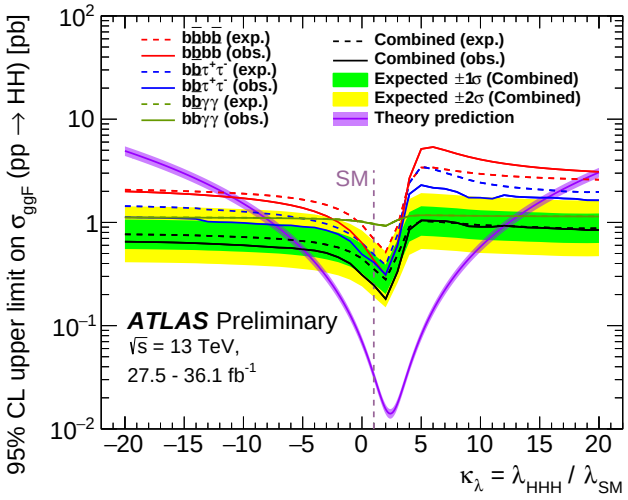

Figure 7.10: Expected and observed di-Higgs combined upper limits on the non-resonant di-Higgs production cross section as a function of k_λ. The yellow and green bands represent the $\pm 2\sigma$ and $\pm 1\sigma$ variations about the expected limit. The upper limits from the *bbbb*, *bbττ* and *bbγγ* channels are overlaid. The theoretical prediction of the cross section as a function of k_λ with $k_t = 1$ is also shown.

on signal are not included.

Figure 7.10 shows the di-Higgs combined upper limits on the non-resonant di-Higgs production cross section as a function of k_λ for $k_t = 1$. From the obtained results it is found that the values $k_\lambda < -5$ and $k_\lambda > 12.1$ are excluded at 95% CL, currently the world most stringent constraints on the anomalous Higgs self-coupling to date. From the comparison of the upper limits from the *bbbb*, *bbττ* and *bbγγ* channels it can be seen that the *bbττ* channel is the most sensitive channel in the region $-13 < k_\lambda < 3$.

Figure 7.11 shows the di-Higgs combined expected and observed upper limits on the resonant di-Higgs production cross section as a function of the resonance mass for the three considered models. For scalar

resonances the mass range 260 GeV $< m_X <$ 462 GeV is excluded at 95% CL for the MSSM with $\tan\beta =$ 2. Randall-Sundrum gravitons are excluded at 95% CL in the mass range 307 GeV $< m_{G_{KK}} <$ 1362 GeV assuming $k/\bar{M}_{Pl} = 1$. In the case of $k/\bar{M}_{Pl} = 2$, the full tested mass range, 260 GeV $< m_{G_{KK}} <$ 1744 GeV, is excluded. In all plots the expected limits from the single channels are also overlaid. The $bb\gamma\gamma$ channel is only included for the scalar interpretation as no graviton interpretation was performed in this channel. It can be seen that the $bb\gamma\gamma$ channel is the most sensitive channel in the low mass region, below 400 GeV, mostly thanks to the larger acceptance times efficiency of this channel for low-mass resonances given by the lower p_{T} thresholds applied in the di-photon triggers and by the high photon reconstruction and identification efficiencies and the good di-photon mass resolution [139]. In the middle mass region, between 400 GeV and 600 GeV the $bbbb$ and $bb\tau\tau$ channels are dominant and have comparable sensitivities. In the high mass region the $bbbb$ channel is the most sensitive, thanks to the implementation of a dedicated technique for the event reconstruction that targets Higgs bosons from the decay of a heavy resonance which are reconstructed as single boosted jets [140]. Above 1 TeV no combination is performed and the esclusion limits come from the $bbbb$ channel results, beacuse the presenece of signals with masses above this value was not tested in the $bb\tau\tau$ and $bb\gamma\gamma$ channels.

7.3 Measurement prospects at the HL-LHC

The results from the ATLAS Run 2 $HH \to b\bar{b}\tau^+\tau^-$ analysis presented in this thesis obtained with 36.1 fb^{-1} of $\sqrt{s} = 14$ TeV pp collisions data are extrapolated to $\sqrt{s} = 14$ TeV and the HL-LHC target integrated luminosity of 3 000 fb^{-1} to obtain an estimation of the sensitivity of this channel to the SM di-Higgs production and to the Higgs self-coupling at the HL-LHC. The results of this extrapolation are also combined with the prospects results from the $b\bar{b}b\bar{b}$ and $b\bar{b}\gamma\gamma$ channels.

The extrapolation procedure adopted in the $bb\tau\tau$ channel developed in this thesis and the results obtained are presented in the following sections. The results of the combination with the other two most sensitive di-Higgs decay channels are also briefly summarised for completeness.

7.3.1 Extrapolation procedure

The BDT distributions for signal and background are scaled to luminosities up to 3 000 fb^{-1} by a mutliplicative factor defined as the ratio of the target luminosity to the luminosity of the Run 2 result. The increase of the centre-of-mass energy from $\sqrt{s} = 13$ TeV to $\sqrt{s} = 14$ TeV is taken into account by scaling signal and backgrounds (estimated using simulations at $\sqrt{s} = 13$ TeV) by the ratio of the corresponding production cross sections. Various extrapolation assumptions on the systematic uncertainties are investigated. In the baseline scenario:

- the uncertainty on the luminosity is assumed to be 1%;
- the performance of the detector are assumed to be the same as the current ones except the b-tagging efficiency which is expected to improve by 8% for a given c- and light-jet rejections due to the upgrade of the inner detector;
- the experimental uncertainties are fixed to the Run 2 values;
- the Z+ heavy flavour background normalisation is scaled by a factor 1.34 obtained from data in the Run 2 analysis;
- the $t\bar{t}$ background normalisation is taken from the MC simulation as its Run 2 normalisation factor obtained from data is consistent with 1;

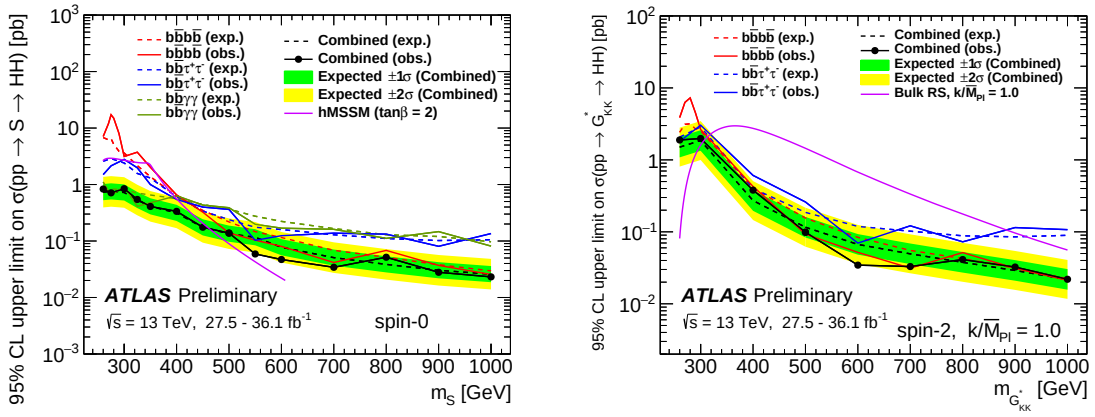

(a) (b)

(c)

Figure 7.11: Expected and observed di-Higgs combined upper limits on the resonant di-Higgs production cross section as a function of the resonance mass for a) the narrow width scalar of the 2HDM, b) the RS graviton with $c = 1$ and c) the RS graviton with $c = 2$. The yellow and green bands represent the $\pm 2\sigma$ and $\pm 1\sigma$ variations about the expected limit. The upper limits from the *bbbb*, *bbττ* and *bbγγ* channels are overlaid. The theoretical predictions of the cross section for the three considered models are also shown.

- since the Z+ heavy flavour and $t\bar{t}$ normalisations are obtained from data, their uncertainty are assumed to be reduced by a factor of approximately 10 compared to the Run 2 values thanks to the increase of the data statistics;
- the statistical uncertainties on the data-driven backgrounds with fake-τ_{had} are adjusted to follow Poisson statistics corresponding to the target dataset size;
- the uncertainties on the single Higgs backgrounds are assumed to be 5% and 10% for ZH and ttH respectively, corresponding to the theory uncertainties;
- MC statistical uncertainties are neglected under the assumption that the size of the MC samples will increase significantly in line with the data luminosity.

In addition to the baseline scenario, an alternative conservative extrapolation is performed in which all the systematic uncertainties are set to their Run 2 values. This extrapolation is split in two scenarios, one where the Run 2 MC statistical uncertainties are adopted and the other one where they are neglected. An additional extrapolation is performed neglecting all systematic uncertainties.

7.3.2 Results

Figure 7.12 shows the SM BDT score distributions in the three $bb\tau\tau$ signal regions extrapolated from the Run 2 analysis. For each extraplation scenario a profile-likelihood fit is performed on these distributions to extract the expected upper limit on the signal strength and the expected significance. The extrapolated number of signal and background events expected in the full signal regions, in the last two bins of the BDTs and in the last bin of the BDTs are reported in Appendix E in Tables E.1, E.2 and E.3 respectively. It should be noticed that the binning criteria are kept the same as the ones used in the Run 2 analysis but the binning itself changes due to the scaling of the expected background events. Therefore the sensitivity improves beyond what is expected from the increase in cross section and luminosities.

Figure 7.13 shows the expected upper limits on the SM di-Higgs signal strength as a function of the integrated luminosity in the four extrapolation scenarios. In the absence of the signal, the analysis is expected to set a 95% CL upper limit at 0.99 times the SM expectation with $3\,000\,\text{fb}^{-1}$ of data in the baseline scenario. The $\tau_{had}\tau_{had}$ channel is the most sensitive and can alone set an upper limit at 1.1 times the SM expectation. Figure 7.14 shows the expected significance for the SM di-Higgs signal as a function of the integrated luminosity in the four extrapolation scenarios. In the baseline scenario a significance of 2σ can be reached with the HL-LHC dataset. The expected upper limits on the non-resonant di-Higgs production cross section as a function of k_λ are shown in Figure 7.15. From the comparison of the expected limits and the theoretical cross section the expected allowed k_λ interval at 95% CL is $1 < k_\lambda < 7$ in the baseline scenario.

Prospect studies for the non-resonant di-Higgs search at the HL-LHC are performed also in the $bbbb$ and $bb\gamma\gamma$ channels. Combining the three channels the expected 95% CL upper limit on the SM di-Higgs production cross section is 0.68 times the SM expectation, while the expected significance for the SM di-Higgs signal is 3σ, corresponding to the threshold needed for claiming evidence of the presence of the signal, and the signal strength is expected to be measured with an accuracy of 40%.

These results are very important as they motivate the continuation of development of the di-Higgs searches as they show that only thanks to the increase of the size of the dataset it will be possible to have evidence of this process at the HL-LHC. By further improving the analyses strategies it could be possible to reach evidence for di-Higgs production even with a smaller dataset.

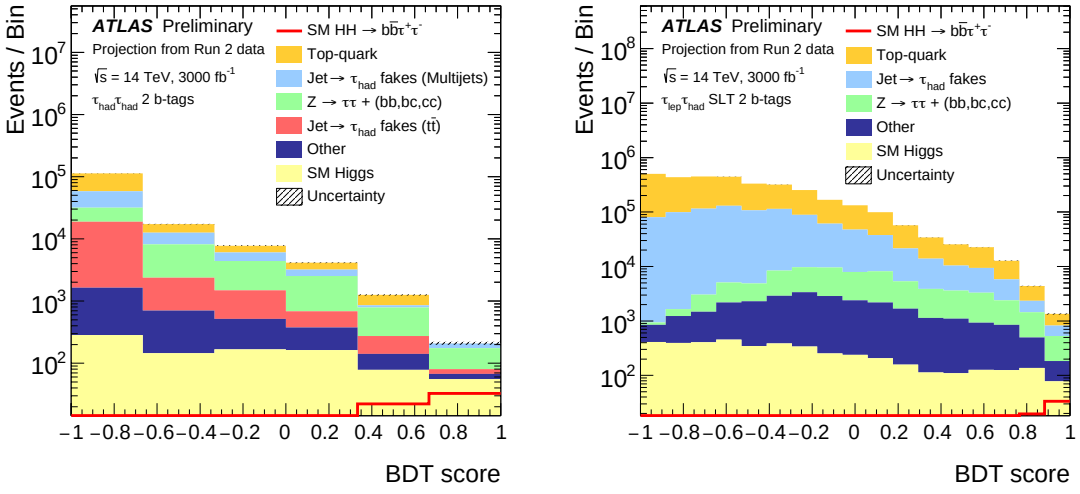

(a)

(b)

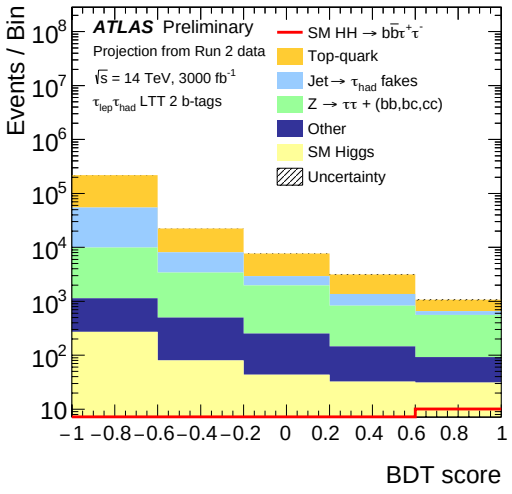

(c)

Figure 7.12: Extrapolated distributions of the SM BDTs in the a) $\tau_{had}\tau_{had}$ b) $\tau_{lep}\tau_{had}$ SLT and c) $\tau_{lep}\tau_{had}$ LTT channel signal regions.

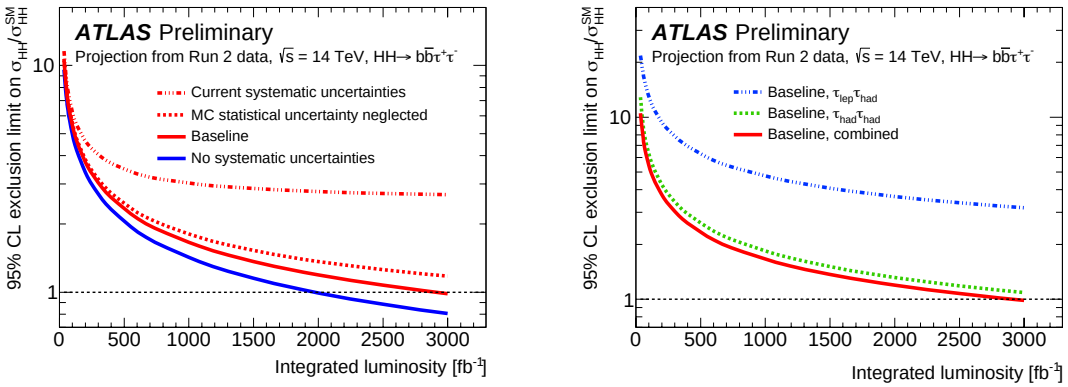

(a) (b)

Figure 7.13: Expected upper limits on the SM di-Higgs signal strength as a function of the integrated luminosity. Combined results are shown in a) for each extrapolation scenario and in b) and for the baseline scenario also separately for the $\tau_{lep}\tau_{had}$ and$\tau_{had}\tau_{had}$ channels.

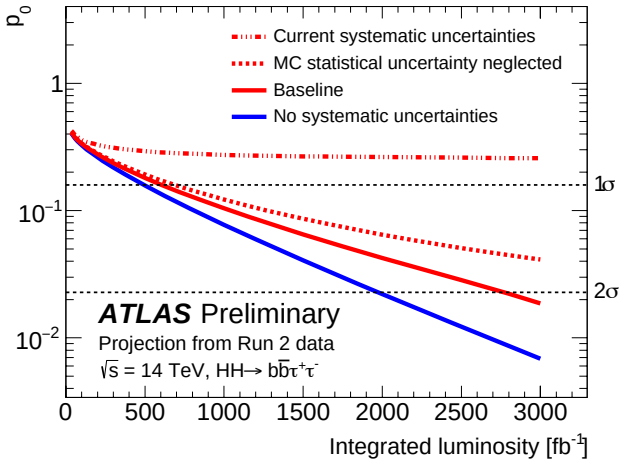

Figure 7.14: Expected significance, and p_0, of the discrepancy from the background-only hypothesis when the predicted SM di-Higgs signal is injected as a function of the integrated luminosity for each extrapolation scenario.

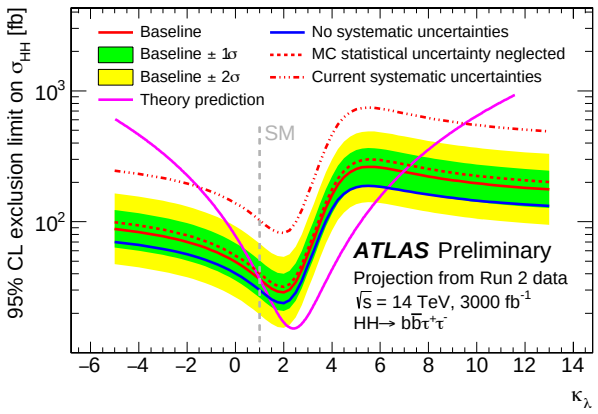

Figure 7.15: Expected and observed upper limits on the non-resonant di-Higgs production cross section as a function of k_λ. The yellow and green bands represent the $\pm 2\sigma$ and $\pm 1\sigma$ variations about the expected limit. The theoretical prediction of the cross section as a function of k_λ with $k_t = 1$ is also shown.

CHAPTER 8

Search for third generation scalar leptoquarks in the $b\tau_{had}b\tau_{had}$ channel

This chapter describes the search for pair production of third generation scalar leptoquarks (LQ_3) in the $b\tau_{had}b\tau_{had}$ channel, where each LQ_3 decays into a b-quark and a τ-lepton which then decays hadronically. This analysis is based on the ATLAS Run 2 di-Higgs analysis described in Chapter 6, as the final state is the same, but it is optimised for the search of a leptoquark signal. Here the differences with respect to the di-Higgs analysis in the event selection, signal LQ_3 candidates reconstruction and multivariate analysis developed in this thesis are described. The same fit strategy and statistical model as the ones developed within this thesis for the di-Higgs search are used.

The results of the search in the $b\tau_{had}b\tau_{had}$ channel described here are combined with the ones obtained in the $b\tau_{lep}b\tau_{had}$ channel. The combined $b\tau b\tau$ results are presented as upper limits on the production cross section of pairs of scalar leptoquarks as a function of the leptoquark mass assuming a BR (B) into charged leptons (τ) of $B = 1$ and also as limits on the branching ratio into charged leptons as a function of the leptoquark mass. They are part of the ATLAS Run 2 search for third generation scalar leptoquarks and the $b\tau b\tau$ combined results are reported here and published in Reference [13], together with the results from four reinterpretations of ATLAS searches for supersymmetric particles to pair production of leptoquark searches covering all possible decays of the pair-produced LQ_3^u and LQ_3^d into a quark (t, b) and a lepton (τ, ν) of the third generation.

8.1 Data and Monte Carlo samples

Data and MC background samples used by this analysis are the same described in Section 6.1 for the $HH \to bb\tau_{had}\tau_{had}$ analysis.

8.1.1 Signal samples

Signal samples of pair-produced up-type and down-type scalar LQ_3 were generated at next-to-leading order in QCD with MadGraph5_aMC@NLO [67] using the NNPDF3.0 NNLO [141] PDFs and interfaced with Pythia 8 [71] using the A14 set of tuned parameters [107] for the parton shower and hadronisation. The decay of the LQ_3 is simulated using MadSpin [108]. The leptoquark signal production cross sections are assumed to be the same as the ones derived from calculations of direct top-squark pair production [142], as both are massive, coloured, scalar particles with the same production modes. The calculations are at NLO plus next-to-leading-logarithm accuracy, with uncertainties determined by

variations of factorisation and renormalisation scales, α_s and PDF variations.

There are three parameters to be set in the leptoquark signal simulation: the coupling parameter λ, the model parameter β and the mass of the leptoquark m_{LQ}. The coupling to the charged lepton (τ) is given by $\sqrt{\beta}\lambda$ and the coupling to the τ-neutrino by $\sqrt{1-\beta}\lambda$. The parameter λ is set to 0.3, resulting in a LQ width of about 0.2% of its mass, and β is set to 1 such that each leptoquark decays into a b-quark and a τ-lepton, having a branching ratio to the charged lepton $B = 1$. The signal samples are generated for leptoquark masses ranging from 200 GeV to 1.5 TeV: 200, 225, 250, 275, 300, 325, 350, 400, 450, 500, 550, 600, 700, 800, 900, 1000, 1100, 1200, 1300, 1400 and 1500 GeV.

8.2 Object selection

Objects arising from the pp collision products are reconstructed in ATLAS as described in Chapter 5. In the $LQ_3LQ_3 \to b\tau b\tau$ analysis presented here the same reconstruction and identification criteria described in Section 6.2 for the $HH \to bb\tau\tau$ analysis are used.

8.3 Event selection

An event selection is applied in order to select events compatible with containing a $b\tau^+_{had}b\tau^-_{had}$ final state. All selections are the same as the ones described in Section 6.3 for the di-Higgs analysis except:

- for DTT events the leading $\tau_{had-vis}$ p_{T} threshold is increased to 60 GeV (instead of 40 GeV);
- the $m^{MMC}_{\tau\tau}$ threshold of 60 GeV is removed;
- exactly one or two jets must be b-tagged.

Events are split into two categories according to the multiplicity of b-tagged jets, forming two orthogonal signal regions with one or two b-tagged jets respectively. The acceptance times efficiency of this selection for up-type and down-type LQ_3 as a function of the LQ mass is shown in Figure 8.1. The analysis was optimised for the up-type leptoquark signal $LQ^u_3LQ^u_3 \to b\tau b\tau$, but signal events from the down-type LQ signal enter the signal regions as well. The sensitivity to the down-type leptoquark decay channel is due to the final state $t\tau t\tau \to Wb\tau Wb\tau$ where the W bosons decay into jets. Since this analysis does not veto additional jets it is sensitive to this decay chain.

The 1 b-tag signal region is included in this analysis, differently from the di-Higgs analysis, because it significantly improves the signal acceptance times efficiency at high LQ masses above 500 GeV as shown in Figure 8.1. This is due to the decrease in b-tagging efficiency for high-p_{T} jets coming from the decay of a high mass LQ. Jets from the leptoquark decay have p_{T} spectra peaking around 300 GeV and 800 GeV for leptoquark masses of 500 GeV and 1500 GeV respectively. The inclusion of the 1 b-tag signal region was not as important in the di-Higgs analysis because jets coming from the decay of a heavy resonance, through its decay into a SM Higgs boson pair, have p_{T} spectra peaking around 300 GeV for a resonance with a mass of 1000 GeV (which is the highest mass tested).

8.4 Signal LQ candidates reconstruction: b-τ pairing

As the signal process in this analysis is $LQ_3LQ_3 \to b\tau b\tau$, it is necessary to define a strategy to correctly identify which b-jet and τ-lepton would originate from the same leptoquark and reconstruct the two LQ

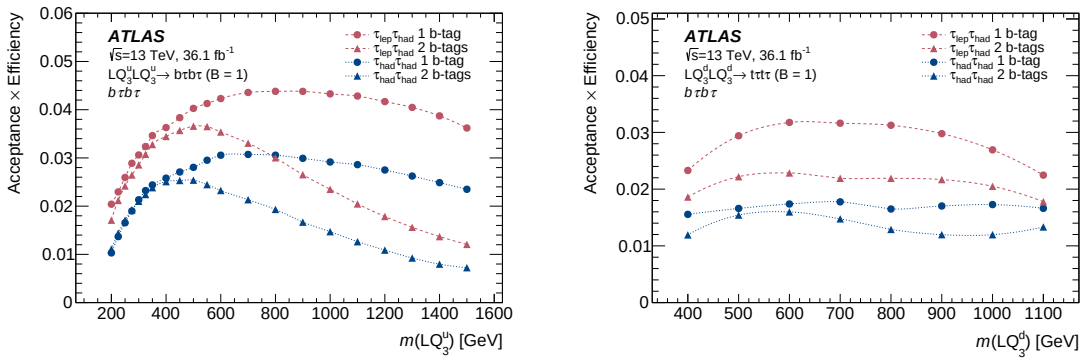

(a) (b)

Figure 8.1: Acceptance times efficiency of the $b\tau^+_{had}b\tau^-_{had}$ event selection (blue lines) for the a) $LQ^u_3LQ^u_3$ and b) $LQ^d_3LQ^d_3$ signals as a function of the LQ mass. Values for the $b\tau_{lep}b\tau_{had}$ event selection are also shown (red lines).

candidates. Several approaches were explored in this thesis work in order to identify the method that allows to correctly pair the final state particles in a most efficient way:

- pairing that minimises the quantity $|\Delta M(LQ1, LQ2)|$;
- pairing that minimises the quantity $|\Delta p_T(LQ1, LQ2)|$;
- pairing that minimises the quantity $|\pi - \Delta\Phi(LQ1, LQ2)|$;
- pairing that minimises the quantity $|\pi - \Delta R(\tau, jet)_{LQ1}| + |\pi - \Delta R(\tau, jet)_{LQ2}|$;
- pairing that maximises the quantity $\Delta R(\tau, jet)_{LQ1} + \Delta R(\tau, jet)_{LQ2}$.

$LQ1$ and $LQ2$ are the two reconstructed leptoquark candidates, with $LQ1$ being the one to which the leading p_{T} τ-lepton is associated. In the 2 b-tags region the two b-tagged jets are considered to be the ones coming from the LQs, while in the 1 b-tag region the b-tagged jet and the second jet with the highest p_{T} are chosen. The tested pairing methods exploit the information that the two LQs should have the same mass and therefore also the same p_{T} and they are expected to be back-to-back. These methods are tested and compared in this thesis by measuring the efficiency of correctly pairing the b-jet and τ-lepton originating from the same LQ using truth-information available in the signal MC samples. Figure 8.2 shows the efficiency of correctly pairing the b-jet and τ-lepton originating from the same LQ as a function of the LQ mass using the different pairing methods. It is found that the pairing that minimises the difference between the invariant masses of the two reconstructed LQ candidates has the best recontruction efficiency over the full mass range in the 1 b-tag region and up to masses of 1 TeV in the 2 b-tags region. For masses above 1 TeV it has performance comparable to the ones obtained using pairing methods based on ΔR information. Thus, the minimum ΔM method is used for pairing the τ-leptons and the b-jets in order to reconstruct the two LQ candidates.

8.5 Background estimation

The background estimation for this analysis uses the same methods as used in the di-Higgs analysis and described in Section 6.4. For the estimation of the multi-jet background and of the $t\bar{t}$ background

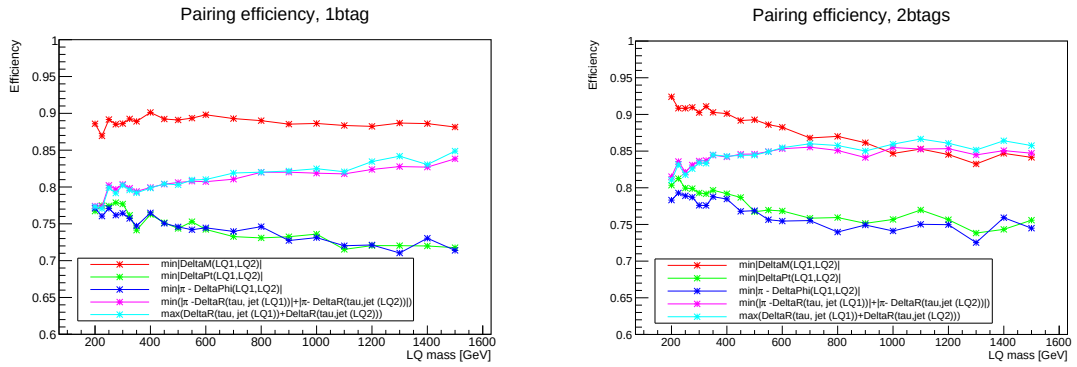

(a) (b)

Figure 8.2: Efficiency of correctly pairing the b-jet and τ-lepton originating from the same LQ_3^u as a function of the LQ mass using the different pairing methods.

with fake-τ_{had}, the fake-factors and the fake-rates from data were re-derived and applied using the event selection dedicated to this analysis.

8.6 Multivariate analysis

The $LQ_3LQ_3 \rightarrow b\tau b\tau$ analysis uses BDTs to separate the signal from the total expected background. The BDT training for the $b\tau_{had}b\tau_{had}$ channel analysis was developed in this thesis work. It is performed following the same strategy and using the same settings adopted in the di-Higgs analysis and described in Section 6.5. BDTs are trained targeting each LQ_3^u mass point considered in the analysis, separately in the 1 b-tag and 2 b-tags regions. The choice of the BDT input variables is the outcome of an optimisation procedure performed in this thesis according to the same criteria used for the di-Higgs analysis. The final list of BDT inputs consists of five variables:

- $\Delta R(\tau, jet)_{LQ1}$: the ΔR between the leading p_{T} τ-lepton and the jet associated with the same reconstructed $LQ1$ candidate;
- S_T: the scalar sum of the missing tranverse energy, the p_{T} of the two τ-leptons and of the two jets associated with the reconstructed LQ candidates in the event;
- E_T^{miss} Φ centrality: variable that quantifies the angular position in Φ of the E_T^{miss} with respect to the two τ-leptons;
- $m_{(\tau,jet)_{LQ1}}$: the invariant mass of the reconstructed $LQ1$ candidate from the leading p_{T} τ-lepton and its paired jet;
- p_T^{τ}: p_{T} of the leading τ-lepton.

The BDT input variables distributions for a $LQ_3^uLQ_3^u$ signal with $m_{LQ} = 500$ GeV and for the background are shown in Figure 8.3 for the 1 b-tag region and Figure 8.5 for the 2 b-tags region. Their linear correlation coefficients are shown in Figure 8.4 for the 1 b-tag region and Figure 8.6 for the 2 b-tags region. The results of the BDT trainings for the $LQ_3^uLQ_3^u$ signal with $m_{LQ} = 500$ GeV are shown in Figure 8.7.

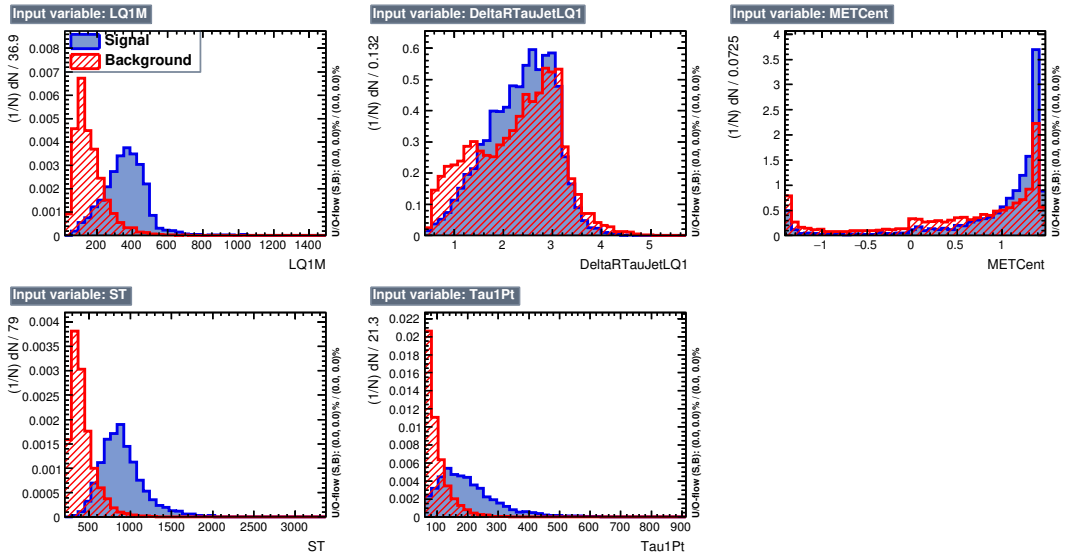

Figure 8.3: BDT input variables distributions for the LQ_3^u signal with $m_{LQ} = 500$ GeV (blue) and for the background (red) in the 1 b-tag region.

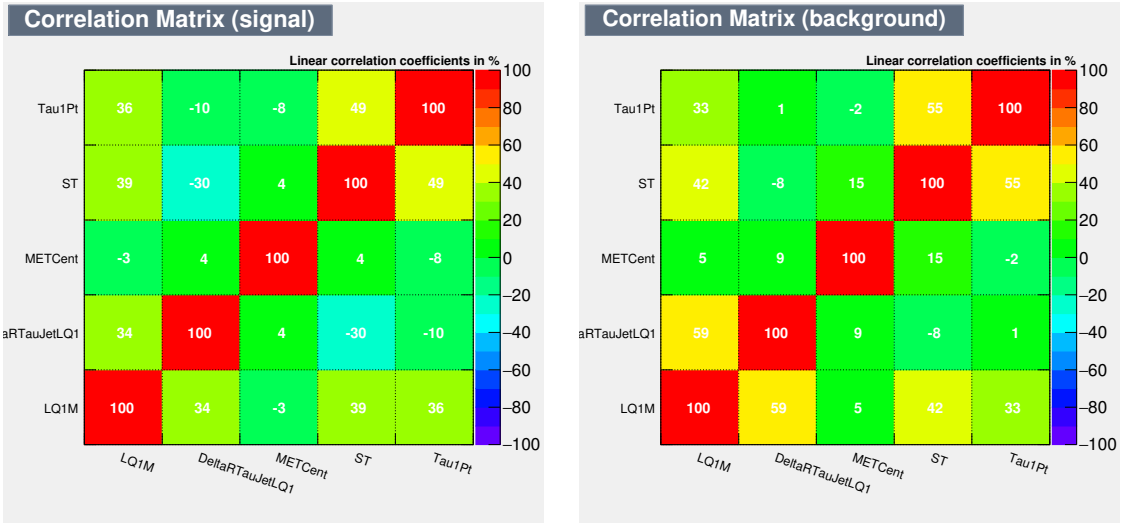

(a) (b)

Figure 8.4: BDT input variables linear correlation coefficients for a) the LQ_3^u signal with $m_{LQ} = 500$ GeV b) the background in the 1 b-tag region.

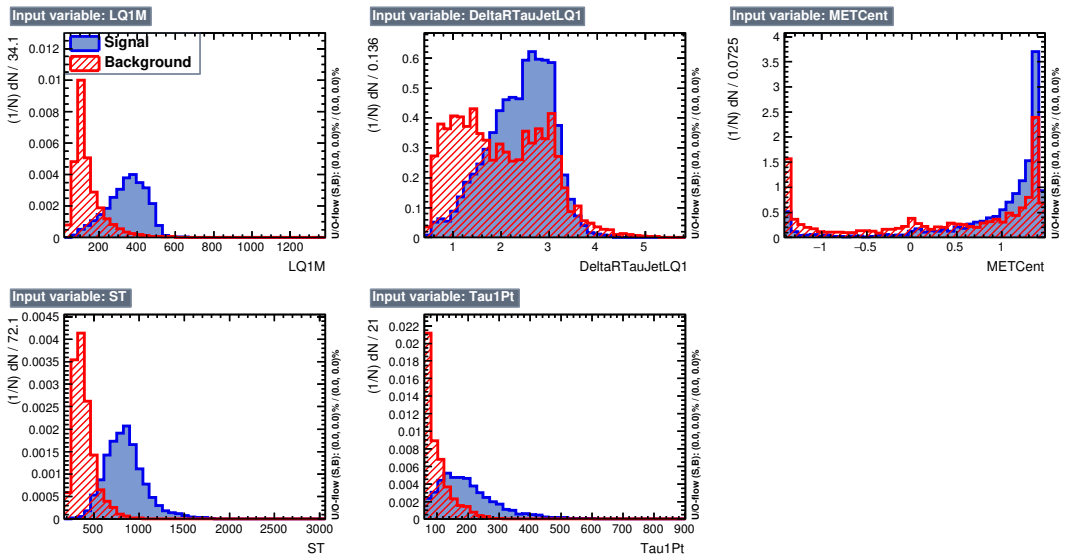

Figure 8.5: BDT input variables distributions for the LQ_3^u signal with m_{LQ} = 500 GeV (blue) and for the background (red) in the 2 b-tags region.

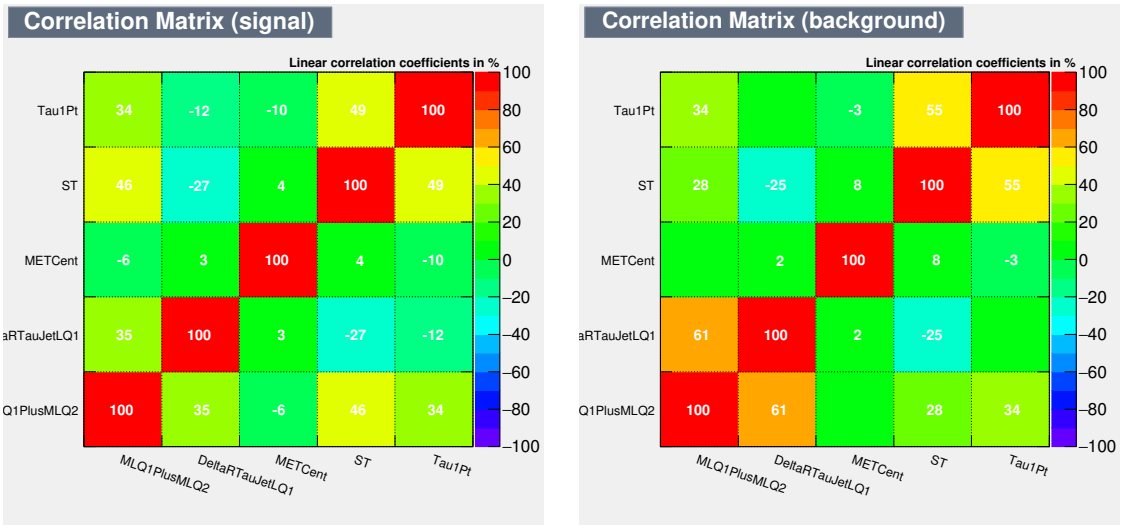

(a) (b)

Figure 8.6: BDT input variables linear correlation coefficients for a) the LQ_3^u signal with m_{LQ} = 500 GeV b) the background in the 2 b-tags region.

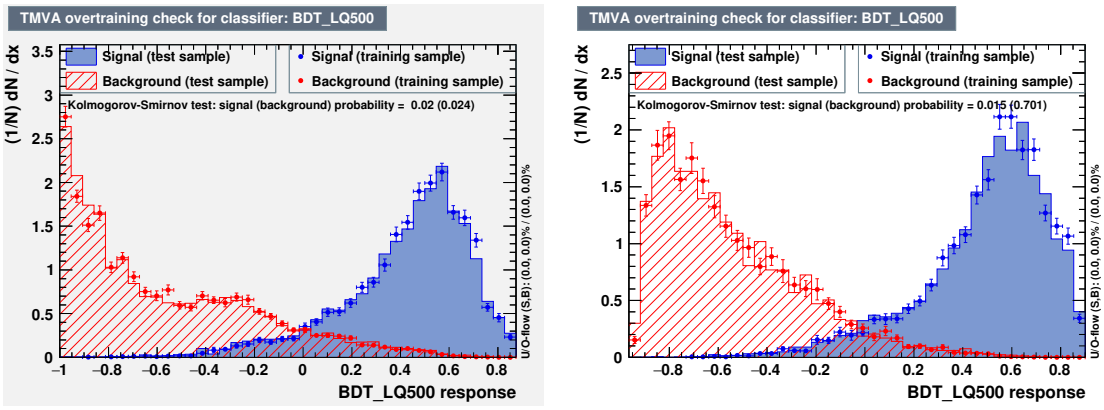

(a) (b)

Figure 8.7: BDT score distributions for the LQ_3^u signal with m_{LQ} = 500 GeV (blue) and the background (red) in a) in the 1 b-tag region and b) the 2 b-tags region.

The BDT input variables distributions, their linear correlation matrices and the BDT scores for other BDT trainings used in the analysis are included in Appendix F.

The BDT score distributions are used as final discriminant variables in the statistical analysis as done in the di-Higgs analysis and described in Section 6.7.

8.7 Systematic uncertainties

The same experimental systematic uncertainties as for the di-Higgs search described in Section 6.6 are considered in this analysis.

The modelling uncertainties were re-derived for this analysis using the same methods described for the di-Higgs analysis. Particularly, here the shape uncertainties on the $t\bar{t}$ background are parameterised as a function of the S_T variable and the shape uncertainties on the Z + heavy flavour background are parameterised as a function of the m_{LQ1}, as those variables show the strongest variation. The uncertainties on the data-driven fake-τ_{had} backgrounds are also re-computed using the same methods adopted in the di-Higgs analysis. In the di-Higgs analysis the non-closure systematic uncertainty on the multi-jet background was computed in the 1 b-tag OS validation region and the shape was parameterised as a function of m_{HH}. As in this analysis the 1 b-tag region is a signal region, this uncertainty is derived here in the 0 b-tags validation region and it is parametersied as a function of the m_{LQ1} which is showing the strongest non-closure shape.

8.8 Results

The fit strategy follows the one of the di-Higgs analysis described in Section 6.7 for the $\tau_{had}\tau_{had}$ channel and 7.1 for the combination with the $\tau_{lep}\tau_{had}$ channel. The BDT output score is used as the discriminating variable for all channels and signal hypotheses in a combined fit of all signal and control regions. The data are found to be consistent with the background-only predictions, as can be seen in Figure 8.8 showing as an example the post-fit BDT score distribution for the LQ_3^u signal with a mass of m_{LQ} = 400 GeV in the $\tau_{had}\tau_{had}$ 1 b-tag and 2 b-tags signal regions. Thus, the data are used to set upper limits on the LQ_3LQ_3 production cross section. The analysis was optimised for the up-type leptoquark signal $LQ_3^uLQ_3^u$, but

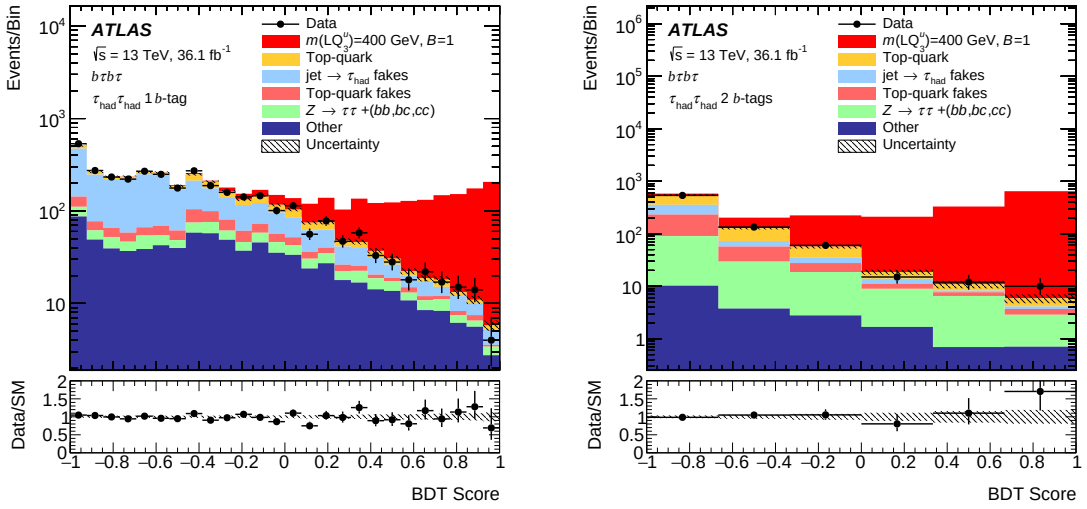

(a) (b)

Figure 8.8: Post-fit distributions of the BDT score for the LQ_3^u signal with a mass of $m_{LQ} = 400$ GeV in the $\tau_{had}\tau_{had}$ a) 1 b-tag and b) 2 b-tags signal regions. All background components are scaled to their normalisations as determined in the fit. The pre-fit normalisation of the sum of all background components predicted by the simulated events is given by the dashed blue line. The LQ_3^u signal distribution is also shown with a normalisation given by the expected cross section. The shaded bands represent the total post-fit uncertainty with NPs profiled to the data.

as signal events from the down-type leptoquark signal enter the signal regions as well, upper limits are set on the cross section for both up-type and down-type leptoquark pair production. Figure 8.9 shows the expected and observed 95% CL upper limits on the cross section for scalar up-type and down-type leptoquark pair production as a function of the leptoquark mass for the combined $\tau_{had}\tau_{had}$ and $\tau_{lep}\tau_{had}$ channels. The theoretical prediction for the cross section of scalar leptoquark pair production is also shown, along with the uncertainties. From the comparison of the obtained upper limits to the theoretical predictions up-type LQs with masses below 1030 GeV and down-type LQs with masses below 930 GeV are excluded at 95% CL for the case of $B = 1$.

Limits are also set on the LQ decay BR into charged leptons as a function of the LQ mass, shown in Figure 8.10 for the $b\tau b\tau$ analysis and for the four reinterpretations of ATLAS searches for supersymmetric particles to pair production of leptoquark searches. Considering all channels, masses below 800 GeV are excluded for both LQ_3^u and LQ_3^d independently of the branching ratio.

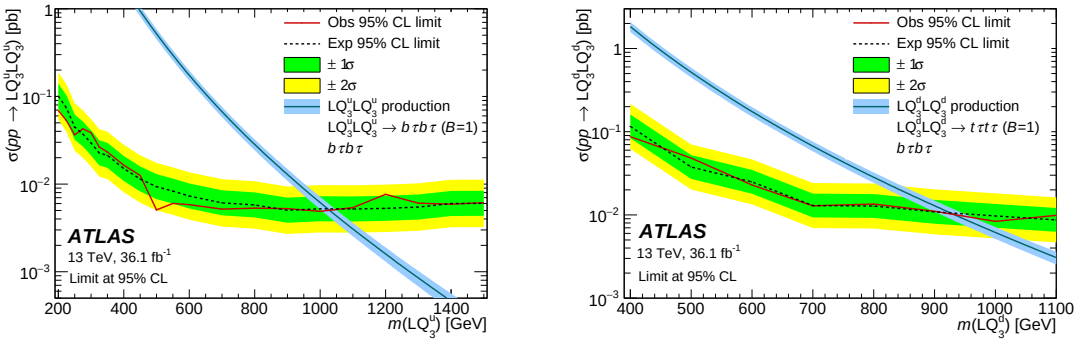

(a) (b)

Figure 8.9: Expected and observed $b\tau b\tau$ combined upper limits on the cross section for a) up-type and b) down-type scalar leptoquark pair production with $B = 1$ as a function of the leptoquark mass. The theoretical prediction for the cross section is also shown and the thickness of the theory curve represents the theoretical uncertainty from PDFs, renormalisation and factorisation scales, and the strong coupling constant α_s.

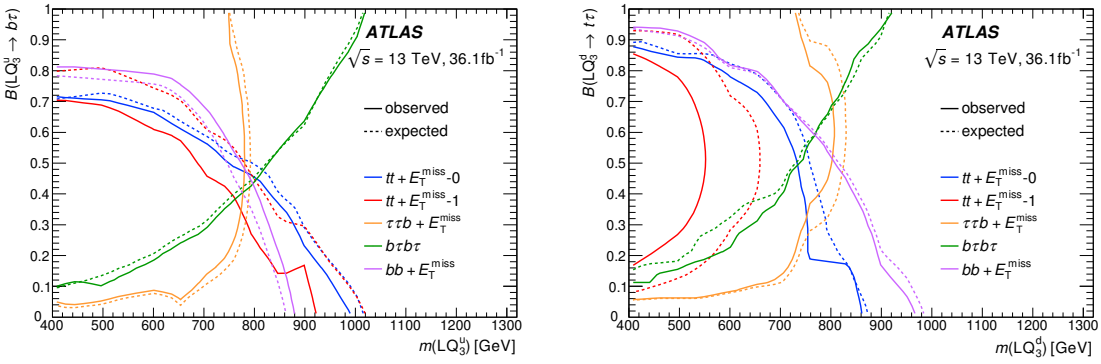

(a) (b)

Figure 8.10: Expected and observed limits on the branching ratio into charged leptons for scalar third-generation a) up-type and b) down-type leptoquark pair production as a function of the leptoquark mass. The region to the left of the contour lines is excluded at 95% confidence level.

CHAPTER 9

Summary

In this thesis a search for the Standard Model (SM) Higgs boson pair production and new physics phenomena in the $b\bar{b}\tau^{+}_{had}\tau^{-}_{had}$ channel, where both τ-leptons decay hadronically, is presented. The search uses 36.1 fb^{-1} of pp collisions data at a centre-of-mass energy of 13 TeV provided by the Large Hadron Collider (LHC) and recorded by the ATLAS experiment in 2015 and 2016.

The di-Higgs production process is searched both in the non-resonant and resonant modes to test the sensitivity to the SM di-Higgs production process and search for new physics that could manifest as modifications of the couplings involved in the non-resonant production, the triple Higgs self-coupling and the top-quark Yukawa coupling, or as production of a heavy resonance decaying into two Higgs bosons. The main challenges of this channel, which was never studied before by the ATLAS Collaboration, are the estimation of backgrounds with jets faking hadronically decaying τ-leptons and the optimisation of the signal-to-background separation to improve the sensitivity to small signals as the SM di-Higgs signal or possible BSM signals with small cross sections. The complete di-Higgs analysis in this channel was developed in this thesis work, with focus on the implementation and validation of data-driven methods for the estimation of backgrounds with fake-τ_{had}, the development of the multivariate analysis, fit strategy and the statistical interpretation. The results from the non-resonant analysis performed in this thesis are interpreted in the context of the SM di-Higgs production as an upper limit on the cross section and as upper limits on the cross section as a function of the varied triple Higgs self-coupling and top-quark Yukawa coupling to set constraints on them. The observed (expected) upper limit is 16.4 (17.4) times the SM expectation, assuming SM couplings, and it is the world best upper limit on this process obtained from a single decay channel analysis up to date. The CMS Collaboration obtained in the same decay channel, using a dataset of the same size, an observed (expected) upper limit on the cross section of 52 (34) times the SM expectation, adopting a cut-based approach to define the signal region and using the M_{T2} variable as final discriminant [143]. The best sensitivity obtained in this channel with the analysis developed in this thesis is the result of the use of Boosted Decision Trees to separate signal and background and of the use of the BDT score distribution as final discriminant for the statistical analysis. The allowed intervals at 95% CL obtained in this thesis work for the analysed Higgs boson couplings are $-9 < k_\lambda < 17$, assuming $k_t = 1$, and $-1.7 < k_t < 2$, assuming $k_\lambda = 1$. The results of the search for resonant di-Higgs production performed in this thesis are presented as exclusion limits on the cross section times $bb\tau\tau$ BR as a function of the resonance mass for a narow width scalar X of the two-Higgs-doublet model (2HDM) and for the Randall-Sundrum (RS) graviton G_{KK} with $k/\bar{M}_{Pl} = 1$ and $k/\bar{M}_{Pl} = 2$. For scalar resonances, the results are interpreted in a simplified minimal supersymmetric model, the MSSM: the mass range 329 GeV $< m_X <$ 376 GeV is excluded at 95% CL for $\tan\beta = 2$, where $\tan\beta$ is the ratio of the vacuum expectation values of the scalar doublets. Randall-Sundrum

gravitons are excluded at 95% CL in the mass range 334 GeV $< m_{G_{KK}} <$ 839 GeV assuming $k/\bar{M}_{Pl} = 1$. In the case of $k/\bar{M}_{Pl} = 2$, the full tested mass range, 260 GeV $< m_{G_{KK}} <$ 1000 GeV, is excluded.

The results from the $bb\tau_{had}\tau_{had}$ channel are combined in this thesis with the ones from the $bb\tau_{lep}\tau_{had}$ channel to provide the final $bb\tau\tau$ results published by the ATLAS Collaboration in Reference [7]. The $bb\tau\tau$ combined observed (expected) upper limit is 12.7 (14.8) times the SM expectation and the allowed intervals at 95% CL for the couplings are $-7 < k_\lambda < 16$, assuming $k_t = 1$, and $-1.6 < k_t < 1.8$, assuming $k_\lambda = 1$. For scalar resonances the mass range 305 GeV $< m_X <$ 402 GeV is excluded at 95% CL for the MSSM with $\tan\beta = 2$. Randall-Sundrum gravitons are excluded at 95% CL in the mass range 325 GeV $< m_{G_{KK}} <$ 885 GeV assuming $k/\bar{M}_{Pl} = 1$. Most of the $bb\tau\tau$ combined sensitivity comes from the $bb\tau_{had}\tau_{had}$ channel in the non-resonant analysis and in the resonant analysis for all considered models for masses below 700 GeV, while in the high mass region the two sub-channels have comparable sensitivities.

Furthermore, the $bb\tau\tau$ results are combined with the results from the $bbbb$ and $bb\gamma\gamma$ channels and the results are published by the ATLAS Collaboration in Reference [8]. In the non-resonant analysis the observed (expected) limit on the di-Higgs production cross section corresponds to 6.7 (10.4) times the SM expectation and the triple Higgs self-coupling is constrained to $-5 < k_\lambda < 12.1$, results driven by the sensitivity of the $bb\tau\tau$ channel and currently the world most stringent constraints on the di-Higgs production cross section and on the anomalous Higgs self-coupling to date. In the resonant analysis, for scalar resonances the mass range 260 GeV $< m_X <$ 462 GeV is excluded at 95% CL for the MSSM with $\tan\beta = 2$. Randall-Sundrum gravitons are excluded at 95% CL in the mass range 307 GeV $< m_{G_{KK}} <$ 1362 GeV assuming $k/\bar{M}_{Pl} = 1$. In the case of $k/\bar{M}_{Pl} = 2$, the mass range 260 GeV $< m_{G_{KK}} <$ 1744 GeV is excluded. The $bb\tau\tau$ channel, together with the $bbbb$ channel, is most sensitive in the mass region between 400 GeV and 600 GeV, while the $bb\gamma\gamma$ and $bbbb$ are most sensitive in the low mass and high mass regions respectively.

Moreover, a prospect study for the non-resonant di-Higgs search is performed in the $bb\tau\tau$ channel in this thesis and combined with the prospects of the other two di-Higgs most sensitive decay channels ($bbbb$ and $bb\gamma\gamma$) assuming 3 000 fb^{-1} at $\sqrt{s} = 14$ TeV expected to be collected at the HL-LHC. The results of these studies, published by the ATLAS Collaboration in Reference [9] and by the Physics of the HL-LHC Working Group Collaboration in Reference [10], show that the SM di-Higgs production can possibly be observed at the LHC with a significance of 3σ and that significant constraints on the value of the triple Higgs self-coupling can be set. Further improvements of the sensitivity are possible with the ongoing work on the optimisation of the di-Higgs searches, currently being performed using the full Run 2 available data statistics, exploiting improvements in the objects reconstruction and identification and exploring new multivariate methods.

In addition to the non-resonant and resonant di-Higgs searches, pair production of third generation scalar leptoquarks is also searched for in this thesis in the $b\tau_{had}b\tau_{had}$ final state, with an analysis based on the di-Higgs one as the final state is the same. The results of this search are combined with the ones from the $b\tau_{lep}b\tau_{had}$ channel and are published by the ATLAS Collaboration in Reference [13]. Up-type leptoquarks with masses below 1030 GeV and down-type leptoquarks with masses below 930 GeV are excluded at 95% CL assuming a branching ratio to charged leptons of 100%. Similar results are obtained by the CMS Collaboration, using a dataset of the same size, excluding leptoquarks with masses below 1020 GeV [144].

Bibliography

[1] LHC Higgs Cross Section Working Group web page, (2016), URL: https://twiki.cern.ch/twiki/bin/view/LHCPhysics/LHCHXSWG (cit. on pp. 1, 17, 18, 85).

[2] LHC Higgs Cross Section Working Group, *Handbook of LHC Higgs Cross Sections: 4. Deciphering the Nature of the Higgs Sector*, CERN Yellow Reports: Monographs (2016), URL: http://cds.cern.ch/record/2227475 (cit. on pp. 1, 16, 18, 64, 85).

[3] S. Borowka et al., *Higgs Boson Pair Production in Gluon Fusion at Next-to-Leading Order with Full Top-Quark Mass Dependence*, Phys. Rev. Lett. **117** (1 2016) 012001, URL: https://link.aps.org/doi/10.1103/PhysRevLett.117.012001 (cit. on pp. 1, 18, 60, 85).

[4] S. Borowka et al., *Full top quark mass dependence in Higgs boson pair production at NLO*, Journal of High Energy Physics **2016** (2016) 107, ISSN: 1029-8479, URL: https://doi.org/10.1007/JHEP10(2016)107 (cit. on pp. 1, 18, 60, 85).

[5] CMS Collaboration, *Search for Higgs boson pair production in the $bb\tau\tau$ final state in proton-proton collisions at $\sqrt{(s)} = 8$ TeV*, Phys. Rev. **D96** (2017) 072004, arXiv: 1707.00350 [hep-ex] (cit. on p. 2).

[6] ATLAS Collaboration, *Searches for Higgs boson pair production in the $hh \to bb\tau\tau, \gamma\gamma WW^*, \gamma\gamma bb, bbbb$ channels with the ATLAS detector*, Phys. Rev. **D92** (2015) 092004, arXiv: 1509.04670 [hep-ex] (cit. on p. 2).

[7] ATLAS Collaboration, *Search for resonant and non-resonant Higgs boson pair production in the $b\bar{b}\tau^+\tau^-$ decay channel in pp collisions at $\sqrt{s} = 13$ TeV with the ATLAS detector*, Phys. Rev. Lett. **121** (2018) 191801, arXiv: 1808.00336 [hep-ex] (cit. on pp. 2, 59, 103, 134).

[8] ATLAS Collaboration, *Combination of searches for Higgs boson pairs in pp collisions at 13 TeV with the ATLAS experiment.*, tech. rep. ATLAS-CONF-2018-043, CERN, 2018, URL: http://cds.cern.ch/record/2638212 (cit. on pp. 2, 103, 134).

[9] ATLAS Collaboration, *Measurement prospects of the pair production and self-coupling of the Higgs boson with the ATLAS experiment at the HL-LHC*, tech. rep. ATL-PHYS-PUB-2018-053, CERN, 2018, URL: http://cds.cern.ch/record/2652727 (cit. on pp. 2, 103, 134).

[10] M. Cepeda et al., *Higgs Physics at the HL-LHC and HE-LHC*, (2019), arXiv: 1902.00134 [hep-ph] (cit. on pp. 2, 103, 134).

[11] CMS Collaboration, *Search for pair production of third-generation scalar leptoquarks and top squarks in proton–proton collisions at $\sqrt{s}$=8 TeV*, Phys. Lett. **B739** (2014) 229, arXiv: 1408.0806 [hep-ex] (cit. on p. 2).

[12] ATLAS Collaboration, *Search for third generation scalar leptoquarks in pp collisions at $\sqrt{s} = 7$ TeV with the ATLAS detector*, JHEP **06** (2013) 033, arXiv: 1303.0526 [hep-ex] (cit. on p. 2).

[13] ATLAS Collaboration, *Searches for third-generation scalar leptoquarks in $\sqrt{s}$ = 13 TeV pp collisions with the ATLAS detector*, (2019), arXiv: 1902.08103 [hep-ex] (cit. on pp. 2, 123, 134).

[14] S. L. Glashow, *Partial Symmetries of Weak Interactions*, Nucl. Phys. **22** (1961) 579 (cit. on p. 5).

[15] S. Weinberg, *A Model of Leptons*, Phys. Rev. Lett. **19** (1967) 1264 (cit. on p. 5).

[16] A. Salam, *Weak and Electromagnetic Interactions*, Conf. Proc. **C680519** (1968) 367 (cit. on p. 5).

[17] P. W. Higgs, *Broken Symmetries and the Masses of Gauge Bosons*, Phys. Rev. Lett. **13** (1964) 508 (cit. on p. 5).

[18] P. W. Higgs, *Spontaneous Symmetry Breakdown without Massless Bosons*, Phys. Rev. **145** (1966) 1156 (cit. on p. 5).

[19] F. Englert and R. Brout, *Broken Symmetry and the Mass of Gauge Vector Mesons*, Phys. Rev. Lett. **13** (1964) 321 (cit. on p. 5).

[20] C. Patrignani et al., *Review of Particle Physics*, Chin. Phys. **C40** (2016) 100001 (cit. on pp. 5, 16, 19).

[21] ATLAS Collaboration, *Observation of a new particle in the search for the Standard Model Higgs boson with the ATLAS detector at the LHC*, Phys. Lett. B **716** (2012) 1, URL: https://cds.cern.ch/record/1471031 (cit. on pp. 5, 15).

[22] CMS Collaboration, *Observation of a new boson at a mass of 125 GeV with the CMS experiment at the LHC*, Phys. Lett. B **716** (2012) 30, URL: https://cds.cern.ch/record/1471016 (cit. on pp. 5, 15).

[23] D. Galbraith, *UX: Standard Model of the Standard Model*, (2012), URL: http://davidgalbraith.org/portfolio/ux-standard-model-of-the-standard-model/ (cit. on p. 7).

[24] J. Ellis, *Illustration of the Higgs potential*, (2017), URL: https://cds.cern.ch/record/1638469/files/higgspotential.png (cit. on p. 12).

[25] ATLAS and CMS Collaborations, *Combined Measurement of the Higgs Boson Mass in pp Collisions at $\sqrt{s}$ = 7 and 8 TeV with the ATLAS and CMS Experiments*, Phys. Rev. Lett. **114** (2015) 191803, arXiv: 1503.07589 [hep-ex] (cit. on p. 15).

[26] ATLAS Collaboration, *Evidence for the spin-0 nature of the Higgs boson using ATLAS data*, Phys. Lett. **B726** (2013) 120, arXiv: 1307.1432 [hep-ex] (cit. on p. 15).

[27] ATLAS Collaboration, *Measurements of Higgs boson production and couplings in the four-lepton channel in pp collisions at center-of-mass energies of 7 and 8 TeV with the ATLAS detector*, Phys. Rev. **D91** (2015) 012006, arXiv: 1408.5191 [hep-ex] (cit. on p. 15).

[28] ATLAS Collaboration, *Measurements of Higgs boson production and couplings in diboson final states with the ATLAS detector at the LHC*, Phys. Lett. **B726** (2013) 88, [Erratum: Phys. Lett.B734,406(2014)], arXiv: 1307.1427 [hep-ex] (cit. on p. 15).

[29] ATLAS Collaboration,
Observation and measurement of Higgs boson decays to WW^* with the ATLAS detector,
Phys. Rev. D **92** (2014) 012006. 84 p, URL: https://cds.cern.ch/record/1975394
(cit. on p. 15).

[30] ATLAS Collaboration, *Observation of Higgs boson production in association with a top quark pair at the LHC with the ATLAS detector*, Phys. Lett. B **784** (2018) 173,
URL: https://cds.cern.ch/record/2621167 (cit. on p. 15).

[31] ATLAS Collaboration,
Observation of $H \to b\bar{b}$ decays and VH production with the ATLAS detector,
Phys. Lett. **B786** (2018) 59, arXiv: 1808.08238 [hep-ex] (cit. on p. 15).

[32] ATLAS Collaboration, *Cross-section measurements of the Higgs boson decaying into a pair of τ-leptons in proton-proton collisions at $\sqrt{s} = 13$ TeV with the ATLAS detector*, (2018),
arXiv: 1811.08856 [hep-ex] (cit. on p. 15).

[33] B. Dumont, K. Nishiwaki and R. Watanabe,
LHC constraints and prospects for S_1 scalar leptoquark explaining the $\overline{B} \to D^{(*)}\tau\overline{\nu}$ anomaly,
Phys. Rev. D **94** (3 2016) 034001,
URL: https://link.aps.org/doi/10.1103/PhysRevD.94.034001 (cit. on pp. 22, 26).

[34] LHCb Collaboration, *Test of Lepton Universality Using $B^+ \to K^+\ell^+\ell^-$ Decays*,
Phys. Rev. Lett. **113** (15 2014) 151601,
URL: https://link.aps.org/doi/10.1103/PhysRevLett.113.151601
(cit. on pp. 22, 26).

[35] S. P. Martin, *A Supersymmetry primer*,
(1997) 1, [Adv. Ser. Direct. High Energy Phys.18,1(1998)], arXiv: hep-ph/9709356 [hep-ph]
(cit. on p. 22).

[36] A. Djouadi and J. Quevillon, *The MSSM Higgs sector at a high M_{SUSY}: reopening the low tanβ regime and heavy Higgs searches*, JHEP **10** (2013) 028, arXiv: 1304.1787 [hep-ph]
(cit. on p. 22).

[37] A. Djouadi et al., *The post-Higgs MSSM scenario: Habemus MSSM?*,
Eur. Phys. J. **C73** (2013) 2650, arXiv: 1307.5205 [hep-ph] (cit. on p. 22).

[38] G. C. Branco et al., *Theory and phenomenology of two-Higgs-doublet models*,
Phys. Rept. **516** (2012) 1, arXiv: 1106.0034 [hep-ph] (cit. on p. 23).

[39] Y.-X. Liu, "Introduction to Extra Dimensions and Thick Braneworlds", 2018 211,
arXiv: 1707.08541 [hep-th] (cit. on p. 24).

[40] L. Randall and R. Sundrum, *A Large mass hierarchy from a small extra dimension*,
Phys. Rev. Lett. **83** (1999) 3370, arXiv: hep-ph/9905221 [hep-ph] (cit. on p. 24).

[41] A. Oliveira, *Gravity particles from Warped Extra Dimensions, predictions for LHC*, (2014),
arXiv: 1404.0102 [hep-ph] (cit. on p. 25).

[42] I. Doršner et al., *Physics of leptoquarks in precision experiments and at particle colliders*,
Physics Reports **641** (2016) 1, ISSN: 0370-1573,
URL: http://www.sciencedirect.com/science/article/pii/S0370157316301314
(cit. on p. 26).

[43] W. Buchmuller, R. Ruckl and D. Wyler, *Leptoquarks in Lepton - Quark Collisions*,
Phys. Lett. **B191** (1987) 442, [Erratum: Phys. Lett.B448,320(1999)] (cit. on p. 26).

[44] M. Bauer and M. Neubert,
Minimal Leptoquark Explanation for the $R_{D^{(*)}}$, R_K , and $(g-2)_g$ Anomalies,
Phys. Rev. Lett. **116** (2016) 141802, arXiv: 1511.01900 [hep-ph] (cit. on p. 26).

[45] M. Tanaka and R. Watanabe, *New physics in the weak interaction of $\overline{B} \to D^{(*)}\tau\overline{\nu}$*,
Phys. Rev. D **87** (3 2013) 034028,
URL: https://link.aps.org/doi/10.1103/PhysRevD.87.034028 (cit. on p. 26).

[46] Y. Sakaki et al., *Testing leptoquark models in $\overline{B} \to D^{(*)}\tau\overline{\nu}$*, Phys. Rev. D **88** (9 2013) 094012,
URL: https://link.aps.org/doi/10.1103/PhysRevD.88.094012 (cit. on p. 26).

[47] I. Doršner et al.,
Minimally flavored colored scalar in $\overline{B} \to D^{(*)}\tau\overline{\nu}$ and the mass matrices constraints,
Journal of High Energy Physics **2013** (2013) 84, ISSN: 1029-8479,
URL: https://doi.org/10.1007/JHEP11(2013)084 (cit. on p. 26).

[48] B. Gripaios, M. Nardecchia and S. A. Renner,
Composite leptoquarks and anomalies in B-meson decays,
Journal of High Energy Physics **2015** (2015) 6, ISSN: 1029-8479,
URL: https://doi.org/10.1007/JHEP05(2015)006 (cit. on p. 26).

[49] S. Bifani et al., *Beauty quarks test lepton universality*, CERN COURIER (2018),
URL: https://cerncourier.com/beauty-quarks-test-lepton-universality/
(cit. on p. 26).

[50] ATLAS Collaboration, *ATLAS detector and physics performance: Technical Design Report, 1*,
Technical Design Report ATLAS, CERN, 1999,
URL: https://cds.cern.ch/record/391176 (cit. on pp. 29, 37).

[51] ATLAS Collaboration, *ATLAS detector and physics performance: Technical Design Report, 2*,
Technical Design Report ATLAS, CERN, 1999,
URL: https://cds.cern.ch/record/391177 (cit. on p. 29).

[52] ATLAS Collaboration, *The ATLAS Experiment at the CERN Large Hadron Collider*,
JINST **3** (2008) S08003 (cit. on pp. 29, 38).

[53] L. Evans and P. Bryant, *LHC Machine*, JINST **3** (2008) S08001 (cit. on pp. 29, 30).

[54] S. Chatrchyan et al., *The CMS Experiment at the CERN LHC*, JINST **3** (2008) S08004
(cit. on p. 29).

[55] K. Aamodt et al., *The ALICE experiment at the CERN LHC*, JINST **3** (2008) S08002
(cit. on p. 29).

[56] A. A. Alves Jr. et al., *The LHCb Detector at the LHC*, JINST **3** (2008) S08005 (cit. on p. 30).

[57] G. Anelli et al., *The TOTEM experiment at the CERN Large Hadron Collider*,
JINST **3** (2008) S08007 (cit. on p. 30).

[58] O. Adriani et al., *The LHCf detector at the CERN Large Hadron Collider*,
JINST **3** (2008) S08006 (cit. on p. 30).

[59] ATLAS Collaboration, *Luminosity Public Results*, URL: https:
//twiki.cern.ch/twiki/bin/view/AtlasPublic/LuminosityPublicResultsRun2
(cit. on p. 32).

[60] A. D. Rosso, *HL-LHC updates in Japan. Projet HL-LHC : une réunion fait le point au Japon*,
(2014) 4, URL: https://cds.cern.ch/record/1975962 (cit. on p. 33).

[61] J. C. Collins and D. E. Soper, *Parton Distribution and Decay Functions*, Nucl. Phys. **B194** (1982) 445 (cit. on p. 33).

[62] A. D. Martin et al., *Parton distributions for the LHC*, Eur. Phys. J. **C63** (2009) 189, arXiv: 0901.0002 [hep-ph] (cit. on pp. 33, 34).

[63] G. Altarelli and G. Parisi, *Asymptotic Freedom in Parton Language*, Nucl. Phys. **B126** (1977) 298 (cit. on p. 33).

[64] S. Agostinelli et al., *GEANT4: A Simulation toolkit*, Nucl. Instrum. Meth. **A506** (2003) 250 (cit. on pp. 36, 64).

[65] ATLAS Collaboration, *The ATLAS Simulation Infrastructure*, Eur. Phys. J. C **70** (2010) 823, URL: https://cds.cern.ch/record/1267853 (cit. on pp. 36, 64).

[66] J. Alwall et al., *MadGraph 5 : Going Beyond*, JHEP **06** (2011) 128, arXiv: 1106.0522 [hep-ph] (cit. on pp. 36, 60).

[67] J. Alwall et al., *The automated computation of tree-level and next-to-leading order differential cross sections, and their matching to parton shower simulations*, JHEP **07** (2014) 079, arXiv: 1405.0301 [hep-ph] (cit. on pp. 36, 60, 123).

[68] S. Alioli et al., *A general framework for implementing NLO calculations in shower Monte Carlo programs: the POWHEG BOX*, JHEP **06** (2010) 043, arXiv: 1002.2581 [hep-ph] (cit. on pp. 36, 63).

[69] T. Gleisberg et al., *Event generation with SHERPA 1.1*, JHEP **02** (2009) 007, arXiv: 0811.4622 [hep-ph] (cit. on pp. 36, 64).

[70] T. Sjostrand, S. Mrenna and P. Z. Skands, *PYTHIA 6.4 Physics and Manual*, JHEP **05** (2006) 026, arXiv: hep-ph/0603175 [hep-ph] (cit. on pp. 36, 64).

[71] T. Sjöstrand et al., *An Introduction to PYTHIA 8.2*, Comput. Phys. Commun. **191** (2015) 159, arXiv: 1410.3012 [hep-ph] (cit. on pp. 36, 60, 123).

[72] M. Bahr et al., *Herwig++ Physics and Manual*, Eur. Phys. J. **C58** (2008) 639, arXiv: 0803.0883 [hep-ph] (cit. on pp. 36, 60).

[73] D. J. Lange, *The EvtGen particle decay simulation package*, Nucl. Instrum. Meth. **A462** (2001) 152 (cit. on pp. 36, 64).

[74] J. Pequenao, "Computer generated image of the whole ATLAS detector", 2008, URL: https://cds.cern.ch/record/1095924 (cit. on p. 38).

[75] ATLAS Collaboration, *ATLAS magnet system: Technical Design Report, 1*, Technical Design Report ATLAS, CERN, 1997, URL: https://cds.cern.ch/record/338080 (cit. on p. 39).

[76] ATLAS Collaboration, *ATLAS inner detector: Technical Design Report, 1*, Technical Design Report ATLAS, CERN, 1997, URL: https://cds.cern.ch/record/331063 (cit. on p. 40).

[77] ATLAS Collaboration, *ATLAS inner detector: Technical Design Report, 2*, Technical Design Report ATLAS, CERN, 1997, URL: https://cds.cern.ch/record/331064 (cit. on p. 40).

[78] J. Pequenao, "Computer generated image of the ATLAS inner detector", 2008, URL: https://cds.cern.ch/record/1095926 (cit. on p. 41).

[79] ATLAS Collaboration, *ATLAS Insertable B-Layer Technical Design Report*, tech. rep. CERN-LHCC-2010-013. ATLAS-TDR-19, 2010, URL: https://cds.cern.ch/record/1291633 (cit. on p. 40).

[80] ATLAS Collaboration, *ATLAS calorimeter performance: Technical Design Report*, Technical Design Report ATLAS, CERN, 1996, URL: https://cds.cern.ch/record/331059 (cit. on p. 42).

[81] J. Pequenao, "Computer Generated image of the ATLAS calorimeter", 2008, URL: https://cds.cern.ch/record/1095927 (cit. on p. 42).

[82] ATLAS Collaboration, *ATLAS muon spectrometer: Technical Design Report*, Technical Design Report ATLAS, CERN, 1997, URL: https://cds.cern.ch/record/331068 (cit. on p. 44).

[83] ATLAS Collaboration, *Performance of the ATLAS Trigger System in 2015*, Eur. Phys. J. C **77** (2016) 317. 76 p, URL: https://cds.cern.ch/record/2235584 (cit. on p. 45).

[84] J. Pequenao, "Event Cross Section in a computer generated image of the ATLAS detector.", 2008, URL: https://cds.cern.ch/record/1096081 (cit. on p. 47).

[85] ATLAS Collaboration, *Performance of the ATLAS Track Reconstruction Algorithms in Dense Environments in LHC run 2*, Eur. Phys. J. C **77** (2017) 673. 44 p, URL: https://cds.cern.ch/record/2261156 (cit. on p. 48).

[86] R. Frühwirth, *Application of Kalman filtering to track and vertex fitting*, Nucl. Instrum. Methods Phys. Res., A **262** (1987) 444. 19 p, URL: https://cds.cern.ch/record/178627 (cit. on p. 48).

[87] ATLAS Collaboration, *Performance of primary vertex reconstruction in proton-proton collisions at $\sqrt{s}$ =7 TeV in the ATLAS experiment*, tech. rep. ATLAS-CONF-2010-069, CERN, 2010, URL: https://cds.cern.ch/record/1281344 (cit. on p. 48).

[88] R. Frühwirth, W. Waltenberger and P. Vanlaer, *Adaptive Vertex Fitting*, tech. rep. CMS-NOTE-2007-008, CERN, 2007, URL: https://cds.cern.ch/record/1027031 (cit. on p. 48).

[89] ATLAS Collaboration, *Electron efficiency measurements with the ATLAS detector using the 2015 LHC proton-proton collision data*, tech. rep. ATLAS-CONF-2016-024, CERN, 2016, URL: https://cds.cern.ch/record/2157687 (cit. on pp. 48, 49).

[90] W. Lampl et al., *Calorimeter Clustering Algorithms: Description and Performance*, tech. rep. ATL-LARG-PUB-2008-002. ATL-COM-LARG-2008-003, CERN, 2008, URL: https://cds.cern.ch/record/1099735 (cit. on p. 49).

[91] ATLAS Collaboration, *Muon reconstruction performance of the ATLAS detector in proton–proton collision data at $\sqrt{s}$=13 TeV*, Eur. Phys. J. C **76** (2016) 292. 45 p, URL: https://cds.cern.ch/record/2139897 (cit. on p. 49).

[92] ATLAS Collaboration, *Topological cell clustering in the ATLAS calorimeters and its performance in LHC Run 1*, Eur. Phys. J. C **77** (2016) 490. 87 p, URL: https://cds.cern.ch/record/2138166 (cit. on p. 50).

[93] M. Cacciari, G. P. Salam and G. Soyez, *The anti- k t jet clustering algorithm*, Journal of High Energy Physics **2008** (2008) 063, URL: http://stacks.iop.org/1126-6708/2008/i=04/a=063 (cit. on p. 50).

[94] ATLAS Collaboration, *Jet energy scale measurements and their systematic uncertainties in proton-proton collisions at $\sqrt{s}$ = 13 TeV with the ATLAS detector*, Phys. Rev. D **96** (2017) 072002. 36 p, URL: https://cds.cern.ch/record/2257300 (cit. on pp. 50, 82).

[95] ATLAS Collaboration, *Jet energy resolution in proton-proton collisions at $\sqrt{s}$ = 7 TeV recorded in 2010 with the ATLAS detector*, Eur. Phys. J. **C 73** (2013), URL: https://cds.cern.ch/record/1489592 (cit. on pp. 50, 82).

[96] ATLAS Collaboration, *Performance of b-jet identification in the ATLAS experiment*, Journal of Instrumentation **11** (2016) P04008, URL: http://stacks.iop.org/1748-0221/11/i=04/a=P04008 (cit. on pp. 51, 82).

[97] ATLAS Collaboration, *Optimisation of the ATLAS b-tagging performance for the 2016 LHC Run*, tech. rep. ATL-PHYS-PUB-2016-012, CERN, 2016, URL: https://cds.cern.ch/record/2160731 (cit. on pp. 51, 52).

[98] ATLAS Collaboration, *Evidence for the $H \to b\bar{b}$ decay with the ATLAS detector*, JHEP **12** (2017) 024. 68 p, URL: https://cds.cern.ch/record/2278245 (cit. on p. 53).

[99] ATLAS Collaboration, *Performance of missing transverse momentum reconstruction with the ATLAS detector using proton-proton collisions at $\sqrt{s}$ = 13 TeV*, tech. rep. CERN-EP-2017-274, CERN, 2018, URL: https://cds.cern.ch/record/2305380 (cit. on pp. 54, 82).

[100] ATLAS Collaboration, *Identification and energy calibration of hadronically decaying tau leptons with the ATLAS experiment in pp collisions at $\sqrt{s}$=8 TeV*, Eur. Phys. J. C **75** (2014) 303. 21 p, URL: https://cds.cern.ch/record/1978197 (cit. on p. 55).

[101] ATLAS Collaboration, *Reconstruction, Energy Calibration, and Identification of Hadronically Decaying Tau Leptons in the ATLAS Experiment for Run-2 of the LHC*, tech. rep. ATL-PHYS-PUB-2015-045, CERN, 2015, URL: https://cds.cern.ch/record/2064383 (cit. on pp. 55–58, 82).

[102] A. Elagin et al., *A New Mass Reconstruction Technique for Resonances Decaying to di-tau*, Nucl. Instrum. Meth. **A654** (2011) 481, arXiv: 1012.4686 [hep-ex] (cit. on p. 56).

[103] The ATLAS Collaboration, *The ATLAS Simulation Infrastructure*, The European Physical Journal C **70** (2010) 823, ISSN: 1434-6052, URL: https://doi.org/10.1140/epjc/s10052-010-1429-9 (cit. on p. 59).

[104] H.-L. Lai et al., *New parton distributions for collider physics*, Phys. Rev. D **82** (7 2010) 074024, URL: https://link.aps.org/doi/10.1103/PhysRevD.82.074024 (cit. on p. 60).

[105] S. Gieseke, C. Röhr and A. Siódmok, *Colour reconnections in Herwig++*, The European Physical Journal C **72** (2012) 2225, ISSN: 1434-6052, URL: https://doi.org/10.1140/epjc/s10052-012-2225-5 (cit. on p. 60).

[106] R. D. Ball et al., *Parton distributions with LHC data*, Nuclear Physics B **867** (2013) 244, ISSN: 0550-3213, URL: http://www.sciencedirect.com/science/article/pii/S0550321312005500 (cit. on p. 60).

[107] *ATLAS Run 1 Pythia8 tunes*, tech. rep. ATL-PHYS-PUB-2014-021, CERN, 2014, URL: https://cds.cern.ch/record/1966419 (cit. on pp. 60, 123).

[108] P. Artoisenet et al., *Automatic spin-entangled decays of heavy resonances in Monte Carlo simulations*, Journal of High Energy Physics **2013** (2013) 15, ISSN: 1029-8479, URL: https://doi.org/10.1007/JHEP03(2013)015 (cit. on pp. 63, 123).

[109] P. Z. Skands, *Tuning Monte Carlo generators: The Perugia tunes*, Phys. Rev. D **82** (7 2010) 074018, URL: https://link.aps.org/doi/10.1103/PhysRevD.82.074018 (cit. on p. 64).

[110] M. Czakon et al., *Constraints on the gluon PDF from top quark pair production at hadron colliders*, Journal of High Energy Physics **2013** (2013) 167, ISSN: 1029-8479, URL: https://doi.org/10.1007/JHEP07(2013)167 (cit. on pp. 64, 84).

[111] M. Aliev et al., *HATHOR – HAdronic Top and Heavy quarks crOss section calculatoR*, Computer Physics Communications **182** (2011) 1034, ISSN: 0010-4655, URL: http://www.sciencedirect.com/science/article/pii/S0010465510005333 (cit. on p. 64).

[112] P. Kant et al., *HatHor for single top-quark production: Updated predictions and uncertainty estimates for single top-quark production in hadronic collisions*, Computer Physics Communications **191** (2015) 74, ISSN: 0010-4655, URL: http://www.sciencedirect.com/science/article/pii/S0010465515000454 (cit. on p. 64).

[113] N. Kidonakis, *Two-loop soft anomalous dimensions for single top quark associated production with a W^- or H^-*, Phys. Rev. D **82** (5 2010) 054018, URL: https://link.aps.org/doi/10.1103/PhysRevD.82.054018 (cit. on p. 64).

[114] The NNPDF collaboration, *Parton distributions for the LHC run II*, Journal of High Energy Physics **2015** (2015) 40, ISSN: 1029-8479, URL: https://doi.org/10.1007/JHEP04(2015)040 (cit. on p. 64).

[115] C. Anastasiou et al., *High-precision QCD at hadron colliders: Electroweak gauge boson rapidity distributions at next-to-next-to leading order*, Phys. Rev. D **69** (9 2004) 094008, URL: https://link.aps.org/doi/10.1103/PhysRevD.69.094008 (cit. on p. 64).

[116] M. L. Ciccolini, S. Dittmaier and M. Krämer, *Electroweak radiative corrections to associated WH and ZH production at hadron colliders*, Phys. Rev. D **68** (7 2003) 073003, URL: https://link.aps.org/doi/10.1103/PhysRevD.68.073003 (cit. on p. 64).

[117] O. Brein, A. Djouadi and R. Harlander, *NNLO QCD corrections to the Higgs-strahlung processes at hadron colliders*, Physics Letters B **579** (2004) 149, ISSN: 0370-2693, URL: http://www.sciencedirect.com/science/article/pii/S0370269303017234 (cit. on p. 64).

[118] G. Ferrera, M. Grazzini and F. Tramontano, *Associated Higgs-W-Boson Production at Hadron Colliders: A Fully Exclusive QCD Calculation at NNLO*, Phys. Rev. Lett. **107** (15 2011) 152003, URL: https://link.aps.org/doi/10.1103/PhysRevLett.107.152003 (cit. on p. 64).

[119] O. Brein et al., *Top-quark mediated effects in hadronic Higgs-Strahlung*, The European Physical Journal C **72** (2012) 1868, ISSN: 1434-6052, URL: https://doi.org/10.1140/epjc/s10052-012-1868-6 (cit. on p. 64).

[120] G. Ferrera, M. Grazzini and F. Tramontano, *Higher-order QCD effects for associated WH production and decay at the LHC*, Journal of High Energy Physics **2014** (2014) 39, ISSN: 1029-8479, URL: https://doi.org/10.1007/JHEP04(2014)039 (cit. on p. 64).

[121] G. Ferrera, M. Grazzini and F. Tramontano, *Associated ZH production at hadron colliders: The fully differential NNLO QCD calculation*, Physics Letters B **740** (2015) 51, ISSN: 0370-2693, URL: http://www.sciencedirect.com/science/article/pii/S0370269314008429 (cit. on p. 64).

[122] J. M. Campbell, R. K. Ellis and C. Williams, *Associated production of a Higgs boson at NNLO*, Journal of High Energy Physics **2016** (2016) 179, ISSN: 1029-8479, URL: https://doi.org/10.1007/JHEP06(2016)179 (cit. on p. 64).

[123] The ATLAS collaboration, *Measurement of the Z/γ* boson transverse momentum distribution in pp collisions at $\sqrt{s} = 7$ and 8 TeV with the ATLAS detector*, Journal of High Energy Physics **2014** (2014) 145, ISSN: 1029-8479, URL: https://doi.org/10.1007/JHEP09(2014)145 (cit. on p. 64).

[124] L. Altenkamp et al., *Gluon-induced Higgs-strahlung at next-to-leading order QCD*, Journal of High Energy Physics **2013** (2013) 78, ISSN: 1029-8479, URL: https://doi.org/10.1007/JHEP02(2013)078 (cit. on p. 64).

[125] B. Hespel, F. Maltoni and E. Vryonidou, *Higgs and Z boson associated production via gluon fusion in the SM and the 2HDM*, Journal of High Energy Physics **2015** (2015) 65, ISSN: 1029-8479, URL: https://doi.org/10.1007/JHEP06(2015)065 (cit. on p. 64).

[126] R. V. Harlander et al., *Soft gluon resummation for gluon-induced Higgs Strahlung*, Journal of High Energy Physics **2014** (2014) 82, ISSN: 1029-8479, URL: https://doi.org/10.1007/JHEP11(2014)082 (cit. on p. 64).

[127] R. V. Harlander, S. Liebler and T. Zirke, *Higgs Strahlung at the Large Hadron Collider in the 2-Higgs-doublet model*, Journal of High Energy Physics **2014** (2014) 23, ISSN: 1029-8479, URL: https://doi.org/10.1007/JHEP02(2014)023 (cit. on p. 64).

[128] O. Brein, R. V. Harlander and T. J. Zirke, *vh@nnlo—Higgs Strahlung at hadron colliders*, Computer Physics Communications **184** (2013) 998, ISSN: 0010-4655, URL: http://www.sciencedirect.com/science/article/pii/S0010465512003785 (cit. on p. 64).

[129] ATLAS Collaboration, *Summary of ATLAS Pythia 8 tunes*, tech. rep. ATL-PHYS-PUB-2012-003, CERN, 2012, URL: https://cds.cern.ch/record/1474107 (cit. on p. 64).

[130] The ATLAS collaboration, *Evidence for the H to $b\bar{b}$ decay with the ATLAS detector*, Journal of High Energy Physics **2017** (2017) 24, ISSN: 1029-8479, URL: https://doi.org/10.1007/JHEP12(2017)024 (cit. on pp. 73, 84, 93, 106).

[131] A. Hocker et al., *TMVA - Toolkit for Multivariate Data Analysis*, (2007), URL: https://arxiv.org/pdf/physics/0703039.pdf (cit. on pp. 74, 75, 78).

[132] ATLAS Collaboration, *Luminosity determination in pp collisions at $\sqrt{s}$ = 8 TeV using the ATLAS detector at the LHC*, The European Physical Journal C **76** (2016) 653, ISSN: 1434-6052, URL: https://doi.org/10.1140/epjc/s10052-016-4466-1 (cit. on p. 81).

[133] ATLAS Collaboration, *Measurement of the Inelastic Proton-Proton Cross Section at $\sqrt{s}$ = 13 TeV with the ATLAS Detector at the LHC*, Phys. Rev. Lett. **117** (18 2016) 182002, URL: https://link.aps.org/doi/10.1103/PhysRevLett.117.182002 (cit. on p. 81).

[134] J. Butterworth et al., *PDF4LHC recommendations for LHC Run II*, J. Phys. **G43** (2016) 023001, arXiv: 1510.03865 [hep-ph] (cit. on p. 84).

[135] ATLAS Collaboration, *Search for resonances decaying to a W or Z boson and a Higgs boson in the $\nu\nu bb$, $\ell\nu bb$ and $\ell\ell bb$ final states with $\sqrt{s}$ = 13 TeV ATLAS data in the context of models with 2 Higgs doublets or additional heavy vector triplets*, tech. rep. ATL-COM-PHYS-2016-479, CERN, 2016, URL: https://cds.cern.ch/record/2151842 (cit. on p. 84).

[136] ATLAS Collaboration, *Evidence for the associated production of the Higgs boson and a top quark pair with the ATLAS detector*, Phys. Rev. D **97** (7 2018) 072003, URL: https://link.aps.org/doi/10.1103/PhysRevD.97.072003 (cit. on p. 84).

[137] G. Cowan et al., *Asymptotic formulae for likelihood-based tests of new physics*, The European Physical Journal C **71** (2011) 1554, ISSN: 1434-6052, URL: https://doi.org/10.1140/epjc/s10052-011-1554-0 (cit. on p. 89).

[138] A. L. Read, *Presentation of search results: theCLstechnique*, Journal of Physics G: Nuclear and Particle Physics **28** (2002) 2693, URL: https://doi.org/10.1088%2F0954-3899%2F28%2F10%2F313 (cit. on pp. 90, 97).

[139] ATLAS Collaboration, *Search for Higgs boson pair production in the $\gamma\gamma b\bar{b}$ final state with 13 TeV pp collision data collected by the ATLAS experiment*, JHEP **11** (2018) 040, arXiv: 1807.04873 [hep-ex] (cit. on p. 116).

[140] ATLAS Collaboration, *Search for pair production of Higgs bosons in the $b\bar{b}b\bar{b}$ final state using proton-proton collisions at $\sqrt{s}$ = 13 TeV with the ATLAS detector*, JHEP **1901** (2018) 030. 50 p, URL: https://cds.cern.ch/record/2313703 (cit. on p. 116).

[141] R. D. Ball et al., *Parton distributions for the LHC Run II*, JHEP **04** (2015) 040, arXiv: 1410.8849 [hep-ph] (cit. on p. 123).

[142] C. Borschensky et al., *Squark and gluino production cross sections in pp collisions at $\sqrt{s}$ = 13, 14, 33 and 100 TeV*, Eur. Phys. J. **C74** (2014) 3174, arXiv: 1407.5066 [hep-ph] (cit. on p. 123).

[143] CMS Collaboration, *Search for Higgs boson pair production in events with two bottom quarks and two tau leptons in proton–proton collisions at $\sqrt{s}$ =13TeV*, Phys. Lett. **B778** (2018) 101, arXiv: 1707.02909 [hep-ex] (cit. on p. 133).

[144] CMS Collaboration, *Search for heavy neutrinos and third-generation leptoquarks in hadronic states of two τ leptons and two jets in proton-proton collisions at $\sqrt{s}$ = 13 TeV*, Submitted to: JHEP (2018), arXiv: 1811.00806 [hep-ex] (cit. on p. 134).

APPENDIX A

BDT trainings for the BSM $HH \to b\bar{b}\tau^{+}_{had}\tau^{-}_{had}$ analysis

As described in Section 6.5, separate dedicated BDTs are trained to target the several signal hypotheses considered in the analysis.

A.0.1 Choice of the signal training samples

The choice of the signal training samples for the BSM signals is the result of a study performed to obtain the best possible sensitivity over the full scan of BSM scenarios.

For the non-resonant signals with variations of the coupling k_λ a BDT trained on the non-resonant signal with $k_\lambda = 20$ is used. This training gives performance which are compatible with the ones obtained with dedicated trainings done at each specific k_λ value over the full tested k_λ range and provides more stable results, obtained using only one BDT training, which are less affected by statistical fluctuations compared to several dedicated trainings. This is shown in Figure A.1 where the median expected upper limits on the cross section times $bb\tau\tau$ BR as a function of k_λ obtained using the SM BDT training, dedicated BDTs trained at each k_λ value and the BDT trained on the $k_\lambda = 20$ signal are compared.

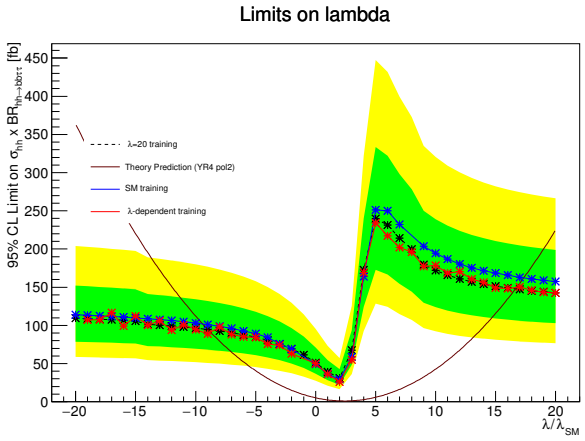

Figure A.1: Median expected upper limits on the cross section times $bb\tau\tau$ BR for the non-resonant signals as a function of k_λ obtained using the SM BDT (blue), dedicated BDTs trained at each k_λ value (red) and the BDT trained on the $k_\lambda = 20$ signal (black).

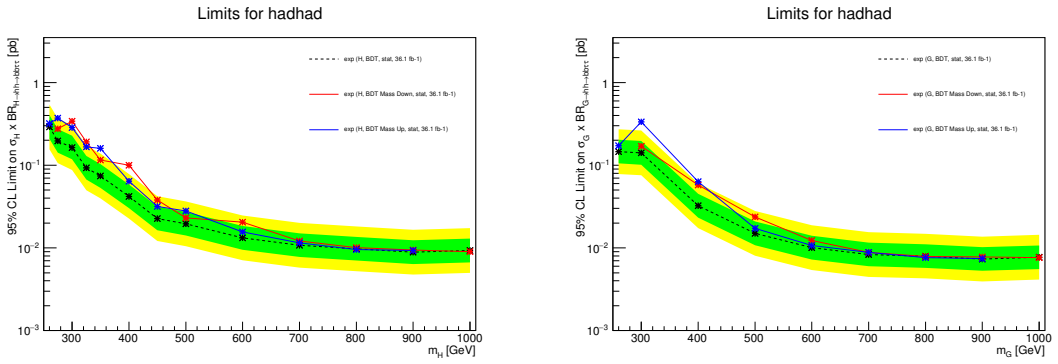

(a) (b)

Figure A.2: Median expected upper limits on the cross section times $bb\tau\tau$ BR for the resonant signals as a function of the resonance mass obtained using BDTs trained at each mass point (black), the BDTs trained at the lower mass point (red) and the BDTs trained at the upper mass point (blue). The limits are shown for the a) 2HDM signals and b) RS graviton with $c = 1$ signals.

For the resonant signals, one dedicated training targeting each mass value of each of the three considered models is used. The trainings are done separately for the 2HDM, RS graviton with $c = 1$ and $c = 2$ signals because the widths of the resonances are very different between the three models and, especially at low masses, this has a large impact on the training and on its performance. The best performance over the full mass range are obtained with BDTs trained on each specific signal mass value. Unfortunately, this trainings have a significantly reduced sensitivity for mass values which are different from the training mass. This is shown in Figure A.2 where the median expected upper limits on the cross section times $bb\tau\tau$ BR as a function of the resonance mass obtained using the dedicated trainings at each mass point are compared to the ones obtained using the trainings of the neighbouring mass points (below and above, red and blue lines respectively). The difference between the expected limits exceeds the 2σ band implying that this BDTs are too sensitive to the mass of the resonance for being used to set smooth upper limits over the full tested mass range, as they are really sub-optimal discriminants for masses which are different from the targeting mass.

To solve this problem the BDT targeting each mass point is trained including the two neighbouring mass points in the signal training sample (e.g. the BDT targeting the 300 GeV mass point is trained on a signal training sample containing the 275 GeV, 300 GeV and 325 GeV signals). The result of this method is shown in Figure A.3 where the median expected upper limits obtained with the nominal merged-3-mass-points trainings are compared to the ones obtained using the merged-3-mass-points trainings targeting the neighbouring mass points (below and above, red and blue lines respectively) and to the ones obtained using the single mass trainings (grey line). The overall performance of the analysis is slightly worse using the merged-3-mass points-trainings, however the test using the BDTs trained targeting the neighbouring mass points shows that the expected limits are more stable (differences are within the 1σ band) as the analysis is less sensitive to the value of the mass.

Moreover, signal injection tests are performed to check the sensitivity of the analysis to the presence of a signal. The results of these tests are shown in Figure A.4 for the injection of signals with masses of 300 GeV, 400 GeV and 500 GeV in the Asimov dataset. The tests show that the analysis designed in this way, with the BDTs trained on the merged-3-mass-points signal samples, is sensitive to the presence of a signal that falls in between the available MC generated mass points, as the injected signals give an excess in the upper limit not only at the injected mass but also at the neighbouring masses.

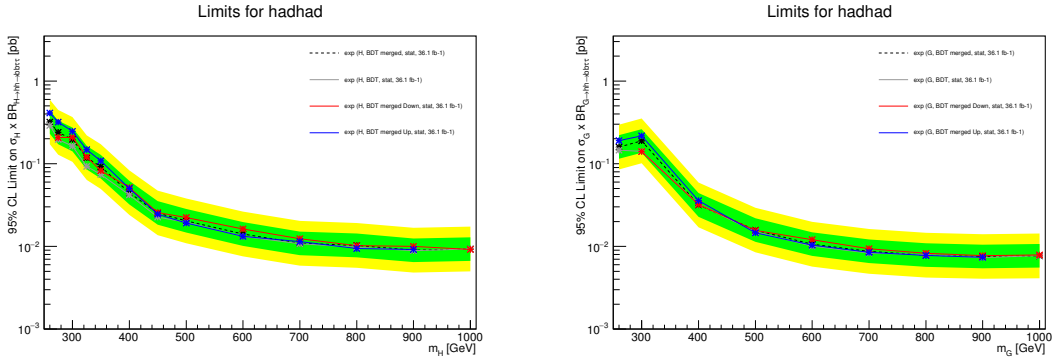

(a) (b)

Figure A.3: Median expected upper limits on the cross section times $bb\tau\tau$ BR for the resonant signals as a function of the resonance mass obtained using BDTs trained on the merged-3-mass samples (black), the BDTs trained at the lower mass point (red), the BDTs trained at the upper mass point (blue) and the single mass trainings (grey). The limits are shown for the a) 2HDM signals and b) RS graviton with $c = 1$ signals.

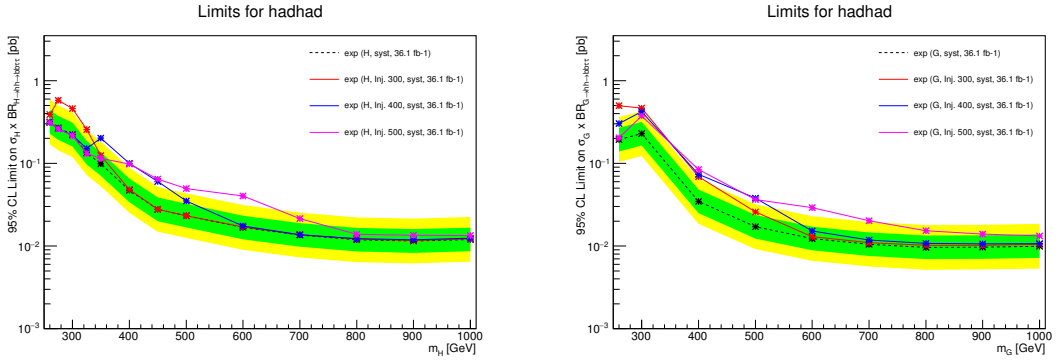

(a) (b)

Figure A.4: Median expected upper limits on the cross section times $bb\tau\tau$ BR for the resonant signals as a function of the resonance mass for Asimov data with $\mu = 0$ (black) and for Asimov data with $\mu = 1$ for 300 GeV (red), 400 GeV (blue) and 500 GeV (magenta). The limits are shown for the a) 2HDM signals and b) RS graviton with $c = 1$ signals.

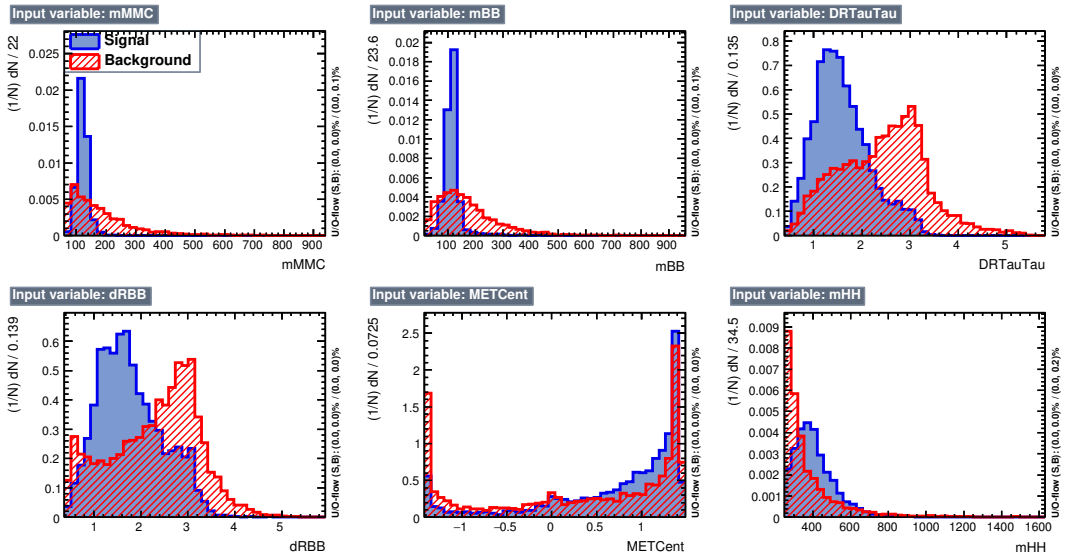

Figure A.5: BDT input variables distributions for the non-resonant signal with $k_\lambda = 20$ (blue) and for the background (red).

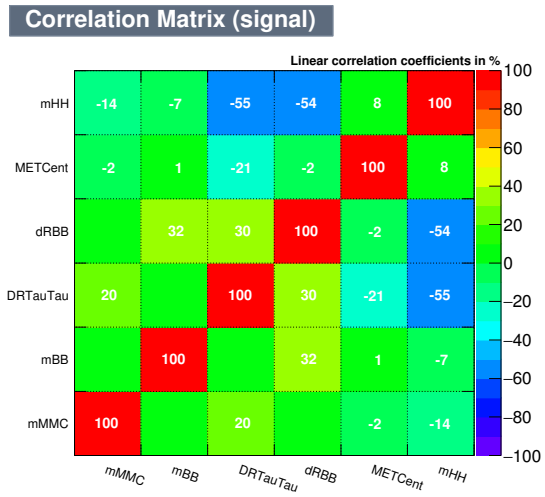

Figure A.6: BDT input variables linear correlation coefficients for the non-resonant signal with $k_\lambda = 20$.

A.0.2 Input variables distributions, correlation matrices, BDT scores and ROC curves

In Section 6.5 only plots for the SM di-Higgs signal are provided. In this section the BDT input variables distributions, the correlation matrices, the BDT scores and the ROC curves are included for the non-resonant signal with $k_\lambda = 20$ and for some mass points (300, 500, 1000 GeV) for the 2HDM and the RS graviton with $c = 1, 2$ signals.

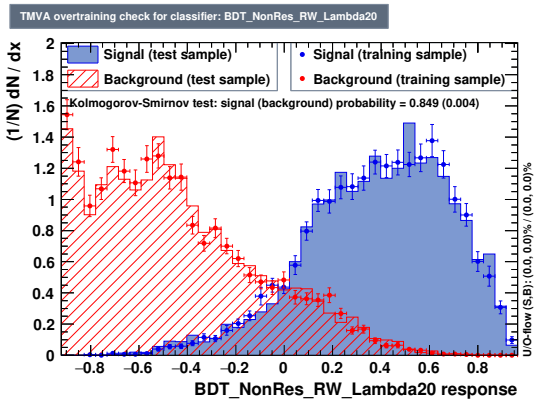

Figure A.7: BDT score distribution for the non-resonant signal with $k_\lambda = 20$ (blue) and the background (red).

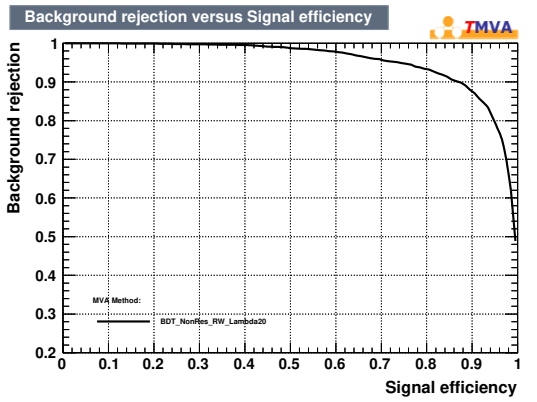

Figure A.8: ROC curve for the non-resonant signal with $k_\lambda = 20$ BDT.

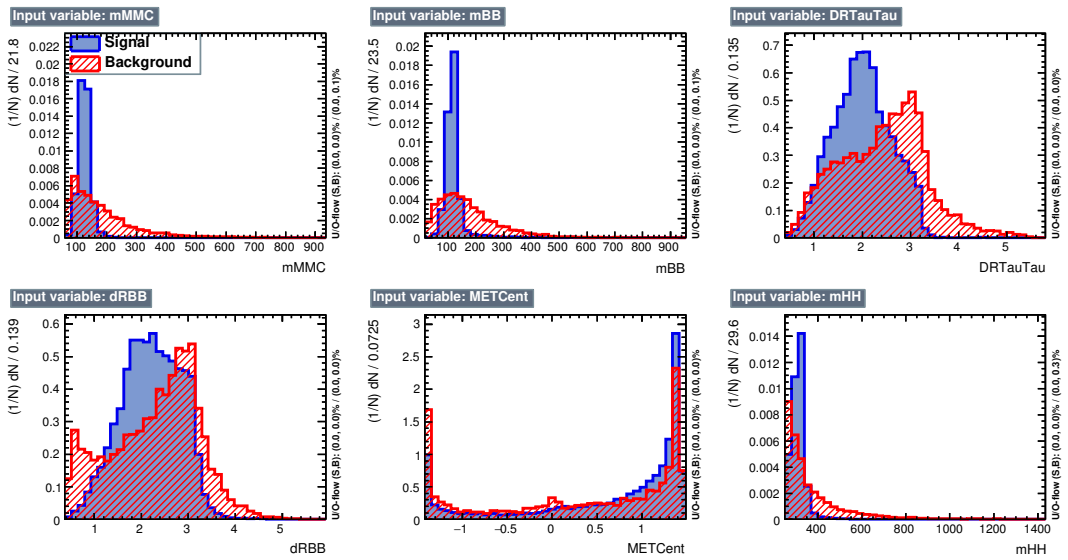

Figure A.9: BDT input variables distributions for the 2HDM signal with $m_X = 300\,\text{GeV}$ (blue) and for the background (red).

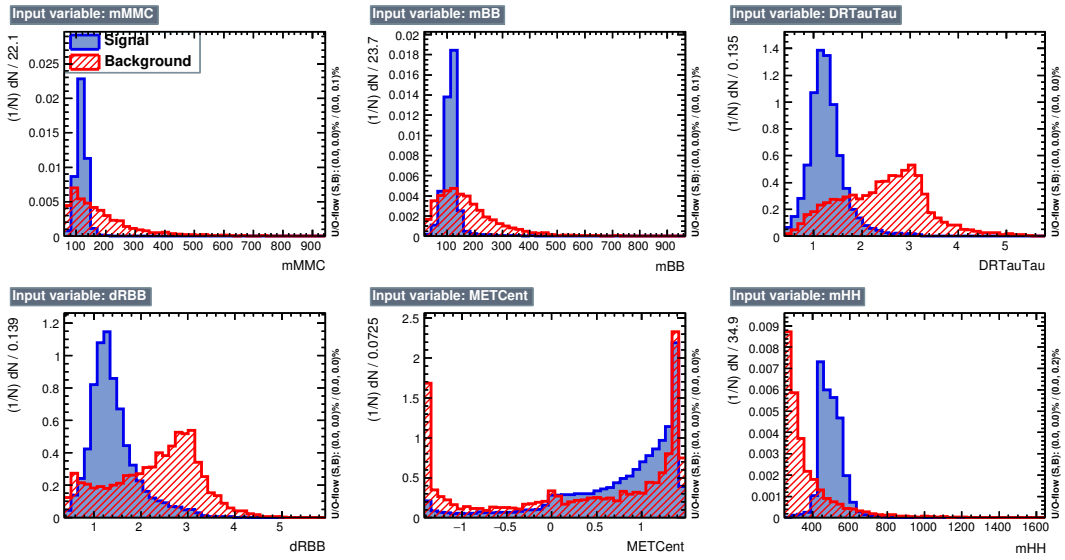

Figure A.10: BDT input variables distributions for the 2HDM signal with $m_X = 500$ GeV (blue) and for the background (red).

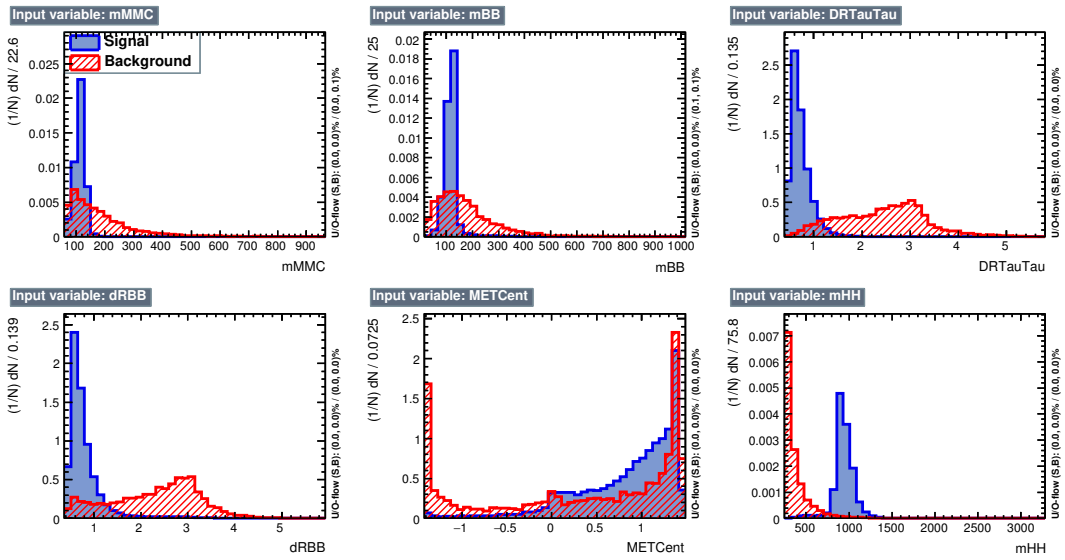

Figure A.11: BDT input variables distributions for the 2HDM signal with $m_X = 1000$ GeV (blue) and for the background (red).

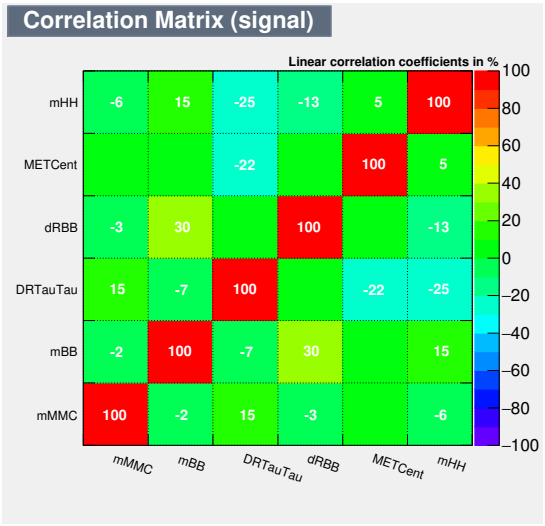

(a)

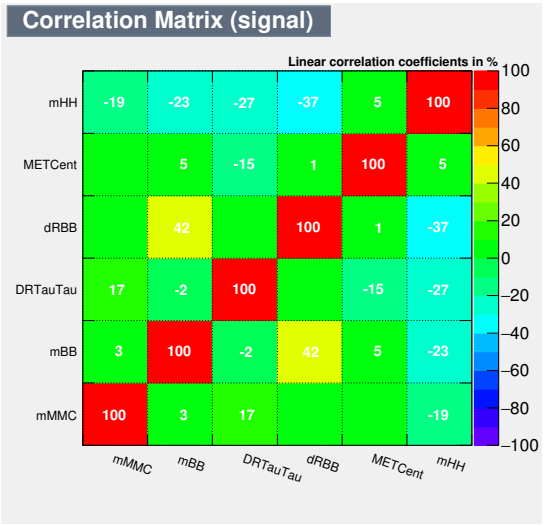

(b)

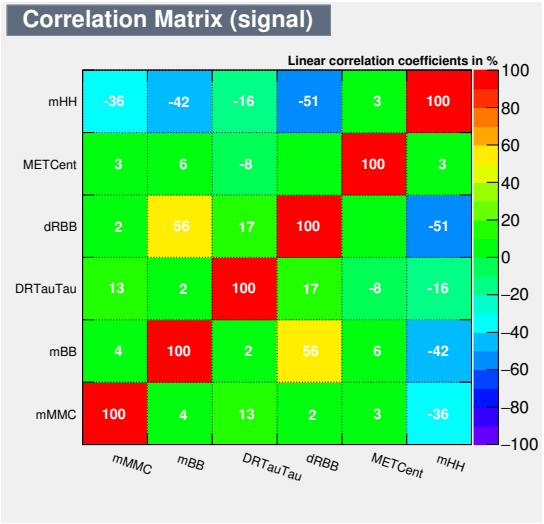

(c)

Figure A.12: BDT input variables linear correlation coefficients for the 2HDM signal with a) $m_X = 300$ GeV b) $m_X = 500$ GeV and c) $m_X = 1000$ GeV.

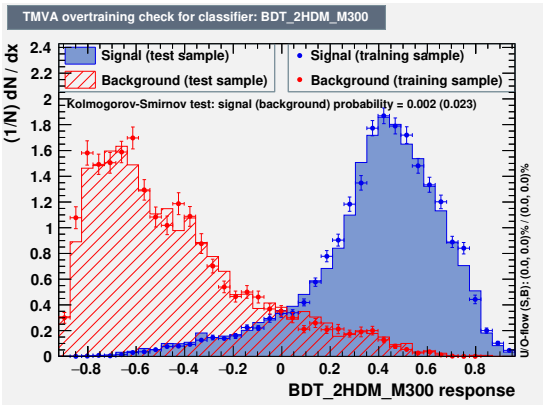

(a)

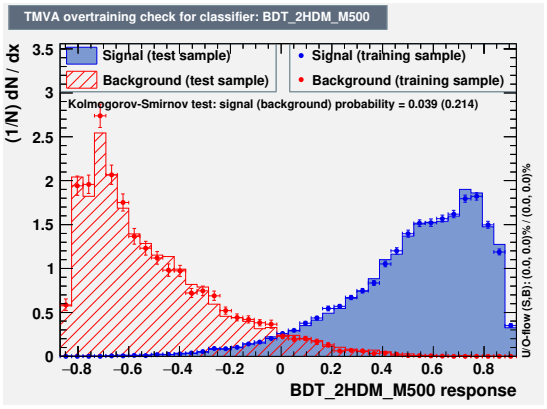

(b)

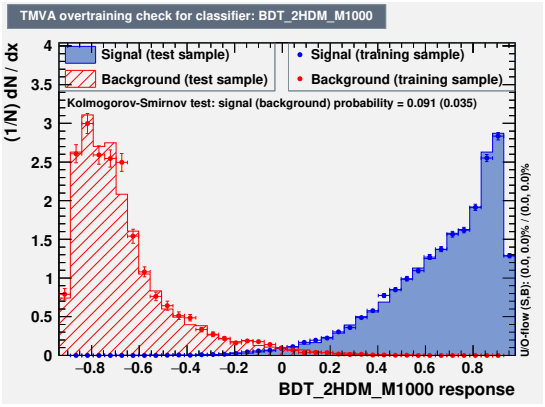

(c)

Figure A.13: BDT score distribution for the 2HDM signal (blue) with a) $m_X = 300$ GeV b) $m_X = 500$ GeV and c) $m_X = 1000$ GeV and for the background (red).

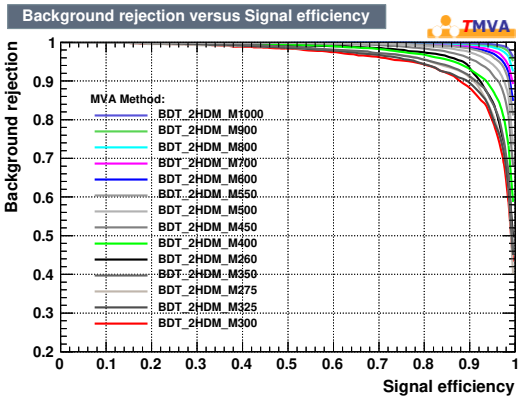

Figure A.14: ROC curves for the 2HDM signals BDTs.

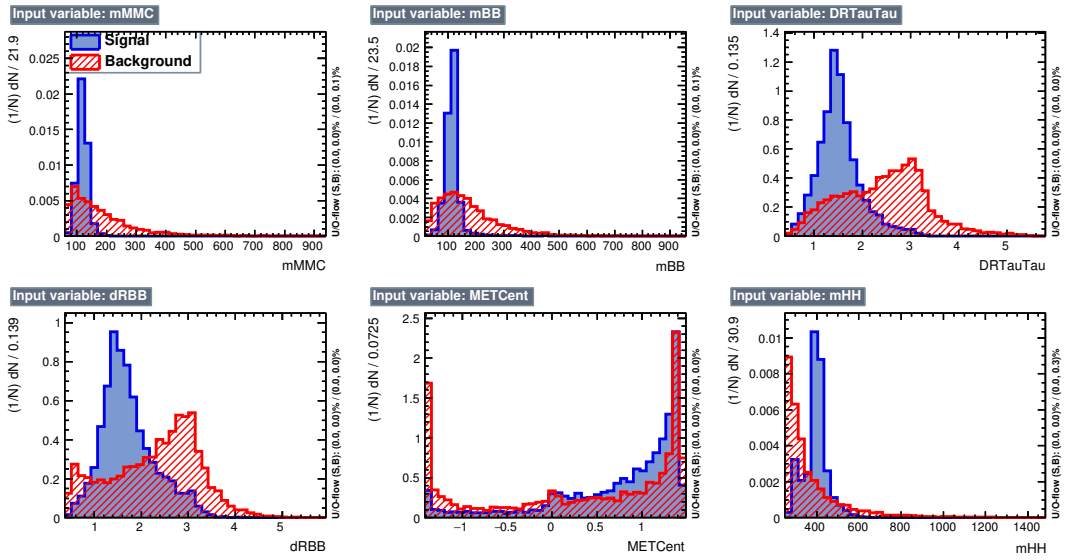

Figure A.15: BDT input variables distributions for the RS graviton signal with $c = 1$ and $m_G = 300$ GeV (blue) and for the background (red).

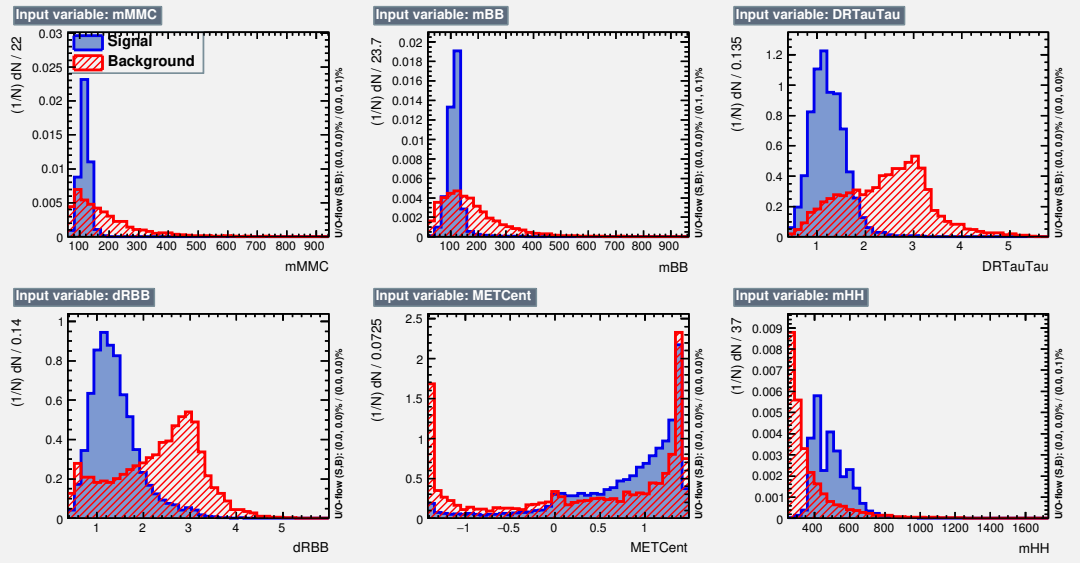

Figure A.16: BDT input variables distributions for the RS graviton signal with $c = 1$ and $m_G = 500$ GeV (blue) and for the background (red).

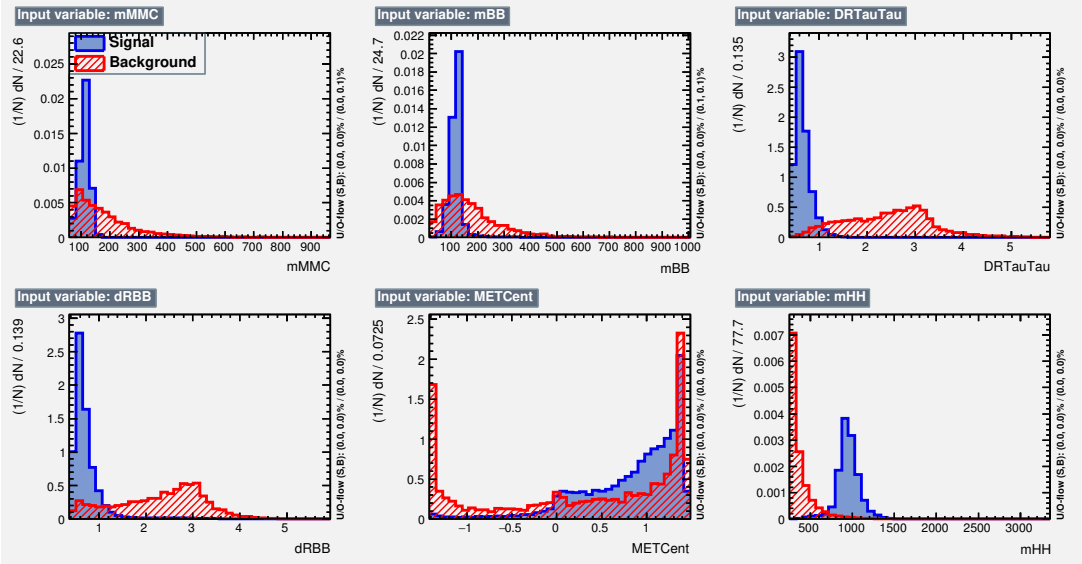

Figure A.17: BDT input variables distributions for the RS graviton signal with $c = 1$ and $m_G = 1000$ GeV (blue) and for the background (red).

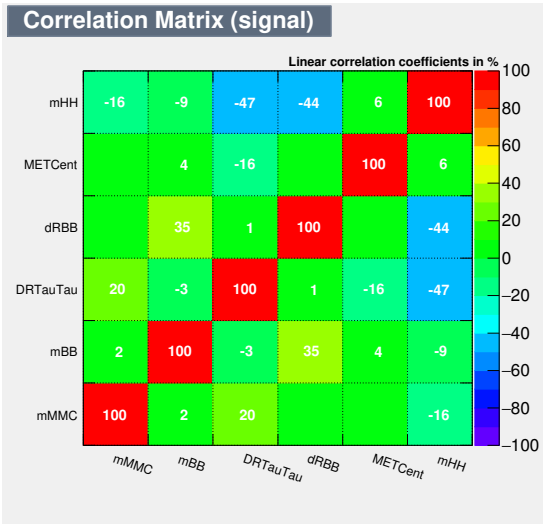

(a)

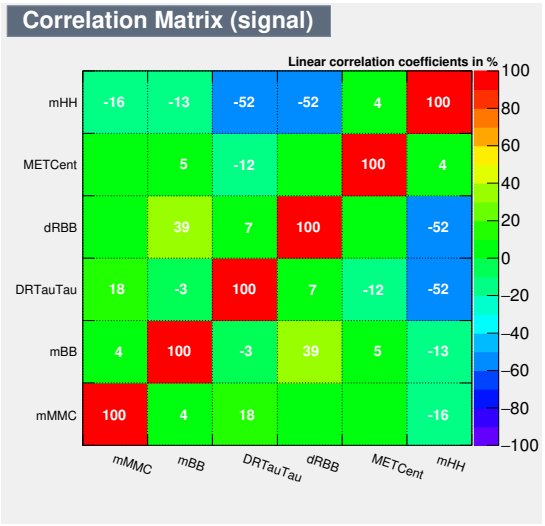

(b)

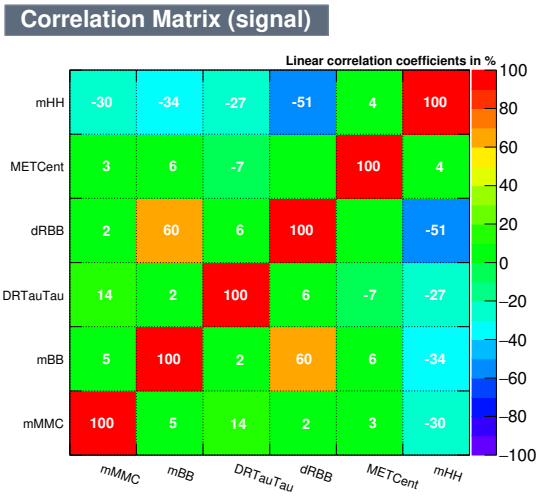

(c)

Figure A.18: BDT input variables linear correlation coefficients for the RS graviton signal with $c = 1$ and a) $m_G = 300$ GeV b) $m_G = 500$ GeV and c) $m_G = 1000$ GeV.

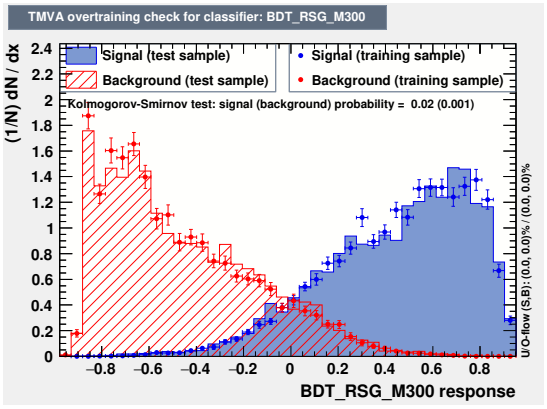

(a)

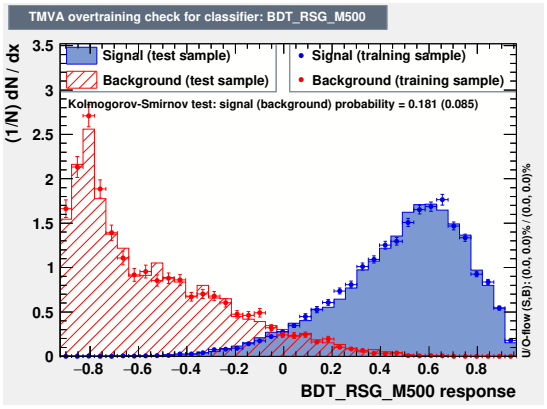

(b)

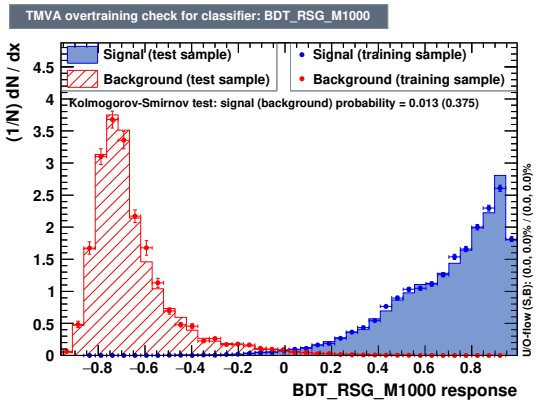

(c)

Figure A.19: BDT score distribution for the RS graviton signal (blue) with $c = 1$ and a) $m_G = 300$ GeV b) $m_G = 500$ GeV and c) $m_G = 1000$ GeV and for the background (red).

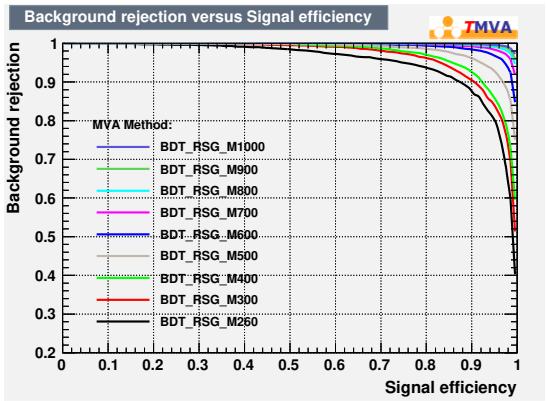

Figure A.20: ROC curves for the RS graviton with $c = 1$ signals BDTs.

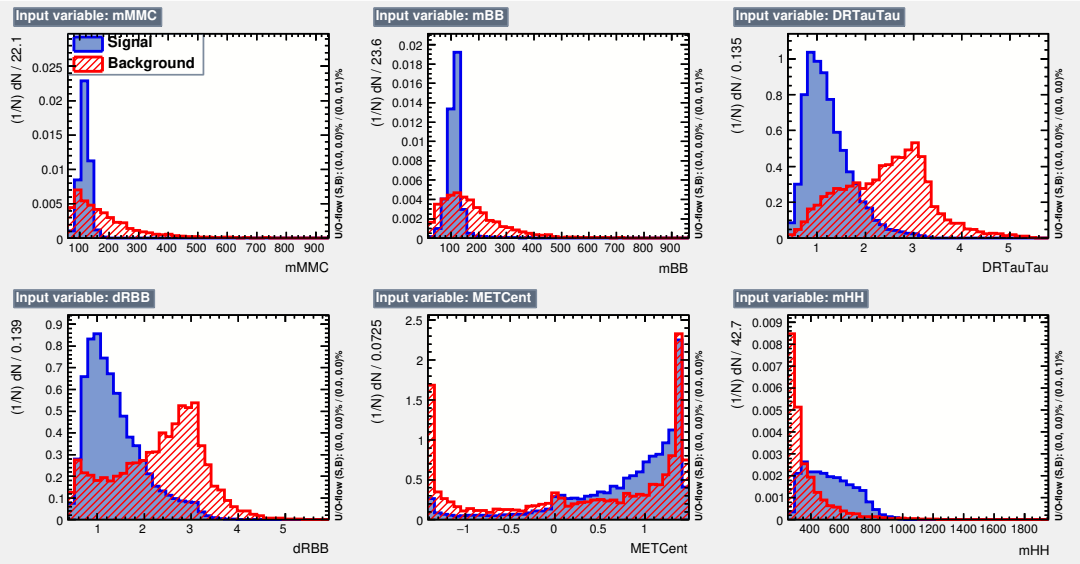

Figure A.21: BDT input variables distributions for the RS graviton signal with $c = 2$ and $m_G = 300$ GeV (blue) and for the background (red).

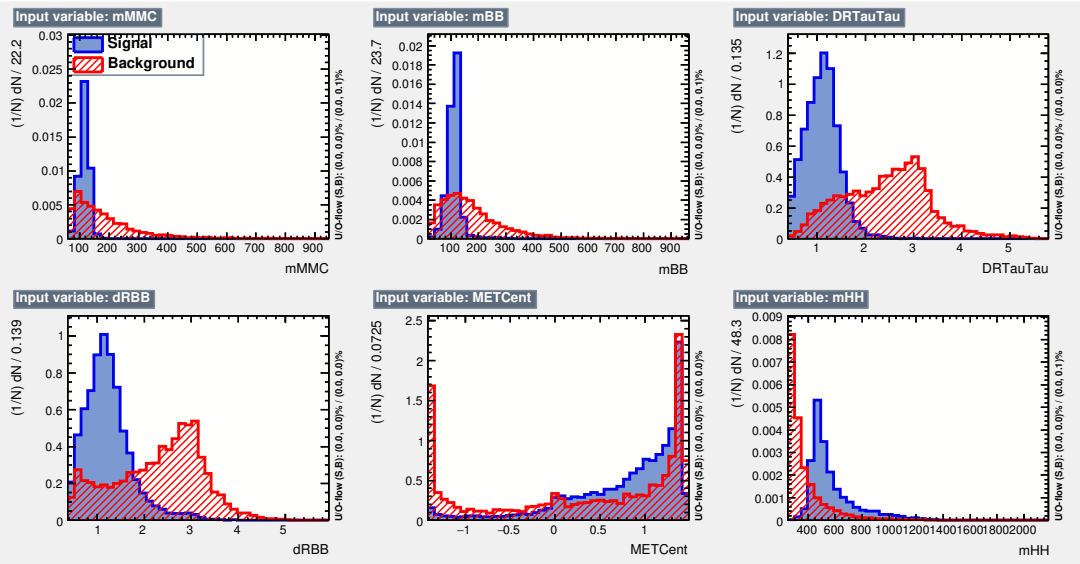

Figure A.22: BDT input variables distributions for the RS graviton signal with $c = 2$ and $m_G = 500$ GeV (blue) and for the background (red).

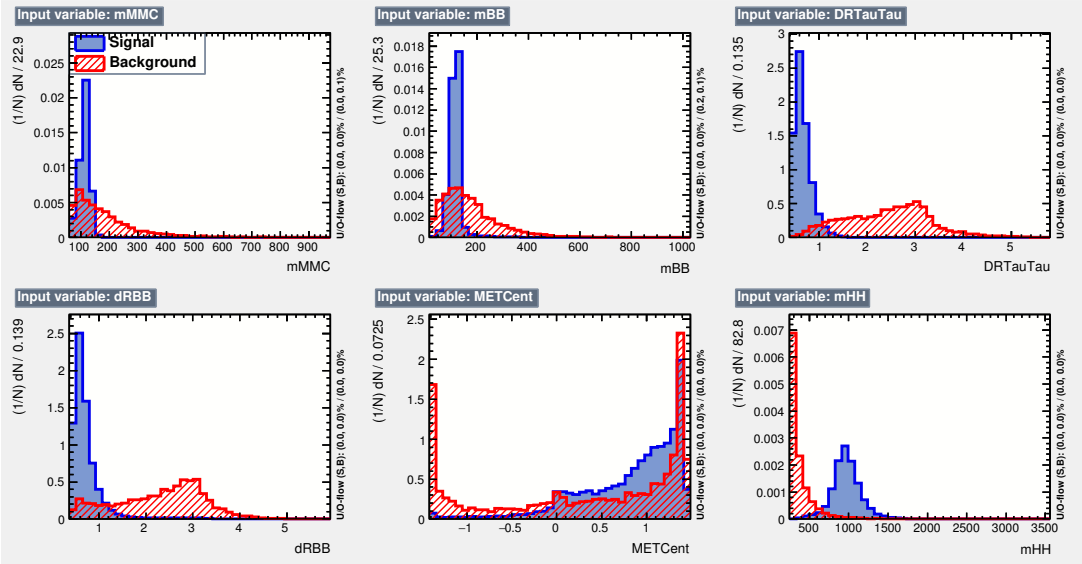

Figure A.23: BDT input variables distributions for the RS graviton signal with $c = 2$ and $m_G = 1000$ GeV (blue) and for the background (red).

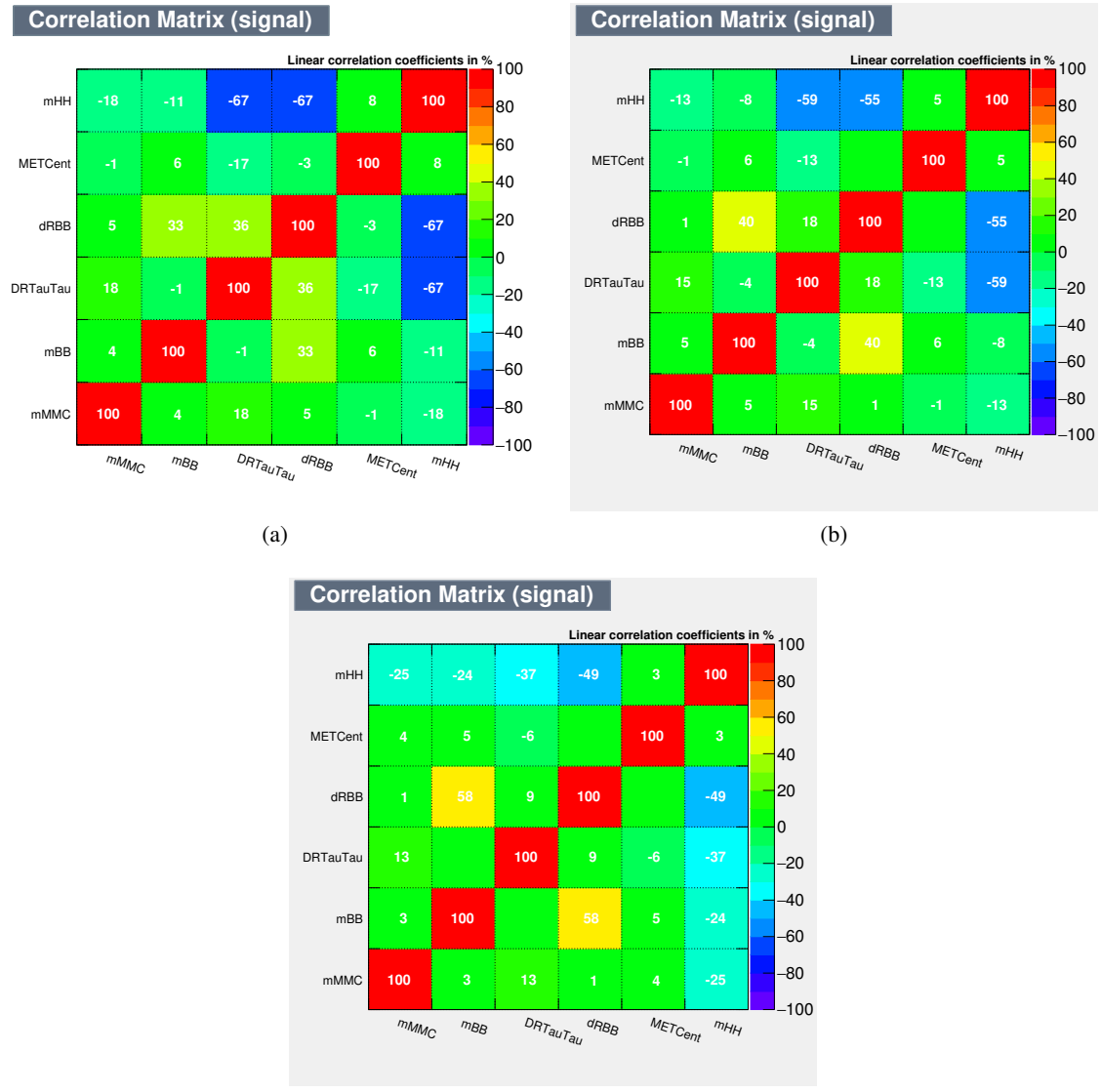

Figure A.24: BDT input variables linear correlation coefficients for the RS graviton signal with $c = 2$ and a) $m_G = 300$ GeV b) $m_G = 500$ GeV and c) $m_G = 1000$ GeV.

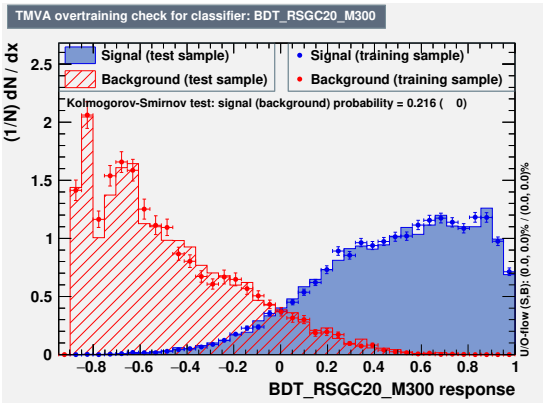

(a)

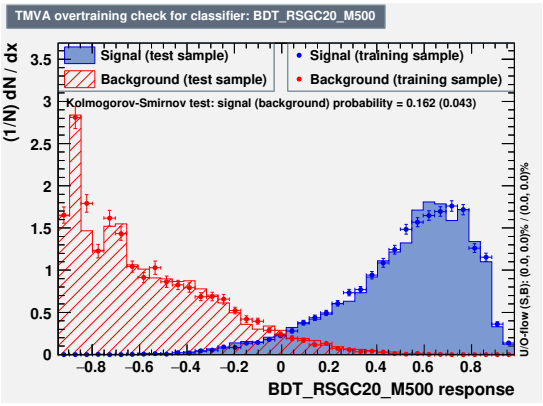

(b)

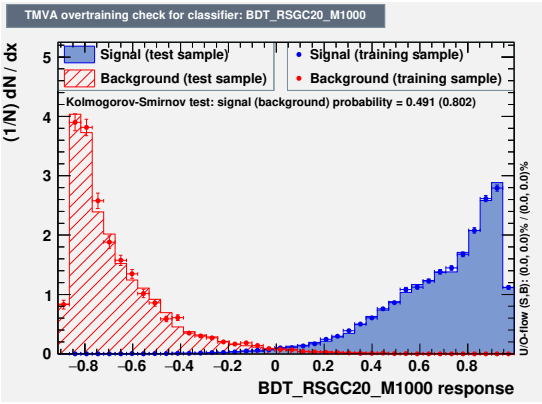

(c)

Figure A.25: BDT score distribution for the RS graviton signal (blue) with $c = 2$ and a) $m_G = 300$ GeV b) $m_G = 500$ GeV and c) $m_G = 1000$ GeV and for the background (red).

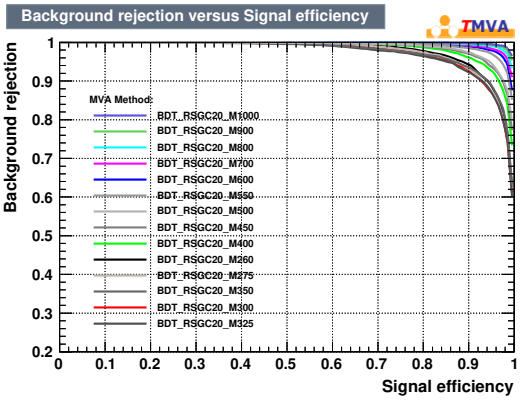

Figure A.26: ROC curves for the RS graviton with $c = 2$ signals BDTs.

APPENDIX B

Profile likelihood fit: test of the background-only hypothesis for the BSM $HH \to b\bar{b}\tau^{+}_{had}\tau^{-}_{had}$ analysis

As described in Section 6.7, a profile likelihood fit is performed on each BDT score distribution to test the background-only hypothesis. Moreover, the background plus signal fit is also performed to check the behaviour of the NP pulls and impact on the fitted signal strength μ. The description of the NPs is given in Tables B.1, B.2, B.3. In Section 6.7 only the plots from the SM BDT fit are shown. In this Section, the post-fit BDT score distributions, the NP pulls and rankings are included for the non resonant signal with $k_\lambda = 20$ and for some mass points (300, 500, 1000 GeV) for the 2HDM and the RS graviton with $c = 1, 2$ signals.

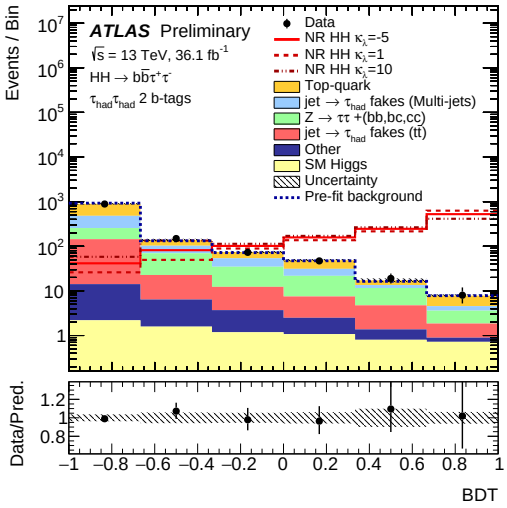

Figure B.1: Post-fit distribution of the non-resonant with $k_\lambda = 20$ BDT. All background components are scaled to their normalisations as determined in the fit. The pre-fit normalisation of the sum of all background components predicted by the simulated events is given by the dashed blue line. The non-resonant di-Higgs signal distributions with $k_\lambda = -5, 1, 10$ are also shown with a normalisation scaled to the total background normalisation. The shaded bands represent the total post-fit uncertainty with NPs profiled to the data.

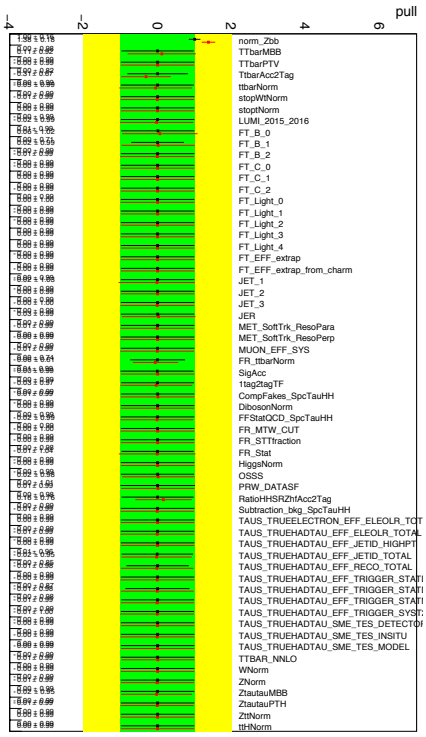

Figure B.2: NP pulls from the fit of the non-resonant with $k_\lambda = 20$ BDT to an Asimov dataset with $\mu = 0$ (black) and to the observed data (red).

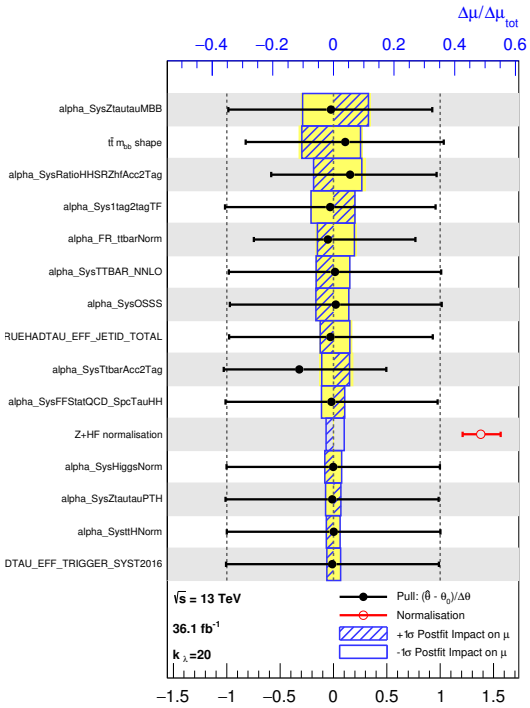

Figure B.3: Fractional impact of the NPs on the non-resonant $k_\lambda = 20$ signal best fit value of the signal strength μ.

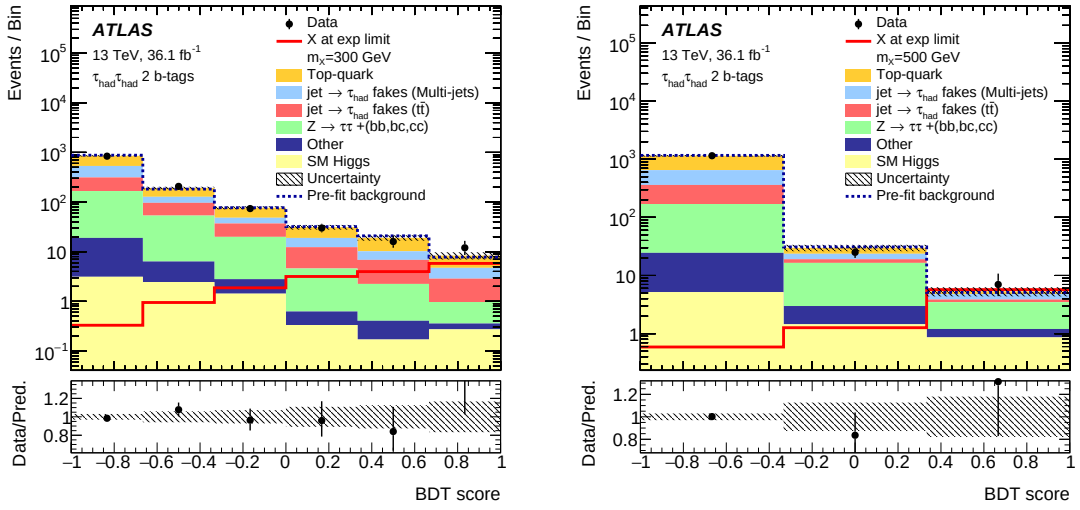

Figure B.4: Post-fit distribution of the 2HDM signal BDTs with a) $m_X = 300$ GeV b) $m_X = 500$ GeV and c) $m_X = 1000$ GeV. All background components are scaled to their normalisations as determined in the fit. The pre-fit normalisation of the sum of all background components predicted by the simulated events is given by the dashed blue line. The 2HDM signal distribution is also shown with a normalisation scaled to expected upper limit. The shaded bands represent the total post-fit uncertainty with NPs profiled to the data.

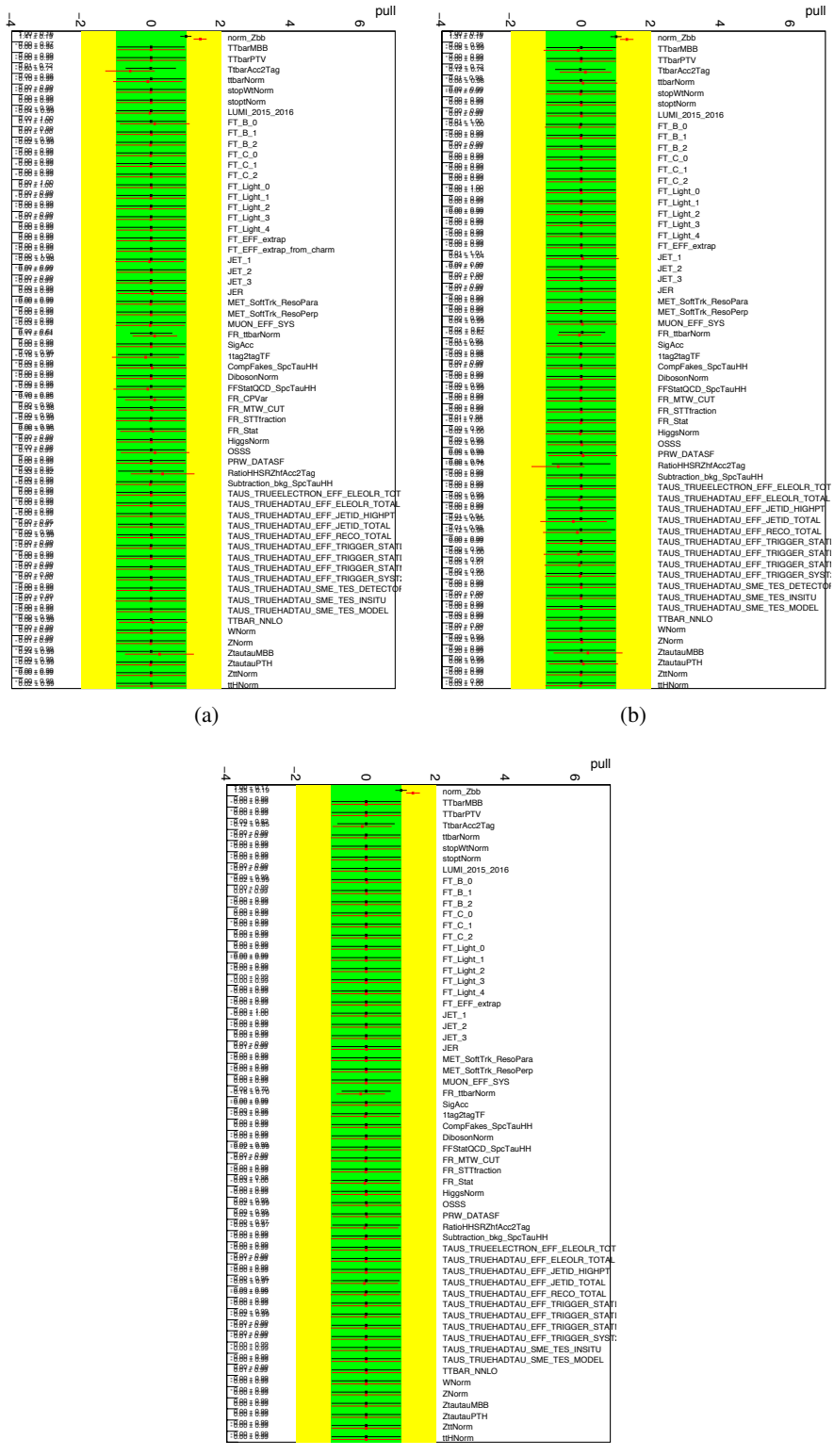

(a) (b)

(c)

Figure B.5: NP pulls from the fit of the 2HDM BDT to an Asimov dataset with $\mu = 0$ (black) and to the observed data (red) for the 2HDM signal with a) $m_X = 300$ GeV b) $m_X = 500$ GeV and c) $m_X = 1000$ GeV.

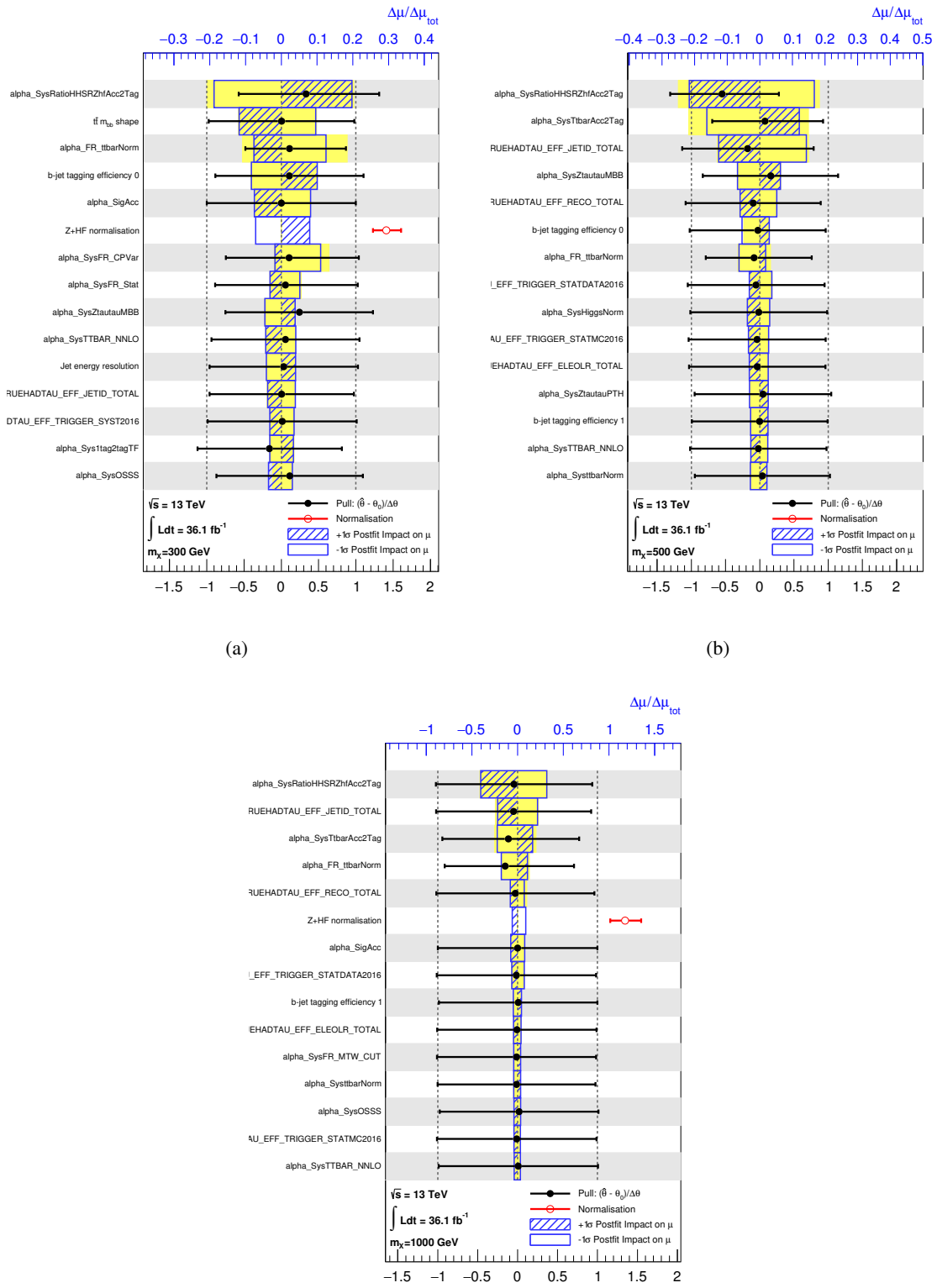

(a) (b)

(c)

Figure B.6: Fractional impact of the NPs on the 2HDM signal best fit value of the signal strength μ for the 2HDM signal with a) $m_X = 300$ GeV b) $m_X = 500$ GeV and c) $m_X = 1000$ GeV.

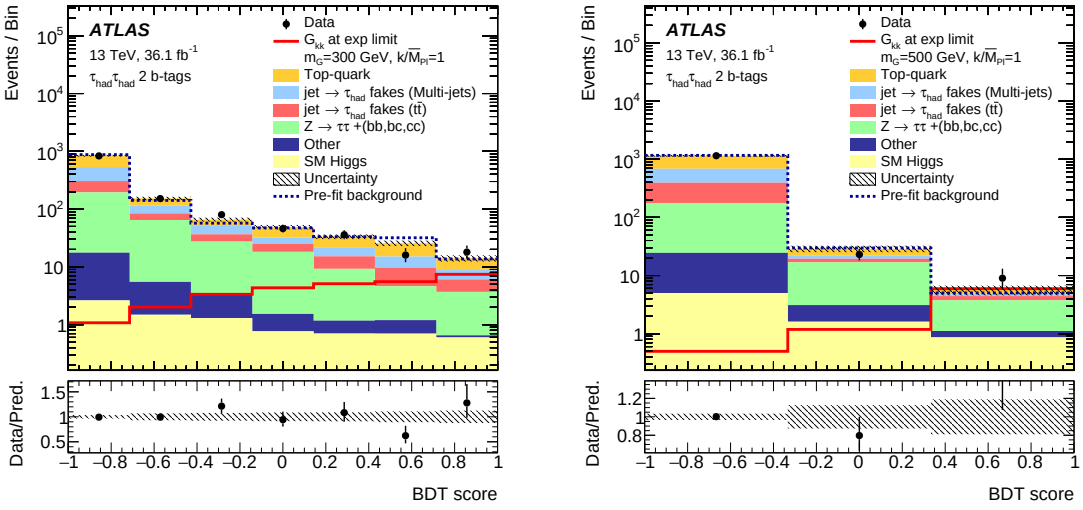

(a)

(b)

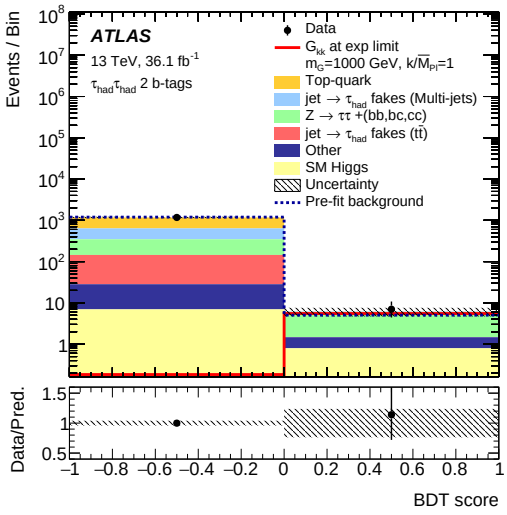

(c)

Figure B.7: Post-fit distribution of the RS graviton signal with $c = 1$ BDTs with a) $m_G = 300$ GeV b) $m_G = 500$ GeV and c) $m_G = 1000$ GeV. All background components are scaled to their normalisations as determined in the fit. The pre-fit normalisation of the sum of all background components predicted by the simulated events is given by the dashed blue line. The RS graviton with $c = 1$ signal distribution is also shown with a normalisation scaled to expected upper limit. The shaded bands represent the total post-fit uncertainty with NPs profiled to the data.

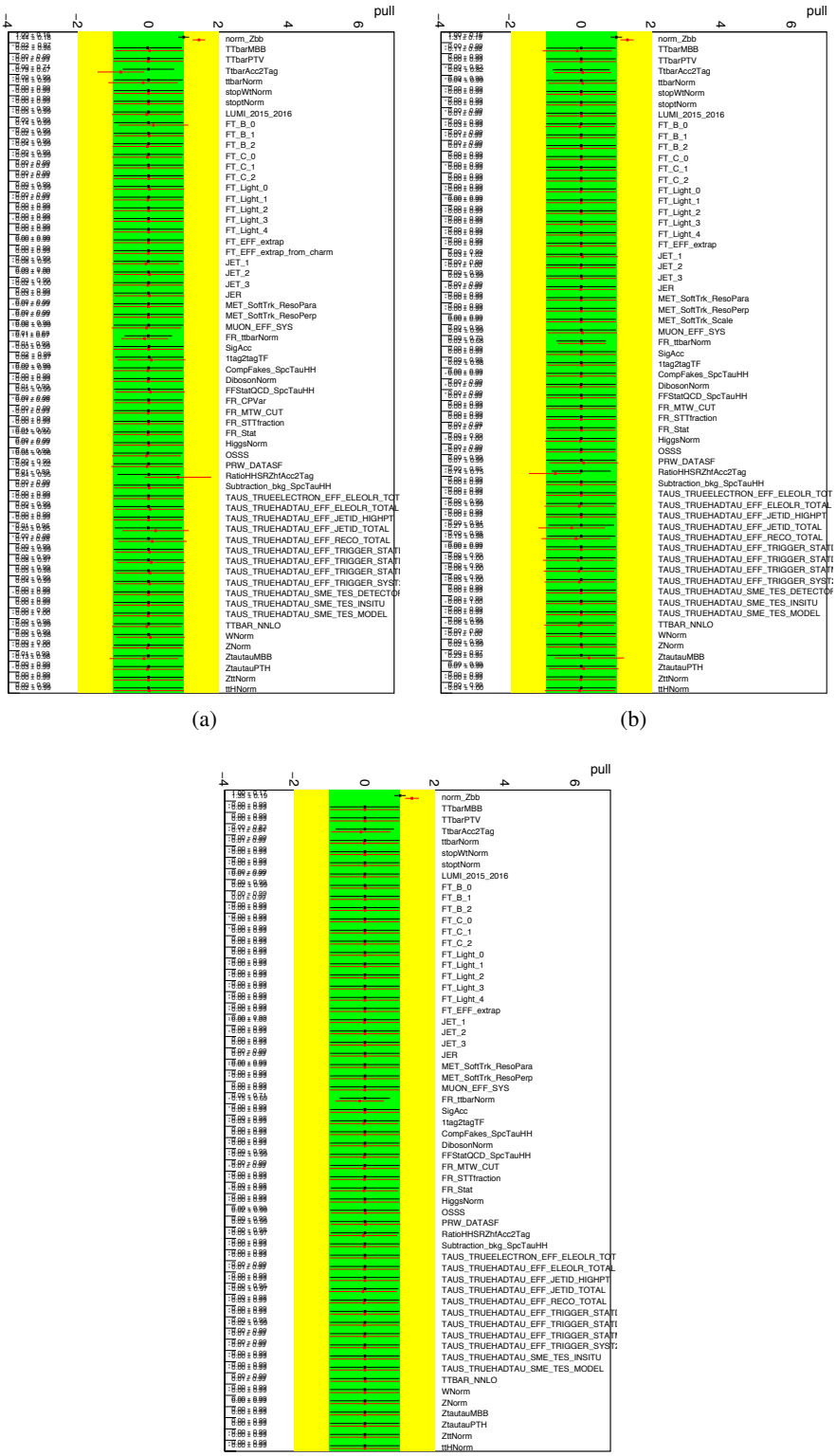

Figure B.8: NP pulls from the fit of the RS graviton BDT to an Asimov dataset with $\mu = 0$ (black) and to the observed data (red) for the RS graviton signal with $c = 1$ and a) $m_G = 300$ GeV b) $m_G = 500$ GeV and c) $m_G = 1000$ GeV.

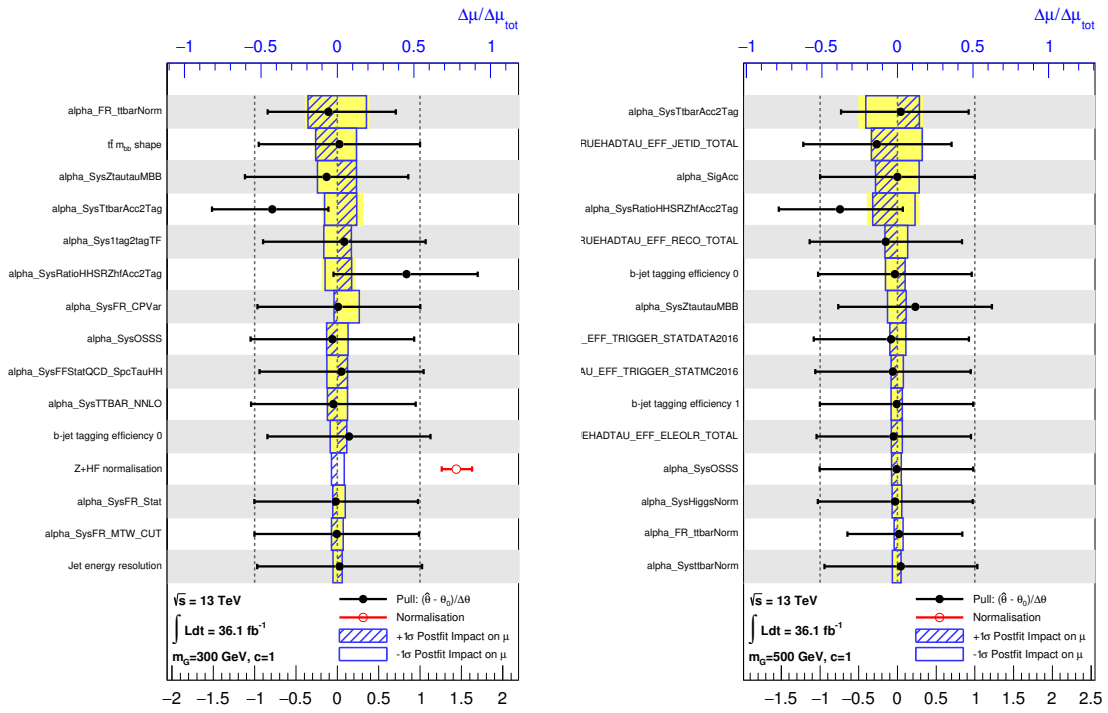

(a) (b)

(c)

Figure B.9: Fractional impact of the NPs on the RS graviton signal best fit value of the signal strength μ for the RS graviton signal with $c = 1$ and a) $m_G = 300$ GeV b) $m_G = 500$ GeV and c) $m_G = 1000$ GeV.

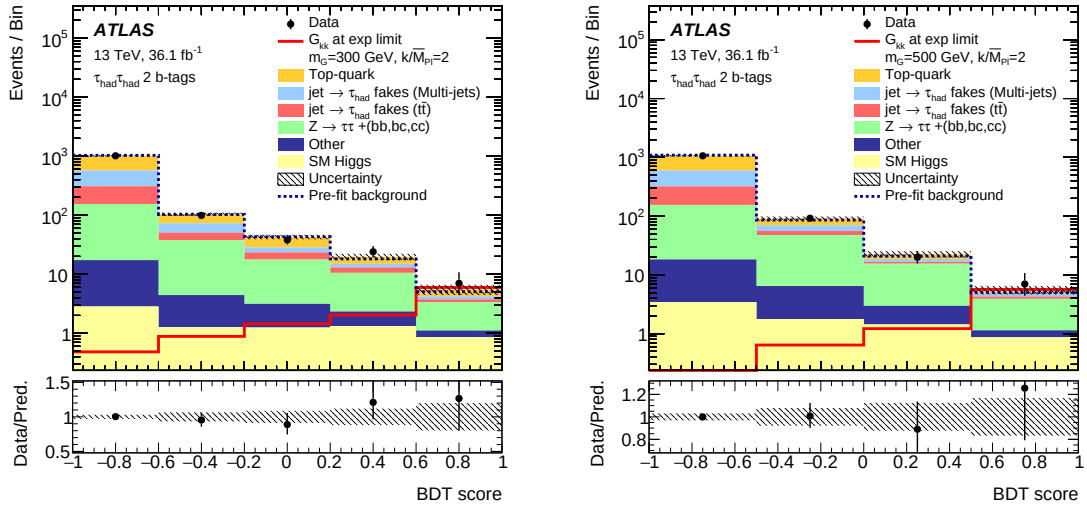

(a)

(b)

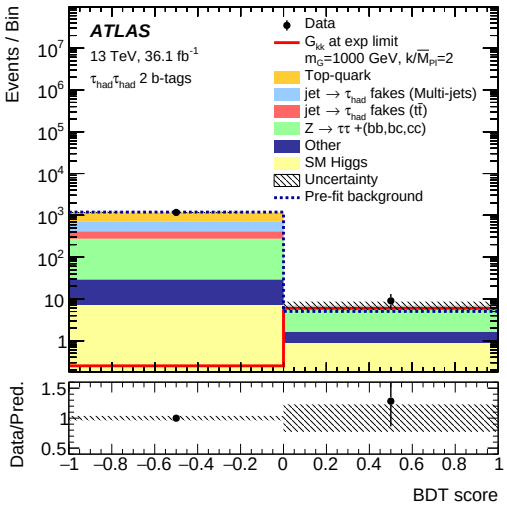

(c)

Figure B.10: Post-fit distribution of the RS graviton signal with $c = 2$ BDTs with a) $m_G = 300$ GeV b) $m_G = 500$ GeV and c) $m_G = 1000$ GeV. All background components are scaled to their normalisations as determined in the fit. The pre-fit normalisation of the sum of all background components predicted by the simulated events is given by the dashed blue line. The RS graviton with $c = 1$ signal distribution is also shown with a normalisation scaled to expected upper limit. The shaded bands represent the total post-fit uncertainty with NPs profiled to the data.

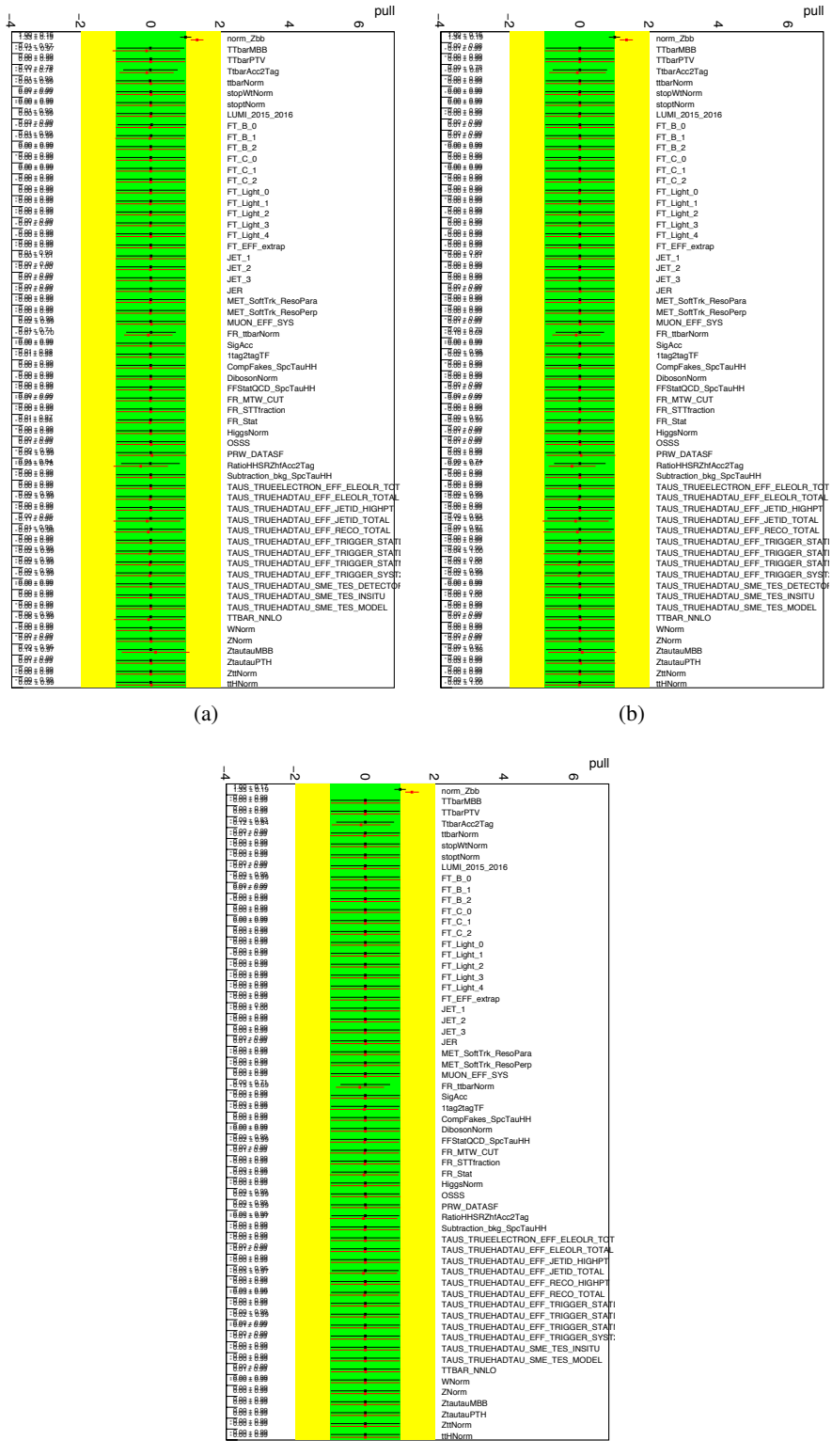

(a) (b)

(c)

Figure B.11: NP pulls from the fit of the RS graviton BDT to an Asimov dataset with $\mu = 0$ (black) and to the observed data (red) for the RS graviton signal with $c = 2$ and a) $m_G = 300$ GeV b) $m_G = 500$ GeV and c) $m_G = 1000$ GeV.

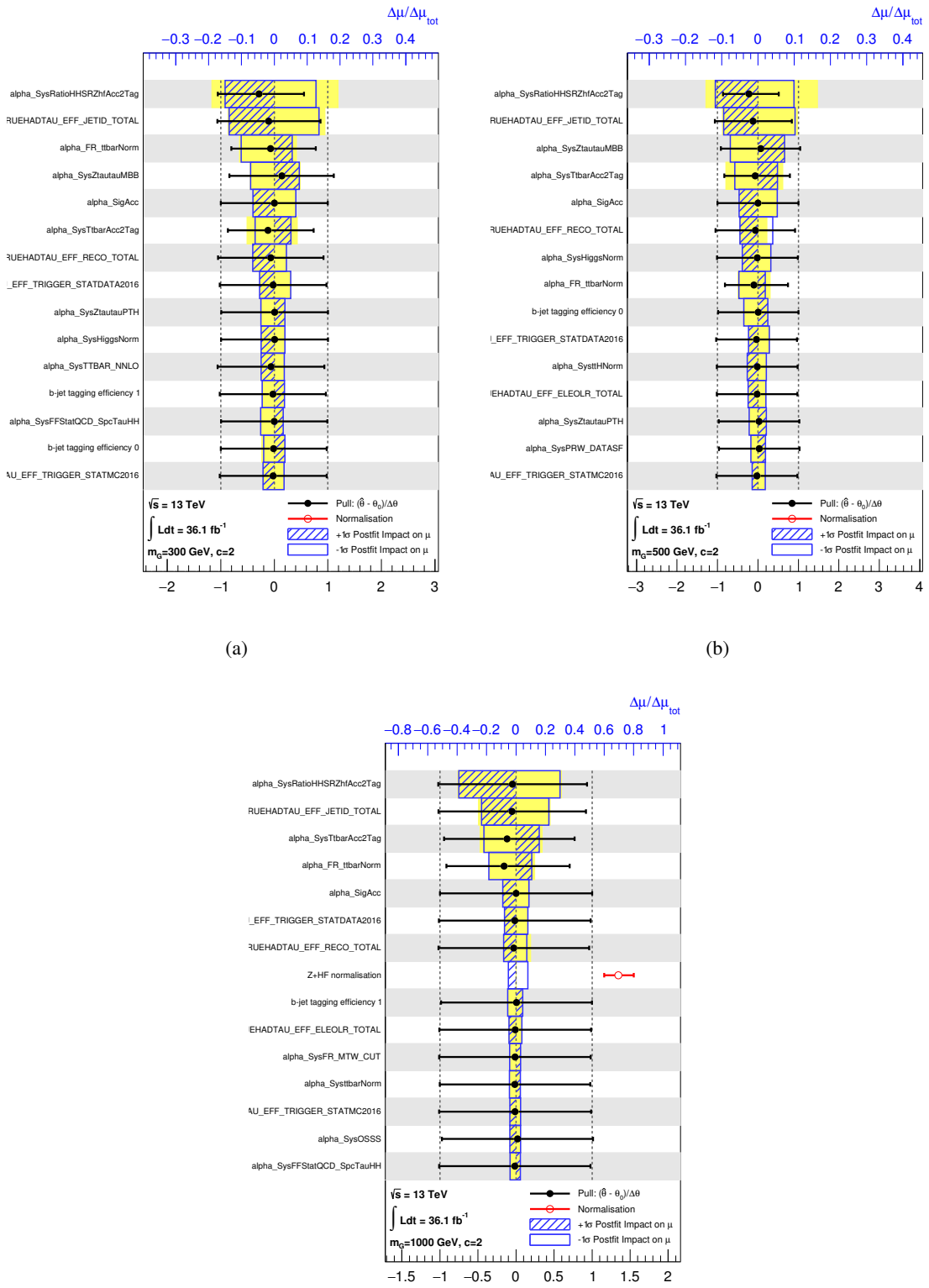

Figure B.12: Fractional impact of the NPs on the RS graviton signal best fit value of the signal strength μ for the RS graviton signal with $c = 2$ and a) $m_G = 300$ GeV b) $m_G = 500$ GeV and c) $m_G = 1000$ GeV.

NP name	Description
LUMI_2015_2016	integrated luminosity
PRW_DATASF	pile-up reweighting
TAUS_TRUEHADTAU_EFF_TRIGGER_STATDATA2015	τ trigger efficiency
TAUS_TRUEHADTAU_EFF_TRIGGER_STATDATA2016	τ trigger efficiency
TAUS_TRUEHADTAU_EFF_TRIGGER_STATMC2016	τ trigger efficiency
TAUS_TRUEHADTAU_EFF_TRIGGER_SYST2016	τ trigger efficiency
TAUS_TRUEHADTAU_EFF_RECO_TOTAL	τ reconstruction efficiency
TAUS_TRUEHADTAU_EFF_JETID_TOTAL	τ identification efficiency
TAUS_TRUEHADTAU_EFF_JETID_HIGHPT	τ identification efficiency
TAUS_TRUEHADTAU_EFF_ELEOLR_TOTAL	τ-electron overlap removal
TAUS_TRUEHADTAU_SME_TES_DETECTOR	τ energy scale
TAUS_TRUEHADTAU_SME_TES_INSITU	τ energy scale
TAUS_TRUEHADTAU_SME_TES_MODEL	τ energy scale
JET_1	jet energy scale
JET_2	jet energy scale
JET_3	jet energy scale
JER	jet energy resolution
FT_B_0	jet flavour tagging
FT_B_1	jet flavour tagging
FT_B_2	jet flavour tagging
FT_C_0	jet flavour tagging
FT_C_1	jet flavour tagging
FT_C_2	jet flavour tagging
FT_Light_0	jet flavour tagging
FT_Light_1	jet flavour tagging
FT_Light_2	jet flavour tagging
FT_Light_3	jet flavour tagging
FT_Light_4	jet flavour tagging
FT_EFF_extrap	jet flavour tagging
MET_SoftTrk_ResoPara	E_T^{miss}
MET_SoftTrk_ResoPerp	E_T^{miss}
MUON_EFF_SYS	muon identification

Table B.1: Experimental uncertainties NPs.

NP name	Description
ZttNorm	$Z \rightarrow \tau\tau$+ light flavour jets cross section
ZNorm	$Z \rightarrow$ others+ light flavour jets cross section
DibosonNorm	Diboson cross section
stopWtNorm	single-top cross section
stoptNorm	single-top cross section
WNorm	W+jets cross section and acceptance normalisation
HiggsNorm	ZH normalisation
ttHNorm	ttH normalisation
ttbarNorm	$t\bar{t}$ cross section
TtbarAcc2Tag	$t\bar{t}$ acceptance normalisation
TTbarMBB	$t\bar{t}$ shape
TTbarPTV	$t\bar{t}$ shape
TTBAR_NNLO	$t\bar{t}$ shape
norm_Zbb	Z+ HF floating normalisation
RatioHHSRZhfAcc2Tag	Z+ HF relative acceptance normalisation between control region and signal region
ZtautauMBB	Z+ HF shape
ZtautauPTH	Z+ HF shape
SigNorm	signal cross section
SigAcc	signal acceptance normalisation

Table B.2: MC background and signal modelling uncertainties NPs.

NP name	Description
FFStatQCD_SpcTauHH	multi-jet from FF statistics
Subtraction_bkg_SpcTauHH	multi-jet from MC background subraction
1tag2tagTF	multi-jet from TF statistics
OSSS	multi-jet from SS to OS extrapolation
CompFakes_SpcTauHH	multi-jet from non-closure
FR_Stat	fake-τ_{had} $t\bar{t}$ from FR statistics
FR_ttbarNorm	fake-τ_{had} $t\bar{t}$ from true-τ_{had} MC subtraction
FR_MTW_CUT	fake-τ_{had} $t\bar{t}$ from extrapolation from control region to signal region
FR_STTfraction	fake-τ_{had} $t\bar{t}$ from missing STT p_{T} cuts

Table B.3: Data-driven fake-τ_{had} uncertainties NPs.

APPENDIX C

Choice of the analysis strategy

The choice of using the BDT score distribution as final discriminant variable in the profile likelihood ratio fit is the result of a study performed in this thesis to define the strategy providing the best sensitivity.

At first, a cut-based approach was used. The signal region was defined starting from the event selection described in Section 6.3 and applying additional requirements, with cuts chosen by maximising the ATLAS standard significance formula, to make a tighter selection.

For the non-resonant analysis the following selection is added:

- the invariant mass of the di-b-jet system must be $80 < m_{bb} < 140$ GeV.

Then, the $M_{\tau\tau}^{MMC}$ in this signal region is used as final discriminant in the fit.

For the resonant analysis the following selections are added:

- the invariant mass of the di-b-jet system must be $80 < m_{bb} < 140$ GeV;
- the invariant mass of the di-τ system reconstructed with the MMC must be $85 < m_{\tau\tau}^{MMC} < 140$ GeV;
- the transverse momentum of the di-b-jet system must be, depending on the signal mass:
  - $p_T^{bb} > 100$ GeV for $400 \leq m < 500$ GeV;
  - $p_T^{bb} > 150$ GeV for $500 \leq m < 800$ GeV;
  - $p_T^{bb} > 200$ GeV for $m \geq 800$ GeV.

Then, the di-Higgs invariant mass m_{HH} in the signal region is used as final discriminant in the fit.

A second approach was tested in which a BDT was used to separate signal and background and define the signal region. The BDT was trained using the input variables listed in Section 6.5 except the di-Higgs invariant mass. The signal region was then defined starting from the event selection described in Section 6.3 and applying a cut on the BDT score, with the cut value chosen by maximising the significance, and the di-Higgs invariant mass was used as final discriminant in the fit.

Finally, the BDT was trained with the list of variables reported in Section 6.5 and the BDT score distribution was used as final discrimininant variable in the signal region defined as in Section 6.3.

The comparison of the expected upper limits on the SM di-Higgs production signal strength obtained with the three different strategies is given in Table C.1. The comparison of the expected upper limits on the resonant di-Higgs production cross section times $bb\tau\tau$ BR obtained with the three different strategies is shown in Figure C.1. This comparisons shows that the use of a BDT to define the signal region improved the results by about a factor 1.6 compared to the simple cut-based approach in the non-resonant

	Median expected limit on μ
Cut-based	43
BDT-cut	27
BDT-fit	17

Table C.1: Expected upper limits on the SM di-Higgs production signal strength obtained with the cut-based analysis, cutting on the BDT score and fitting the BDT score.

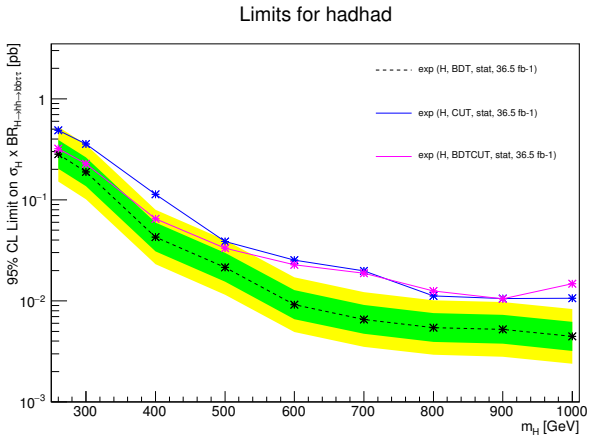

Figure C.1: Expected upper limits on the resonant di-Higgs production cross section times $bb\tau\tau$ BR as a function of the resonance mass for the narrow width scalar of the 2HDM obtained with the cut-based analysis (blue), cutting on the BDT score (magenta) and fitting the BDT score (black).

analysis and in resonant analysis in the low mass region below 500 GeV but does not improve the results for high masses, while fitting the BDT score distribution improved the results by about a factor 2.5 both in the non-resonant analysis and in the resonant analysis over the full tested mass range.

APPENDIX D

Profile likelihood fit: test of the background-only hypothesis for the BSM $HH \to b\bar{b}\tau^{+}\tau^{-}$ analysis combination

In Section 7.1 describing the $bb\tau\tau$ combination only the plots from the $bb\tau\tau$ combined SM BDT fit are shown. In this Section the NP pulls and rankings are included for the non resonant signal with $k_\lambda = 20$ and for some mass points (300, 500, 1000 GeV) for the 2HDM and the RS graviton with $c = 1, 2$ signals.

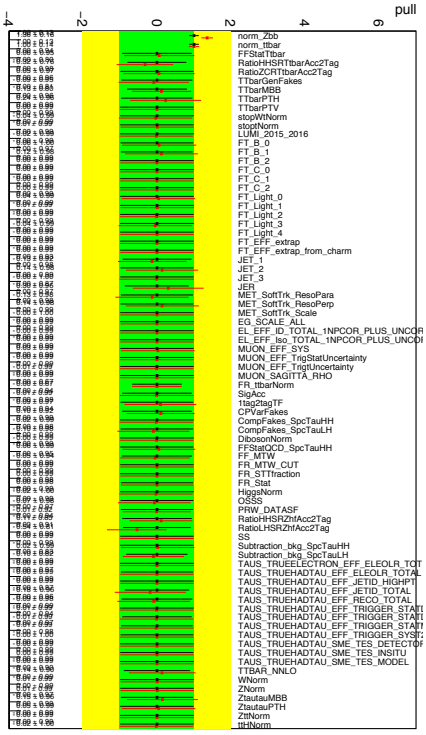

Figure D.1: NP pulls from the $bb\tau\tau$ combined fit of the non resonant with $k_\lambda = 20$ BDT to an Asimov dataset with $\mu = 0$ (black) and to the observed data (red).

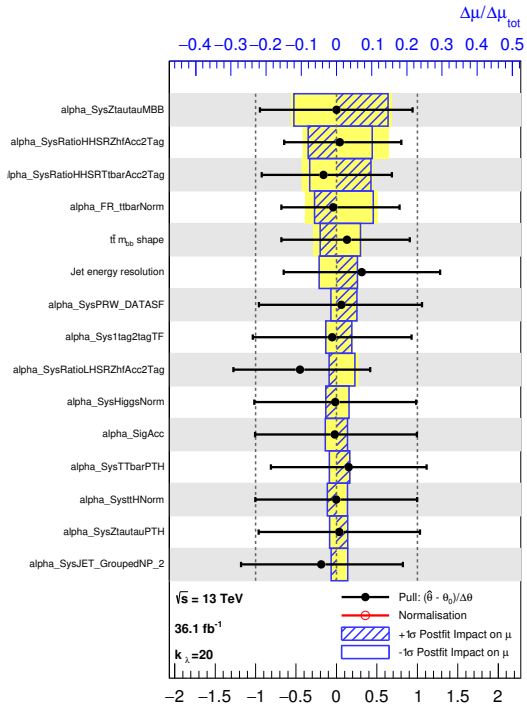

Figure D.2: Fractional impact of the NPs on the non resonant $k_\lambda = 20$ signal $bb\tau\tau$ combined best fit value of the signal strength μ.

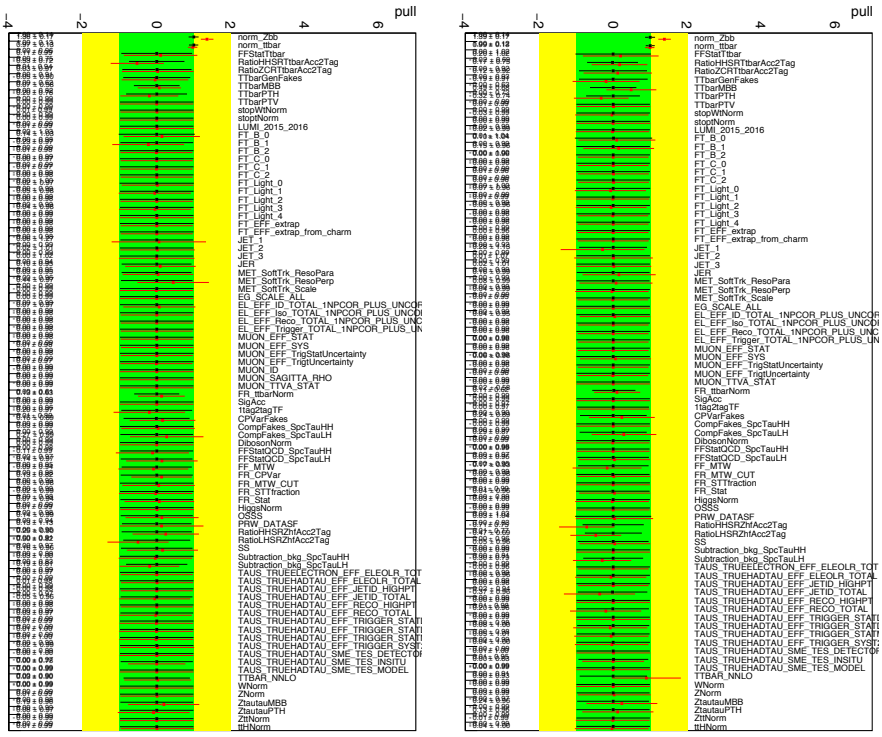

(a)

(b)

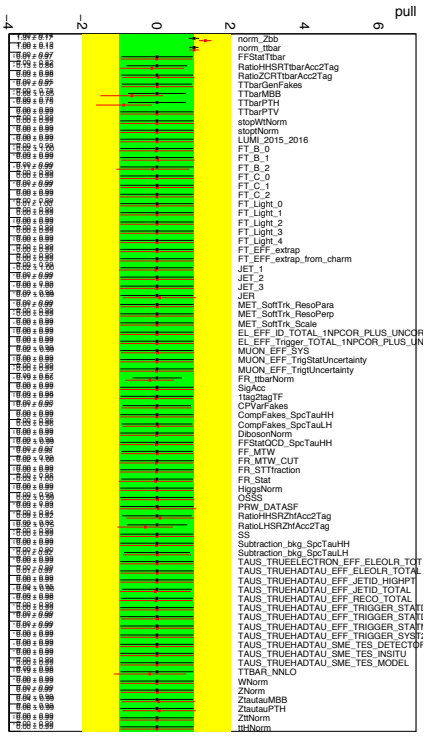

(c)

Figure D.3: NP pulls from the $bb\tau\tau$ combined fit of the 2HDM BDT to an Asimov dataset with $\mu = 0$ (black) and to the observed data (red) for the 2HDM signal with a) $m_X = 300$ GeV b) $m_X = 500$ GeV and c) $m_X = 1000$ GeV.

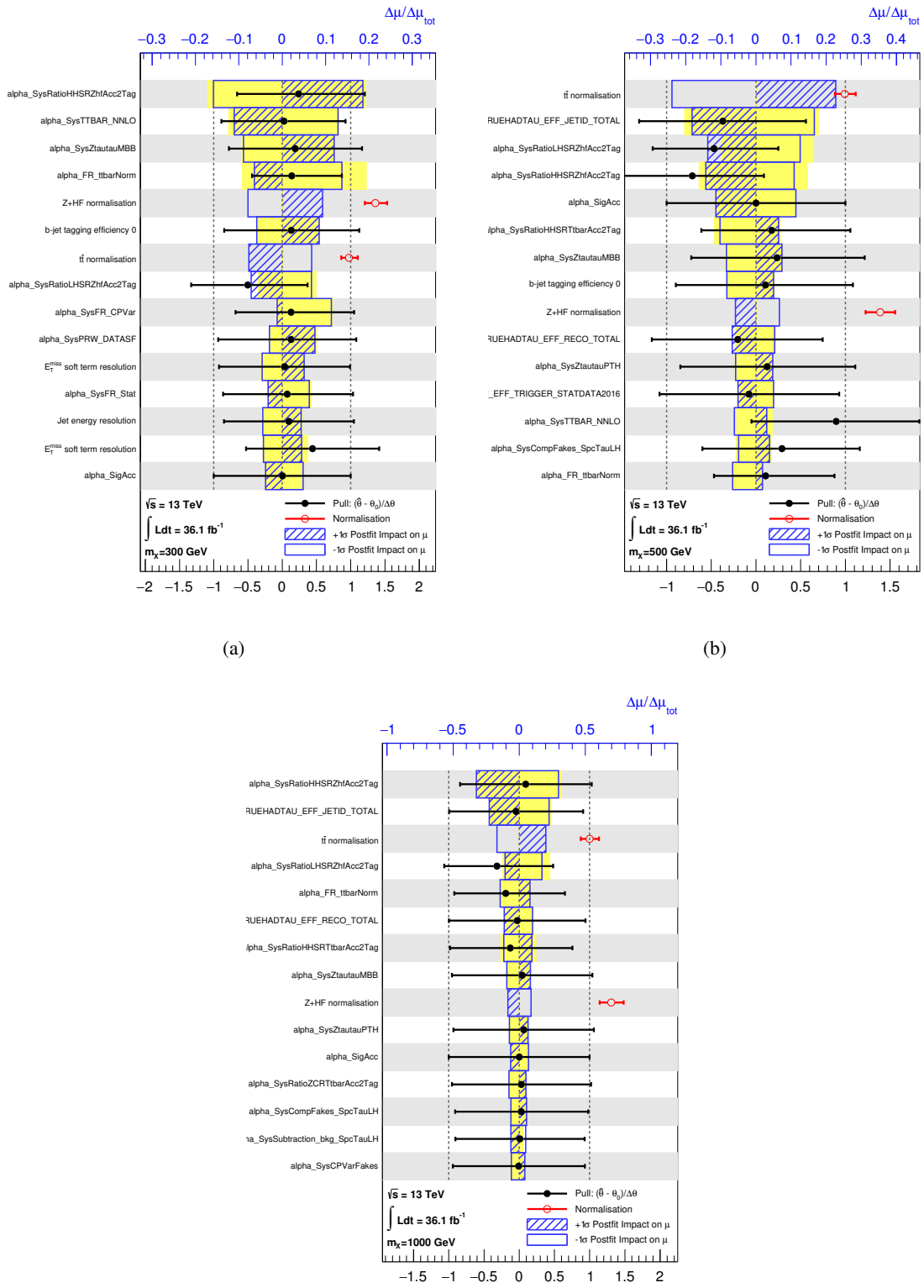

Figure D.4: Fractional impact of the NPs on the 2HDM signal $bb\tau\tau$ combined best fit value of the signal strength μ for the 2HDM signal with a) $m_X = 300$ GeV b) $m_X = 500$ GeV and c) $m_X = 1000$ GeV.

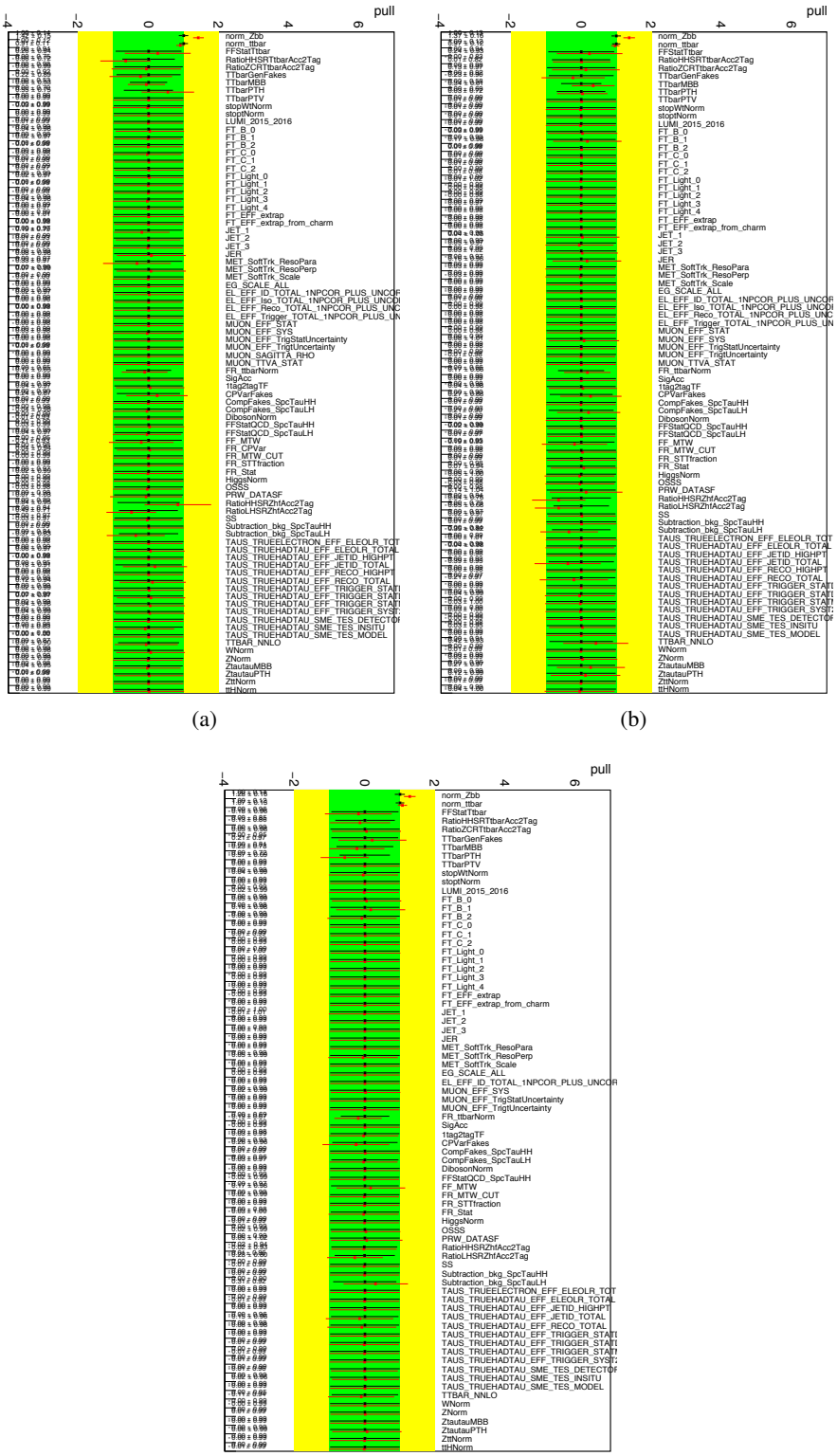

(a) (b)

(c)

Figure D.5: NP pulls from the $bb\tau\tau$ combined fit of the RS graviton BDT to an Asimov dataset with $\mu = 0$ (black) and to the observed data (red) for the RS graviton signal with $c = 1$ and a) $m_G = 300$ GeV b) $m_G = 500$ GeV and c) $m_G = 1000$ GeV.

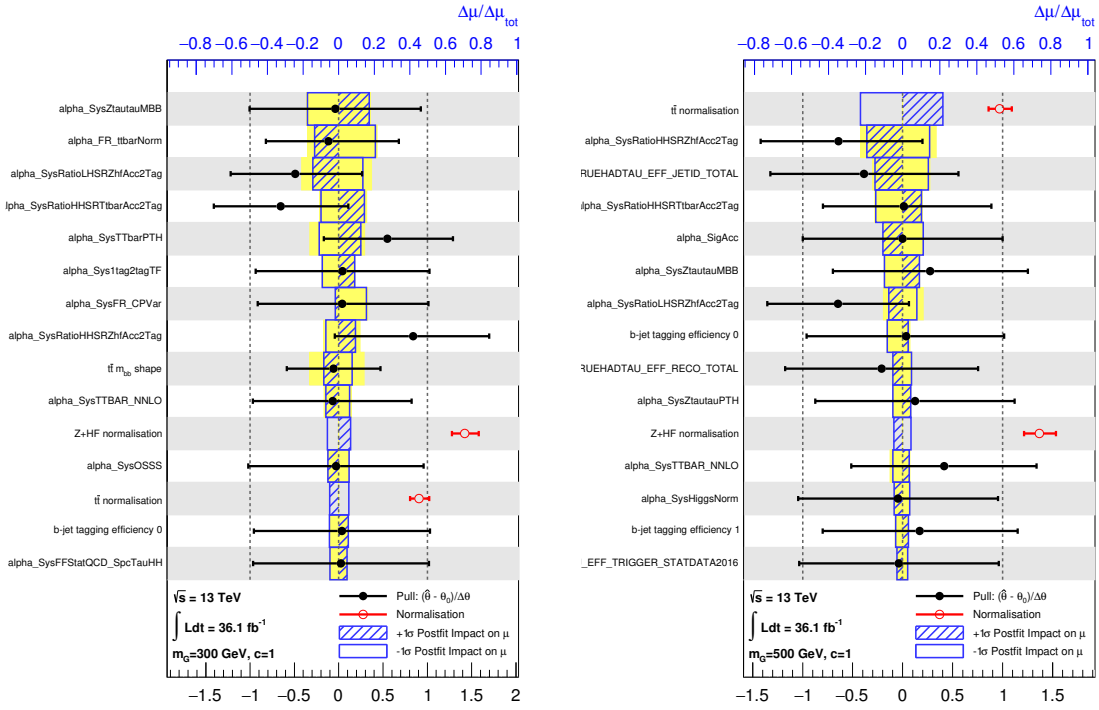

(a) (b)

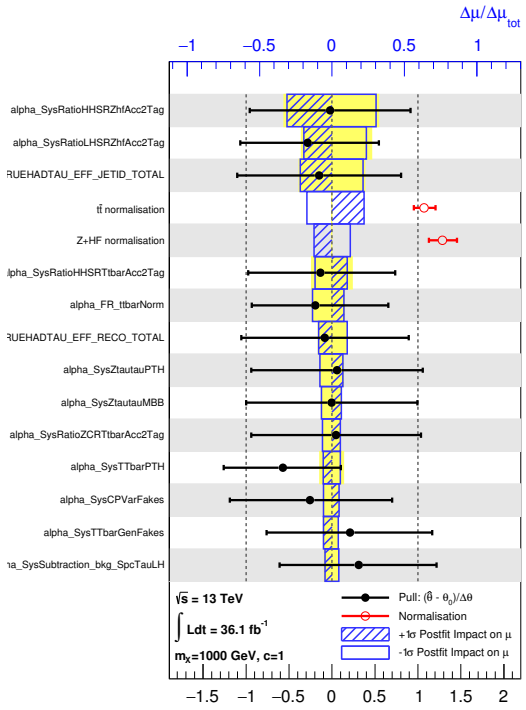

(c)

Figure D.6: Fractional impact of the NPs on the RS graviton signal $bb\tau\tau$ combined best fit value of the signal strength μ for the RS graviton signal with $c = 1$ and a) $m_G = 300$ GeV b) $m_G = 500$ GeV and c) $m_G = 1000$ GeV.

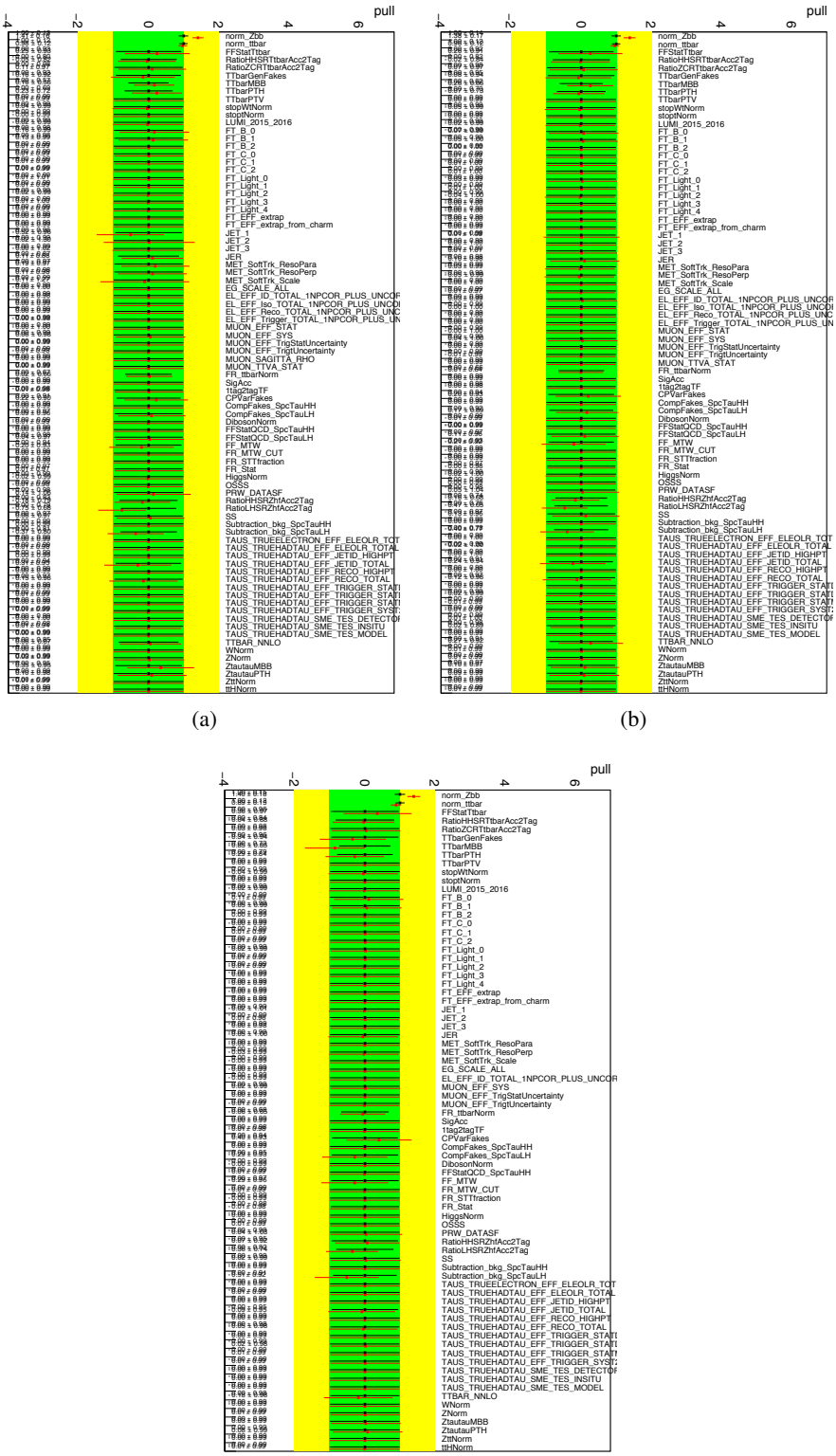

(a) (b)

(c)

Figure D.7: NP pulls from the $bb\tau\tau$ combined fit of the RS graviton BDT to an Asimov dataset with $\mu = 0$ (black) and to the observed data (red) for the RS graviton signal with $c = 2$ and a) $m_G = 300$ GeV b) $m_G = 500$ GeV and c) $m_G = 1000$ GeV.

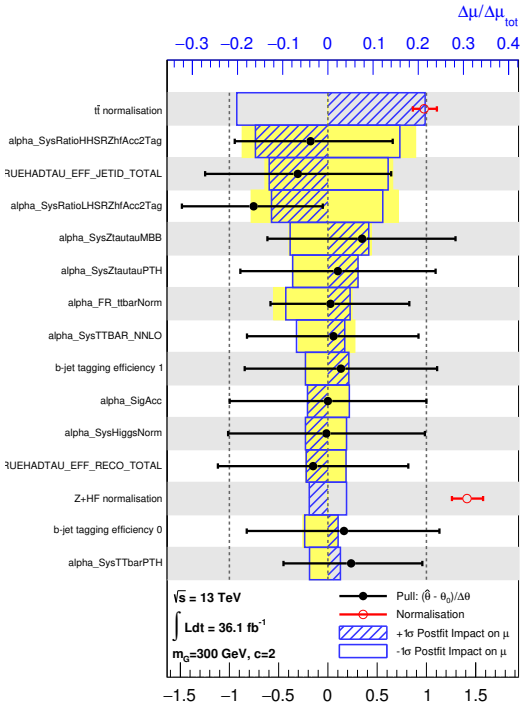

(a)

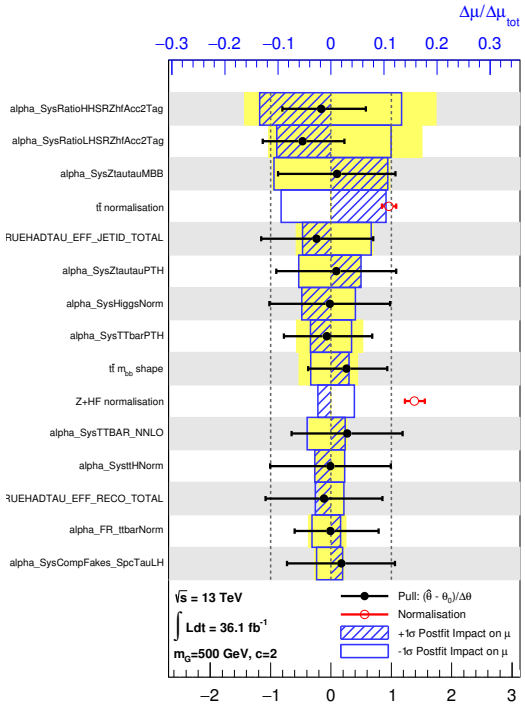

(b)

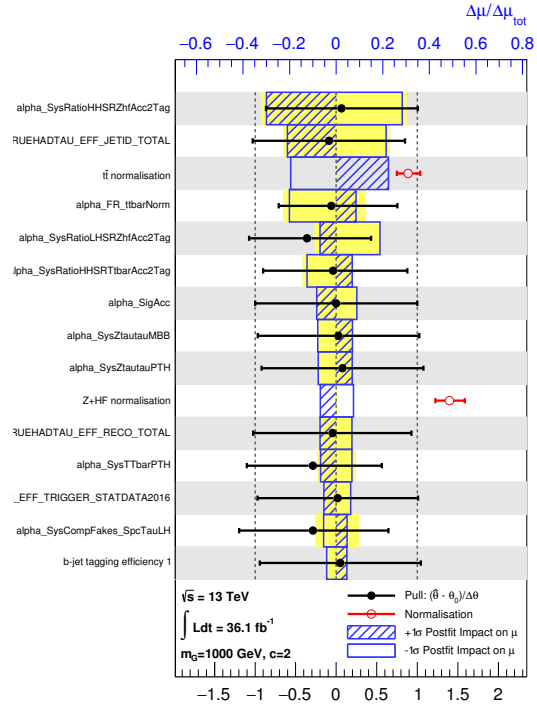

(c)

Figure D.8: Fractional impact of the NPs on the RS graviton signal $bb\tau\tau$ combined best fit value of the signal strength μ for the RS graviton signal with $c = 2$ and a) $m_G = 300$ GeV b) $m_G = 500$ GeV and c) $m_G = 1000$ GeV.

APPENDIX E

Measurement prospects at the HL-LHC

The extrapolated number of SM di-Higgs signal and background events expected in the full signal regions, in the last two bins of the BDTs and in the last bin of the BDTs are reported in Appendix E in Tables E.1, E.2 and E.3 respectively.

Component	Events in $\tau_{had}\tau_{had}$ SR	Events in $\tau_{lep}\tau_{had}$ SLT SR	Events in $\tau_{lep}\tau_{had}$ LTT SR
$t\bar{t}$	57600 ± 2000	2218000 ± 13000	176000 ± 2300
Single top	4490 ± 150	129200 ± 2800	8240 ± 230
Multi-jet τ-fakes	33500 ± 2100		
$t\bar{t}$ τ-fakes	20400 ± 2200		
τ fakes		867000 ± 13000	51100 ± 2300
Z + HF	23800 ± 1100	51800 ± 2100	14600 ± 600
SM single Higgs	900 ± 60	4280 ± 360	460 ± 40
Other	2550 ± 350	24300 ± 1000	1710 ± 160
Total background	143200 ± 400	3295300 ± 1800	252050 ± 500
SM HH	81 ± 8	107 ± 6	23.9 ± 1.3

Table E.1: Extrapolated expected number of signal and background events in the three $bb\tau\tau$ signal regions. The total background is not identical to the sum of the individual components since the latter are rounded for presentation, while the sum is calculated with the full precision before being subsequently rounded. Systematic uncertainties are included. Due to the large correlations, individual uncertainties can be significantly larger than the total uncertainty.

Component	Events in $\tau_{had}\tau_{had}$ SR	Events in $\tau_{lep}\tau_{had}$ SLT SR	Events in $\tau_{lep}\tau_{had}$ LTT SR
$t\bar{t}$	370 ± 30	1830 ± 40	1780 ± 30
Single top	32.3 ± 2.8	720 ± 20	420 ± 40
Multi-jet τ-fakes	100 ± 20		
$t\bar{t}$ τ-fakes	146 ± 19		
τ-fakes		1210 ± 34	640 ± 40
Z + HF	610 ± 60	1290 ± 70	1150 ± 70
SM single Higgs	134 ± 8	220 ± 10	64 ± 3
Other	80 ± 10	460 ± 20	180 ± 20
Total background	1470 ± 90	5730 ± 90	4230 ± 90
SM HH	54 ± 5	52 ± 3	16.2 ± 0.8

Table E.2: Extrapolated expected number of signal and background events in the last two bins of the SM BDT distribution in the three $bb\tau\tau$ signal regions. The total background is not identical to the sum of the individual components since the latter are rounded for presentation, while the sum is calculated with the full precision before being subsequently rounded. Systematic uncertainties are included. Due to the large correlations, individual uncertainties can be significantly larger than the total uncertainty.

Component	Events in $\tau_{had}\tau_{had}$ SR	Events in $\tau_{lep}\tau_{had}$ SLT SR	Events in $\tau_{lep}\tau_{had}$ LTT SR
$t\bar{t}$	0	235 ± 6	360 ± 30
Single top	0	283 ± 15	54 ± 3
Multi-jet τ-fakes	33.7 ± 7.2		
$t\bar{t}$ τ-fakes	12.9 ± 2.0		
τ-fakes		300 ± 10	97 ± 9
Z + HF	95 ± 16	340 ± 20	470 ± 40
SM single Higgs	55 ± 3	78 ± 4	31 ± 2
Other	12.2 ± 2.1	105 ± 5	61 ± 7
Total background	209 ± 17	1343 ± 25	1069 ± 55
SM HH	32 ± 3	32.8 ± 1.6	9.8 ± 0.5

Table E.3: Extrapolated expected number of signal and background events in the last bin of the SM BDT distribution in the three $bb\tau\tau$ signal regions. The total background is not identical to the sum of the individual components since the latter are rounded for presentation, while the sum is calculated with the full precision before being subsequently rounded. Systematic uncertainties are included. Due to the large correlations, individual uncertainties can be significantly larger than the total uncertainty.

APPENDIX F

BDT trainings for the $LQ_3LQ_3 \rightarrow b\tau_{had}b\tau_{had}$ analysis

As described in Section 8.6, dedicated BDTs are trained to target the several LQ_3^u mass hypotheses considered in the analysis, separately in the 1 b-tag and 2 b-tags regions. In Section 8.6 only plots for a LQ_3^u signal with a mass of $m_{LQ} = 500$ GeV are provided. In this section the BDT input variables distributions, the correlation matrices and the BDT scores are included for some other mass points (300, 1000, 1500 GeV).

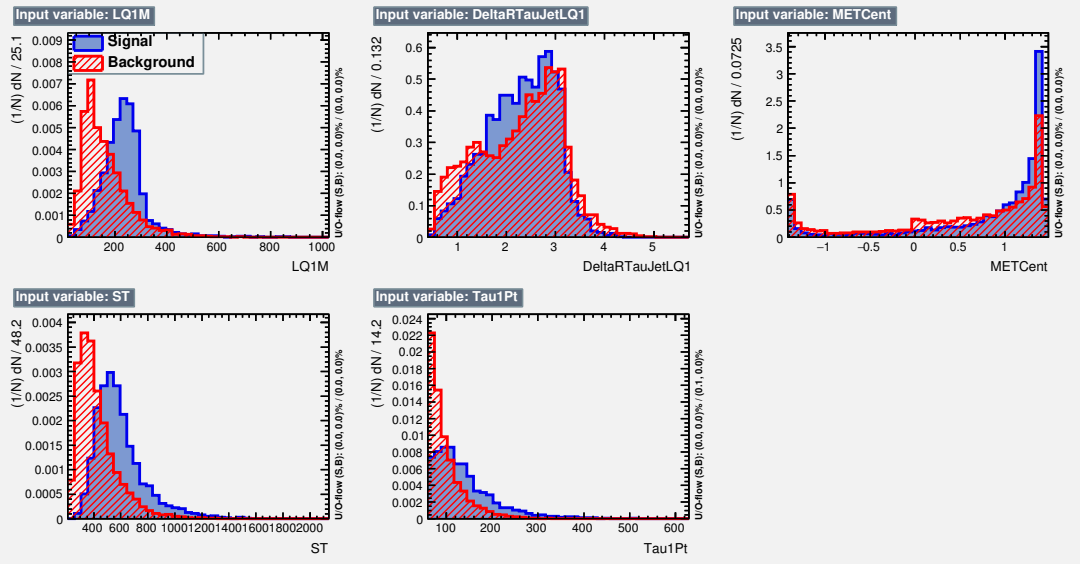

Figure F.1: BDT input variables distributions for the LQ_3^u signal with $m_{LQ} = 300$ GeV (blue) and for the background (red) in the 1 b-tag region.

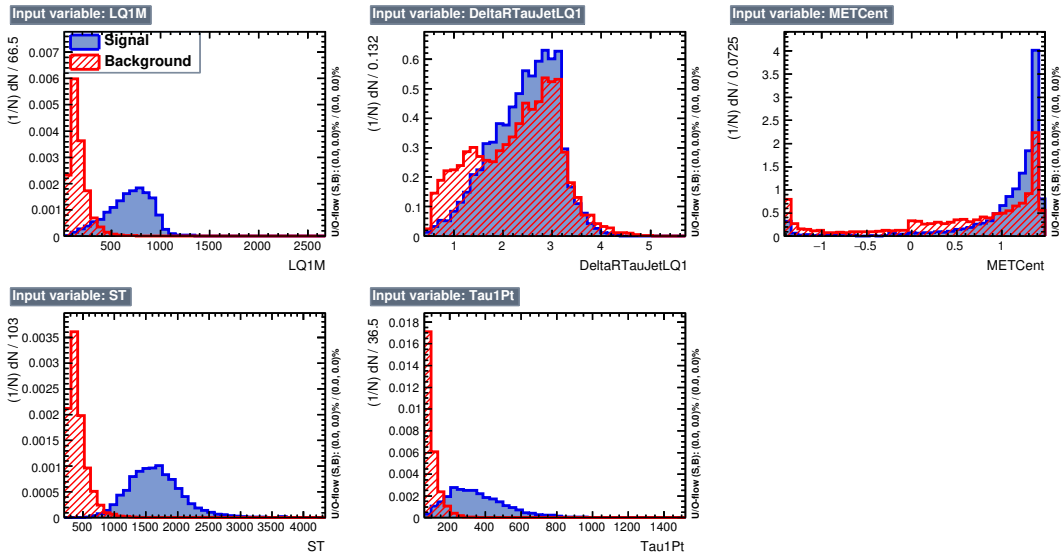

Figure F.2: BDT input variables distributions for the LQ_3^u signal with $m_{LQ} = 1000\,\text{GeV}$ (blue) and for the background (red) in the 1 b-tag region.

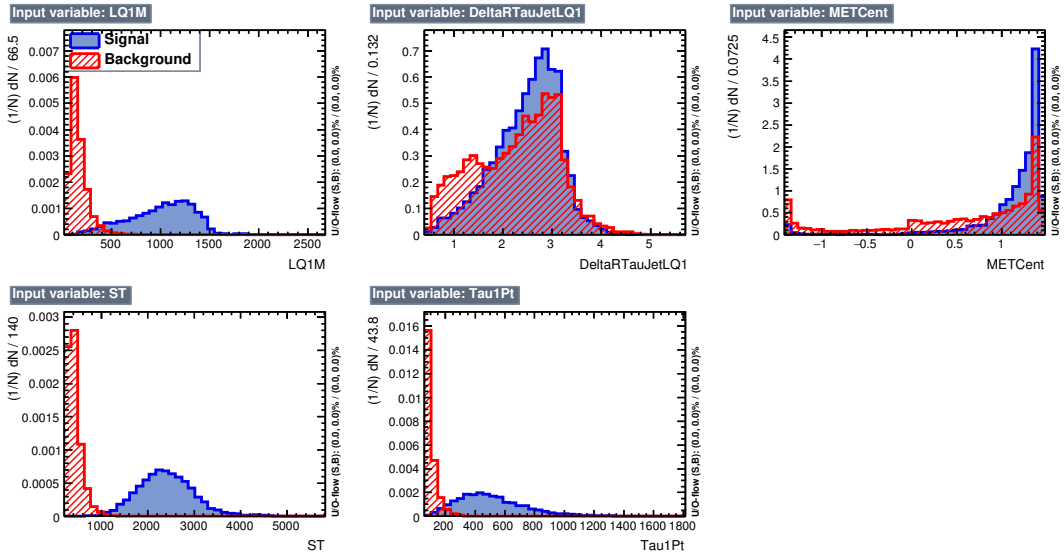

Figure F.3: BDT input variables distributions for the LQ_3^u signal with $m_{LQ} = 1500\,\text{GeV}$ (blue) and for the background (red) in the 1 b-tag region.

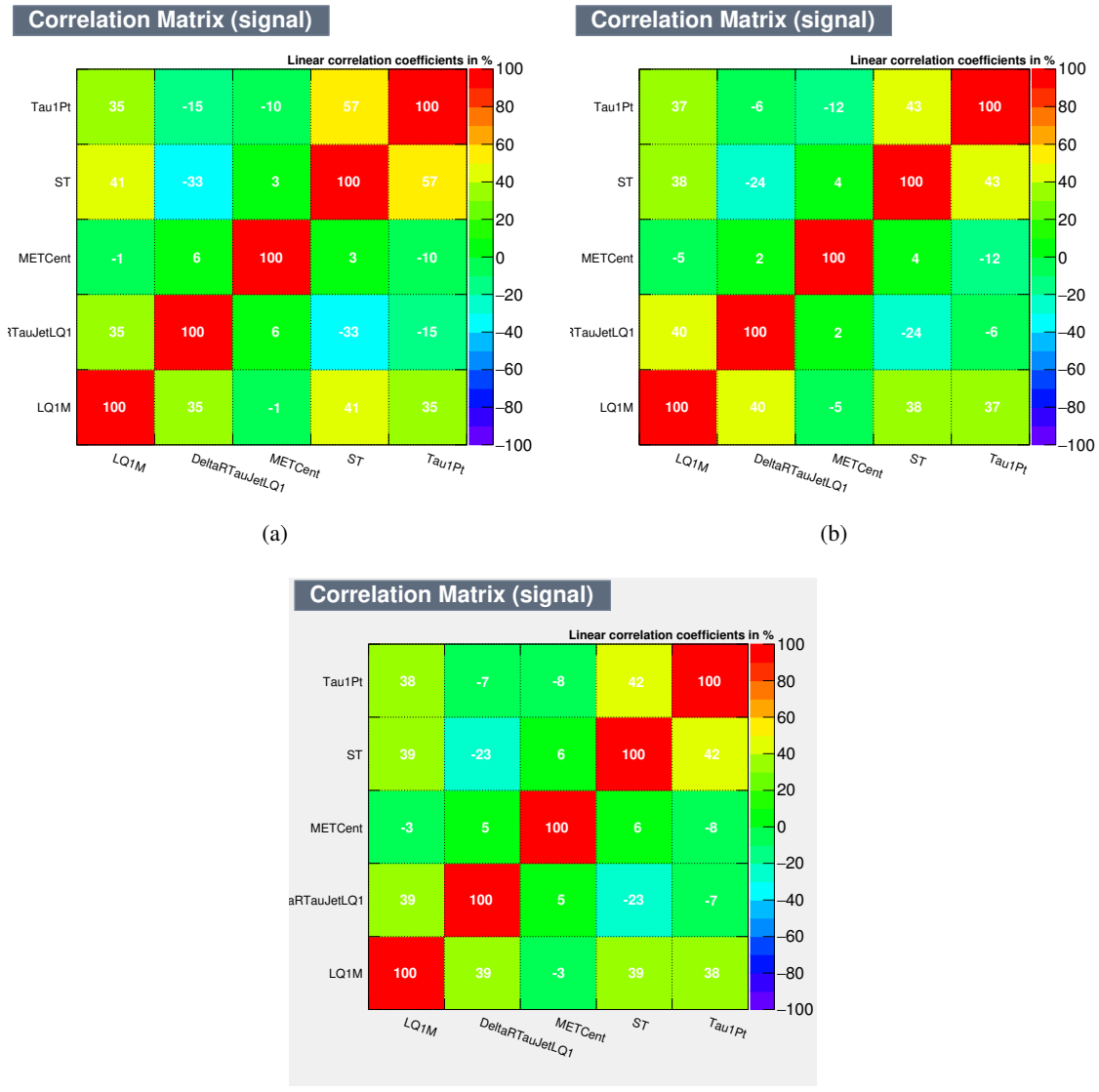

(a) (b)

(c)

Figure F.4: BDT input variables linear correlation coefficients for the LQ_3^u signal with a) m_{LQ} = 300 GeV b) m_{LQ} = 1000 GeV and c) m_{LQ} = 1500 GeV in the 1 b-tag region.

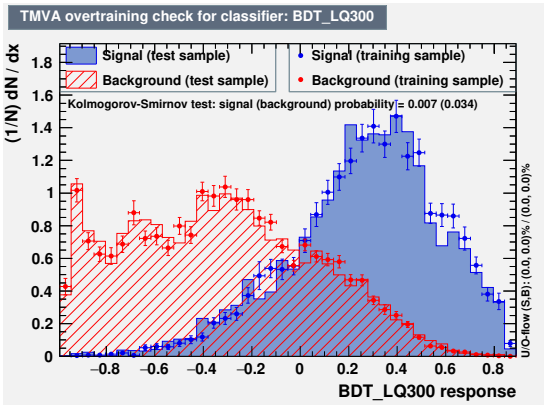

(a)

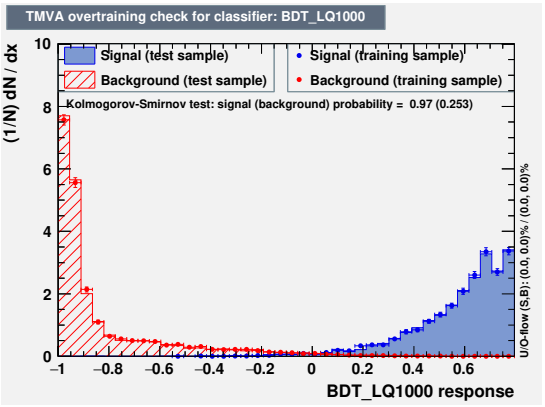

(b)

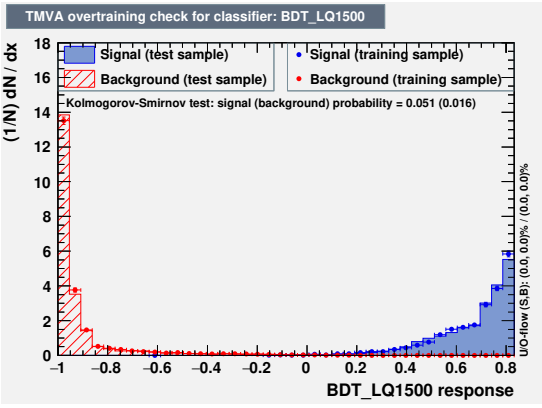

(c)

Figure F.5: BDT score distribution for the LQ_3^u signal (blue) with a) m_{LQ} = 300 GeV b) m_{LQ} = 1000 GeV and c) m_{LQ} = 1500 GeV and for the background (red) in the 1 b-tag region.

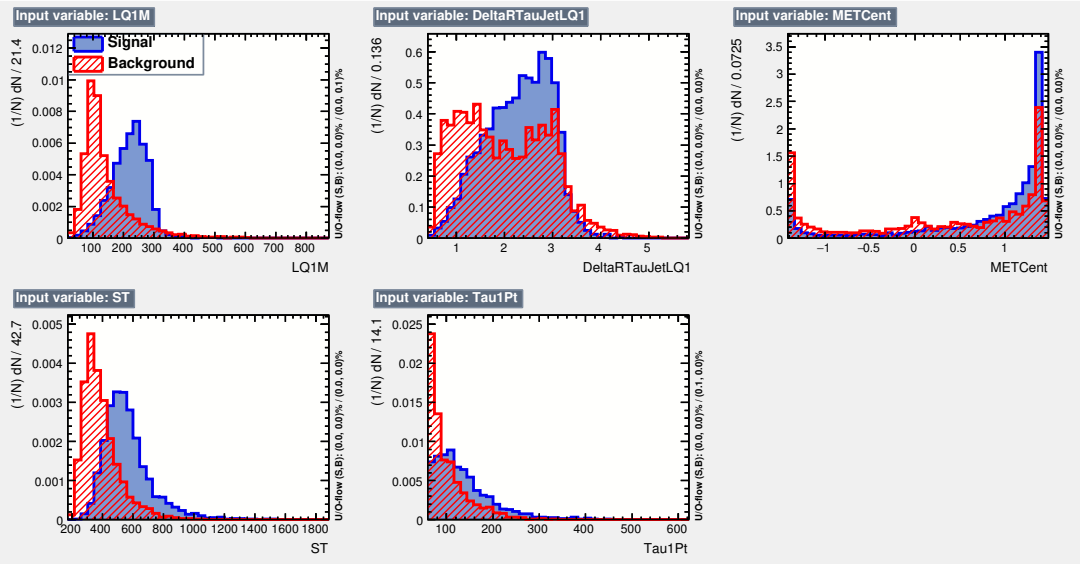

Figure F.6: BDT input variables distributions for the LQ_3^u signal with $m_{LQ} = 300$ GeV (blue) and for the background (red) in the 2 b-tags region.

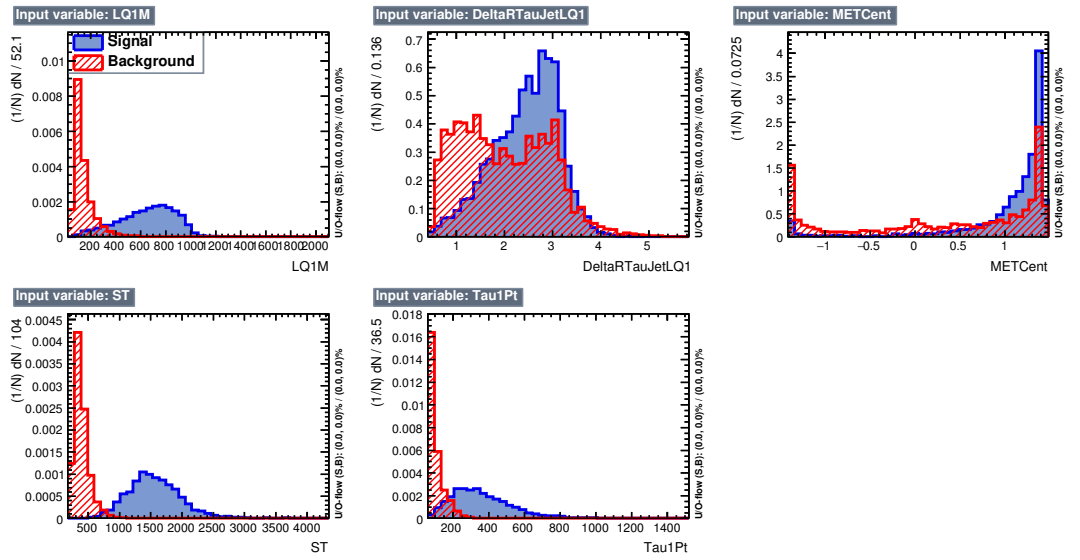

Figure F.7: BDT input variables distributions for the LQ_3^u signal with $m_{LQ} = 1000$ GeV (blue) and for the background (red) in the 2 b-tags region.

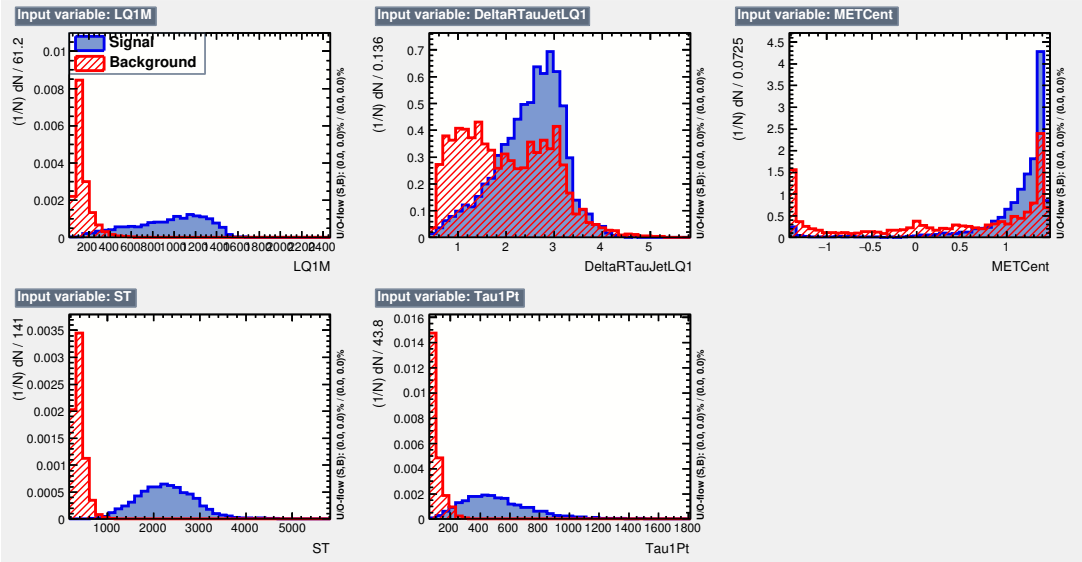

Figure F.8: BDT input variables distributions for the LQ_3^u signal with $m_{LQ} = 1500\,\text{GeV}$ (blue) and for the background (red) in the 2 b-tags region.

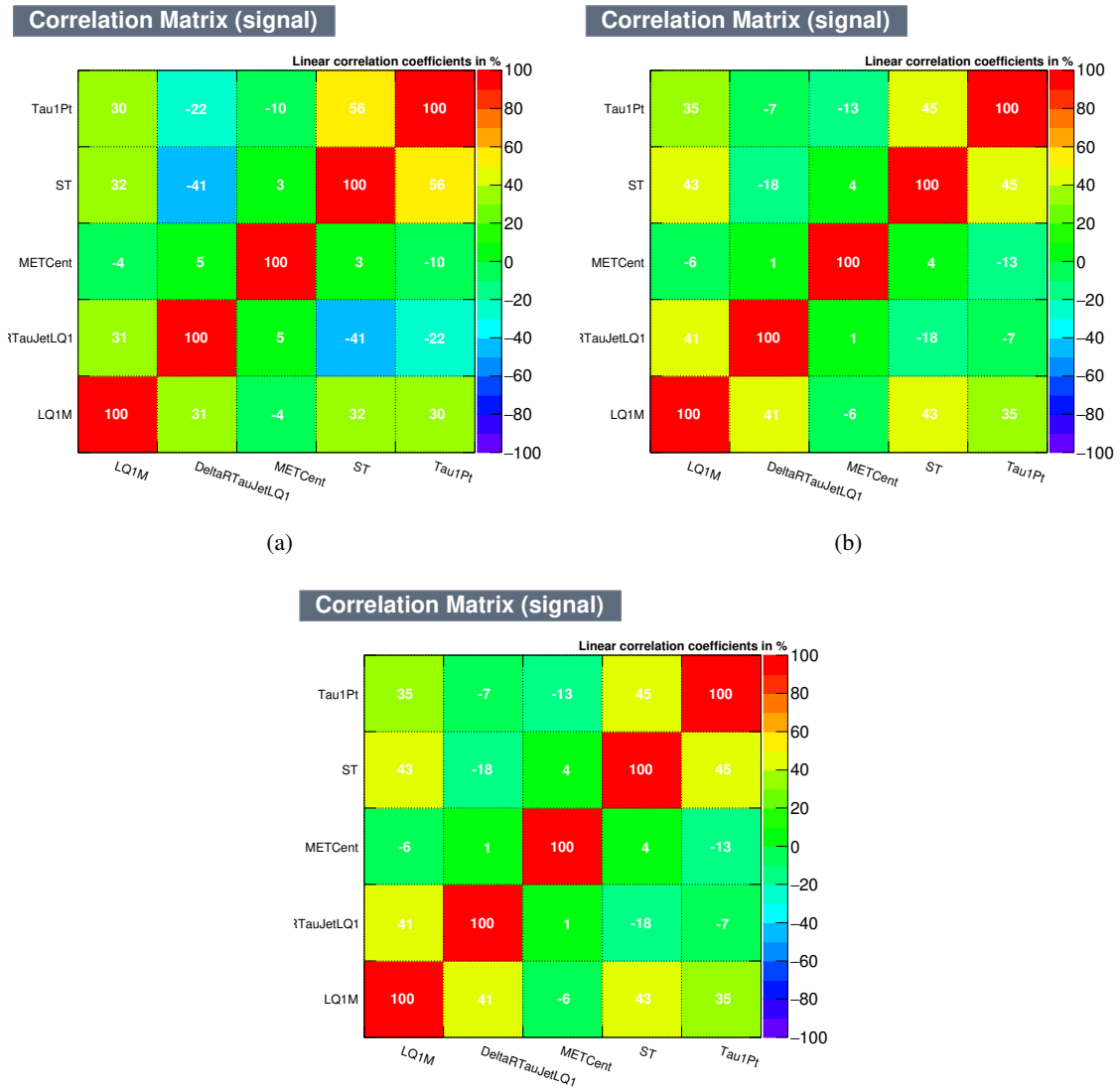

Figure F.9: BDT input variables linear correlation coefficients for the LQ_3^u signal with a) $m_{LQ} = 300$ GeV b) $m_{LQ} = 1000$ GeV and c) $m_{LQ} = 1500$ GeV in the 2 b-tags region.

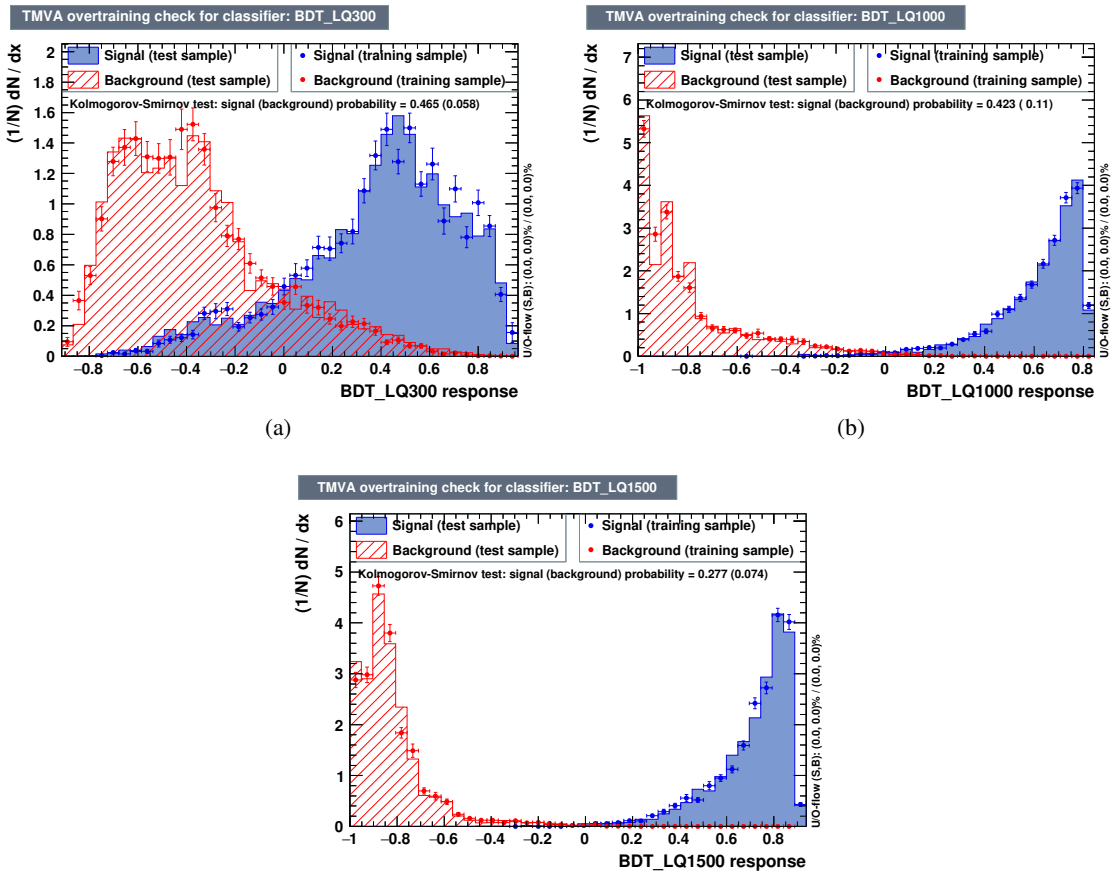

Figure F.10: BDT score distribution for the LQ_3^u signal (blue) with a) m_{LQ} = 300 GeV b) m_{LQ} = 1000 GeV and c) m_{LQ} = 1500 GeV and for the background (red) in the 2 b-tags region.

List of Figures

List of Tables